S-band electron LINAC for ThomX

Muath Alkadi

université
PARIS-SACLAY

S-band electron LINAC for ThomX

LINAC à électrons en bande S pour ThomX

Thèse de doctorat de l'université Paris-Saclay

École doctorale n°576 Particules, hadrons, énergie et noyau: instrumentation, imagerie, cosmos et simulation (PHENIICS)
Spécialité de doctorat: Physique des accélérateurs
Graduate School : Physique. Référent: Faculté des sciences d'Orsay

Thèse préparée dans l'unité de recherche **IJCLab** (Université Paris-Saclay, CNRS),
sous la direction de **Marie JACQUET**, directrice de recherche,
la co-direction de **Christelle BRUNI**, chargée de recherche,
et la co-direction de **Mohamed EL KHALDI**, ingénieur de recherche

Thèse soutenue à Paris-Saclay, le 28 Septembre 2022, par

Muath ALKADI

Composition du jury

Fabian ZOMER Professeur des universités, Université Paris-Saclay	Président
Turki ALKHURAIJI Professeur des universités, KACST	Rapporteur & Examinateur
Benito GIMENO MARTÍNEZ Professeur des universités, University of Valencia	Rapporteur & Examinateur
Ayash ALRASHDI Maître de conférences, KACST	Examinateur
Adel DOUAHI Ingénieur, Thales LAS France SAS	Examinateur
Marie JACQUET Directrice de recherche, IJCLab	Directrice de thèse

THESE DE DOCTORAT
NNT : 2022UPASP097

université PARIS-SACLAY

ÉCOLE DOCTORALE
Particules, hadrons, énergie et noyau : instrumentation, imagerie, cosmos et simulation (PHENIICS)

Titre: LINAC à électrons en bande S pour ThomX

Mots clés: ThomX, Bande S, Accélérateur linéaire, Photo-injecteur, RF, Dynamique du faisceau, Rayons X, Diffusion Compton inverse, Électrons.

Résumé:

ThomX est une source de rétrodiffusion qui vise à fournir un flux moyen de photons d'environ 10^{12}-10^{13} ph/s dans la gamme des rayons X durs (40-90) keV. Ma thèse porte sur l'étude et la conception du linac ThomX et du son upgrade en bande S, à savoir le canon RF et les deux sections accélératrices que sont des structures à ondes progressives. Tout d'abord, la thèse met en évidence la physique de la diffusion Compton inverse avec une description de la cinématique des collisions entre photons et électrons. En outre, elle donne une explication générale du flux de photons Compton et de la luminosité ainsi que les principales applications possibles de la machine ThomX sont discutées. En outre, la thèse explique en détail la source radiofréquence (RF) de haute puissance pour la machine ThomX, à savoir le modulateur qui est du type ScandiNova K2-2 et le Klystron qui est du type Toshiba E 37310, y compris les résultats des tests d'acceptation. Elle comprend également le développement des composants du réseau, tels que le diviseur de puissance, le circulateur de puissance, les déphaseurs et les atténuateurs, ainsi que les tests de faible puissance RF de ces composants. Ma thèse fournit également les caractéristiques électromagnétiques du linac ThomX, à savoir la structure quasi gradient de l'injecteur linac LEP (LIL) et le canon RF, ainsi que la configuration des solénoïdes en utilisant CST Studio Suite®. Je présente également les caractéristiques du système de refroidissement du linac ThomX, l'analyse thermique et les tests du système de vide. Le commissioning du linac ThomX est effectuée en deux parties: le conditionnement RF et l'obtention du premièr faisceau. La mesure de la charge, à l'aide de l'ICT, et les mesures d'énergie, à l'aide d'aimants orientables ont étaient utilisés pour charactariser le faisceau. En outre, des modèles d'approximation analytiques pour l'énergie et la propagation de l'énergie dans les structures à ondes stationnaires et progressives sont proposés et ajustés aux mesures. En outre, un travail expérimental réalisé sur le photoinjecteur PHIL est présenté pour les mesures de l'énergie du faisceau et de la propagation de l'énergie en utilisant un aimant dipôle dans le but d'acquérir des compétences pratiques avant la mise en service de ThomX. Ma thèse présente également la simulation et l'analyse électromagnétique de la structure à gradient constant (CG) à double alimentation qui sera installée en remplacement de la structure LIL. Ma thèse détaille le processus de fabrication de cette structure, tel que l'usinage, le brasage et l'alignement, qui sont réalisés en collaboration avec la société Research Instruments (RI) en Allemagne. Pour finir, le test de faible puissance et la mise en accord de la structure sont effectués en utilisant la technique du "bead-pull" et les résultats sont comparés aux résultats de la simulation et aux spécifications techniques.

université PARIS-SACLAY

ÉCOLE DOCTORALE
Particules, hadrons, énergie et noyau : instrumentation, imagerie, cosmos et simulation (PHENIICS)

Title: S-band Electron LINAC for ThomX

Keywords: ThomX, S-Band, LINAC, Photo-injector, RF, Beam dynamics, X-ray, Inverse Compton Scattering, Electrons.

Abstract:

ThomX is a back scattering source that aims to provide an average photon flux of about 10^{12}-10^{13} ph/s in the hard X-ray range (40-90) keV. The framework of my thesis focuses on the design study of the S-band ThomX linacs, namely the RF gun and the travelling wave accelerating structures. First, the thesis highlights the physics of Inverse Compton Scattering with a description of the kinematics of the photon and electron collisions. In addition, it gives a general explanation of the Compton photon flux and the brightness. The main possible applications of the ThomX machine are briefly discussed. Moreover, the thesis describes in detail the high power radio-frequency (RF) source used for the ThomX machine, namely the ScandiNova modulator K2-2 and the Toshiba Klystron E 37310 including the acceptance test results. As well as, it includes the development of the network components, such as the power divider, power circulator, phase shifters and attenuators performing the RF low power tests of these components. Additionally, the dissertation also provides the electromagnetic characteristics of the ThomX linac, namely the LEP injector linac (LIL) quasi gradient structure and the RF gun, and solenoid configuration using CST Studio Suite®. Moreover, it introduces the cooling system characteristics of the ThomX linac, the thermal analysis and the vacuum system tests. The commissioning of the ThomX linac is performed including the RF conditioning and the first beam commissioning. During the beam commissioning, the charge measurement using an integrated current transformer (ICT), and the energy measurements using steerer magnets are described. Furthermore, analytical approximation models for the energy and the energy spread, in standing and travelling wave structures, are proposed and fitted with measurements. In addition, an experimental work carried out at the PHIL photoinjector is introduced for the beam energy and energy spread measurements, using a dipole magnet for a purpose of acquiring practical skills before the ThomX commissioning. The dissertation also demonstrates the electromagnetic simulation and analysis of the dual feed constant gradient (CG) structure, which will be installed as a replacement of the LIL structure. The fabrication process of this structure such as machining, brazing, alignment and backing out, which are performed in collaboration with research instruments (RI) company in Germany, are explained in detail. Finally, the tuning and the low power test are performed using the bead-pull technique, and the results are compared with simulation data and with the technical specifications.

To my parents, whose prayers always surrounded me until I become what I am now. To my wife, who was always with me through the journey of struggles and the moments of success. To my lovely little daughters, who when I see their inspirational eyes, all the difficulties of my life become easy. And to my brothers, sister, uncles, aunts and all who are proud of my achievements.

Acknowledgements

Undertaking this PhD has been a truly life-changing experience for me and it would not have been possible to do without the support and guidance that I received from many people. I wish to express my deep gratitude to all those who have helped me to complete this work successfully.

First and foremost, I am grateful to the Almighty God. Without him, I would not have the strength to do this thesis.

Furthermore, I would like to thank the jury members for accepting to judge this work and to the effort they made to provide advice and propositions to improve it.

In addition, I would like to thank my PhD supervisors Marie Jacquet, Mohamed El khaldi and Christelle Bruni who supervised this thesis and provided useful comments and recommendations with a lot of encouragement.

Furthermore, I would like to express my sincere thanks to my parents, wife, daughters (Hissah and Norah) and all of my family members who have been very patient and helpful.

Moreover, I would like to express my sincere thanks to the ThomX team for their helps and supports during my PhD period.

Contents

List of Figures

List of Tables

Introduction

Nowadays, there is a high demand for bright, tunable and monochromatic X-ray sources for applications in medicine, industry, material science and cultural heritage. The best quality sources for both brightness and tunability are synchrotron radiation facilities, but there are strong constraints on their use and wide diffusion owing to their significant dimensions, cost of construction and operation, and the availability of access to beamlines. Nevertheless, compact Compton scattering machines are able to provide a quasi-monochromatic X-ray beam with a compatible size experimental room, and at lower costs compared to synchrotrons. In such machines, electron bunches interact with laser pulses providing a high X-ray flux by inverse Compton scattering (ICS) where the energy transfers from electrons to photons. These machines can produce X-ray with relatively low electron energy in comparison with synchrotron machines. They can also be compact, and can be installed into lab-scale environments such as hospitals, laboratories or museums. Thanks to recent developments in both laser and optical systems, these machines can now deliver high X-ray fluxes and consequently, high brightnesses [1]. Currently, there are different Compton sources which either produce X-ray beams or are under construction. One example of a machine is the Compact Light Source (CLS) in Munich, which delivers daily X-ray beams for users with a photon flux of about 10^{10}-10^{11} ph/s and an X-ray energy of between 15 keV-35 keV [2, 3]. The Tsinghua Thomson X-ray Source (TTX) produces 50 keV X-rays with a flux of 10^{7} ph/s [4]. The Southern European Thomson source for Applied Research (STAR) project is under construction to produce an X-ray flux of around 10^{9} ph/s at energies from 20 to 140 keV [5]. At higher energies (ranging from 0.2 to 20 MeV), the Extreme-Light-Infrastructure Nuclear-Physics Gamma-Beam-Source project produces X-ray beams with a photon flux of 10^{8} ph/s [6–8]. There are also some machines operating in wider

energy ranges such as the SPARC project in Italy (from 20 keV to 500 keV) with an X-ray flux of 10^{10} ph/s, NESTOR in Ukraine (from 10 keV to 900 keV) with an X-ray flux of 10^{13} ph/s [9, 10]. All these machines show different designs for the electron beam and the laser systems: a linear accelerator (linac) or a storage ring for the electron beam, a single shot, an optical multi-pass or a Fabry-Perot cavity for the laser beam. A non-exhaustive list of different Compton machines, their design and performance can be found in Refs.[1, 11, 12]. Among them is the ThomX project, built at the Irène Joliot-Curie Laboratory (IJCLab) on the Orsay campus of Paris-Saclay University. ThomX is designed to produce a total X-ray flux of 10^{13} ph/s and a brightness of 10^{11}ph/s/mm^2/mrad^2/0.1% bandwidth with a tunable energy range (45 keV to 90 keV). To achieve these performances, both electron bunches and laser pulses are stacked respectively in a storage ring and in a high gain Fabry-Pérot cavity [13].

The commissioning of ThomX linac has been ongoing since July 2021.

The scope of my PhD thesis is the design study of the ThomX linac installed to produce and accelerate an electron beam up to a range of 50 to 70 MeV to be injected into a storage ring for interaction with laser pulses in a Fabry Perot cavity for X-ray production.

The thesis consists of 4 main chapters. Chapter 1 highlights the physics of inverse Compton scattering with a description of the kinematics of the photon and electron collisions. In addition, it gives a brief explanation of the Compton photon flux and brightness. Moreover, two main schemes of Compton sources are briefly discussed, showing the advantages and disadvantages of each type. The chapter also includes a description of the ThomX machine, its layout and applications.

Chapter 2 illustrates in detail the high power radio-frequency (RF) source for ThomX, namely the ScandiNova modulator K2-2 and the Toshiba Klystron E 37310. Next, it describes the RF power distribution network with its low power tests (the power divider, the motorised phase shifter, the motorised attenuators and the power circulator). This chapter also presents the simulation results for the ThomX linear accelerator, the standing wave RF gun and the travelling wave LIL section. Moreover, the cooling system, the thermal analysis and the vacuum system of the ThomX linac are described.

Chapter 3 mainly focuses on the commissioning of the ThomX linac (the LIL accelerating structure

and the RF gun) in terms of RF conditioning and first beam in the linac. It describes in detail the charge emission and the energy measurements in both standing and travelling wave structures. Furthermore, the basic principles of the photoinjector and analytical models for the energy and the energy spread of the two structures are studied. Lastly, this chapter includes an experimental work at the PHIL photoinjector facility at IJCLab in Orsay to acquire practical skills before joining the commissioning of ThomX.

Chapter 4 presents the development of a dual feed travelling wave structure, fabricated by research instruments company (RI) in Germany, which is foreseen to be installed as an upgrade to replace the LIL accelerating structure to reach up to 70 MeV of electron energy. This chapter also shows the electromagnetic simulations and analyses of this structure. Moreover, the manufacturing process is presented, i.e. the machining, the brazing, the leak test and the structure alignment. This chapter deals with the tuning and the low power test of the structure, using the bead-pull technique to acquire the minimum reflection of the power and the right phase advance between adjacent cells, to avoid limitations in the overall accelerating gradient.

Chapter 1

Inverse Compton Scattering

Nowadays, the challenging research experiments for obtaining a bright X-ray in the energy range (10-100 keV) are only achievable using Free Electron Laser (FELs) and synchrotron light sources machines. However, such machines have some limitations such as maintenance, cost and difficult access to the experimental areas. Additionally, the most efficient X-ray tube, which is able to provide a photon flux of around 10^{10} ph/s, has a fixed and not tunable energy. These constrains do not allow carrying out many applications because a narrow energy bandwidth and/or a high photon flux are required. Another method to obtain a high X-ray flux is by Inverse Compton Scattering (ICS) where electron bunches interact with laser pulses. The ICS machines can produce X-rays with a relatively low electron energy in comparison with synchrotron machines. They can also be compact and installed into lab-scale environments such as hospitals, laboratories or museums. The third-generation synchrotron sources are composed of permanent undulators and wigglers which characterise the emitted X-rays through the parameters γ (the electron Lorentz factor) and λ_u (the spatial period of the undulator). The wavelength of the emitted X-ray from the undulator is $\lambda_u/2\gamma^2$. The spatial period of an undulator λ_u is typically a few centimeters thus γ has to be in the order of 10^4 to obtain a wavelength of the Angstrom range (Å = 10^{-10}m). In comparison, with ICS sources, the produced radiation has a shorter wavelength than the wavelength of the incident laser (λ_l) and scales $\lambda_l/4\gamma^2$. Using a laser of $\approx 1\mu$m wavelength and $\gamma \approx 50$ (corresponds to electron energy around 25 MeV) is sufficient to produce X-rays with a wavelength in the Angstrom range. Hence,

ICS sources can provide hard X-rays with an electron energy typically two orders of magnitude lower than in large synchrotron sources. This allows the machine size to be reduced to a few tens of meter squares (compact machine). Currently, ICS sources are considered as a very promising compact technology for high flux X-ray production. However, ICS sources are not comparable to the current FELs and synchrotron machines in terms of photon brightness and flux but they offer an attractive possibility to produce a high flux of hard X-rays with a compact machine. In this chapter, the physics of the inverse Compton scattering between electron beams and laser pulses is highlighted as well as the X-ray beam brightness and flux. Moreover, a brief description of two main schemes of ICS sorce is mentioned. Finally, a general description of the Compton source ThomX is presented, together with its applications.

1.1 Physics of Inverse Compton Scattering

The Compton process is the interaction between photons and atomic electrons. In this process, photons are incident on electrons of the atoms of the valence shell, which are the electrons loosely bound by the force of the nucleus. On the assumption that the colliding photon has more energy than the bonding energy between the nucleus and the electron, these atomic electrons tend to leave the atom and the photon is scattered at a different angle to the colliding one [14]. Fig1.1 shows a schematic diagram of the Compton scattering process.

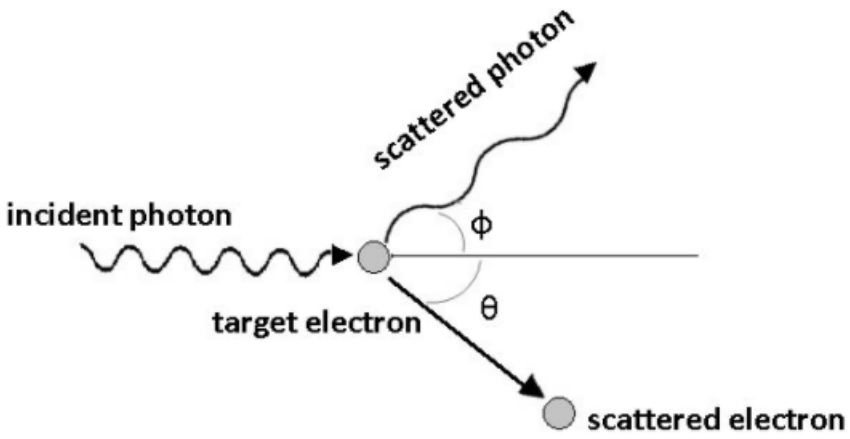

Figure 1.1: Schematic diagram of the Compton scattering process [15].

The final energy of the photon is smaller than its initial energy because a part of the photon energy is transferred to the electron. At this point we suppose that the electron is at rest in the atom when it is hit by a photon. Both are scattered at different angles after collision.

1.1.1 Kinematics

As it is known, energy and momentum follow the law of conservation. The relation between the initial energy, final energy, and angle of photon after scattering is [16]:

$$\hbar\omega_f = \frac{\hbar\omega_i}{1 + \frac{\hbar\omega_i}{m_0c^2}(1 - \cos(\varphi))} \tag{1.1}$$

where $\hbar\omega_f$ and $\hbar\omega_i$ are the photon energies after and before the collision respectively, φ is the photon scattered angle and m_0c^2 is the electron rest mass. When a photon collides with an ultra-relativistic electron, it gains energy. This process is known as "Inverse Compton Scattering". In Fig 1.2, an electron moves with velocity v parallel to the x-axis having an angle Ψ with an incoming photon of frequency *v* (left). In the electron frame, the photon is incoming with a different frequency *v'* making an angle Ψ' with the velocity vector of the electron (right).

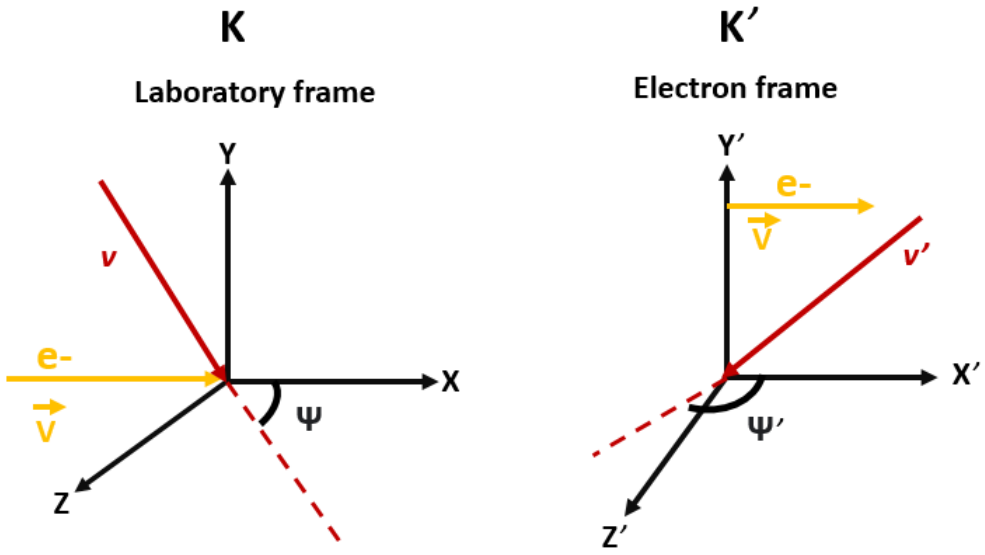

Figure 1.2: Diagram of the electron-photon interaction in the laboratory (left) and electron (right) frames [14].

In the electron frame $K^{'}$, moving along the x-axis with velocity v=βc, it is possible to calculate the frequency and the incident angle of the photon using the relativistic Doppler effect [17].

$$\omega_i^{'} = \gamma\omega_i(1 - \beta\cos\Psi) \tag{1.2}$$

$$k_x^{'} = \frac{\omega_i^{'}}{c}\cos\Psi^{'} = \gamma\frac{\omega_i}{c}(\cos\Psi - \beta) \tag{1.3}$$

$$k_y^{'} = \frac{\omega_i^{'}}{c}\sin\Psi^{'} = \frac{\omega_i}{c}\sin\Psi \tag{1.4}$$

where γ is the Lorentz factor of the electron. Transforming Eq.1.2 with respect to the incident angle of the photon in $K^{'}$ gives:

$$\omega_i^{'} = \frac{\omega_i}{(1 + \beta\cos\Psi^{'})} \tag{1.5}$$

The energy of the scattered photon is given by the formula 1.1. When the photon energy $\hbar\omega_i^{'}$ is much smaller than m_0c^2, the scattered energy is conserved after collision. At that point, the interaction between the electron and the photon is considered in the Thomson regime. The energy of the photon before and after the collision is the same and independent of the scattering angle:

$$\hbar\omega_f^{'} = \hbar\omega_i^{'} \tag{1.6}$$

Fig 1.3 shows the scattered photon in the electron frame (left) and in the reference frame (right).

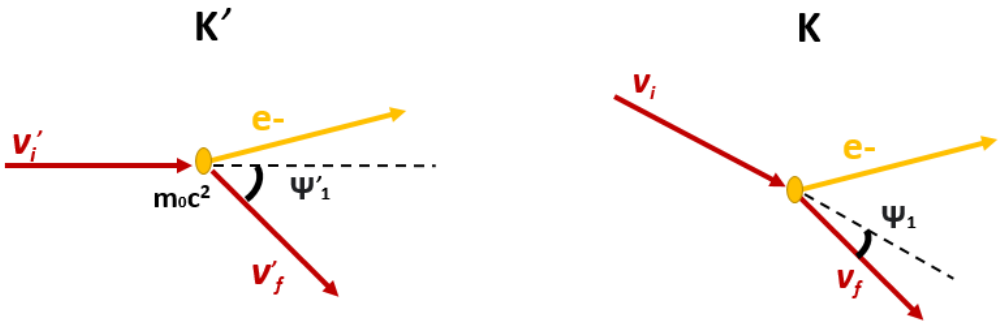

Figure 1.3: In the electron frame of reference, the photon is scattered with an angle Ψ'_1 according to the conservation of energy and momentum (left). In the frame of reference K, the scattering angle is Ψ_1 (right) [14].

In Fig 1.3, the frequency of the scattered photon in the electron frame K becomes:

$$\omega_f = \omega'_f(1 + \beta \cos \Psi'_1) \tag{1.7}$$

where Ψ'_1 is the scattering angle of the photon. When the photon incident angle Ψ and the observation angle Ψ_1 are taken into account, Eq.1.7 becomes:

$$\omega_f = \omega_i \frac{1 - \beta \cos \Psi}{1 - \beta \cos \Psi_1} \tag{1.8}$$

Eq.1.8 shows that the energy of the scattered photon in the reference frame is depending on the incident angle Ψ and the observation angle Ψ_1. In the case of a very small observation angle ($\Psi_1 << 1$) with ultra-relativistic electrons ($\gamma >> 1$ and $\beta \approx 1$), Eq.1.8 becomes:

$$\omega_f = \omega_i \frac{2\gamma^2(1 - \cos \Psi)}{1 + \gamma^2 \Psi_1^2} \tag{1.9}$$

The head-on collision between the photon and the electron occurs when $\Psi = \pi$, Eq.1.9 becomes in that case:

$$\omega_f = \omega_i \frac{4\gamma^2}{1 + \gamma^2 \Psi_1^2} \tag{1.10}$$

Scattering photons have a maximum energy $\hbar\omega_f^{max}$ when Ψ_1=0 (on-axis photons):

$$\hbar\omega_f^{max} = 4\gamma^2\hbar\omega_i \tag{1.11}$$

Eq.1.11 shows the dependency of the energy of on-axis scattered photons on the incident photon and the electron energies. Thus, an inverse Compton scattering source can produce a broad energy range of scattered photons by varying the energy of the electron beam. For example, an electron bunch of energy 50-70 MeV colliding with an incident laser of wavelength 1030 nm produces an X-ray beam of 45-90 keV.

1.1.2 Flux

The cross section of the Compton Scattering process is denoted by the Thomson cross section $\sigma_{Th} = 6.65 \times 10^{-29} m^2$. It can be described as a scatter probability of one photon travelling one meter to a target having a density of one electron per one cubic meter. The number of scattered photon per second is the product of the luminosity of the interaction by the cross section. Assuming that both the electron bunch and the laser pulse have Gaussian distributions in three dimensions, that their vertical and horizontal dimensions are equal, the number of photons emitted per second (case of head-on collisions) is [18]:

$$F_{tot} = \sigma_{Th}\frac{N_e N_L f_{rep}}{2\pi(\sigma_e^2 + \sigma_L^2)} \tag{1.12}$$

where N_e is the number of electrons per bunch, N_L the number of photons per laser pulse, f_{rep} the repetition frequency of the collision, σ_e and σ_L the rms transverse sizes of the electron bunch and the laser pulse respectively. Due to the low cross section σ_{Th}, a high Compton flux requires a high laser power, a high electron bunch charge, small transverse sizes of the electron beam and the laser pulse, and a large collision rate. Currently with the progress of the accelerators, lasers and optical cavities, it is possible to produce fluxes higher than 10^{12} ph/s if the repetition frequency f_{rep} is of order of 10-100 MHz [18]. For example, flux of $\approx 10^{13}$ ph/s can be obtained with f_{rep} = 20 MHz, photon pulses of 10 mJ, electron bunches of 1 nC and transverse sizes of photon pulses and electron bunches of $\approx$ 40 μm at the interaction point. Such laser pulses of $\approx$ 10 mJ can be produced thanks to the

amplification in an optical cavity such as a Fabry-Perot cavity [19]. Electron bunches can be produced with a powerful RF photo-injector. Current photo-injectors can produce 1 nC electron bunches with a transverse size of 50 μm. The high repetition frequency f_{rep} can be obtained with a small storage ring ($\approx$ 15 m circumference) where electrons revolve in the ring at a frequency of a few ten of MHz.

1.1.3 Brightness

The brightness of the light source is the quantity defining the beam intensity with regard to its angular divergence, its spectral purity and its transverse size. It is the number of photons emitted per second, per mm^2 of source area, per unit of solid angle and within 0.1% of spectral bandwidth. The average brightness can be written as:

$$\langle Br \rangle = \frac{p\% F_{tot}}{(2\pi)^2 \sigma_X^2 \sigma_X'^2} \tag{1.13}$$

where p% is the fraction of X-rays emitted within a 0.1% bandwidth of a given energy E_X, σ_X is the transverse size of the source point and $\sigma_X^{'}$ is the angular divergence of the beam around E_X and, the transverse Compton size σ_X can be written as $\sigma_X^2 \approx \frac{(\sigma_e \sigma_L)^2}{(\sigma_e^2+\sigma_L^2)}$, p% and $\sigma_X^{'}$ depend on the angular divergence and the energy spread of the two incident laser and electron beams. With the current performances of laser systems and electron accelerators, the dominant influence on the Compton beam is related to the angular divergence of the electron beam $\sigma_e^{'}$. Taking into account for the brightness calculation only the effect of $\sigma_e^{'}$, and assuming that the divergence of the Compton beam $\sigma_X^{'}$ is equal to the divergence of the electron beam $\sigma_e^{'}$ (which is a very good approximation), the average on-axis brightness can be written as [18]:

$$\langle Br \rangle = 0.0015 \frac{F_{tot}}{(2\pi)^2} \left(\frac{\sigma_e^2 + \sigma_L^2}{\sigma_L^2} \right) \left(\frac{\gamma}{\varepsilon_n^2} \right) \tag{1.14}$$

where ε_n is the normalised transverse emittance of the electron beam in mm.mrad, which is equal to $\gamma \sigma_e \sigma_e^{'}$. Eq.1.14 emphasises that a high flux and low electron beam emittance are crucial parameters in producing high brightness X-ray beams with Compton sources [1].

1.1.4 The ICS source schemes

To obtain high X-ray fluxes, there are two main schemes of ICS machines. The Storage Ring (SR) scheme and the Linac scheme (see Fig 1.4). In the storage ring scheme, illustrated in Fig 1.4 (a), an electron bunch is accelerated in a short linear accelerator to a few tens of MeV and injected in a small storage ring of a circumference $\approx$ 15 meters. The bunch collides many times with a laser pulse. At each turn, the electron bunch length and transverse size increase as a result of the warming up caused by Compton collisions as well as the intra-beam scattering within the bunch. Thus, it is taken out and replaced by a new one each few tens of milliseconds [18]. In this scheme, the ring circumference determines the high repetition frequency f_{rep}, for example, when the circumference is 15 m, the repetition rate f_{rep} is 20 MHz. In the second scheme (Fig 1.4 (b)), an electron bunch collides only one time with the laser pulse. In that case, the high repetition rate f_{rep} is determined by the electron gun itself. To reach fluxes higher than 10^{12} ph/s, the gun has to produce typically a 100 pC electron bunch at an injection frequency of a few tens of MHz. The gun must necessarily be a superconducting device. The technology of such electron guns is not yet mature. In both schemes, highly intense laser pulses at the accelerator repetition frequency are essential to achieve the flux requirement [18].

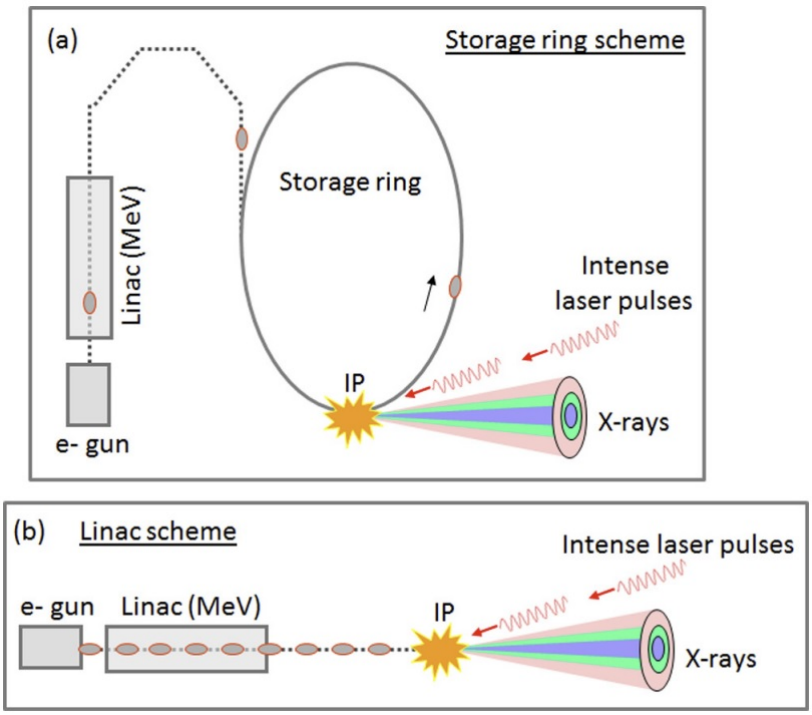

Figure 1.4: Schematic diagrams of compact Compton based X-ray sources; (a) a storage ring scheme, (b) a linac scheme [18].

1.2 The ThomX machine at IJCLab in Orsay

The Thomson scattering X-rays source (ThomX) is a French national project supported by the French ”Agence nationale de la recherche” as a part of the program ”investing in the future” under reference ANR-10-EQPX-51 and the grants are from the Ile-de-France region at a cost of 10 Meuros [14]. ThomX aims to provide an average photon flux of 10^{12}- 10^{13} ph/s in the hard X-ray range (40-90 keV). The machine is composed of six main parts: an electron gun, a travelling wave accelerating section, a transfer line, a storage ring, a laser system and an X-ray line [20].

The components of the ThomX accelerator machine are shown in Fig 1.5.

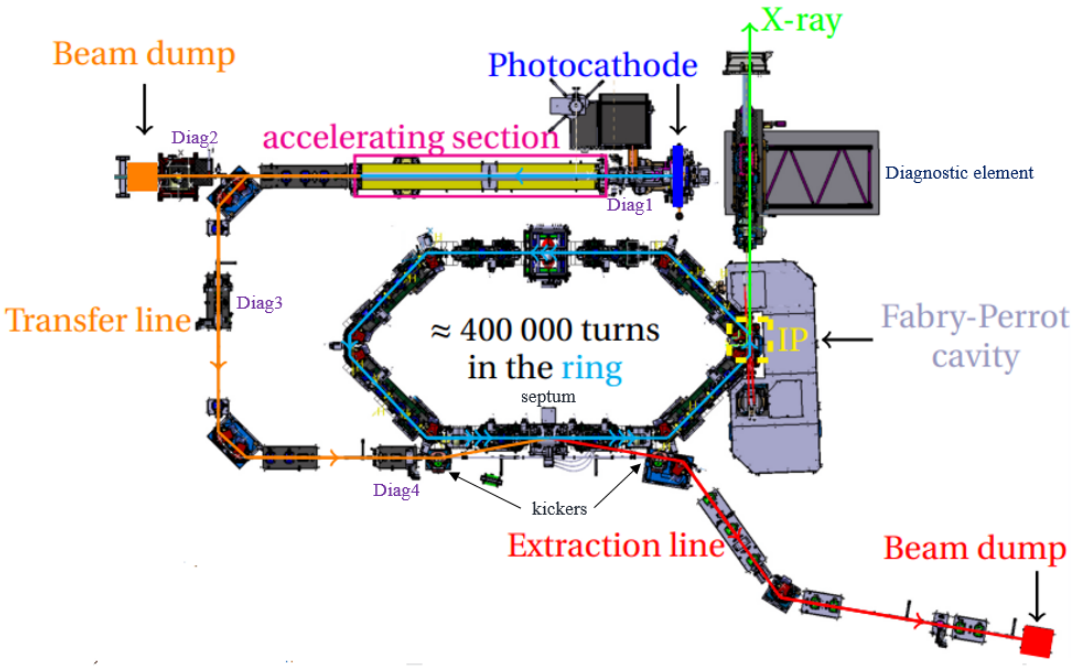

Figure 1.5: Layout of the ThomX accelerator. Courtesy to A. Moutardier.

In the electron gun, laser pulses are incident on a cathode surface to produce an electron bunch of charge 1 nC. These electrons are accelerated in a standing wave (SW) RF photoinjector and travel through a dedicated diagnostics section (Diag1) for bunch measurements. Then, the electron bunch enters a S-band travelling wave (TW) linac to be accelerated up to 50-70 MeV and then passes through a triplet of quadrupoles, used for the emittance measurement performed in the diagnostic section (Diag2) and a dump. For the injection of electrons into the storage ring, a transfer line is installed. This line comprises four quadrapoles, four dipoles of 45 degree to steer the beam and two chambers (Diag3 and Diag4) for the energy spread measurements and beam characterisation. The beam is then injected into the ring of circumference of $\approx$ 18 m by a septum and a fast kicker. Optics of the storage ring are designed to accommodate the transverse size of the electron bunch at around 50-100 μm with a normalised transverse emittance of 5-7 μm rad at the interaction point. The laser system consists of laser pulses firstly amplified by an optical fiber system and sent into a Fabry Perot optical cavity (Fig 1.6) to reach $\approx$ 10-30 mJ per pulse inside the cavity. The transverse size of the laser pulses is $\approx$ 70 μm at the interaction point.

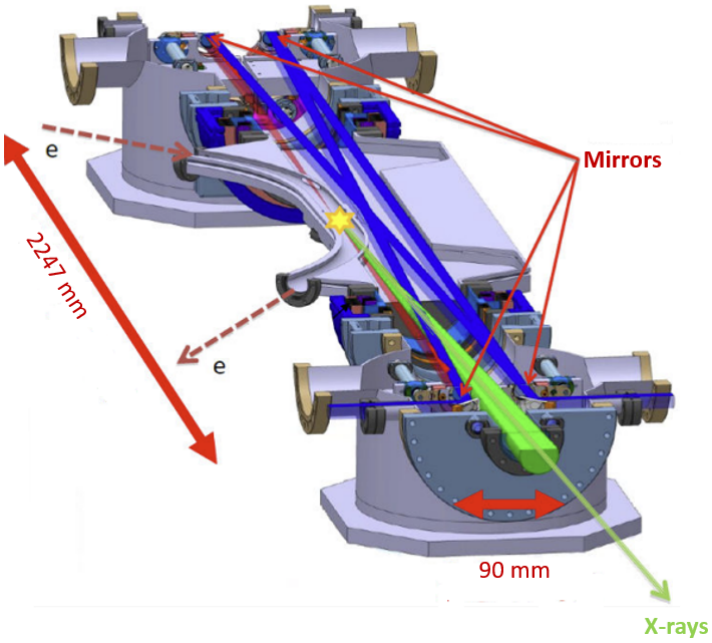

Figure 1.6: Layout of the ThomX Fabry Perot cavity [12].

The collision between electrons and the laser pulse occurs in the Fabry Perot cavity at each electron bunch turn (f_{rep}=16.6 MHz) with a collision angle of 2 degrees. A new electron bunch is re-injected every 20 ms, a second kicker is used to extract the electron beam towards the extraction beam dump. On the basis of the above considerations, ThomX is expected to produce a photon flux of 10^{12}-10^{13} ph/s in the hard X-ray range 40-90 keV. The X-ray beam is extracted via a beryllium window of a diameter of 50 mm. The beam line is splitted into two sections as shown in Fig 1.7. The first optical section, located just after the beryllium exit window, is used for beam monitoring and detection. The second section is used for a complete beam characterisation and the realisation of X-ray experiments [13].

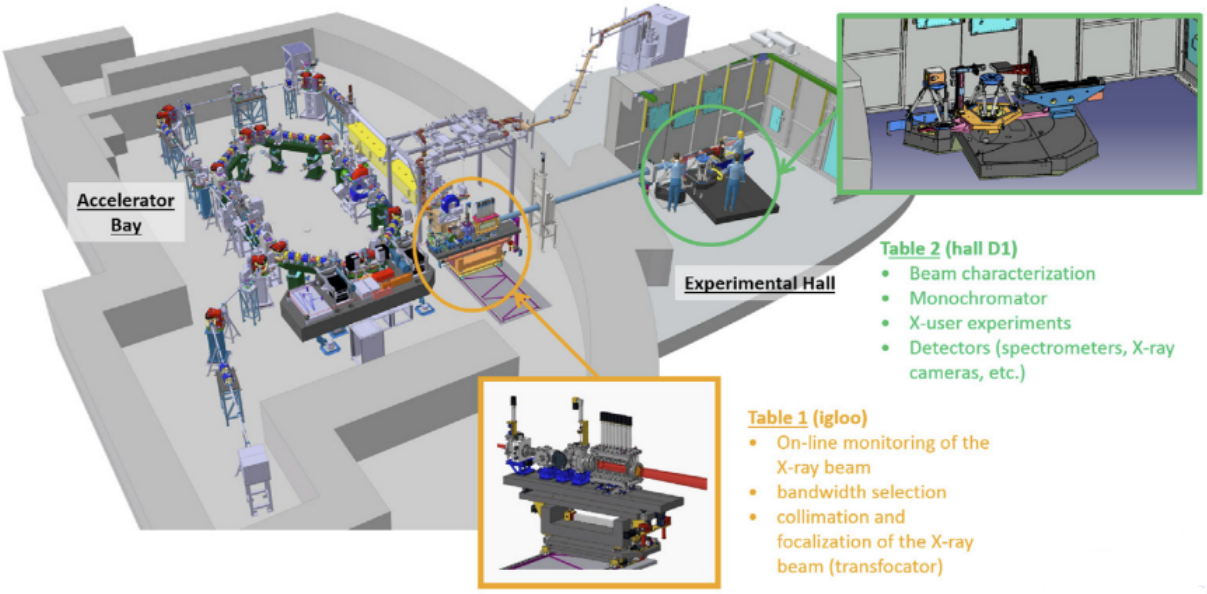

Figure 1.7: Layout of the X-ray line in ThomX [13].

1.2.1 The main applications of the ThomX source

In the cultural heritage preservation and associated fields [21], ThomX should offer many promising applications. Integrating such a source into a museum's laboratory may provide experts with direct access to the masterpieces, thereby, avoiding problems of security and insurance and transportation costs. Additionally, these machines can provide complete materials analyses and non destructive analyses of paintings, allowing the detection of underlying drawings. There is also a demand for such sources in the field of medical applications [18]. For instance, medical imaging resolution could be improved with the phase contrast technique in many case where the conventional imaging is not sufficient. Thanks to the high energy of the X-rays (45-90 keV), to the quasi-monochromaticity of a Compton X-ray beam and to the high expected flux, analysis techniques currently used only at Synchrotron sources could be developed in a lab-size environment as ThomX.

Chapter 2

ThomX S-band Electron Linear Accelerator

2.1 Introduction

In a radiofrequency linear accelerator (LINAC) the electron beam gains energy by means of RF electric fields confined in accelerating structures and generated with high peak power sources. The RF power is distributed to the accelerator unit (LINAC) with a network of waveguides made generally of copper (Fig 2.1). The power source consists of a high power microwave amplifier called a klystron that is pulsed by a high voltage power supply known as a modulator.

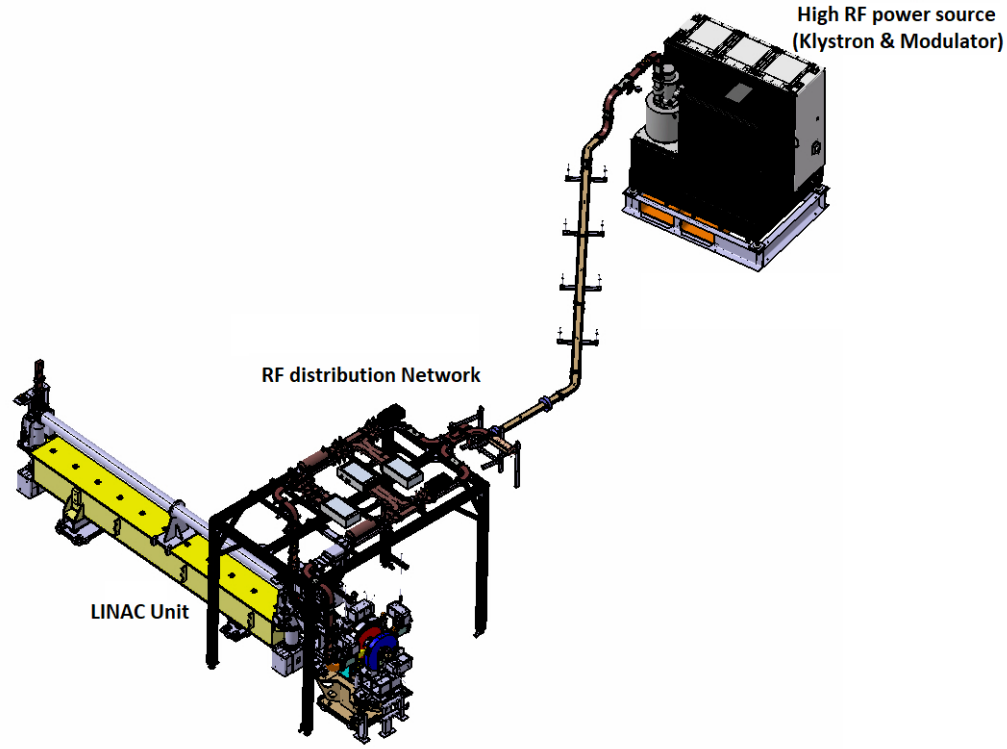

Figure 2.1: 3D model of ThomX linac.

The ThomX linac is composed of a homemade 2.5 cell photocathode RF-gun, placed between two solenoids and an S-band LIL accelerating section, designed in-house and lent by the SOLEIL synchrotron, the major partner in the project. In this chapter the power source of the ThomX linac is described, and the acceptance test results on the modulator and klystron systems are shown. The RF power distribution network of the ThomX linac is described, including tests on some main network devices. The RF gun and S-band accelerating structure will be described in detail. To accelerate the electron beam, the system requires high RF power from klystrons to drive the RF gun and linac structure. The klystrons require low level RF drive and a high voltage pulse from the modulator for a high power RF generation.

2.2 High power RF source

The klystron is an important vacuum tube amplifier device which operates at microwave frequencies and is used in many linear accelerators, especially in units employing LINACs with electron beam

energy levels exceeding 10 MeV. It is used as an RF power amplifier that amplifies the input of a low power RF signal generated by a low power RF source commonly called an RF driver. The klystron powered with a high voltage (HV) pulse modulator generates RF pulses with a peak power of the order of tens of MW which is then distributed to the accelerator structures by a system of waveguides.

2.2.1 Klystron working principle

The physical components of a klystron consist of an electron gun, resonant cavities, a magnetic system to focus the electron beam, and a beam collector. In order to achieve high powers, this electron gun must emit a large number of electrons. A schematic representation of this device is given in Fig 2.2.

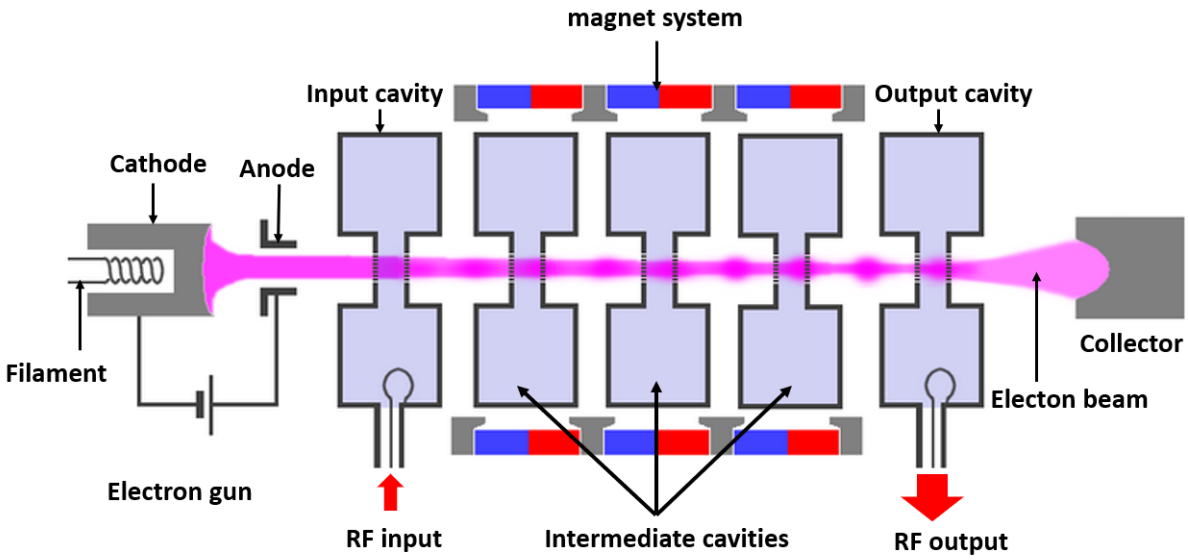

Figure 2.2: Diagram of a klystron tube amplifier.

The electrons injected from the cathode are first accelerated towards the anode by the high DC voltage provided by a modulator. The electron beam travels linearly through a certain number of resonant cavities up to a collector. An RF signal, coupled to the input cavity, accelerates and decelerates electrons in the beam (the variation in electron velocity in the drift space is called velocity modulation). As the beam drifts, faster electrons catch up with slower electrons and this

results in the formation of bunches and an RF current in the beam that grows as the beam moves along. This current is coupled first to intermediate cavities and then to the output cavity. At each intermediate cavity the RF beam current induces a signal, which produces a field that enhances the bunching process in the beam. Finally, the coupling of the intense RF beam current to the last cavity produces an RF power signal at the output of the device. The remaining low energy in the electron beam is then dissipated in the collector. The gain of a klystron can be very large, 60 dB or more, but the bandwidth is usually limited to a few percent (up to 8%). Output power levels can reach tens of megawatts. A more detailed description of the klystron working principles and design can be found in [22].

2.2.2 High voltage pulse modulators

The crucial device in a pulsed power application is a pulse modulator which is an electronic device used to supply high voltage and high current power bursts with great accuracy and precision. Ideally, a modulator acts as a simple switch between a high voltage power supply and its load, for example a klystron. The modulator (pulsed klystron power supply) is one of the most expensive parts in the RF-system of electron accelerators. Conventional pulse modulators, called also line-type modulators, use a pulse forming network (PFN) and vacuum tube switch which drive a pulse transformer to reach the required pulse shape and energy. Typically, a PFN consists of a number of inductor and capacitor (LC) stages as shown in Fig 2.3, which are tuned to provide a fixed-width pulse into a matched load such as a klystron. Typically, the PFN is discharged into the klystron by a hydrogen thyratron or other fast closing switch. These conventional modulators exhibit poor efficiency, low power density, a large footprint and cost, and still limited performance on pulse rise time, pulse flat-top accuracy and AC power line quality (flicker, current harmonic distortion, power factor) [23].

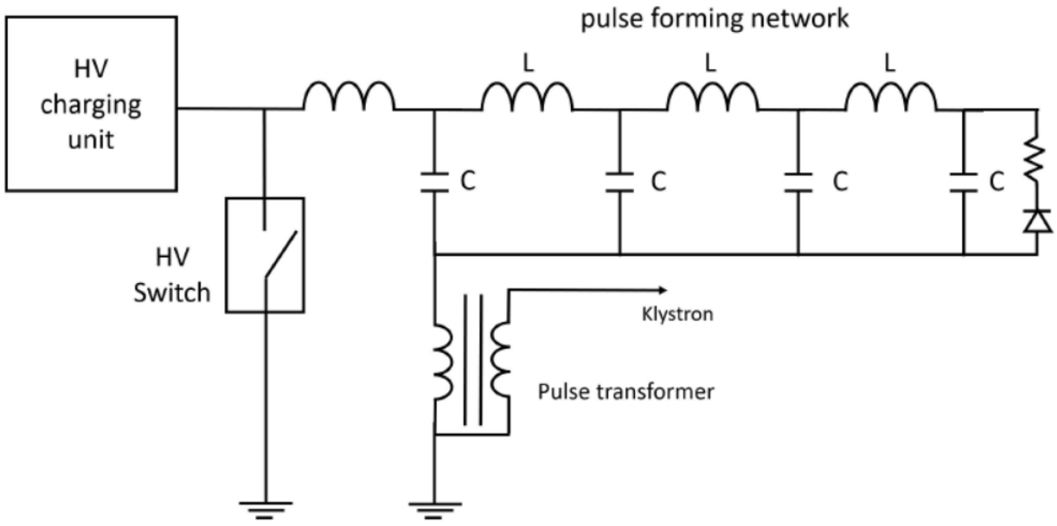

Figure 2.3: Simplified diagram of a pulse forming network connected to a pulse transformer through a switch.

These conventional modulators have been employed for the last 50 years and are commonly used even nowadays in many facilities. Nevertheless, thanks to improvements in solid state switches in terms of speed and sustained peak power, a new generation of pulse modulators, called solid state pulse modulators, has become popular in past years [24 – –27]. Using this solid-state technology, most of the limitations of the conventional high voltage switching inefficiency such as limited lifetime, pulse flexibility, rise time, etc., can be eliminated. These modulators feature state-of-the art insulated gate bipolar transistor (IGBT) switches in series and parallel configurations that allow almost arbitrary high voltages (1 kV-200 kV) and currents (10 A-5 kA) to be reached. They operate as both opening and closing switches, providing extensive flexibility in pulse width, and very fast fault protection. These switches typically open and close in less than 100 – 500 ns, depending on their power rating.

The basic architecture of the solid-state modulator is described below and illustrated in Fig 2.4. A three-phase line voltage is fed to a high voltage DC Power Supply (HV-DCPS). It charges up all the switching module units to a primary voltage of around 1000V. An external trigger pulse enters the modulator, gating all the switches and discharging some of the stored energy. A pulse transformer steps up the voltage to the level needed for the load in use (Klystron). All parts of the modulator are

located inside a common enclosure. The pulse transformer and the load HV-interface are the only parts surrounded by transformer oil. The HV-DCPS, switching modules and control interface are all in air for easy access and maintenance.

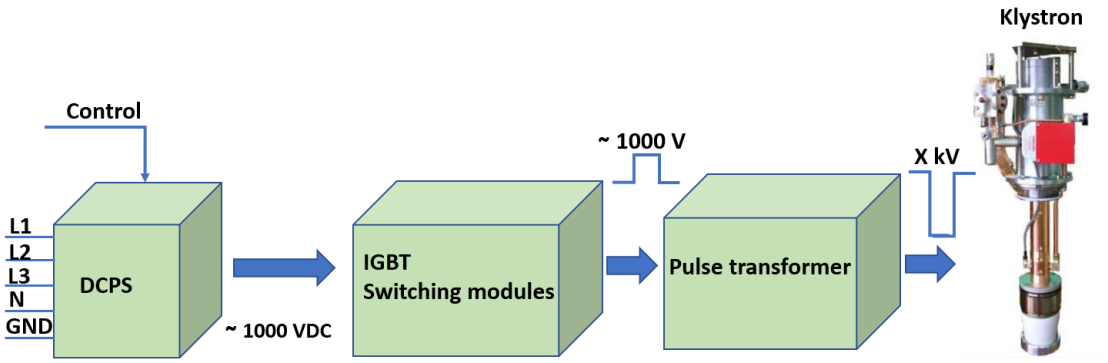

Figure 2.4: The principle of the solid-state pulse modulator system.

A simplified diagram of a typical topology of a solid-state pulse modulator system is represented in Fig 2.5, in which it is possible to distinguish three main subsystems: the DC power supply, the switching units and the pulse transformer.

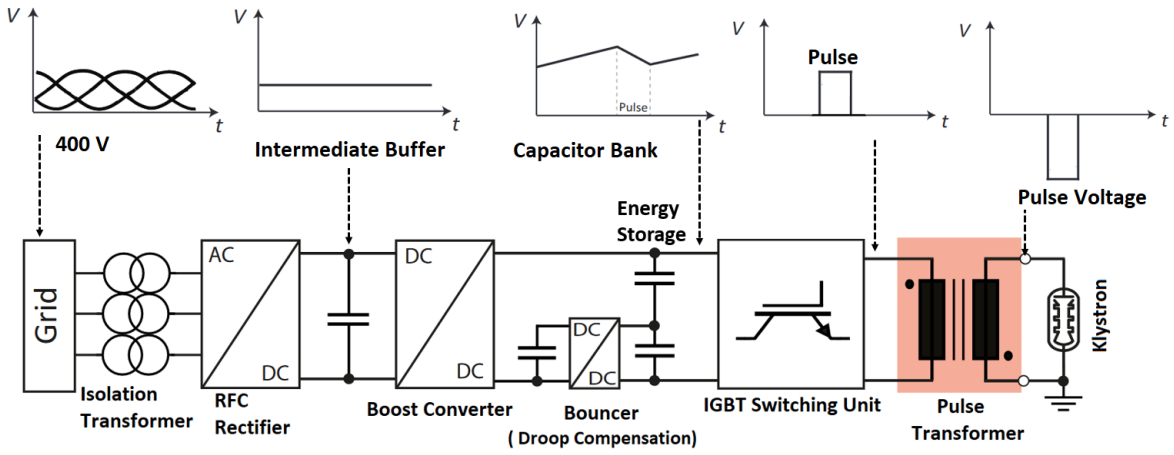

Figure 2.5: Typical topology of the solid-state pulse modulator system.

2.2.3 ThomX high power RF source

The ThomX RF source unit consists of an S-band Klystron E37310 made by Toshiba Electron Tubes & Devices Co Ltd (TETD) [28], a K2-2 model high voltage solid state pulse modulator made by

ScandiNova [29] and a low power RF source, as shown in Fig 2.6. An interlock system protects the RF unit in case of failure. The TOSHIBA E 37310, S-band high power pulsed amplifier klystron is designed for linear accelerators. The E 37310 delivers 37 MW peak output power with a power gain of around 50 dB and an efficiency of more than 40 %. The klystron is incorporated in a ScandiNova K2-2 klystron modulator which delivers high voltage pulses to the E37310 with a maximum amplitude of 330 kV– 350 A and an RF pulse length of 4.5 μs at 50 Hz.

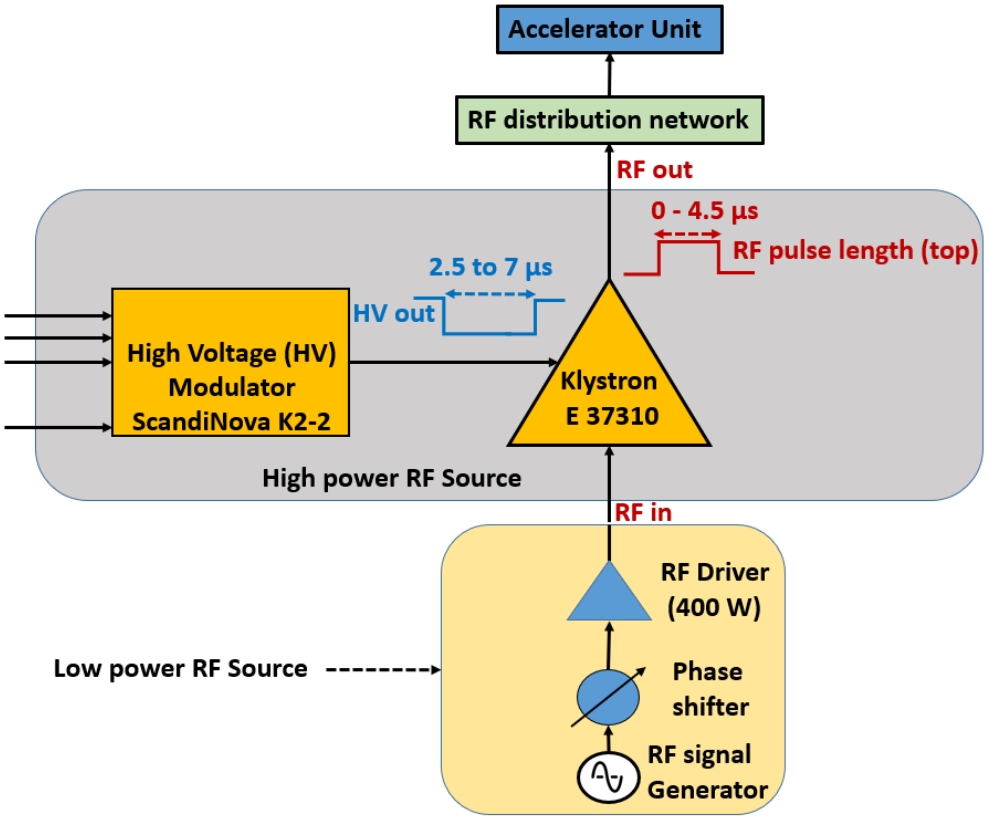

Figure 2.6: The ThomX RF source unit.

All parts of the RF modulator are located inside a common enclosure. The klystron is inserted in the oil tank near the pulse transformer, while the RF amplifier output is directly connected to the klystron input cell. The filament power supply (FPS), the solenoid power supply (SPS) and the ion pump controller are also integrated in the modulator front rack. In Fig 2.7, the 3D model of the K2-2 Scandinova modulator is shown. The master oscillator (RF signal generator) is the heart of the linac which determines its performance. The ThomX master oscillator is an R & S®SMA100A signal generator with long-term frequency stability (frequency error< 10^{-8}) and a very low phase noise of

typ. –134 dBc.

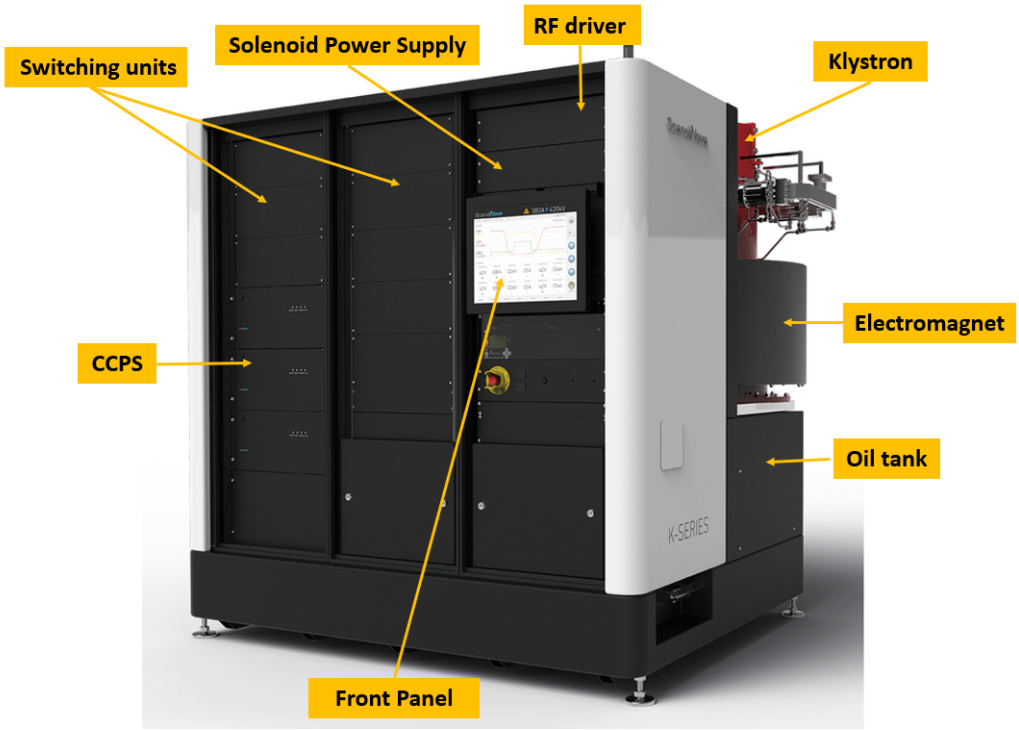

Figure 2.7: 3D model of the Scandinova solid state pulsed modulator system (K2-2 model).

The Scandinova modulator is based on solid state technology and uses several 1.2 kV IGBT switches in parallel to generate the high voltage pulse on the secondary winding of the transformer. The entire schematic representation with all the subsystems of the modulator, is shown in Fig 2.8, where it is possible to recognise the system topology described in the previous section, composed of the capacitive voltage power supplies (CCPSs), the switching units (SUs) (which contain the IGBT switches and the capacitor banks) and the pulse transformer. The K2 modulator has three high voltage power supplies (HVPSs) and seven parallel switching units. Fig 2.8 shows the power distribution unit, the cooling system and the control system. The power distribution unit feeds all the subsystems included in the modulator with 3-phase and single-phase AC power. The cooling system monitors and distributes cooling water to the CCPSs, the SUs and the transformer tank. It also includes four circuits for different parts of the klystron: the collector, the body, the solenoid (VT-689922) and the RF ceramic window. The control system monitors the signal coming from all the modulator subsystems and handles the trigger and interlock signals for the different sub-units. It consists of a PLC controller connected to an FPGA that handles the hardwired interlocks. The

correct operation of the overall system has to be constantly monitored in order to prevent damage to the system itself or danger for the user. The control system for the high-power RF source includes a generic control panel application ATKpanel for the complete control, and status, including interlock signals, of the equipment and TANGO (www.tango-controls.org) device servers (DS), as well as attributes for the complete remote control of the RF unit.

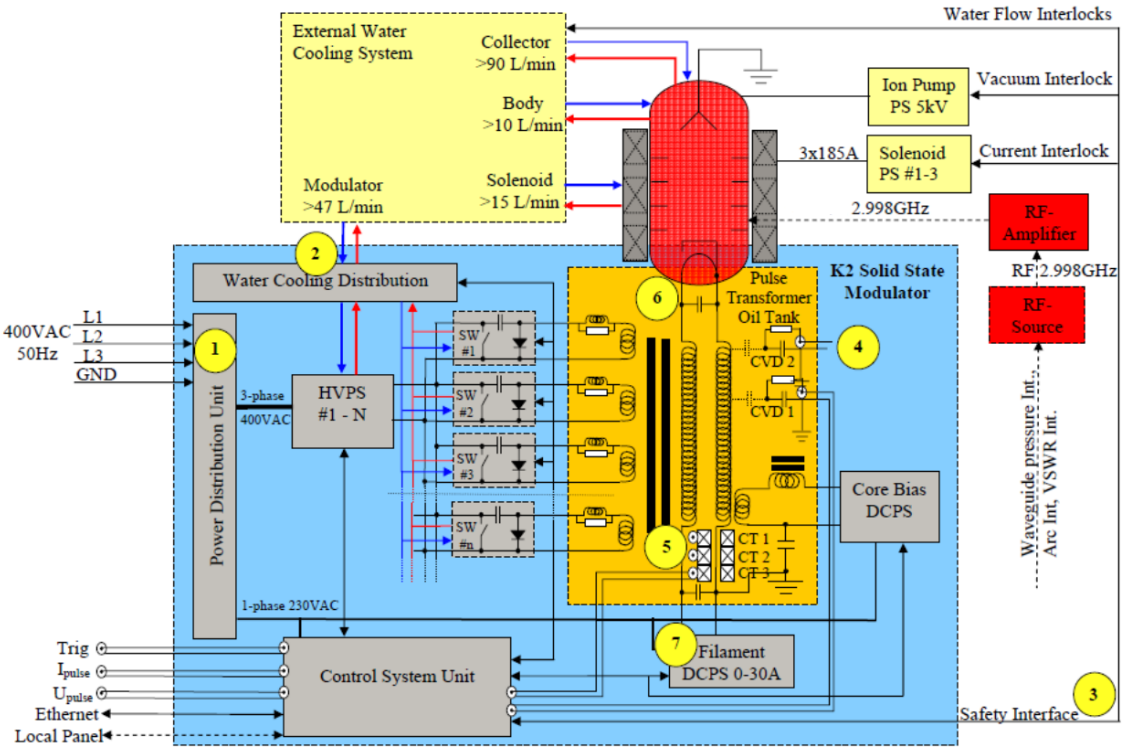

Figure 2.8: Schematic of the K2 solid state pulsed modulator (courtesy of ScandiNova).

The ThomX high power source (klystron and modulator) was tested in factory and on the ThomX site in order to verify its reliability and its conformity with the ThomX requirements. These tests were successfully conducted in the ScandiNova factory in Uppsala, Sweden [30] and on the ThomX site after installation [31]. After characterisation of the pulse, a long run test was performed for around 8 hours at full power. During this test, the output modulator pulse (voltage and current), the RF pulse and all the main parameters of the system were continuously monitored. The results of the measurements taken during the factory acceptance test (FAT) of the RF source are reported in Table 2.1 and Table 2.2.

Table 2.1: ThomX klystron (Toshiba E37310) measured parameters (FAT).

Parameter	Value
RF frequency	2998.5 MHz
Max. peak RF output power ($P_{RF\,out}$)	37.5 MW
RF driver power (klystron input $P_{RF\,in}$)	325 W
Max. RF pulse length (top)	4.5 μ s
Max. pulse repetition rate	50 Hz
Peak klystron gun voltage (U)	285 kV
Peak klystron gun current (I)	308 A
Heater current	17 A
Klystron efficiency $\eta_{\circ} = \frac{P_{RF\,out}}{U.I+P_{RF\,in}}$	43 %
Gain G=10 $\log\frac{P_{RF\,out}}{P_{RF\,in}}$	50 dB
Perveance ($I/U^{3/2}$)	2.02 $\mu A/V^{3/2}$

Table 2.2: ThomX modulator (ScandiNova K2-2) measured parameters (FAT).

Parameter	Value
Max. modulator peak power	92 MW
Max. output pulse voltage	330 kV
Max. output pulse current	350 A
Max. repetition rate	50 Hz
Voltage pulse width	6.2 μs
Rate of rise	346 kV/μs
Rate of fall	278 kV/μs
Pulse top flatness	1.2 % (during 4.5 μs) 0.2 % (during 1 μs)
Pulse-to-pulse time jitter	$< \pm$ 4 ns
Pulse width time jitter	$< \pm$ 8 ns
Amplitude stability	$< \pm$ 0.1 %

Fig 2.9, shows two pictures of the modulator system installed on the ThomX site.

Figure 2.9: Installation of the ThomX RF source (ScandiNova modulator K2-2 & TOSHIBA Klystron E 37310).

2.3 RF Power distribution network

The RF power network is mainly used to transport and distribute the RF power to the RF gun and the acceleration section by means of a network of rectangular oxygen free high conductivity (OFHC) copper WR284 waveguides and other RF components such as bidirectional couplers, a power divider, RF loads, RF windows, a circulator, variable attenuators and a variable phase shifter. The whole network is stabilised at temperature of 24 ± 1 °C, to avoid length variation in the waveguides due to different operating conditions. This is achieved by means of copper pipes with circulating water, welded longitudinally along the external broader surface of the waveguides and the devices. The waveguide network, which connects the klystron E 37310 to the standing wave (SW) RF gun and the travelling wave (TW) accelerating structure, includes different RF devices. The position of such devices in the network layout can be seen in Fig 2.10, where a 3D drawing is provided.

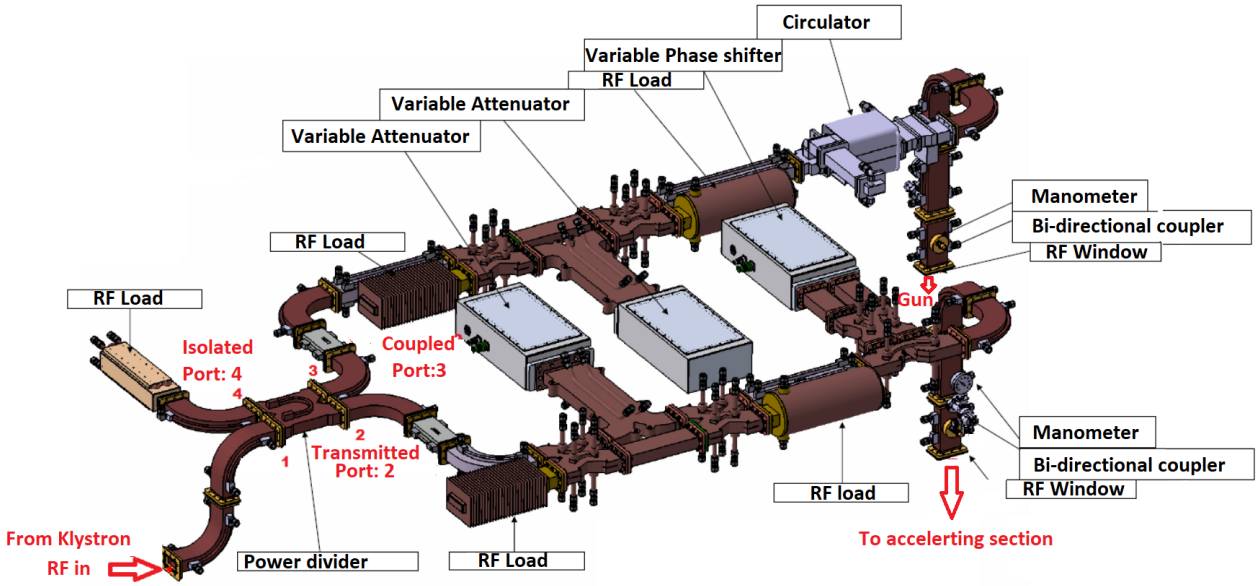

Figure 2.10: 3D drawing of the ThomX Power distribution network.

The RF network is pressurised at 2.5 bars with SF6 between RF ceramic windows inserted at the klystron output, the RF gun and the acceleration structure inputs. These windows are used to transmit and separate the RF power between two regions (the pressurised and the vacuum). The RF power is divided into two channels by a power divider. In the side which runs toward the electron gun, a variable attenuator is installed to change the transmitted power. In addition, there is a circulator to protect the klystron from the reflected RF power that occurs at the rise and fall edges of the RF pulses in case of internal discharges (RF breakdown) in the standing wave (SW) RF gun. In the other side, which transports the power toward the travelling wave (TW) accelerating structure, there is also a variable attenuator, which varies the amplitude of the transmitted signal, and a phase shifter to adjust the relative RF phase between the RF gun and the TW acceleration section. Moreover, RF loads are used to absorb the reflected RF power for the safety of the RF system. For incident and reflected power measurements, 4 couplers are installed in this network. The first is located at the klystron exit, the second is at the RF gun entrance and the last two are at the entrance and exit of the TW section (Fig 2.11). The klystron E37310 delivers 37 MW peak output power with a variable RF top pulse width of up to 4.5 μs and a maximum repetition rate of 50 Hz. This power is divided into the RF standing wave RF gun (1/3 of the input power P_{in}) and the traveling wave accelerating section (2/3 of the input power P_{in}), taking into account the RF losses in the waveguide

network.

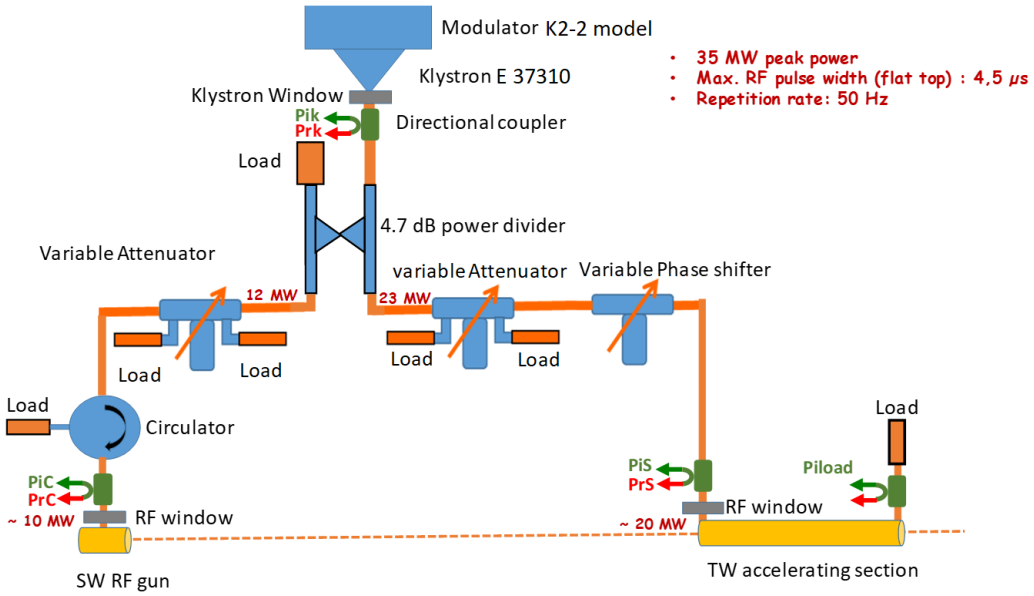

Figure 2.11: Diagram of the ThomX power distribution network.

In this section, low power tests are presented for the main parts of the RF power distribution network, such as the RF power divider, attenuator and phase shifter and the circulator.

2.3.1 ThomX Power divider

In the network design of ThomX, the power divider is installed to divide the input power coming from the RF power source (klystron) to the RF gun and TW accelerating section. It must deliver 33 % of the input power, coming from the klystron, to the RF gun and 67 % to the TW accelerating section. This power divider has four ports, as shown in Fig 2.12. Port (1) is the input port where the power comes from the klystron. Port (2) is the transmitted port where the power from port (1) is transmitted to the TW accelerating section and a portion of the power applied to port (2) will be coupled to port (4), which is usually terminated with a matched load. Port (3) is the port coupled to the RF gun while a portion of the power applied to port (1) appears. Port (4) is the isolated port (matched load).

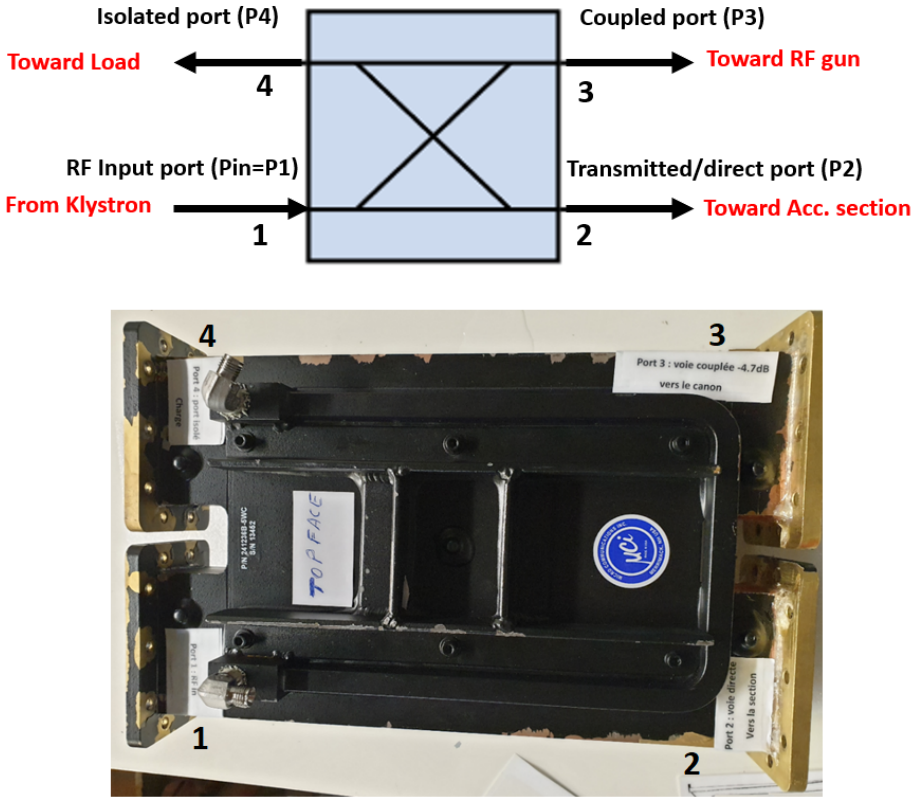

Figure 2.12: Identification of the power divider inputs and outputs.

The required common properties for all power dividers are high directivity, wide operational bandwidth, and good impedance matching at all the ports when the other ports are terminated with loads. The measurements described below were performed using a vector network analyser (VNA) and two matched dry loads. Fig 2.13 illustrates the testing setup and configuration for performing the RF characterisation of this power divider.

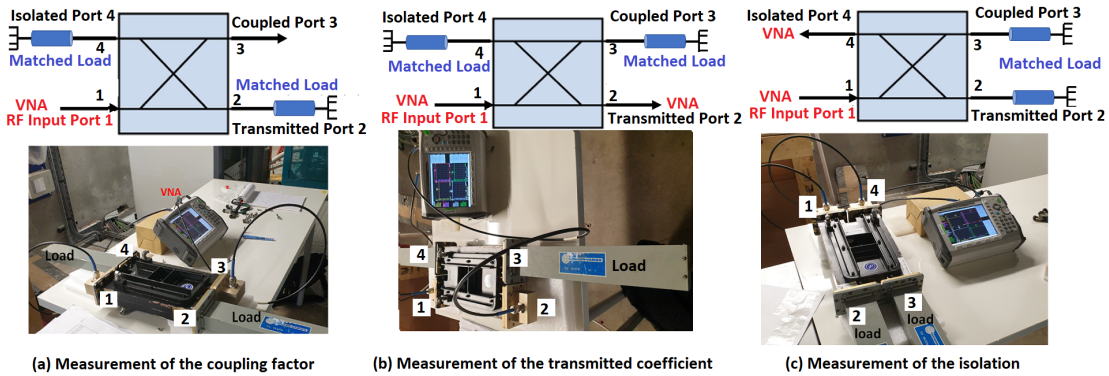

(a) Measurement of the coupling factor (b) Measurement of the transmitted coefficient (c) Measurement of the isolation

Figure 2.13: Testing setup and configuration for performing power divider characterisation.

2.3.1.1 Measurement of the coupling factor

The coupling factor indicating the delivered input power to the RF gun is defined as:

$$C_{3,1} = 10 \log \left(\frac{P_3}{P_1} \right) = |S_{31}| \text{ dB} \tag{2.1}$$

where P_1 is the input power at port (1) and P_3 is the output power from the coupled port (3) and both P_4 and P_2 are terminated with matched loads as can be seen in Fig 2.13 (a). The measurements of the S parameters at 2998.5 MHz are summarised in Table 2.3.

Table 2.3: Measurement summary of the coupling factor.

Parameters	Measured values
Coupling factor $C_{3,1}$=$\|S_{31}\|$	-4.79 dB
Phase S_{31}	-163 °
Return loss $\|S_{11}\|$	-24 dB
Return loss $\|S_{33}\|$	-31 dB

The results show that port (1) and port (3) are well matched and the power feeding the RF gun should be around 33% of the input power P_{in}($C_{3,1}$=-4.79 dB). The measured values of the return losses are negligible.

2.3.1.2 Measurement of the transmitted coefficient

The transmitted power P_2 toward the accelerating section is deduced by measuring the transmitted coefficient S_{21} defined as:

$$|S_{21}| = 10 \log \left(\frac{P_2}{P_1} \right) \tag{2.2}$$

where P_1 is the input power at port (1) and P_2 is the output power from transmitted port (2). Both P_3 and P_4 are terminated with matched loads as shown in Fig 2.13 (b). The measurements of the S parameters at 2998.5 MHz are summarised in Table 2.4. The results show that the port (1) and port (2) are well matched and the power feeding the accelerating section should be around 67 % of the

Table 2.4: Measurement summary of the transmitted coefficient.

Parameters	Measured values
Transmitted coefficient $\|S_{21}\|$	-1.79 dB
Phase S_{21}	-73 °
Return loss $\|S_{11}\|$	-20 dB
Return loss $\|S_{22}\|$	-20 dB

input power P_{in} ($|S_{21}|$=-1.79 dB). The measured values of the return losses are negligible.

2.3.1.3 Measurement of the Isolation

The isolation of this power divider can be defined as the difference in the signal levels in dB between input port (1) and isolated port (4) when the two other ports are terminated by matched loads, as shown in Fig 2.13 (c).

$$I_{4,1} = -10 \log \left(\frac{P_4}{P_1} \right) = -|S_{41}| \text{ dB} \tag{2.3}$$

Table 2.5 summarises the measurements of the S parameters at 2998.5 MHz.

Table 2.5: Measurement summary of the Isolation.

Parameters	Measured values
Isolation $I_{4,1}$	40 dB
Return loss $\|S_{11}\|$	-22 dB
Return loss $\|S_{44}\|$	-24 dB

The isolation between the input and the isolated ports is high (around 40 dB). Generally, Isolation values above 15 dB are considered as perfect.

2.3.1.4 Insertion loss

Insertion loss IL is the loss that occurs while a signal is traveling through a component, for this power divider, IL is defined as:

$$IL = -10 \log \left(\frac{P_2 + P_3}{P_1} \right) \text{ dB} = 0.02 \text{ dB} \tag{2.4}$$

2.3.1.5 Directivity

The directivity is directly related to the isolation and can be defined and deduced as::

$$D_{3,4} = -10 \log\left(\frac{P_4}{P_3}\right) = -10 \log\left(\frac{P_4}{P_1}\right) + 10 \log\left(\frac{P_3}{P_1}\right) = I_{4,1} + C_{3,1} = 35 \text{ dB} \tag{2.5}$$

where P_3 is the output power from coupled port (3) and P_4 is the power output from isolated port (4). The directivity should be as high as possible.

2.3.1.6 Phase balance between the two output ports

The phase difference between the two output ports of this hybrid power divider should be:

$$\Delta\varphi_{2,3} = \varphi(S_{21}) - \varphi(S_{31}) = -73 + 163 = 90^\circ \tag{2.6}$$

In conclusion, this power divider has good performances and characteristics: high isolation and high directivity, low insertion loss and good matching. Table 2.6 summarises the principal characteristics of the power divider.

Table 2.6: A summary of the power divider measurements.

Parameters	Measured values
Frequency	2998.5 $\pm$ 5 MHz
Coupling factor $C_{3,1}$	-4.79 dB
Transmitted coefficient $\lvert S_{21}\rvert$	-1.79 dB
Isolation $I_{4,1}$	40 dB
Directivity $D_{3,4}$	35 dB
Insertion Loss IL	0.02 dB
Phase balance $\Delta\varphi_{2,3}$	90°

2.3.2 ThomX motorised phase shifter (S/N 170117)

Phase shifters are utilised to vary the transmission phase angle (phase of S_{21}) of a two-port network. They have four essential characteristics. The first of them is insertion loss. Ideally, phase shifter provides low insertion loss in all phase states. While the loss of a phase shifter is usually overcome utilising an amplifier stage, lower insertion loss phase shifters need less amplification and lower power to overcome the losses. An another important characteristic is that phase shifter has equal amplitude for all phase states. Many systems using phase shifters must not encounter amplitude variations in signal level as phase states are varied. The third essential characteristic is that most phase shifters are reciprocal networks. This means they can perform successfully on signals going through them in either direction. These characteristics describe the electrical performance of phase shifters. The last characteristic is whether they hand over flat phase versus frequency, or true time delay. The ThomX phase shifter (Fig 2.14) developed by AMSAP in Germany was tested over the complete range of movement controlled by an IcePAP system. IcePAP is a motor control system developed at the The European Synchrotron Radiation Facility (ESRF) and optimised for high resolution position applications [32]. The maximum end positions are provided with limit switches, in order to protect the mechanical components from overpassing. These limit switches must be interrogated by the IcePAP stepper motor controller software, in order to ensure that the required function is maintained and the mechanics are protected.

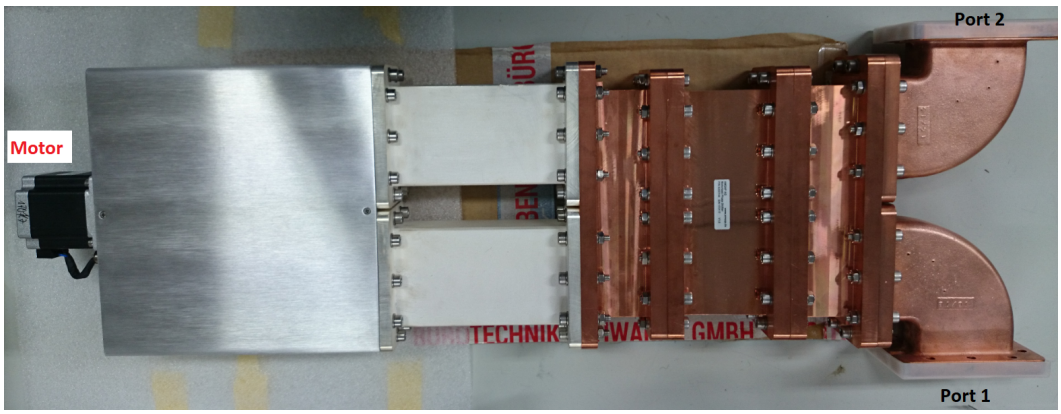

Figure 2.14: Picture of ThomX motorised phase shifter (S/N 170117).

This phase shifter (Fig 2.15) has a very low insertion loss $|S_{21}|$ of less than 0.02 dB and a return loss

$|S_{11}|$ of less than -32 dB (VSWR < 1.05:1), both of which are maintained over all phase states. It is a reciprocal device (S_{21}=S_{12} and S_{11}=S_{22}) with very stable amplitude and a phase change of over 420° at 2998.5 MHz. The step in the phase change is dependent on the programming of the stepping motors and, in our programming case, is below 0.5° per step.

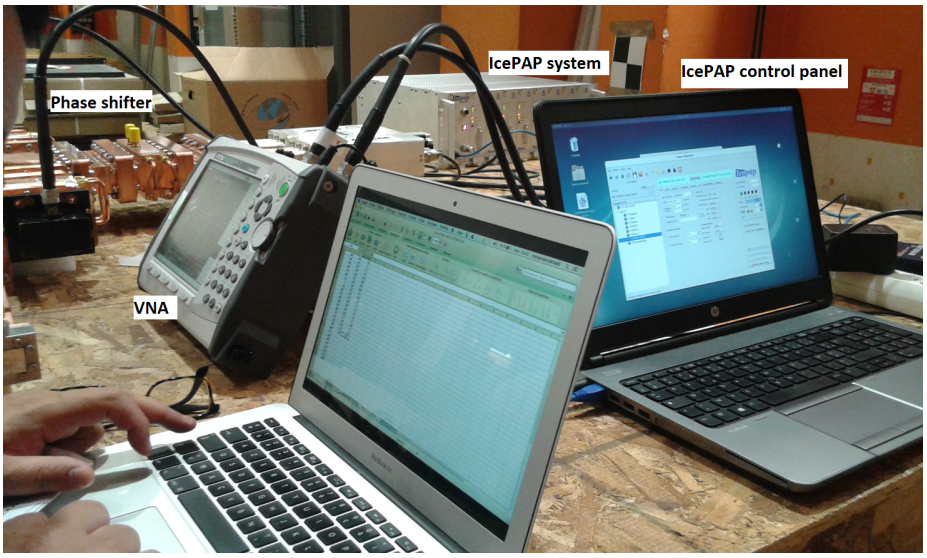

Figure 2.15: ThomX phase shifter under test.

Fig 2.16 shows the measured phase of the transmission coefficient S_{21} as a function of the step motor position.

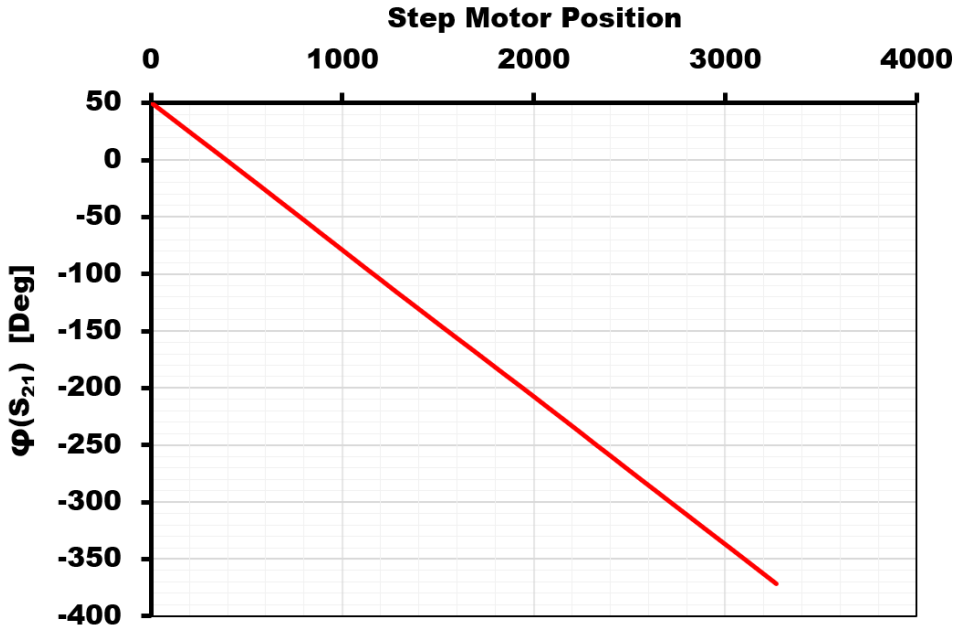

Figure 2.16: S_{21} phase measurement of the ThomX phase-shifter at 2998.5 MHz.

2.3.3 ThomX motorised attenuators (S/N 170126 & S/N 170127)

An attenuator is an electronic device used to decrease the power of the signal without deforming its waveform. It is effectively the opposite of an amplifier, since the amplifier provides gain, whereas the attenuator provides loss or gain of less than 1. The ThomX attenuator (Fig 2.17) developed by AMSAP is an absorbtive attenuator composed of a 3 dB power divider, phase shifters and ferrite loads. Absorbtive attenuators are used to change the transmitted power of a two-port network. The main parameter is an insertion loss (attenuation) = $|S_{21}|$. Ideally, attenuators provide a high range of attenuation variation with a low insertion loss at the starting phase. The attenuators S/N 170126 and S/N 170127 were tested over the complete range of motion of the sliding short circuits controlled by an IcePAP system to show that they meet the attenuation and voltage standing wave ratio (VSWR) specifications. The maximum end positions are provided with limit switches.

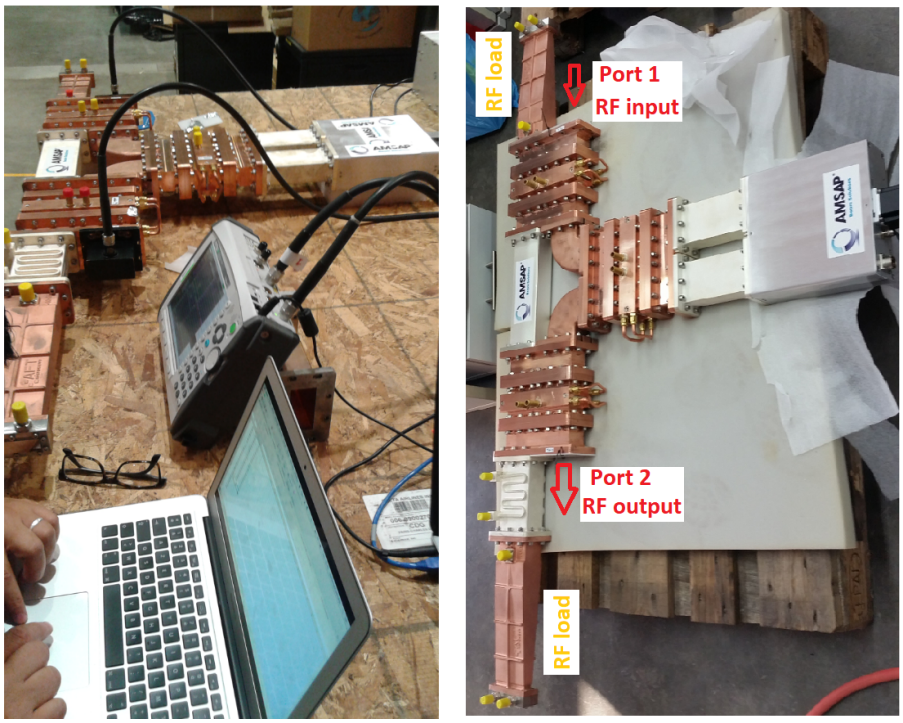

Figure 2.17: ThomX attenuator under test.

The ThomX attenuator has a very low insertion loss of less than 0.02 dB at the starting phase (zero position). It is generally a reciprocal device with a very high range of attenuation of more than 30 dB at 2998.5 MHz. The attenuation change is a non-linear function of the step motor position,

dependent on the programming of the stepping motors. The maximum VSWR recorded is 1.05:1, which is perfectly within the specification limit of 1.10:1. Fig 2.18 shows the measured attenuation of the ThomX atteunators as a function of the step motor position. The best working area would be in the step motor position range 0-1350.

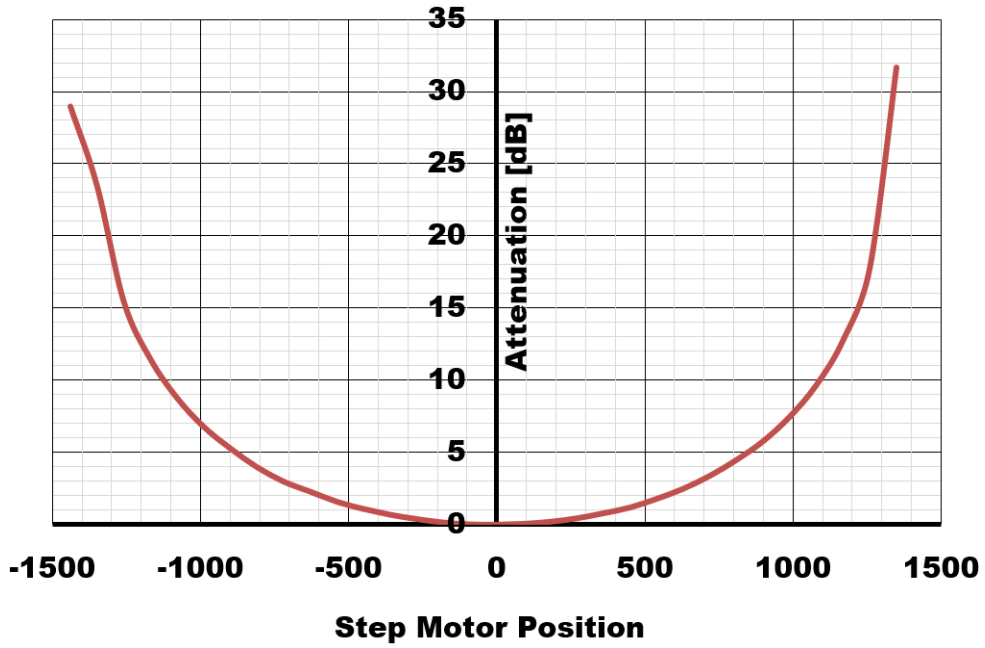

Figure 2.18: Attenuation measurement of the ThomX attenuators at 2998.5 MHz.

2.3.4 Ferrite Circulator/Isolator

The high-power circulator is an important device in the RF accelerator system. It is a multiport passive RF device carring out directional transmission of RF signals. The circulator has the characteristics of forward transmission and reverse isolation. When the RF signal transmits forward, the power is all fed to the RF gun, and the reflection wave from the gun is absorbed by the dummy loads of the circulator. The circulator can therefore provide effective protection for the klystron and improve the reliability of the klystron.

2.3.4.1 Working principle of the ThomX high power ferrite circulator/isolator (SC3-89)

Phase shift circulators are commonly used in high power (up to Mega-Watt) accelerator systems. The ThomX circulator (SC3-89) made by Ferrite Microwave Technologies, LLC, is a conventional

4-port differential phase shift circulator based on a rectangular waveguide in the H10 mode, where thin ferrite slabs are loaded and transversely magnetised. It uses three elements: a folded magic tee, a non-reciprocal phase shifter and a 3 dB-coupler, as shown in Fig 2.19.

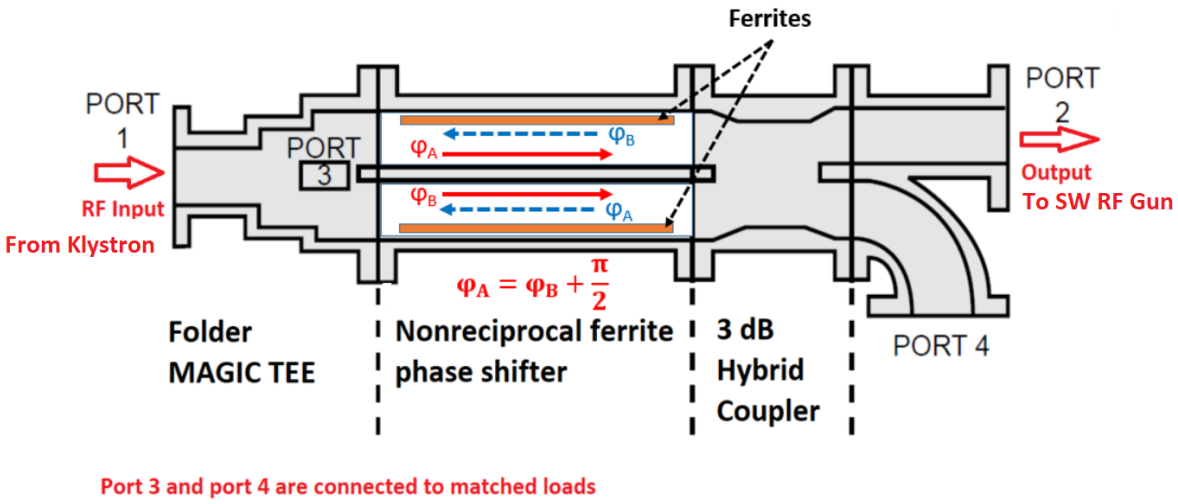

Figure 2.19: Diagram of the 4-port differential phase shift circulator.

An RF wave entering port 1 of the magic tee is split into 2 waves of equal amplitude and equal phase, which enter the non-reciprocal phase shifter. The first wave will be shifted by the non-reciprocal phase shifter by φ_A, and the second wave by φ_B, where $\varphi_A = \varphi_B + \pi/2$. In the 3 dB coupler, the two waves are split again into two equal parts, but the wave going to the other guide is delayed by 90 degrees. The waves therefore add at port 2 and cancel each other at port 4 to be loaded. A wave reflected from the RF gun entering port 2 is split in the 3 dB-coupler into 2 waves with equal amplitude but a 90 degree phase difference. The first wave will be shifted by φ_B, the second by φ_A. In the magic tee, both waves combine and cancel each other at port 1, but combine at port 3 to be absorbed by the termination load, and so on. In the ThomX LINAC RF NETWORK system, port 1 of the circulator is connected toward the klystron and port 2 is connected toward the RF gun. Both port 3 and port 4 are terminated with matched loads. A high power RF signal generated by the klystron is then fed to the RF gun. If breakdown occurs in the SW RF gun, the reflection will occur. The reflected wave will go back to port 2 and transmit to port 3, and it will be absorbed by the dummy load at port 3 with no output wave at isolated port 1.

2.3.4.2 RF low power test results

The RF measurement was performed using a vector network analyser (VNA) connected to input port (1) and output port (2) and two matched loads connected to the port (3) and the port (4). See Fig 2.20. The main parameters measured are Insertion loss IL, isolation, and reflection coefficients at the input and output ports.

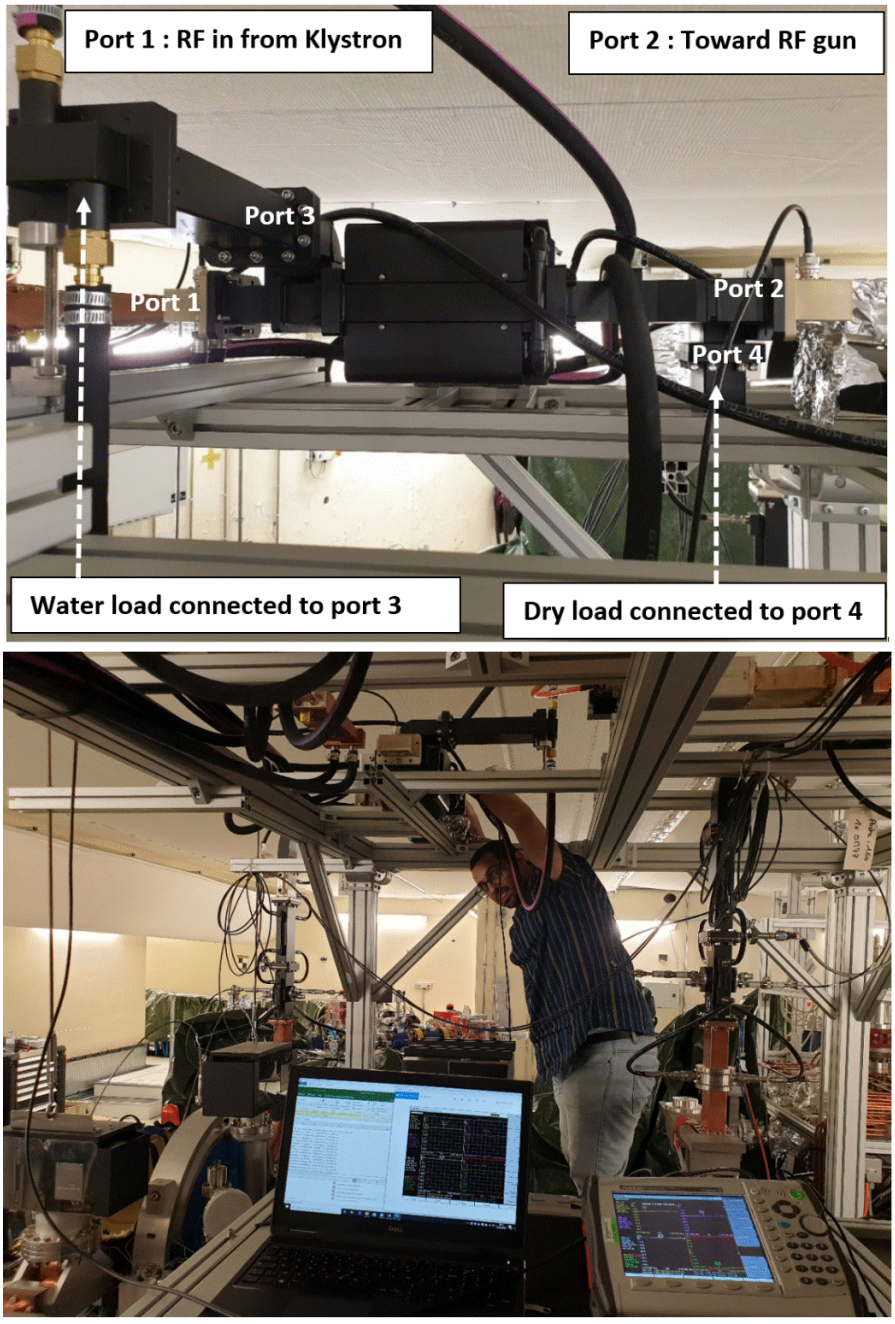

Figure 2.20: ThomX circulator under test.

2.3.4.2.1 Insertion loss (IL) The insertion loss is an important parameter when selecting a circulator. It can be defined as the total amount of energy lost while transmitting the RF signal from one of the circulator port to another. If an RF signal is applied at port (1), which is the input port, it will emerge from port (2), which is the output port, with a loss characteristic called insertion loss, which is the ratio of the output signal to the input signal expressed in dB:

$$\mathrm{IL(dB)} = -10 \log \left(\frac{\mathrm{P_{out}}}{\mathrm{P_{in}}} \right) = -|\mathrm{S_{21}}| \tag{2.7}$$

Typical values are: 0.1 to 0.4 dB. The measured insertion loss of this circulator is IL=0.3 dB, so the power dissipated in the circulator is around a peak of 0.67 MW (100 W average) considering its input power P_{in}=10 MW peak (1.5 kW average), most of which is due to the ohmic losses of the ferrites fixed in the waveguide wall. The dissipation of the power is absorbed by the ferrites and eventually converted into heat. This leads to an increase in the temperature of the ferrites and therefore magnetic saturation will occur, finally causing a degradation in the performance of the circulator. There are two ways to reduce the influence of temperature rising either by choosing ferrites with good temperature stability, or by increasing the cooling area of the ferrites.

2.3.4.2.2 Isolation The ThomX 4-port circulator is made up of an isolator by terminating port (3) and port (4) with matched loads. The circulator must perform a high isolation level. Isolation measures the separation of signal levels between one port of a device and another. A high isolation (in dB) value leads to low interference of the signal between one port and the other. If an RF signal (reflected wave from SW RF gun) is applied at output port (2), it will emerge at port (1) (input) with a high insertion loss called isolation. The measured isolation of the circulator is $I_{1,2}$=| S_{21}|=33 dB. Isolation values above 20 dB are considered good. In conclusion, this 4-port ferrite circulator has good performances and characteristics: high isolation, low insertion loss and good matching. Table 2.7 summarises its principal characteristics.

Table 2.7: Principal characteristics of the ThomX circulator.

Parameters	Measured values
Frequency	2998.5 MHz $\pm$ 2.5 MHz
Insertion Loss IL	0.3 dB
Isolation	33 dB
Input return loss $\mid S_{11} \mid$ (input VSWR)	-21 dB (1.19:1)
Output return loss $\mid S_{22} \mid$ (output VSWR)	-23 dB (1.15:1)

2.4 Description of the ThomX linear accelerator injector for commissioning

In the ThomX machine, the linear accelerator injector is the most important system that accelerates the beam to the desired energy. It is composed by one homemade photocathode RF gun for the electron generation, two solenoids that surround the RF gun for emittance compensation, the beam diagnostic line, vacuum equipment and the LIL-type 4.8 m long travelling wave (TW) accelerating section that boosts the electron beam to the final energy for the ring injection. Fig 2.21 shows the 3D scheme of the ThomX linear accelerator injector.

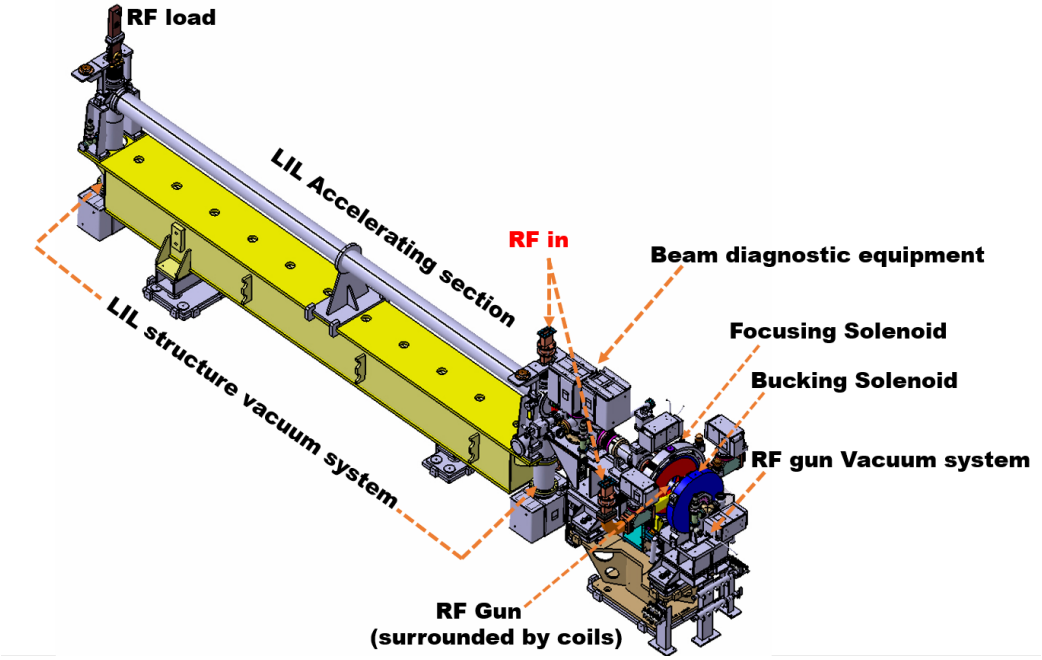

Figure 2.21: 3D scheme of the ThomX linear accelerator injector.

The electron beam is produced by a photo-injector with a copper photo-cathode during the low charge (100 pC) first phase, and a magnesium photo-cathode for the high charge (1 nC) final phase with a laser pulse energy of a few tens of a μJ at a wavelength of 266 nm. The electron beam is then accelerated in an S-band linear accelerator (LINAC). Table 2.8 summarises the nominal linac parameters.

For many years, the LAL (Laboratoire de L'Accélérateur Linéaire at Orsay, France) has designed and built RF guns for different projects, from CANDELA [33] at Orsay in France to ALPHAX for

Table 2.8: Nominal linac parameters .

Parameter	Value
Beam energy	50 MeV (70 MeV upgrade phase)
Cathode laser wavelength and pulse energy	266 nm, 100 μJ
Charge	1 nC
Number of bunches per RF pulse	1 bunch/pulse
RF pulse width (flat top)	3 μs
RF repetition rate	50 Hz
Average current	50 nA
Emittance (rms, normalized)	< 5 mm mrad
Bunch length, rms	< 5 ps
Energy spread, rms	< 1 %

Strathclyde University [34] in the UK, ELYSE [35] for the Laboratoire de Chimie-Physique at Orsay and, recently, for the probe beam and the test beam at CERN/CTF3 [36–38]. The ThomX RF gun has mainly the same design and the same mechanical concept as the CTF3 model. It is a 2.5-cell SW copper cavity with a resonating frequency of 2998.55 MHz (at 30 °C, in vacuum). The homemade RF gun, placed between two solenoids, guarantees a beam energy gain of 5 MeV with an accelerating gradient of 80 MV/m with an input peak power of 6 MW. In order to reach 50 MeV during the commissioning phase, the French National Synchrotron Facility (SOLEIL), as a main partner in the project, lent ThomX a standard LIL-type S-band accelerating structure that serves as a spare for its accelerator injector. This section was designed and manufactured at LAL for the pre-injector of the Large Electron-Positron collider (LEP) at CERN (Fig 2.22). The LEP Injector Linac (LIL) structure is an S-band travelling wave quasi gradient structure. The energy gain in the section is around 45 MeV, corresponding to an average effective accelerating gradient of around 10 MV/m (13 MV/m peak value) with an input RF power of 9 MW. However, the linac should reach higher electron beam energies in order to produce X-rays beyond 45 keV. Since the maximum targeted X-ray energy is 90 keV, the linac design should allow a beam energy of 70 MeV, corresponding to an RF power of 18 MW at the input of the LIL section. Thus, considering the efficiency of RF system, the specification for the total RF power is set at 35 MW. As the LIL structure is the spare for the SOLEIL Injector, the ThomX project is in the process of procuring its own accelerating section with the same goals: final electron beam energies ranging from 50 MeV to

70 MeV.

Figure 2.22: A picture of LIL structure.

This section highlights the RF gun, the configuration solenoids. The RF studies of the TW LIL accelerating structures will also be discussed and explained together with the simulation results.

2.4.1 ThomX RF gun

Photo-cathode RF guns are used in the first stage of electron beam generation and acceleration in particle accelerators. They are copper structures with different internal shapes fed by RF klystrons. They can work at different frequencies (from a few hundred MHz up to several GHz) depending on the different applications. RF photo-injectors are the ultimate choice for generating electron pulses of high bunch charges with low transverse emittance. The proposed ThomX RF gun (Fig 2.24) consists of a 2.5 cell normal conducting cavity produced from oxygen-free high thermal conductivity (OFHC) copper. The cavity operates in the standing wave regime in the π-mode ($TM_{010-\pi}$ mode) with a resonant frequency of 2998.55 MHz under vacuum at a nominal body temperature of 30 °C. The basic components of an RF photoinjector is presented in Fig 2.23. It is composed of an RF gun with a photocathode, a laser and optical system for producing the desired pulse, an RF source (e.g. klystron), and a timing and synchronisation system [39].

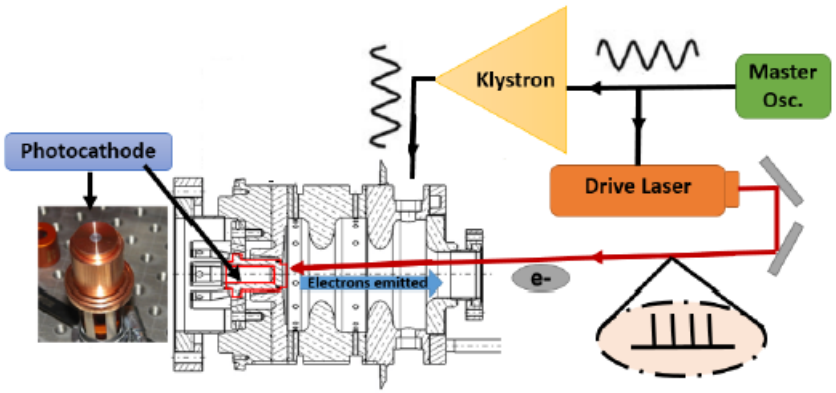

Figure 2.23: Schematic diagram of principal components in the RF phototinjector.

The cathode laser beam, transported to the gun vacuum part reflects from the vacuum mirror and produces a photo-electron bunch by hitting the photocathode surface, which is located in the RF cavity. The produced electron bunch is accelerated by the RF fields and focused by the combination of the static magnetic fields from the focusing and the bucking solenoids. The beam energy at the exit of the RF gun is about 5 MeV with an input peak RF power of 6 MW. A complete simulation of this RF gun was performed [40] with the multi-physics package of the finite element analysis code ANSYS [41]. The ThomX RF gun geometry design comes from the geometry improvement of the probe beam photo-injector (PBPI) of CTF3 [37] that had already designed and constructed by LAL. RF power is fed through one waveguide coupler only; the second waveguide is located 180 degrees opposite the input one and its main purpose is to cancel the field dipole component. The RF cavity shape was optimised with several innovative electromagnetic features including enhanced cell-to-cell coupling to produce a higher mode separation, elliptical irises to reduce the surface electric field, and symmetric couplers for dipole mode minimisation. It is externally fed only by one side to avoid the need for a power splitter, thus making the whole assembly much more compact, easier to handle and cost efficient.

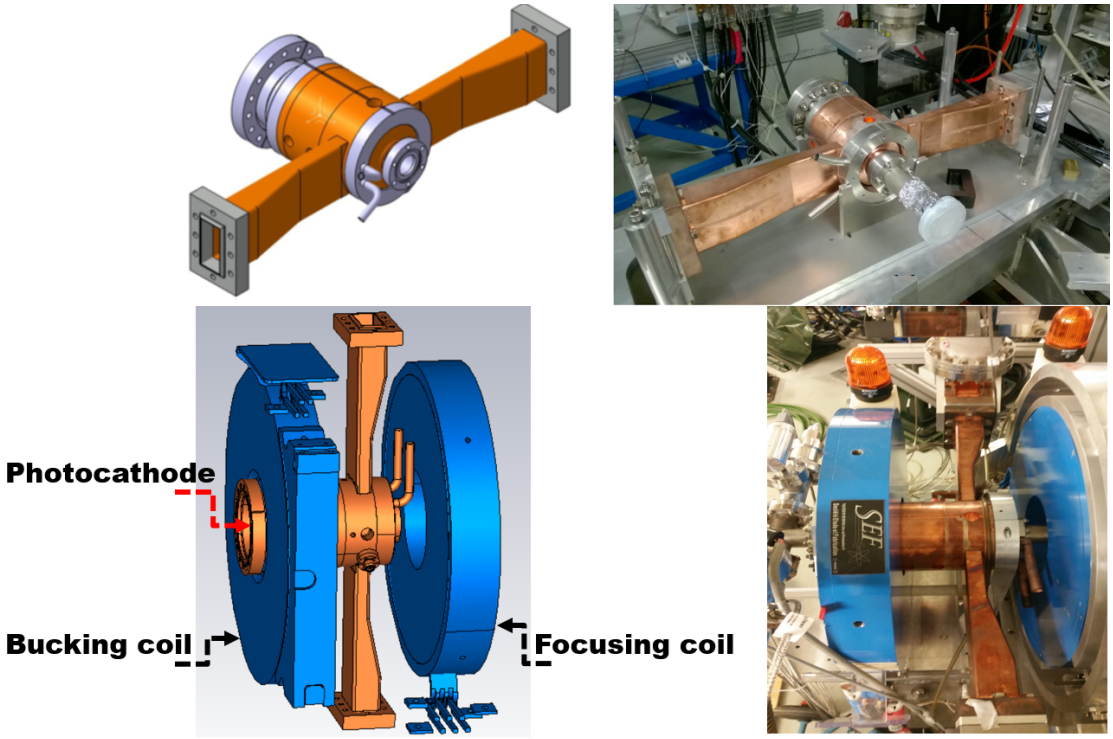

Figure 2.24: ThomX RF gun.

The electromagnetic analysis is performed using CST Studio Suite® [42], which determines resonant mode frequencies, quality factors, shunt impedance, filling time and electromagnetic field distribution. In order to efficiently deliver energy to the electrons, the so-called π-mode of the gun RF fields is used. This means that the fields are combined so that in one cell the electric field is accelerating while in another cell it is decelerating. In other words, the RF field phase advance between cells is 180°. An electron emitted from the cathode accelerates in the first half cell. The length of the first half cell is chosen so that, when the electron comes to the entrance of the second and the third full cell, the field changes its sign and the electron accelerates further into the full cell. The longitudinal electric field distribution (accelerating mode $TM_{010-\pi}$) in ThomX RF gun volume is shown in Fig 2.25.

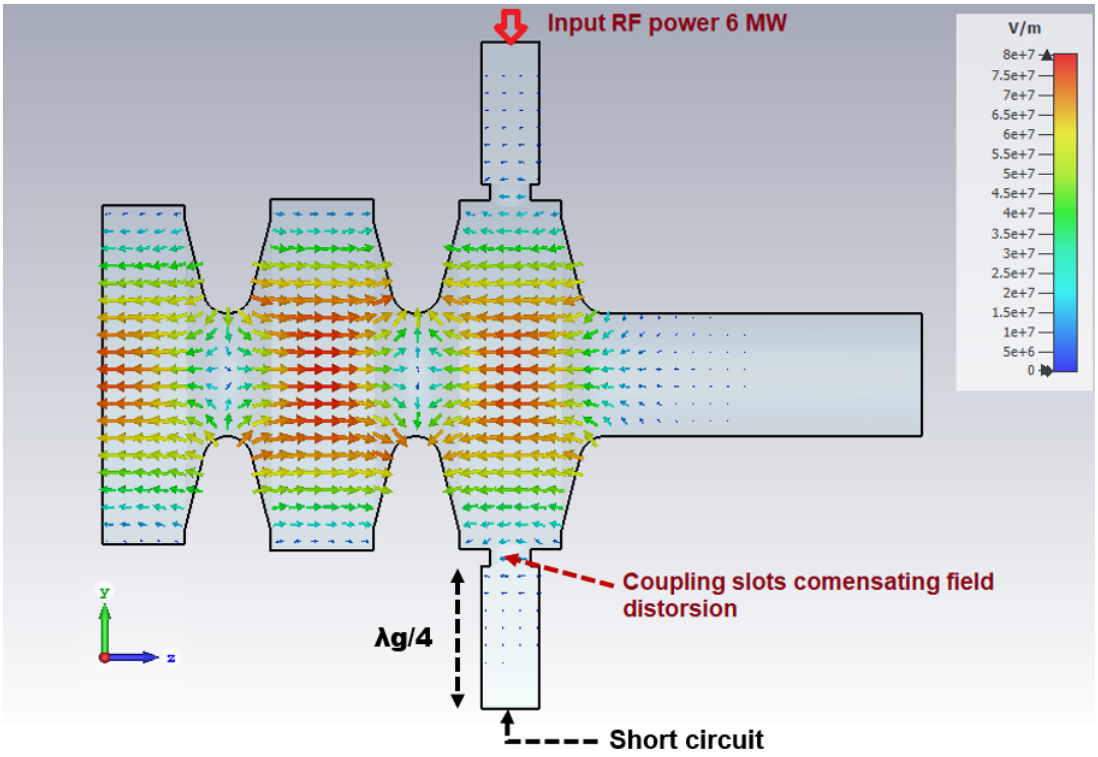

Figure 2.25: Electric field (accelerating mode $TM_{010-\pi}$) distribution in the ThomX photoinjector with a input RF power of 6 MW simulated using CST Studio Suite®.

Fig 2.26 shows the CST simulation result for the electric field profile on the beam axis. As can be seen, the excited electric field in the cavity has a phase advance per cell exactly of 180 °(π) and a good field balance, "field flatness", with a maximum value of 80 MV/m with 6 MW input power. Since the RF gun will be operated at a 50 Hz bunch repetition rate, it can be seen that the low average current is 50 nA, so the field induced by the beam in the cavity can be ignored and there is no need for any beam loading compensation [43].

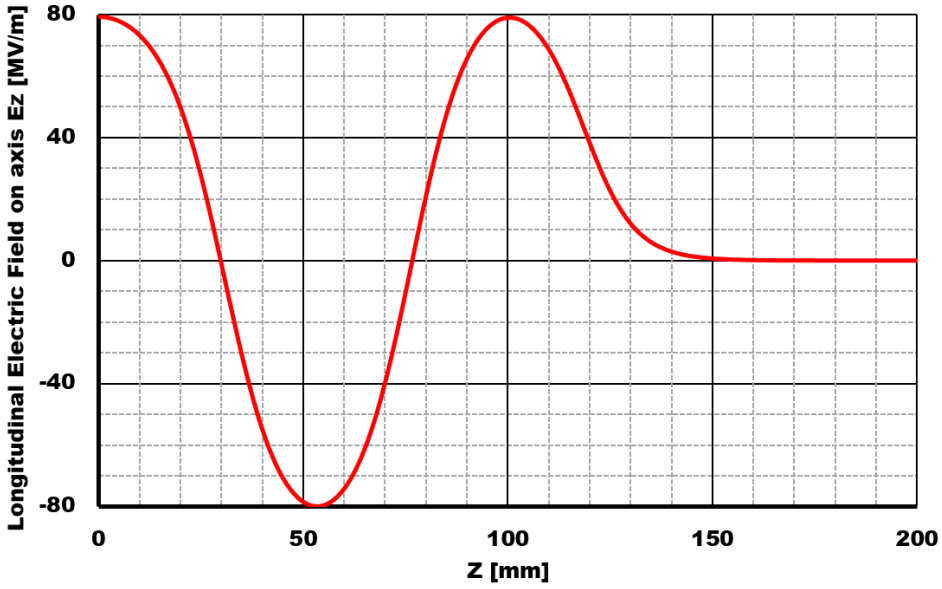

Figure 2.26: On-axis electric field for the π-mode ($TM_{010-\pi}$ mode) of the ThomX RF gun with 6 MW input power.

Slots and apertures, like the aperture of the coupler or the iris of the cavities, are the areas where the surface currents flowing along their edges and can reach very high densities. These high currents can give localised losses and create hot spots that can lead to dangerous breakdown effects. The cause of these phenomena is known as pulsed heating and has to be carefully evaluated and monitored in each place of the designed structure where there are high surface currents (i.e. high magnetic field). An upper limit of the temperature rise per pulse on the inner surface of the RF gun can be analytically estimated by assuming a constant amplitude of the surface magnetic field over the whole pulse length. This limit (ΔT_{max}) is given by the following formula, valid in the case of copper structures [44]:

$$\Delta T_{max}[^{\circ}C] = 127|H_s[MA/m]^2|\sqrt{f_{RF}[GHz]}\sqrt{t_p[\mu s]} \tag{2.8}$$

where f_{RF}, t_p, and $|H_s|$ are the resonant frequency, the RF pulse length and the amplitude of the surface magnetic field, respectively. As a general experimental rule, if this pulsed heating exceeds 110°C, serious damage to the coupler region has a high probability of occurrence. The surface magnetic field with 6 MW input power was calculated using CST Studio Suite® and is shown in Fig 2.27. The temperature increase due to pulsed heating on the coupler aperture is lower than 46 °C for

an RF pulse of 3 μs, while on the regular cell iris, it was evaluated at below 3 °C.

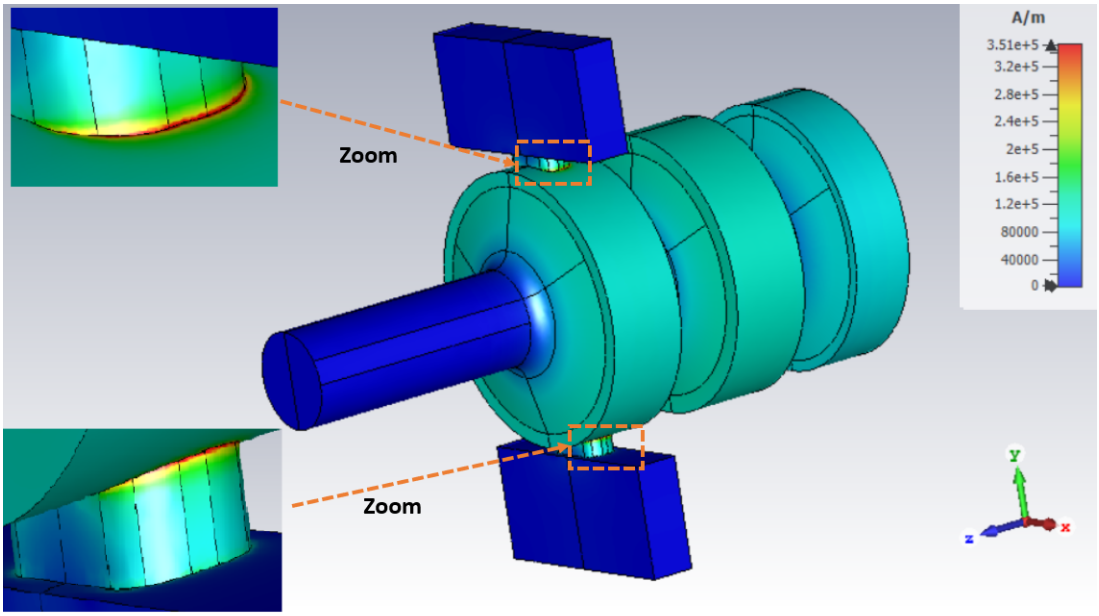

Figure 2.27: Surface magnetic field with an input power of 6 MW.

Fig 2.28 illustrates the energy gain and the longitudinal accelerating gradient E_{max} on axis (peak value) and an effective gradient E_{eff} on axis, seen by the electrons crossing the cells (mean value) as a function of the RF input power.

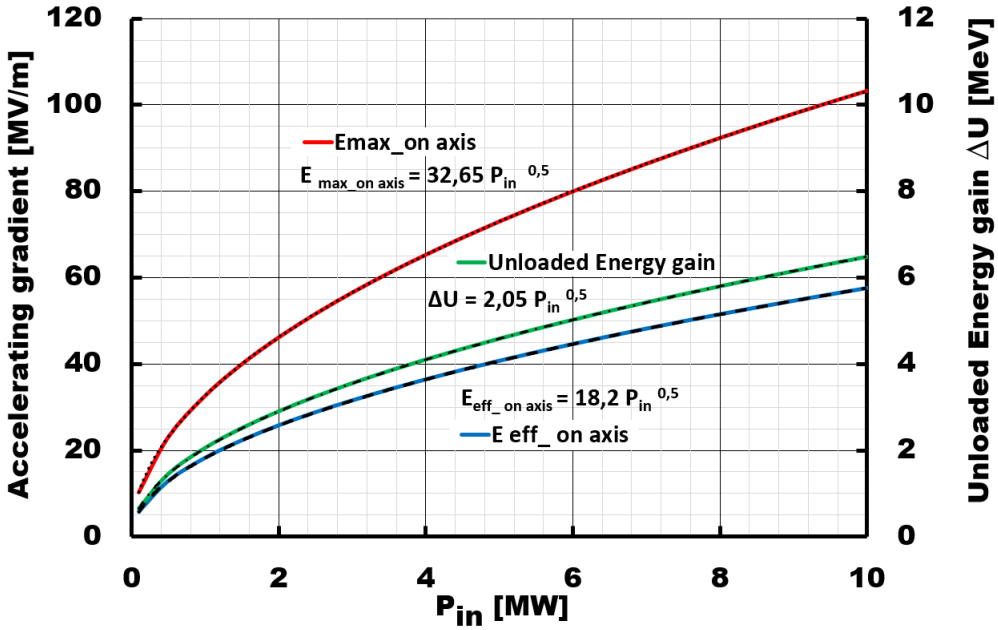

Figure 2.28: Accelerating gradient and energy gain as a function of the RF input power.

For the structure all the important RF quantities are also listed in Table 2.9.

Table 2.9: CST Simulation Results for the ThomX RF gun quantities.

Parameter	Value
Frequency	2.9985 GHz under vacuum
Operational temperature	30°C (stability $\pm$0.1 °C)
Phase advance per cell	π
Unloaded quality factor Q	15000
Shunt impedance r_s	49 MΩ/m
Filling time	0.7 μs
RF pulse width (Flat top) t_p	3 μs
Repetition rate	50 Hz
Input peak power P_{in}	6 MW
Average dissipated power	900 W
Peak accelerating gradient $E_{max-onaxis}$	80 MV/m @ 6 MW
Energy gain ΔU	5 MeV @ 6 MW
$E_{surfmax}/E_{max-onaxis}$	1.07
$\Delta U/\sqrt{P_{in}}$	2.04 MeV/$\sqrt{\text{MW}}$
$E_{max-onaxis}/\sqrt{P_{in}}$	32.65 MV/m/$\sqrt{\text{MW}}$
$E_{eff-onaxis}/\sqrt{P_{in}}$	18.2 MV/m/$\sqrt{\text{MW}}$
Pulsed heating (ΔT) max.	< 46°C @ 6 MW, t_p=3 μs

2.4.2 Solenoid configuration for beam focusing

During the electron beam acceleration in the gun cavity, the beam undergoes strong defocusing due to the space charge effect. In order to compensate this, a solenoid pair is applied (Fig 2.29). The solenoids also help to compensate the emittance during the acceleration in the gun cavity [45].

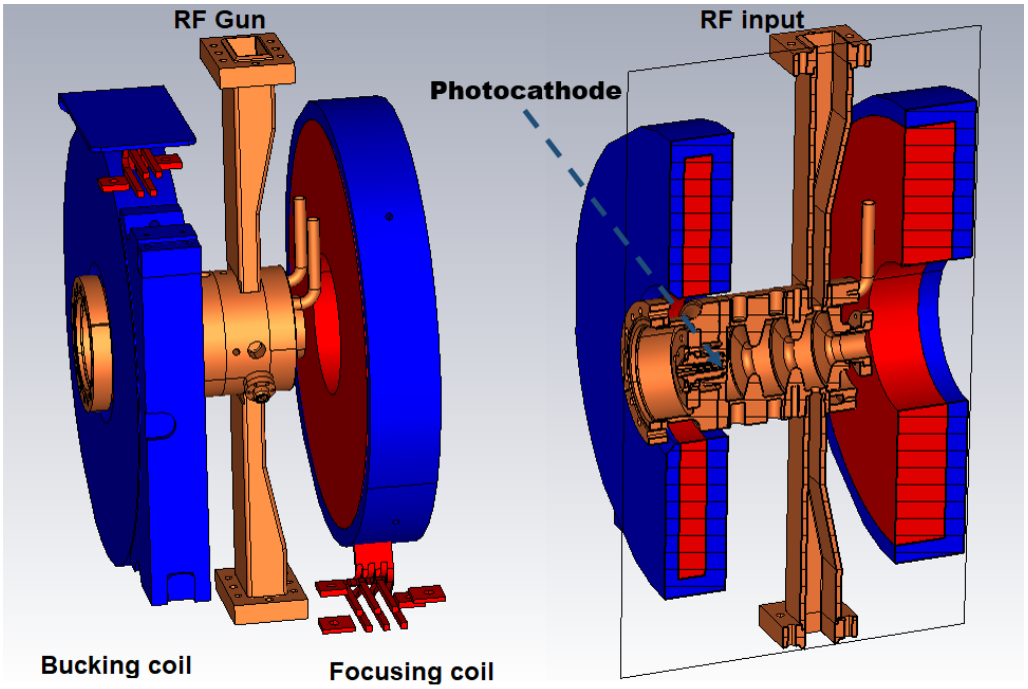

Figure 2.29: 3D drawing of the ThomX RF gun surrounded by the coils.

A magnetic field produced by the main solenoid is used to focus the electron beam at the exit of the gun, and the bucking coil compensates the magnetic field at the cathode. The positions of the coils were calculated and optimised to limit the emittance growth due to space charge forces and in order to move the beam waist closer to the accelerating structure entrance. The magnetic field calculated to maintain this low emittance value is 0.26 T for a bunch charge of 1 nC and E_{max}=80 MV/m on axis (Fig 2.30).

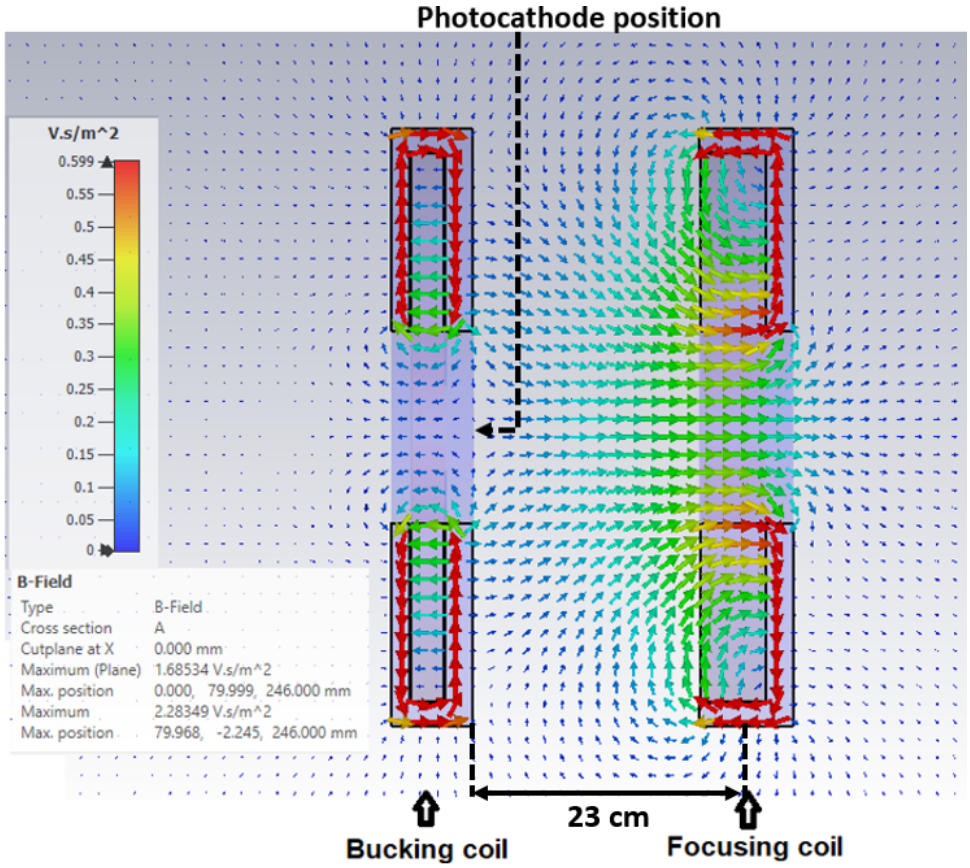

Figure 2.30: Model of the pair of solenoids surrounding the ThomX gun cavity with magnetic field structure. Field structure is simulated using CST Studio Suite®.

Fig 2.31 shows the simulated on-axis magnetic field profile for different values of the circulating current in the coils using CST Studio Suite®. The maximum magnetic field for different couples of currents in the two coils (Fig 2.31) is at position z=23 cm from the cathode position (z=0). Zero magnetic field is observed at the cathode position (z=0) for different couples of currents in the two coils [43].

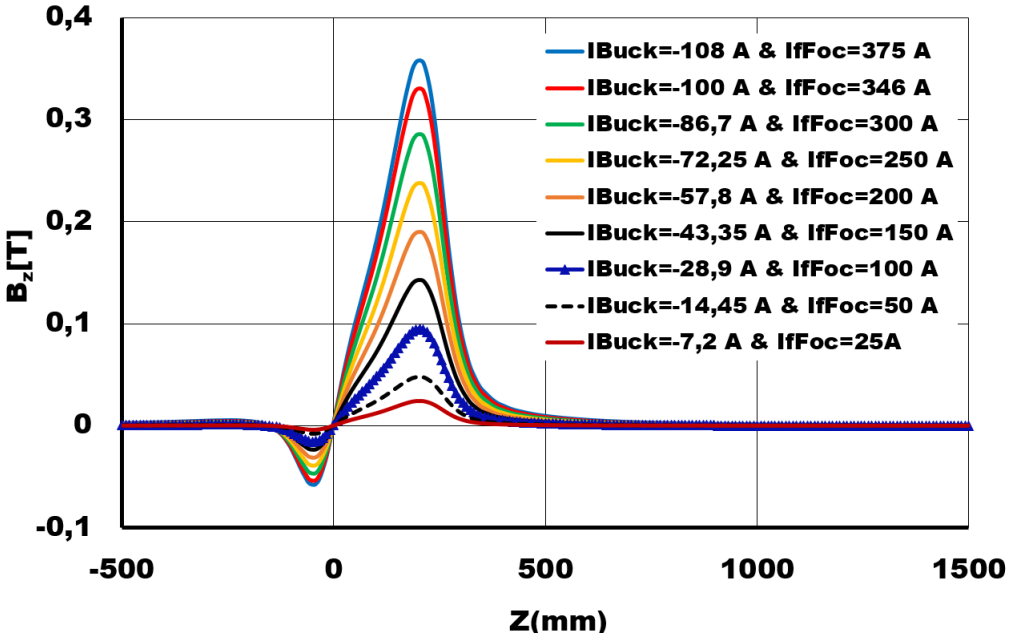

Figure 2.31: Magnetic field strength on the axis for different couples of currents in the two solenoids. CST simulation.

The empirical law for obtaining zero magnetic field at the cathode position (z=0) is presented in Fig 2.32.

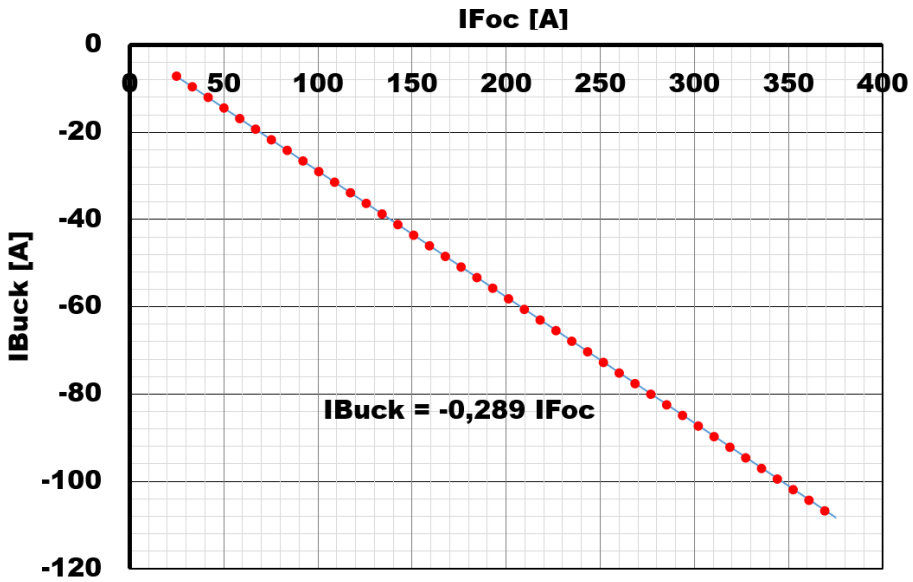

Figure 2.32: Empirical law of the bucking coil current as a function of the focusing coil current for zeroing the magnetic field at the cathode position. CST simulation.

2.4.3 A LIL-type S-band accelerating structure

During the commissioning phase, a 4.8 m long S-band TW LIL section will be used to achieve around 45 MeV for an input power of P_{in}=9 MW corresponding to around 45 keV X-ray energy. The LIL structure [46] is an S-band travelling wave quasi-constant gradient section composed of 135 elementary cells operating at f_{RF} = 2998.55 MHz (30 °C in vacuum) in the 2π/3 mode (Fig 2.33).

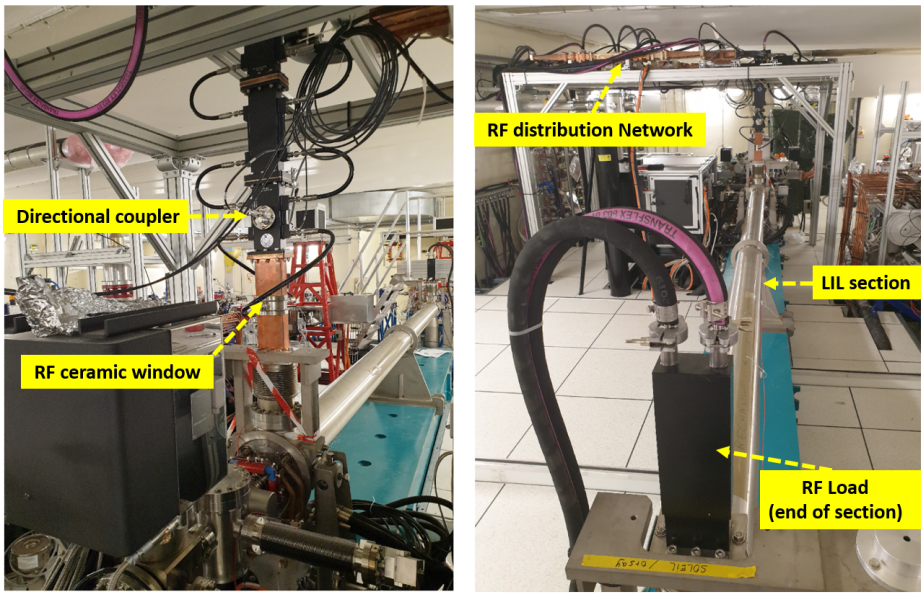

Figure 2.33: Picture of the LIL accelerating section installed in ThomX site.

2.4.3.1 Mechanical parameters

The disc-loaded accelerating section is made of 135 elementary cells (regular cells) and operates at f_{RF}= 2998.55 MHz (30 °C in vacuum) in the 2π/3 mode. Each cell consists of an iris between two half resonant cavities. To reduce the number of different cell types, the section consists of nine constant impedance landings with eleven identical cells per landing, except the input and output landings which each consists of 13 cells (quasi constant gradient structure). From one landing to the next, the iris diameter varies by 875 μm (an iris diameter range of 25 mm to 18 mm) and this causes the required change in group velocity. The step in iris diameter between consecutive landings is made smoother by inserting 4 transition cells which reduce the elementary step to 175 μm. Fig A.1 in Appendix (1) illustrates the distribution of the elementary cells along the LIL structure [47]. The outer cell geometry was designed to meet some contraints such as making four thin holes with a

diameter of 4 mm which help to pump the inner volume through an outer vacuum envelope, and four holes with a diameter of 10 mm around the cell with the wall thickness reduced to 1 mm to allow for an easy tuning deformation using a special tool. Fig 2.34 gives the overall aspect of a LIL cell. The elementary cells are made of oxygen-free copper of high purity and small grain size (Fig 2.35).

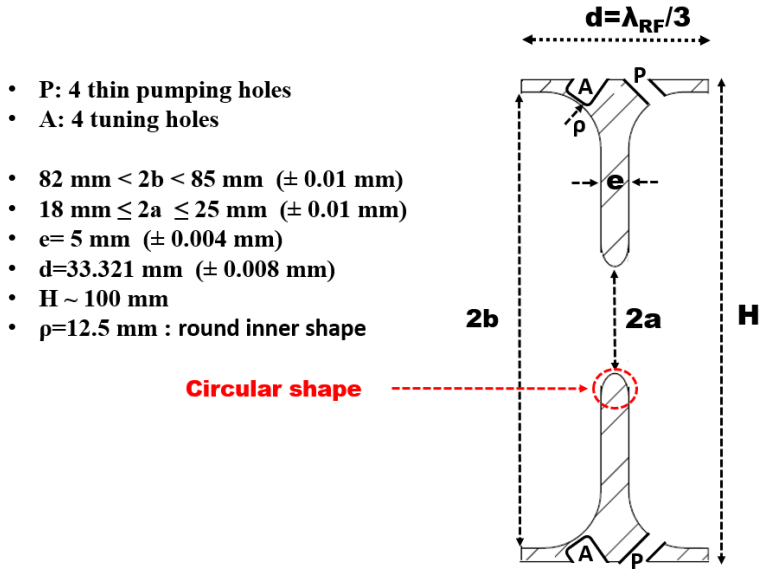

Figure 2.34: Mechanical aspects of a LIL cell unit.

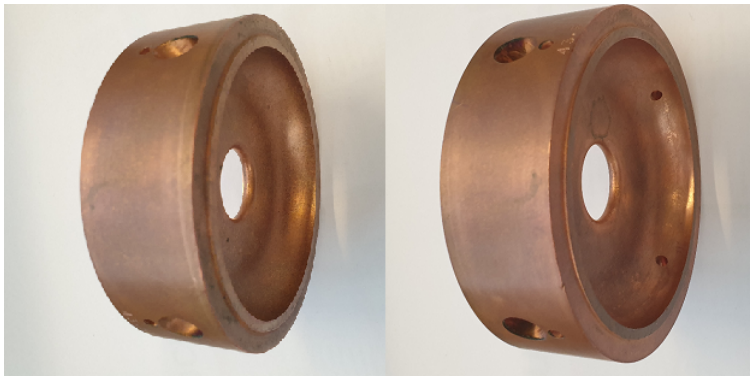

Figure 2.35: Picture of the LIL elementary cell.

The cell iris diameter is variable, see Fig 2.36. This variation along the section is intended to give a quasi-constant field along the structure.

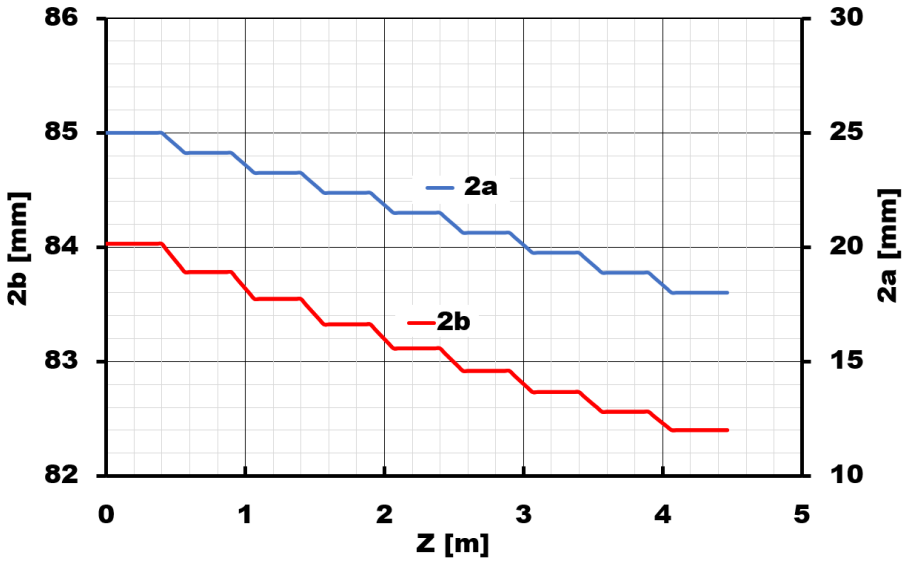

Figure 2.36: Cell iris diameter (2a) and cell inner diameter (2b) as a function of z along the structure.

The inner cell diameter (2b) of the elementary cell was set to maintain the required phase advance $2\pi/3$ at the operating frequency 2998.55 MHz according to a precise law (Fig 2.37). The empirical law between the inner cell diameter (2b) and the iris cell diameter (2a) is a polynomial expression in the form:

$$2b = 0.00015.(2a)^3 + 0.0071.(2a)^2 - 0.0956.(2a) + 81.74 \quad (2.9)$$

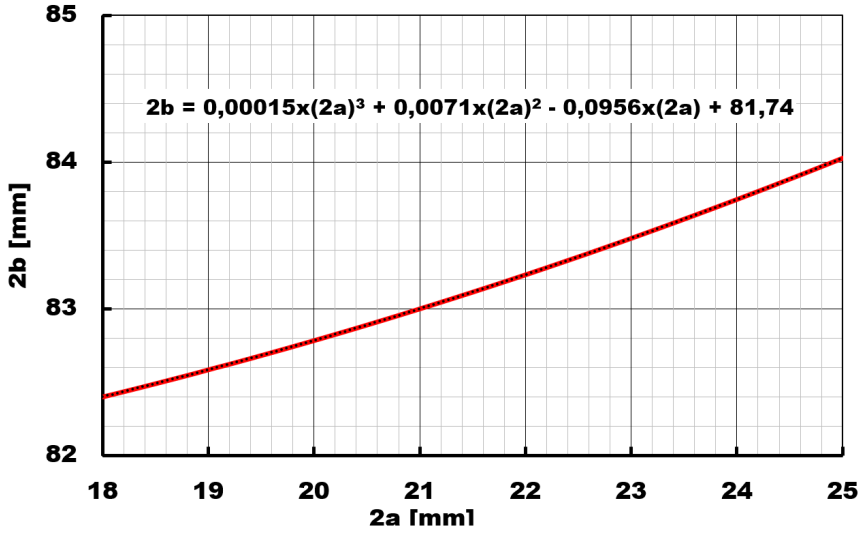

Figure 2.37: Inner cell diameter (2b) as a function of iris cell diameter (2a) at 2998.55 MHz (in vacuum at 30 °C).

In addition to the accelerating elementary cells, there are two couplers, an input coupler and an

output coupler, the latter being matched to a terminating water-cooled resistive load, which absorbs about 20 % of the input power. The two couplers contribute to the acceleration with nearly the same efficiency as the elementary cells. The main design parameters of the couplers are reported in Table 2.10 [48]. Each coupler consists of a resonant coupling cell, whose height is equal to the small size of the rectangular waveguide (and hence differs slightly from λ/3), and a half elementary cell (see section drawings in Appendix (1)). The coupler is fed from the waveguide through an input iris (aperture). The amplitude asymmetry was minimised by shifting the coupler axis away from the input iris by 1.88 mm and 1.13 mm for the input and output couplers respectively. This brought the amplitude asymmetry from 12 % down to 0.5 %. The remaining phase asymmetry is less than 1.5 degrees.

Table 2.10: Main parameters of the RF couplers of the LIL section.

Parameter	Input coupler	Output coupler
Coupling aperture width (transversal to beam) w	29.8 mm	23.36 mm
Coupling aperture length (parallel to beam) h	34 mm	34 mm
Coupling cell inner diameter	75.48 mm	75.24 mm
Coupling cell inner length	34 mm	34 mm
Half-cell iris diameter	25 mm	18 mm
Half-cell inner diameter	83.95 mm	82.35 mm
Cut-off length	66 mm	60 mm
Cut-off inner diameter	25 mm	25 mm
Inner surface roughness Ra	< 0.1 μm	< 0.1 μm
Type of connecting Flange	LIL	LIL
Type of brazing	Ag-Cu, 800 °C, HV	Ag-Cu, 800 °C, HV

After individual tuning and silver plating of the mating surfaces, the cells are mounted on a special bench, assembled with input and output couplers to allow matching of the couplers and global tuning. The LIL section is then brazed by silver diffusion at 350 °C and mounted in a thick-walled vacuum envelope which is machined from long bars of high purity stainless steel.

2.4.3.2 Electromagnetic characteristics

The 3D model of the accelerating cells was built according to the parameter design described previously using CST Studio Suite®. The 3D electromagnetic code CST MWS allows for simulation of periodic structures by using "periodic" boundary conditions and imposing a phase shift of 120 degrees between the two outer faces of the accelerating cell. A scan over the iris cell diameter (2a) along the structure was performed using parameter sweeping in the post processor with the eigenmode solver in order to determine the figures of merit of all accelerating cells along the structure such as: group velocity, filling time, shunt impedance, quality factor, accelerating field, energy gain, etc. See Fig 2.38.

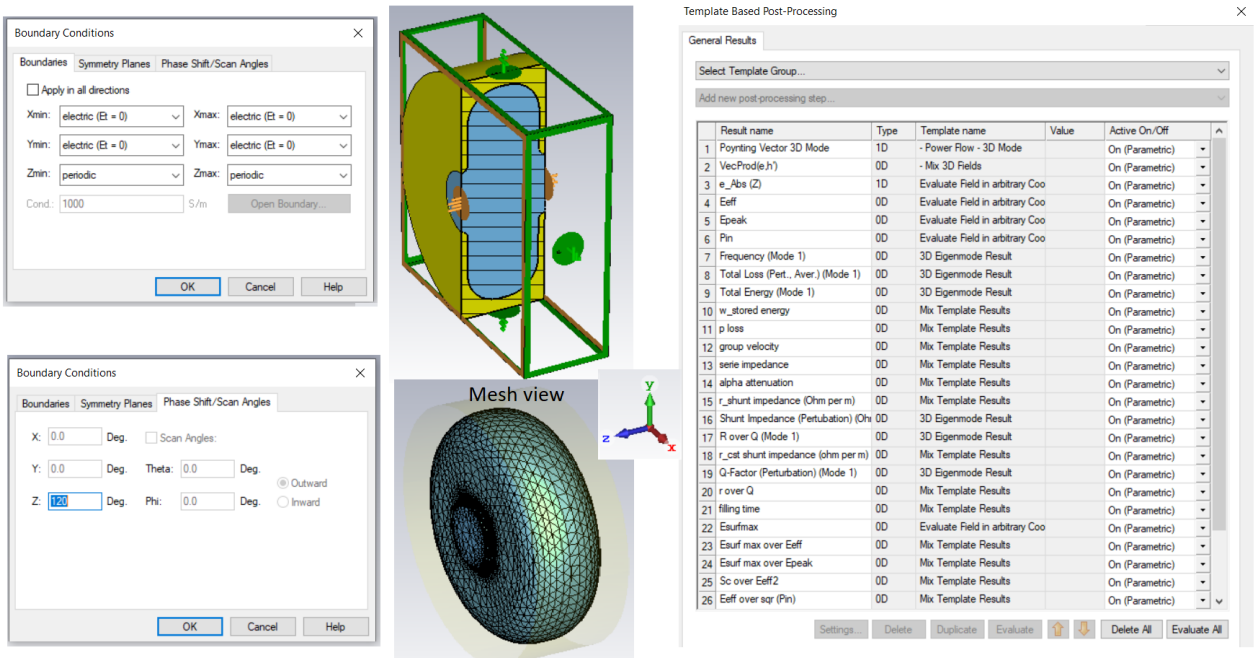

Figure 2.38: 3D CST model of the LIL accelerating cell.

These quantities have to be defined in a 3D simulation solver, for instance CST MWS, and then analysed using its template based post-processing. The main figures of merit for a single cell of a travelling wave structure are given below:

• The group velocity:

$$v_g = \frac{P_{in}}{w_{st}} \tag{2.10}$$

• The average input power (flux power):

$$P_{in} = \int_S \frac{1}{2} \Re(\vec{E} \times \vec{H}^*).\hat{z}.\, dS \tag{2.11}$$

• The stored energy in the cell per unit length:

$$w_{st} = \frac{1}{4d}\mu_\circ \int_V \vec{H}.\vec{H}^* dV + \frac{1}{4d}\varepsilon_\circ \int_V \vec{E}.\vec{E}^* dV \tag{2.12}$$

where d=λ/3 is the cell length and λ is the RF wavelength.

• The effective shunt impedance per unit length:

$$r_s = \frac{E_{eff}^2}{p_{dis}} \tag{2.13}$$

where p_{dis} is the average dissipated power per unit length equals:

$$p_{dis} = \frac{P_{dis}}{d} \tag{2.14}$$

where P_{dis} is the average dissipated power in the cell wall as given:

$$P_{dis} = \frac{1}{2} r_s \int_{S_{ext}} \left|\vec{H}_{tan}\right|^2 dS_{ext} \tag{2.15}$$

where $\vec{H}_{tan}$ is the tangential component of the magnetic field.

Defining E_z as the complex accelerating field on the axis, we obtain:

• The single cell energy gain:

$$eV_z = e \left| \int_0^d E_z e^{j\omega \frac{z}{c}} dz \right| \tag{2.16}$$

• The effective accelerating gradient in the cell seen by a particle (mean value):

$$E_{eff} = \frac{\left| \int_0^d E_z e^{j\omega \frac{z}{c}} dz \right|}{d} \tag{2.17}$$

where ω is the angular frequency and c is the speed of light.

• The quality factor of the cell:

$$Q = 2\pi f_{RF} \frac{w_{st}}{p_{dis}} \tag{2.18}$$

where f_{RF} is the RF frequency. The shunt impedance of an RF accelerator determines how effectively the accelerator can convert supplied RF power to an accelerating gradient; the larger the accelerating field per unit of supplied RF power, the more efficient the accelerator. The quality factor Q of an accelerating structure is a measure of the power loss in the walls of the cavity due to the current flowing through walls of finite resistivity. It determines the maximum energy the cavity can fill to with a given input power. Having a high Q, however, not only means having low surface losses, but also implies a high amount of stored energy. The simulated quality factor Q(z) and the shunt impedance $r_s(z)$ along the structure are displayed in Fig 2.39 [43].

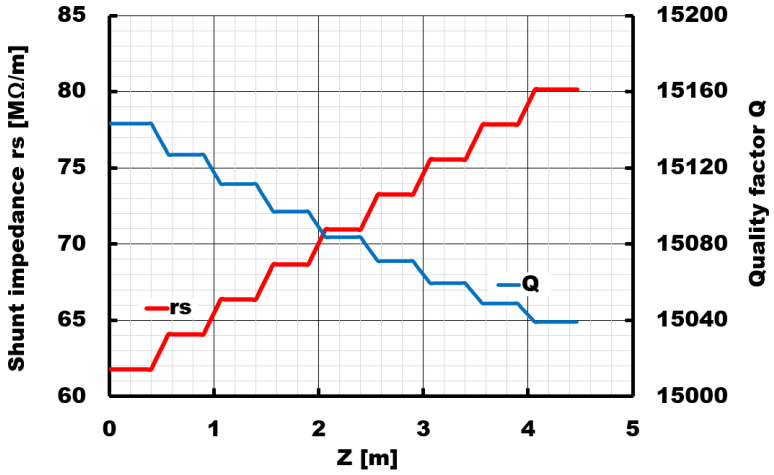

Figure 2.39: Simulated quality factor and shunt impedance along the LIL structure.

The group velocity v_g is the speed at which RF energy flows along the accelerating section. The group velocity depends on the iris cell radius. The filling time t_f is the time required for the electromagnetic energy to propagate at the group velocity from the input to the output end of the structure. Its definition is:

$$FT = \int_0^{L_s} \frac{dz}{v_g(z)} \tag{2.19}$$

where L_s is the length of the structure. A high group velocity (i.e. large iris radius) gives a small

filling time. For linacs operating in pulsed modes, the structure must be filled on each RF pulse before the beam is injected. The simulated filling time of the LIL structure is less than 1.35 μs. Fig 2.40 shows the group velocity $v_g(z)$ and the cumulative filling time (FT) along the LIL structure.

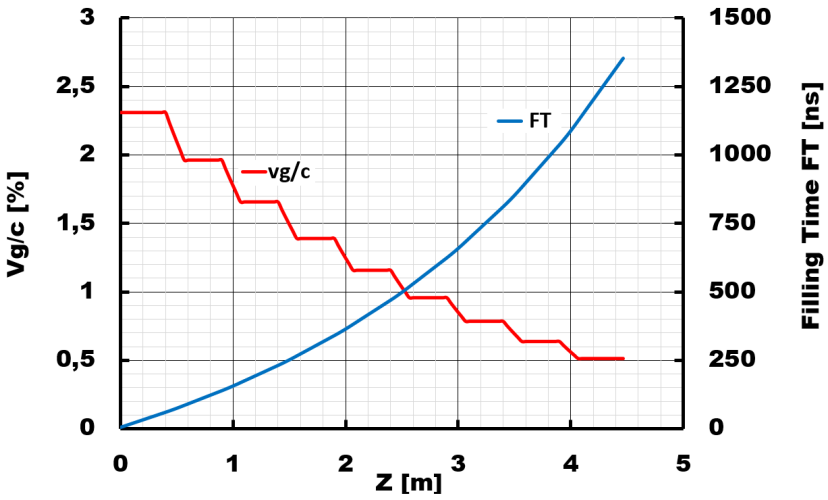

Figure 2.40: Simulated group velocity and filling time along the LIL structure.

The longitudinal electric field amplitude on the axis (accelerating mode $TM_{010-2\pi/3}$) along the LIL structure is reported in Fig 2.41. E_{max} on axis represents the maximum amplitude (peak value) of the longitudinal electric field on the axis at which each data point is monitored at the middle point of a cell. E_{eff} on axis is the effective accelerating gradient (mean value) seen by the electrons crossing the cells. The circulating power decays along the structure (Fig 2.41) and the remaining power at the end of the structure (P_{out}=0.2 P_{in}) is dissipated in a load [43].

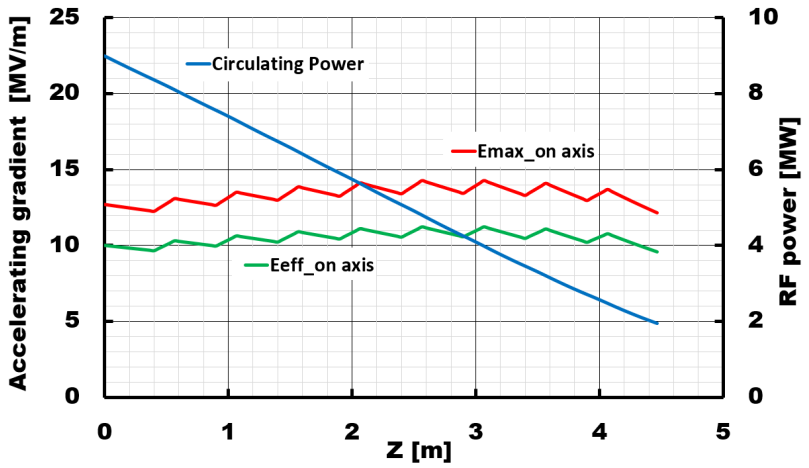

Figure 2.41: Accelerating gradient and circulating power along the structure with an input power of 9 MW.

Fig 2.42 shows the unloaded energy gain along the LIL structure. Considering an energy of around 5 MeV provided by the RF gun, the energy gain of the accelerating section is around 46 MeV with an input power of 9 MW. This should be enough to accomplish the final goal of 50 MeV for the commissioning phase of the ThomX linac.

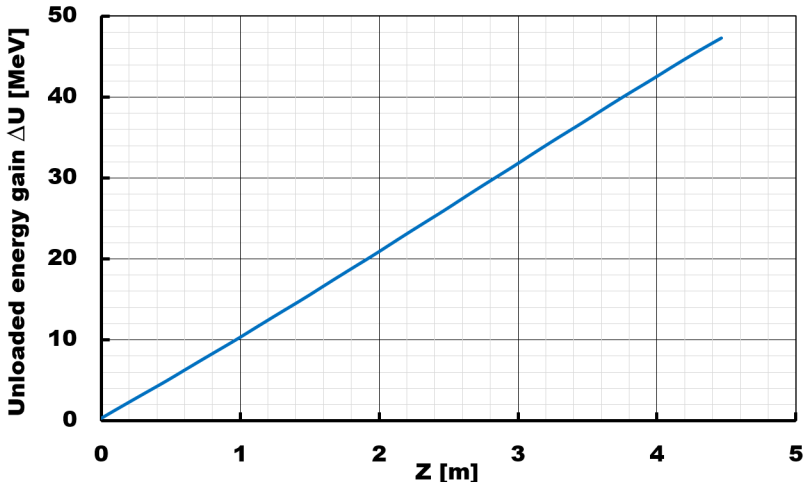

Figure 2.42: Energy gain along the LIL structure with an input power of 9 MW.

Fig 2.43 illustrates the energy gain and the accelerating gradients E_{max} on axis (peak value) and E_{eff} on axis (mean value) as a function of the RF input power.

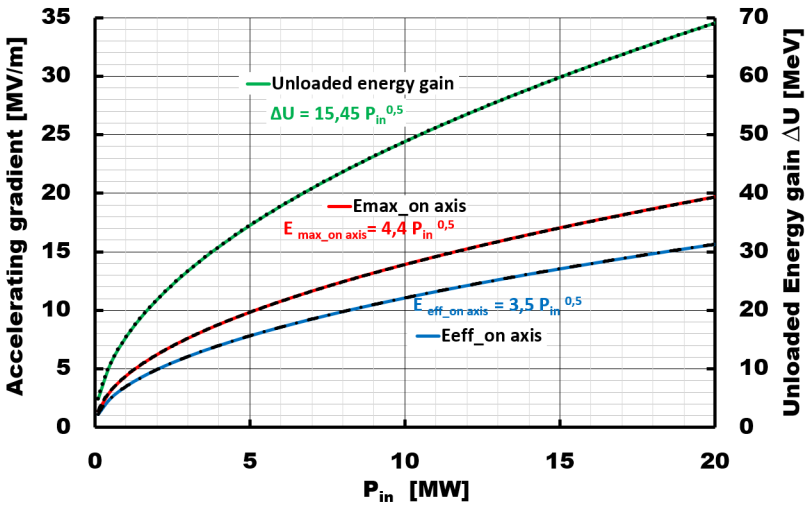

Figure 2.43: Accelerating gradient and energy gain as a function of the RF input power.

Table 2.11 reports the main parameters that are the basis for the LIL accelerating structure design.

Table 2.11: LIL accelerating structure main parameters.

Quantity	Value
Frequency	2.9985 GHz under vacuum
Operational temperature	30°C (stability $\pm$0.1 °C)
Number of cells	135 regular cells + 2 coupler cells
Length structure flange to flange	4.8 m
Iris diameter (2a)	25-18 mm
Inner cell diameter (2b)	84-82.4 mm
Disk thickness (e)	5 mm
Phase advance per cell	$2\pi/3$
Working mode	$TM_{010-2\pi/3}$
Average unloaded quality factor Q	15080
Shunt impedance r_s	61-80 MΩ/m
Group velocity v_g/c	0.023- 0.005
Output power P_{out}	0.2 P_{in}
Filling time	1.35 μs
RF pulse width (Flat top) t_p	3 μs
Repetition rate	50 Hz
Average $<E_{max-onaxis}>$	13.2 MV/m @ P_{in}=9 MW
Average $E_{acc}=<E_{eff-onaxis}>$	10.5 MV/m @ P_{in}=9 MW
Unloaded energy gain ΔU	46 MeV @ P_{in}=9 MW
$E_{surf-max}/ E_{acc}$	1.9
$\Delta U/\sqrt{P_{in}}$	15.45 MeV/$\sqrt{MW}$
$<E_{max}$-on axis$>/\sqrt{P_{in}}$	4.4 MV/m/$\sqrt{MW}$
$<E_{eff}$-on axis$>/\sqrt{P_{in}}$	3.5 MV/m/$\sqrt{MW}$

2.4.4 ThomX linac cooling system and thermal analysis

Cooling is needed to keep the temperature constant, because, if temperature changes are allowed, expanding and mechanical deformations may occur which would mean a change in resonant frequency of the accelerating cavity, which in turn would produce reflection of RF power. Since the gun cavity operates with an RF pulse of 3 μs, a peak power of 6 MW and a 50 Hz repetition rate, the cavity body must be cooled. For this purpose, water cooling channels are integrated in the gun cavity body walls. A complete thermal analysis of this RF gun was performed using ANSYS [40]. Considering an average power dissipation of 900 W into the RF gun corresponding to an input power of 6 MW, and considering a nominal water flow rate of 15 l/min (i.e. 1.5 m^3/hour), the ΔT_{water} between the output water and the input water is calculated as:

$$\Delta T_{water} = T_{outlet} - T_{inlet} \tag{2.20}$$

which is 0.87 °C and $T_{structure}$–T_{inlet} is 3.5 °C. The temperature stabilisation of the LIL accelerating structure is achieved by water flowing through four cylindrical longitudinal copper cooling pipes (4 flow return pipes) with an internal diameter of 12 mm and 9 m in length, brazed on the cavities. Based on our past experience, to reduce the vibrations and corrosion effects of the copper pipes, we have fixed the maximum water flow velocity in each pipe at 3 m/s. Starting from an electromagnetic analysis, the field distributions of the accelerating mode were evaluated. Since the LIL structure is a TW structure, the power decays along the z-direction (the beam direction). The total power dissipated into the LIL structure is P_{dis}=0.8 P_{in}. The increase of the water temperature ΔT_{water}=T_{outlet}-T_{inlet} can be calculated using the following formula:

$$\Delta T_{water} = \frac{P_{dis}}{c_p \dot{m}} \tag{2.21}$$

where c_p is the specific heat capacity and $\dot{m}$ is the mass flow rate. In order to complete the setup for the thermal analysis, we need to model the convection phenomena. First, we calculate the heat transfer coefficient h and the average temperature in the body structure $T_{structure}$. Starting from the

data obtained, the coefficient h can be evaluated as:

$$h = \frac{N_u \lambda}{L} \tag{2.22}$$

where N_u is the Nusselt number, λ is the thermal conductivity and L is the characteristic length of the water pipes. In our case, N_u has the following expression:

$$N_u = 0.023 R_e^{0.8} P_r^{0.333} \tag{2.23}$$

The Reynold number R_e is given by:

$$R_e = \frac{\rho v D}{\mu} \tag{2.24}$$

where ρ is the water density, v is the water velocity, D is the pipe diameter and μ is the dynamic water viscosity. The Prandtl number P_r is given by:

$$P_r = \frac{c_p \mu}{\lambda} \tag{2.25}$$

We now calculate the difference between the inlet water temperature and the average temperature of the structure using the following expression:

$$\Delta T_{str-in} = T_{structure} - T_{inlet} = \frac{P_{dis}}{h \pi D L} \tag{2.26}$$

Considering the average dissipated power into section P_{dis} is 1.08 kW with an input peak power of 9 MW and water flow rate of 60 l/min (i.e. 3.6 m^3/hour), the estimated ΔT_{water} is 0.26 °C and ΔT_{str-in} is 0.05 °C. The cooling system characteristics of the RF gun and the LIL accelerating section are reported in Table 2.12.

Table 2.12: Typical cooling system characteristics of the RF gun and the LIL section.

Quantity	RF gun	LIL section	LIL section
Input peak power (MW)	6	9	18
Incoming water flow rate (l/min)	15	60	80
Water velocity in pipe (m/s)	2.5	2.2	2.95
RF pulse width (μs)	3	3	3
Repetition rate (Hz)	50	50	50
Average dissipated power P_{dis} (W)	900	1080	2160
Heat transfer coefficient ($W/m^2.K$)	10143	8512	10715
Temperature set point: T_{set}=$T_{structure}$ (°C)	30	30	30
Water inlet temperature: T_{inlet} (°C)	26.47	29.95	29.93
Water outlet temperature: T_{outlet} (°C)	27.34	30.21	30.32
ΔT_{water} (°C)	0.87	0.26	0.39

The operating temperature T_{set}=$T_{structure}$ of the RF gun and the LIL section needs to be fixed in order to get the electromagnetic performances we want to achieve. So, when the RF input power is zero, the input water temperature must be set to its nominal value for the operating frequency: T_{inlet}=T_{set}=30 °C. As the input power level increases, the cavity structure will experience RF heating, temperature changes and thermal deformations that influence its RF characteristics in terms of phase velocity. This is not allowed owing to the stringent requirements imposed by the ThomX project and so a thermal control strategy to keep the operational structure temperature as constant as possible with a stability of$\pm$ 0.1°C is implemented using two RT 100 control systems from Regloplas AG (Fig 2.44).

Figure 2.44: Picture of the Regloplas temperature control systems.

By maintaining the water flow rate "constant" while the machine is in operation, we keep the temperature of the structure constant, in the range P_{dis}=[0;Max], thus modifying the input water temperature. The optimal solution would be to decrease the input water temperature linearly when the dissipated power increases, according to:

$$T_{inlet} = T_{set} - k.\Delta T_{water} \tag{2.27}$$

where slope k is evaluated on the basis of the previous thermo-mechanical parameters of each structure. For the RF gun: k = 4.06 with a nominal water flow rate of 15 l/min and for the LIL structure: k=0.17 with a nominal water flow rate of 60 l/min. Fig 2.45 and Fig 2.46 show typical water input and output temperatures for optimising thermal parameters of the structure at different power levels with nominal water flow rates for both the RF gun and the LIL section.

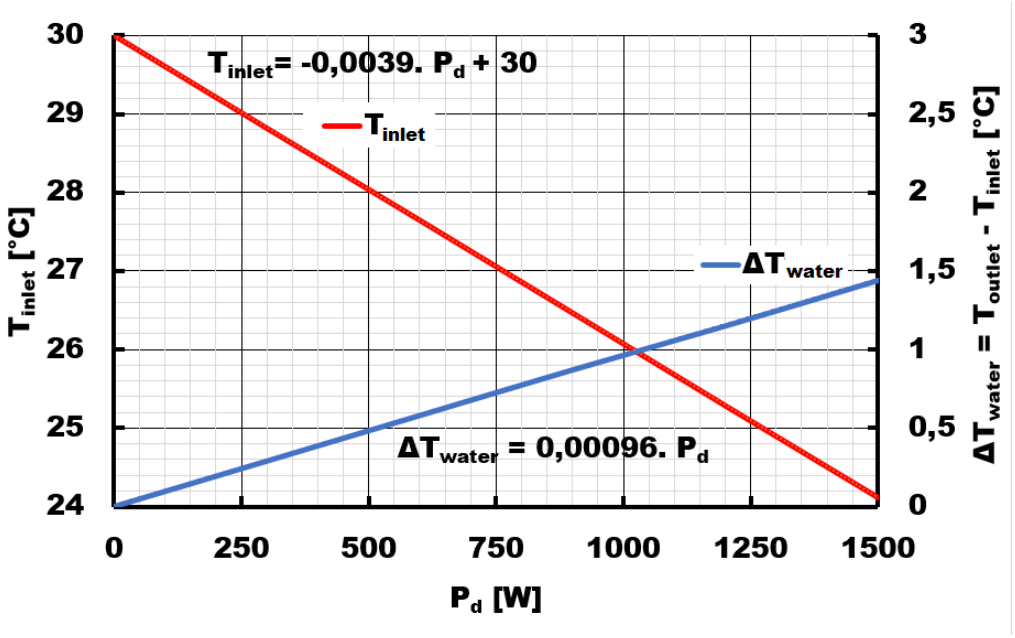

Figure 2.45: Water inlet and outlet temperatures as a function of the dissipated power into the RF gun with a nominal water flow rate of 15 l/min (T_{set} = $T_{structure}$=30°C).

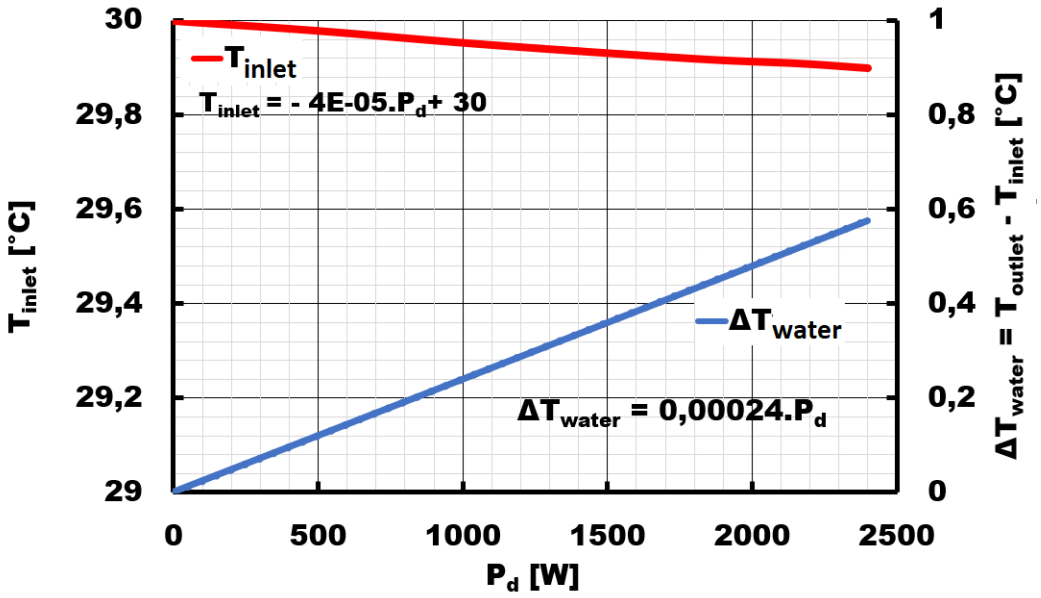

Figure 2.46: Water inlet and outlet temperatures as a function of the dissipated power into the LIL structure with a nominal water flow rate of 60 l/min (T_{set} = $T_{structure}$=30°C).

2.4.5 ThomX linac vacuum system

The RF gun is equipped with sufficient vacuum pumping system, as shown in Fig 2.47, to provide a good vacuum in the photocathode cell that significantly improves the photocathode lifetime. For that

purpose, four ion pumps (IP) are installed, one at the upstream of the photocathode (1 IP Agilent VacIon Plus 40 Starcell of 34 $l.s^{-1}$ pumping speed) to maintain 1.8 10^{-10} mbar, on the waveguides (2 IP Agilent VacIon Plus 75 Starcell of 65 $l.s^{-1}$) assuming 2.1 10^{-10} mbar, and at the exit of the RF gun (1 IP Agilent VacIon Plus 55 Starcell of 50 $l.s^{-1}$) to achieve 2.3 10^{-10} mbar level.

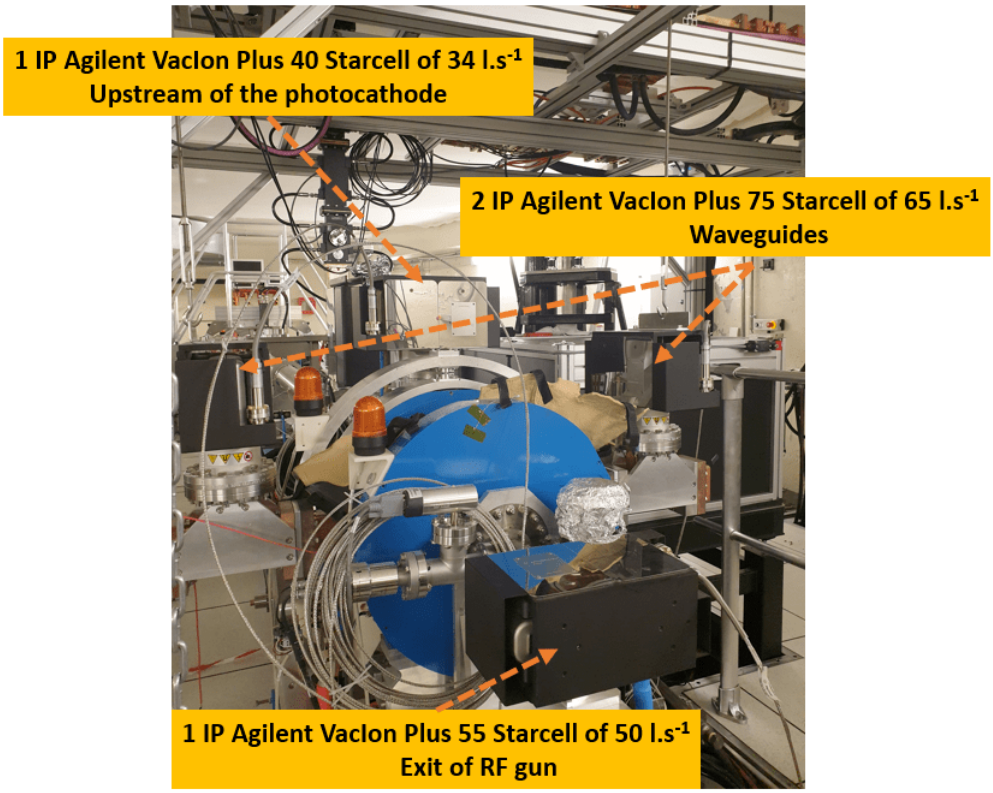

Figure 2.47: Ion pumps installed on the RF gun.

A critical element for the vacuum is the LIL TW accelerating section. This consists of a cylindrical stainless-steel envelope with a minimum internal diameter of 144 mm, containing the copper accelerating structure (outer diameter 102 mm), which is 4.5 m long (135 regular cells) and is pumped (mainly) through 540 holes (4 holes per cell) 4 mm in diameter in the copper outer wall (illustrated in Fig 2.34). A high vacuum is maintained with two ion pumps (Agilent VacIon Plus 300 Starcell model) of 240 $l.s^{-1}$ effective pumping speed at the input and output ends of the section as presented in Fig 2.48. Pressure gauges indicate 1.2 10^{-10} mbar and 4.3 10^{-9} mbar respectively at input and output.

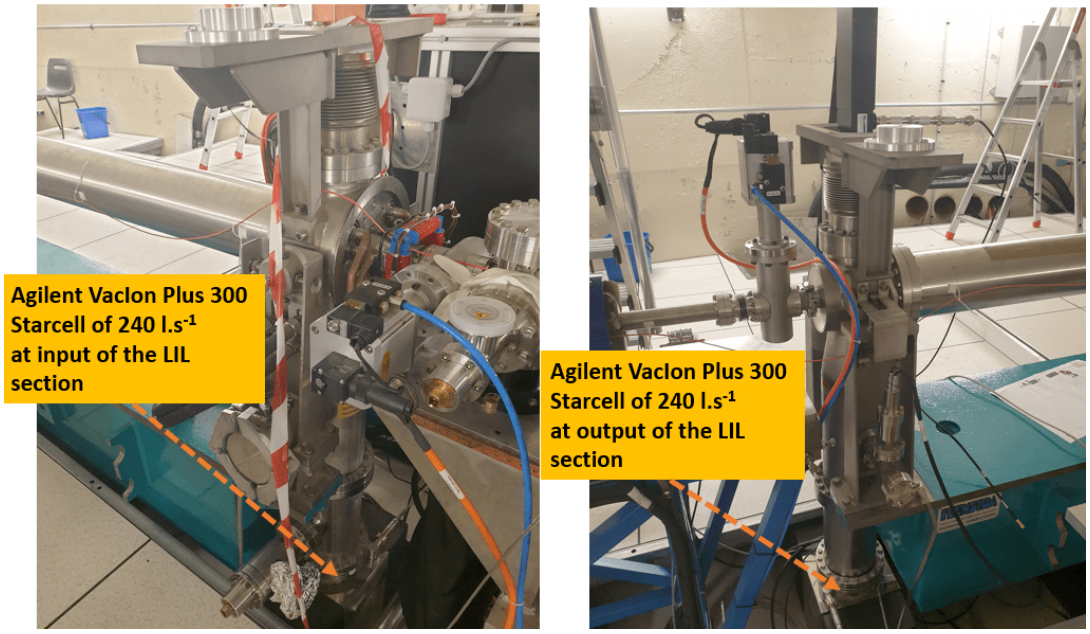

Figure 2.48: Ion pumps installed on the LIL structure.

All the ion pumps are read by the control system and the machine protection system (MPS) through the ion pump controllers arranged in racks.

Chapter 3

Commissioning of the ThomX linac

This chapter describes in detail the commissioning of ThomX linac started in July 2021. I describe the RF conditioning of the RF gun and the LIL structure. Next, I present the commissioning of the first beam of ThomX which consists of the charge measurement using an integrated current transformer (ICT) and the energy measurements using steerer magnets. In addition, analytical approximation models for the kinetic energy and the energy spread of an electron beam in the photoinjector and the travelling wave structure are explained and compared with measurements. This chapter also represents energy measurements using a dipole spectrometer carried out at the PHIL photoinjector facility, located at the "Laboratoire de Physique des 2 Infinis Irène Joliot-Curie" (IJCLab) because such spectrometer measurements are not available in the phase 1 of ThomX.

3.1 RF commissioning of the ThomX linac

Radiofrequency cavities need to be conditioned before being put into operation when they are new, or have been out of operation, or after backfilling to ambient pressure, or vacuum accident etc. The conditioning is done by applying ramped RF power to the system. This cleans the surface via several effects: induced out-gassing due to RF-heating, arcing, multipacting which enhances local heating and desorption. Due to the fact that arcing can destroy components such as RF windows and can burn holes in the RF surfaces, RF conditioning must be done gradually and in a controlled way.

Generally, during the conditioning process different parameters are monitored, such as the vacuum quality inside the RF components and the forward and reflected RF signals at different points of the set-up. These parameters are used to verify progress in the conditioning, but also to generate interlocks in order to protect the components in case of breakdowns. The RF conditioning and high power testing of the RF gun and the LIL accelerating structure were carried out at the ThomX installation site. The first commissioning phase of the ThomX linac started in July 2021 in compliance with the French nuclear safety authority (ASN) authorisation (100 pC, 50 MeV at 10 Hz). A schematic representation of the complete RF system for high power testing is shown in Fig 3.1. A Toshiba Klystron E37310 driven by a K2-2 Scandinova modulator provides up to 37 MW peak output power P_{ik}, which is further divided into two parts through a power divider to drive the RF gun ($1/3 * P_{ik}$) and the LIL accelerating structure ($2/3 * P_{ik}$).

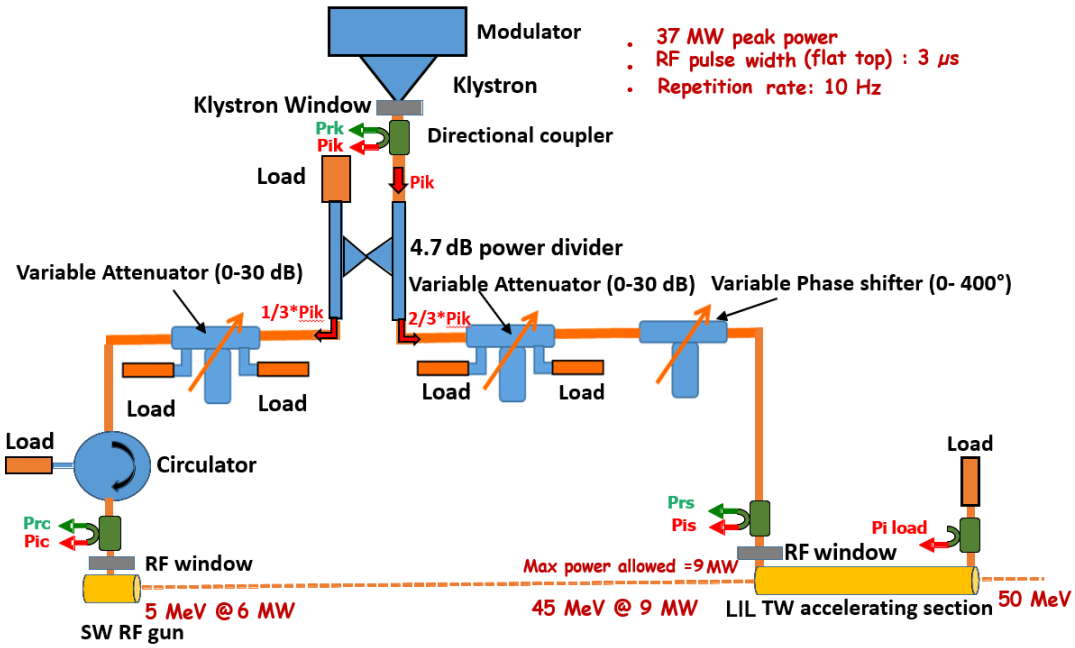

Figure 3.1: Schematic diagram of the high power RF test set-up for the ThomX linac during the first phase of commissioning.

The RF pulse length can be adjusted by controlling a delay generator “ER/SY/RAC.08-DEG.01”, and the repetition rate can be adjusted via an acquisition PLC “R/CC/RAC.05-API.01-DO1”, while the power strength from the klystron is controlled by driving high voltage “HV” of the modulator, keeping the driving power (Preamplifier) for the Klystron input cavity constant at saturation level

$P_{RF\ DRIVE}$=368 W. The RF power delivered by the Klystron was measured at each (HV) voltage level. Fig 3.2 shows the relation between the voltage applied to the Klystron and the measured power P_{ik} provided by the Klystron. The RF power was monitored by a peak power meter.

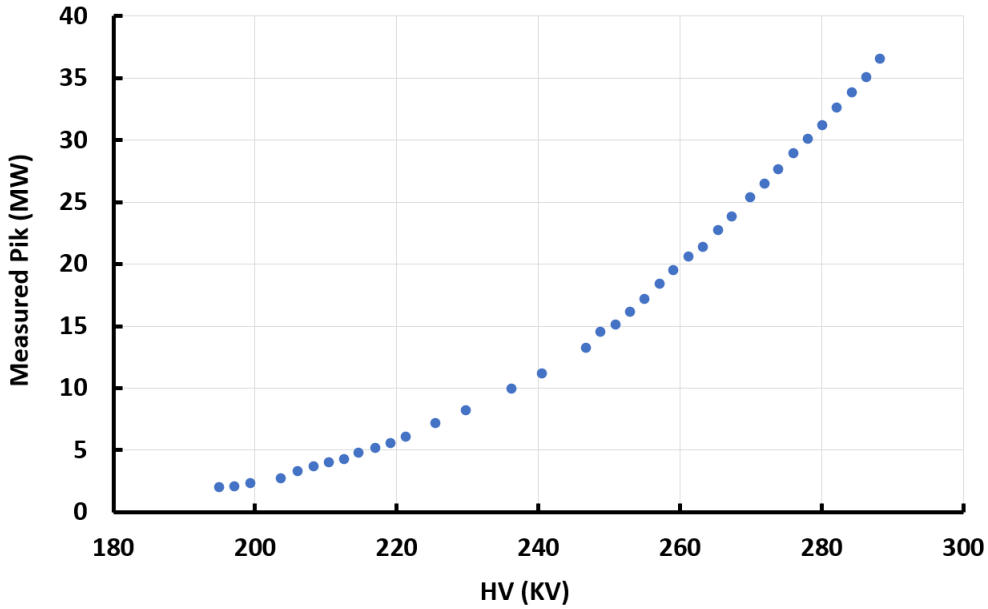

Figure 3.2: P_{ik} vs. voltage (HV) applied to Klystron.

In practical operation, the RF power strength from the klystron is usually kept fixed and two sets of attenuators are used to adjust the strength of input power to the RF gun and the LIL structure. The conditioning procedure was carried out manually with frequent surveillance, and was performed in the ThomX control room. During RF operations, the signals of the directional coupler pickups and the current absorption of the ion pumps were monitored. The forward/reflected RF power signals P_{ic}/P_{rc} and P_{is}/P_{rs} at the input of RF gun and the LIL structure respectively, and the residual power $P_{i\ load}$ dissipated into the RF load connected at the out coupler of the LIL structure, were measured through directional couplers using RF calibrated diodes and an oscilloscope (Fig 3.1.). All measured data were recorded and stored. The gauge signal works as an interlock for the whole system. If the gauge reading is higher than 10^{-6} mbar, the RF power will be shut down to protect the RF system.

3.1.1 The LIL accelerating structure

It is important to make sure that during conditioning the LIL structure is on tune. During RF operation, the temperature of the accelerating structure was maintained at 30 $\pm$ 0.1°C using a precise temperature control system. Fig 3.3 shows that the reflected power P_{rs} = 0 and the incident power P_{is} = 2/3 P_{ik} at the input of the LIL structure, which indicates good RF matching. During the conditioning of the LIL structure, a 20 MW RF load was mounted in the place of the RF gun which was under RF tuning.

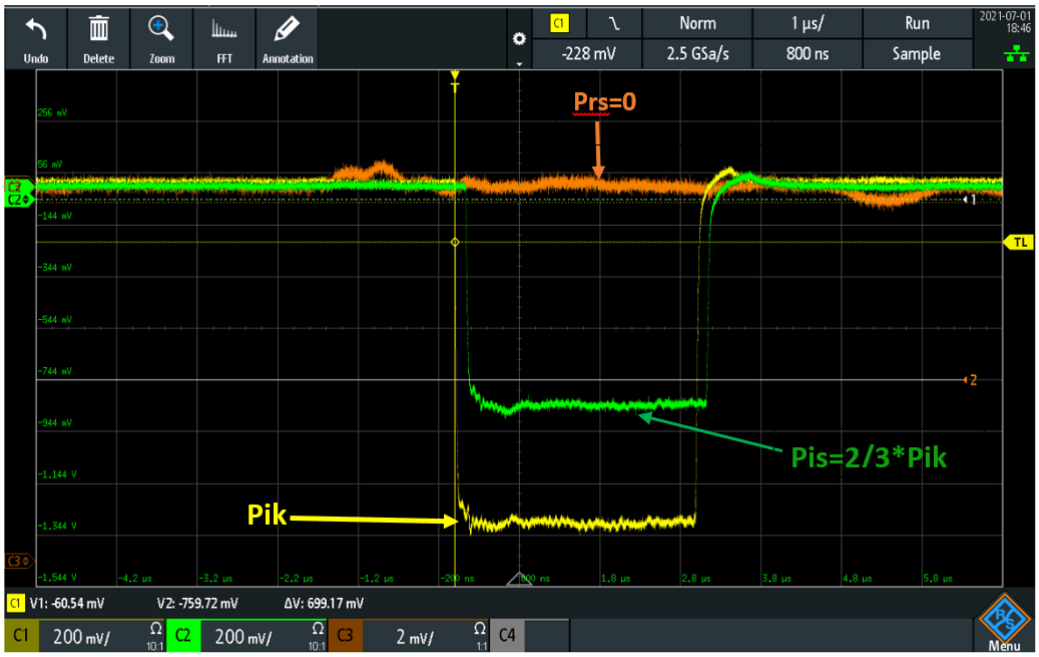

Figure 3.3: RF power signals measured by an oscilloscope (the attenuator located upstream of the LIL structure is set at 0 dB) at low power level.

The conditioning strategy was to progressively increase the RF power acting on the high voltage (HV) of the modulator up to P_{ik}=20 MW and then to progressively adjust the attenuator located upstream of the LIL structure from 10 dB to 1.7 dB to gradually increase the input power (P_{is}) up to 9 MW (Fig 3.4). The goal of the entire test was to reach 9 MW pulse peak power at the input coupler of the LIL accelerating structure, at a repetition rate of 10 Hz with a 3 µs pulse width in order to achieve an effective accelerating gradient of 10 MV/m corresponding to an energy gain of 45 MeV. The conditioning started at a repetition rate of 5 Hz with an RF pulse of 2µs and minimum power.

Reaching the nominal input pulse power P_{is}= 9 MW, the repetition rate was increased and, if the system was stable, the RF pulse length could be increased by restarting the ramp-up from the minimum input power P_{is}. Conditioning was performed at two repetition frequencies, 5 Hz and 10 Hz, and two RF pulse widths, 2μs and 3μs.

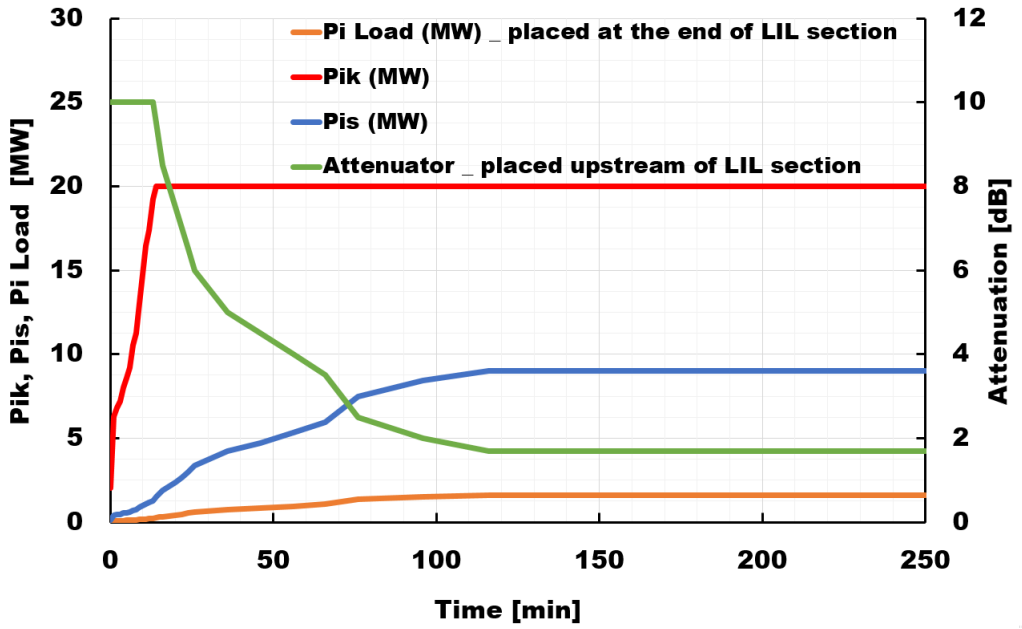

Figure 3.4: RF powers P_{ik}, P_{is} and P_i load and attenuator level as a function of time during the last step of conditioning (3 μs RF pulse @ 10 Hz repetition rate).

The RF conditioning was performed successfully up to 9 MW in approximately 12 hours. The vacuum pressure was measured constantly, both at the beginning (LI/VA/PEG.04/Pressure) and at the end (LI/VA/PEG.05/Pressure) of the LIL structure and, after reaching the final nominal parameters of the structure, was of the order less than 9.10^{-9} mbar. During the conditioning no outgassing phenomena were observed. Fig 3.5 shows the measured vacuum pressure after reaching nominal power and pulse length for several hours before the conditioning process was stopped.

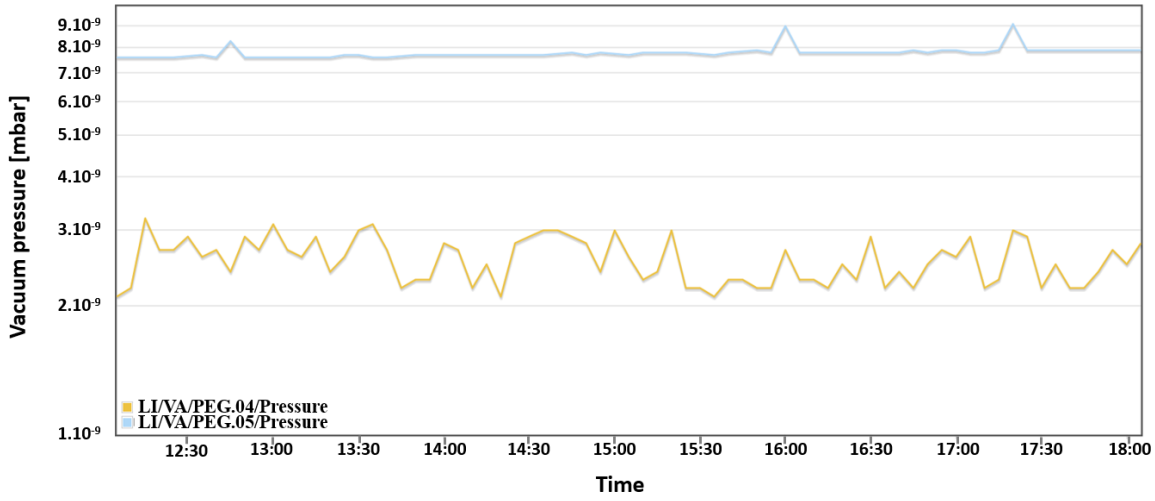

Figure 3.5: Vacuum profile in the LIL structure (P_{is}=9 MW@ 3 µs with 10 Hz).

3.1.2 The RF gun

The conditioning process of the RF gun was carried out for approximately two weeks to reach RF power stability inside the gun (no RF breakdown) with a low and stable vacuum level. The attenuator located upstream of the LIL structure was set at 30 dB to avoid injecting the power into it. As the case for the LIL structure, the conditioning was to increase the input RF power to the RF gun by adjusting the attenuator located upstream of the RF gun from 10 dB to 0.75 dB to reach P_{ic} of 6 MW (the RF power source was fixed during the whole process). The goal of the entire test was to reach 6 MW pulse peak power, at a repetition rate of 10 Hz with a 3 µs pulse width in order to achieve an effective accelerating gradient of a 80 MV/m corresponding to an energy gain of 5 MeV. The conditioning started at a repetition rate of 1 Hz with a RF pulse of 0.5 µs with minimum power. The repetition rate was increased and if the system was stable, the RF pulse length could be increased by re-starting the ramp-up from the minimum input power P_{ic}. The conditioning was performed at 3 repetition frequencies, 1 Hz, 5 Hz and 10 Hz and, five RF pulse widths, 0.5 µs, 1 µs, 1.5 µs, 2µs and 3 µs. At the nominal point, attenuation=1.5 dB (i.e. $\approx$ 5.3 MW, just below 80 MV/m), 3µs at a repetition rate of 5 Hz, some breakdown was observed around the cathode (but not on any other surface of the gun) as shown in Fig 3.6 (fluctuation in the green signal), with an increase in the vacuum level downstream (LI/PEG.01/Pressure) of the RF gun up to $2.5.10^{-7}$mbar, as

shown in Fig 3.7.

Figure 3.6: RF power signals measured by an oscilloscope (P_{ic} in brown, P_{rc} in green and P_{bc}, which is the visualised power inside the cavity, in yellow).

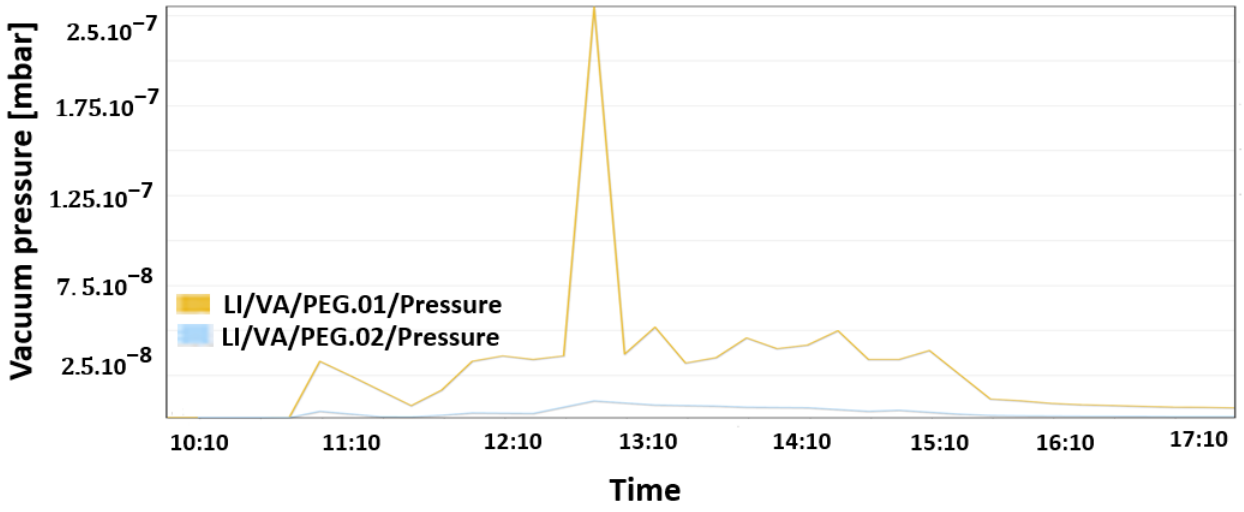

Figure 3.7: Vacuum profile in the RF gun (P_{ic}=5.3 MW @3 µs with 5 Hz).

We stayed at 1.5 dB (nominal point) for 1 hour. Vacuum instability downstream and upstream the gun and RF breakdown tend to be less frequent and disappear with time (Fig 3.8). So, the RF conditioning was continued successfully up to 6 MW without any vacuum bursts or RF breakdown. Thus, we were able to increase the repetition rate to 10 Hz at the pulse duration of 3 µs from 3 dB to 0.75 dB (3.7 MW to 6 MW). The vacuum pressure was constantly measured both at the beginning

(LI/VA/PEG.01/Pressure) and at the end (LI/VA/PEG.02/Pressure) of the RF gun and, after reaching the final nominal parameters of the gun, was of the order of less than 7.10^{-9} mbar.

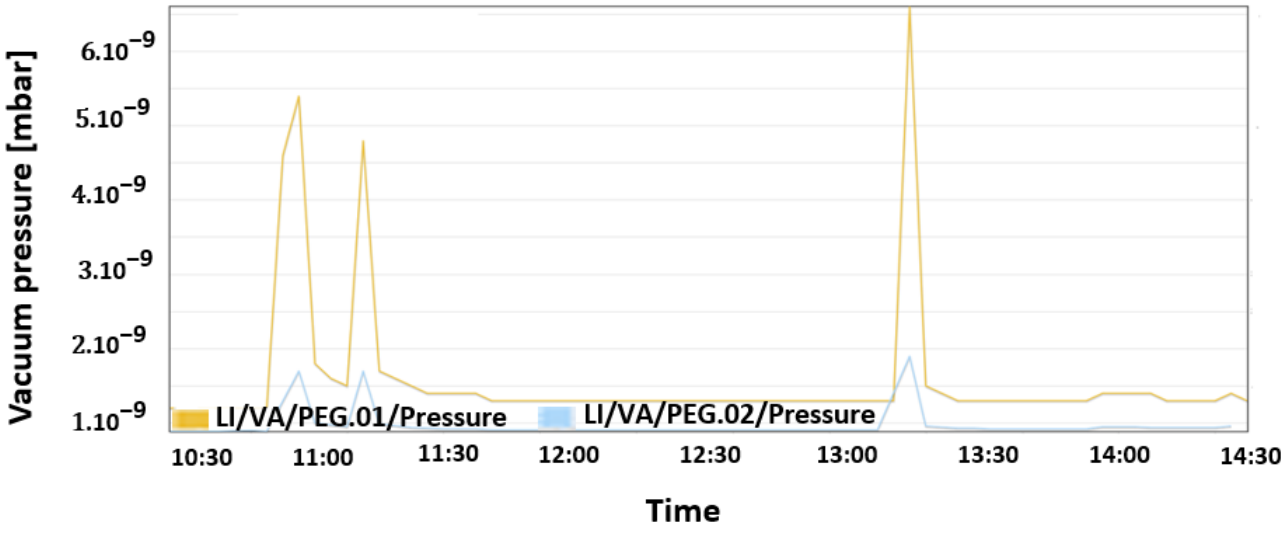

Figure 3.8: Vacuum profile in the RF gun (P_{ic}=6 MW @3μs with 10 Hz).

3.2 First beam commissioning of the ThomX linac

The beam commissioning of ThomX started the phase 1 after obtaining the nuclear authorisation in October 2021. The objective of this phase is to extract an electron charge of 100 pC at a repetition rate of 10 Hz with a beam energy of 50 MeV at the end of the linac. Here, I will present the main measurement allowed in the phase 1: the charge measurement and the beam energy measurements. These measurements are also compared with analytical models. As spectrometer measurements are not available in the phase 1 of ThomX, I will present energy and energy spread measurements carried out at the PHIL photoinjector, using a spectrometer. The energy measurement using a spectrometer is also important because it is the same case of the energy measurement which is planned for phase 2 of the ThomX commissioning.

3.2.1 Charge measurement at ThomX

The charge measurement of the ThomX linac has started since October 2021. The first phase of the beam commissioning aimed to reach an electron charge of 100 pC from the copper cathode at a

repetition rate of 10 Hz with a beam energy of 50 MeV after the LIL structure. The charge was measured by the Diag1 ICT which will be briefly described.

3.2.1.1 An integrated current transformer (ICT)

For the charge measurement, the integrated current transformers (ICTs) are installed after the RF gun and the LIL section (Diag 1 and Diag 2 stations, as shown in Fig 1.5). The working principle of the ICT is the detection of the magnetic field of the beam without intercepting the beam (non-destructive method). The current is characterised by a number of particles N_{part} of charge q per unit of length l or unit of time t and velocity β = v/c. The electrical current passing through a given position is described as:

$$I_{beam} = \frac{qe\ N_{part}}{t} = \frac{qe\ N_{part}}{l}.\beta c \tag{3.1}$$

where e is the electron charge. According to the Biot-Savart law, the magnetic field B of a beam current can be calculated as:

$$d\vec{B}(\vec{r}) = \mu_{\circ} I_{beam} \cdot \frac{\vec{dl} \times \vec{r}}{4\pi r^3} \tag{3.2}$$

where $\mu_{\circ}$ is the permeability of the vacuum ($4\pi.10^7$ Vs/Am), $\vec{dl}$ is the length in direction of the beam and $\vec{r}$ is the distance between the beam centre and the coordinate of field. The beam current can be measured by monitoring the accompanying magnetic field, as shown in Fig 3.9.

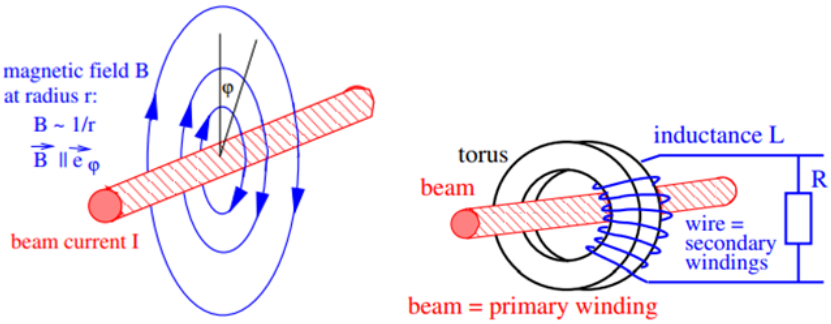

Figure 3.9: Schematic layout and working principle of an ICT.

The beam passing through a torus of a high magnetic permeability μ is considered as the 'primary winding' of the current transformer, whereas an insulated wire wound with N_{sec} turns around the

torus acts as the 'secondary winding', having an inductance L as:

$$L = \frac{\mu}{2\pi} l \, N_{sec}^2 . \ln\left(\frac{r_o}{r_i}\right) \tag{3.3}$$

where l is the torus length in the beam direction, r_i and r_o are the inner and outer radii of the torus respectively. The torus shape is chosen to guide the beam magnetic field-lines, which are mainly along the azimuthal direction $\vec{e_\varphi}$, as shown in Fig 3.9, thus, allowing to maximise the strength of the output signal with almost independence on the beam position inside the vacuum pipe [49]. Fig 3.10 shows a typical signal produced by the ICTs after the RF gun (blue) and after the LIL structure (orange). The beam charge directly corresponds to the area under the curve. More details of signal transformation into charges can be found in [49].

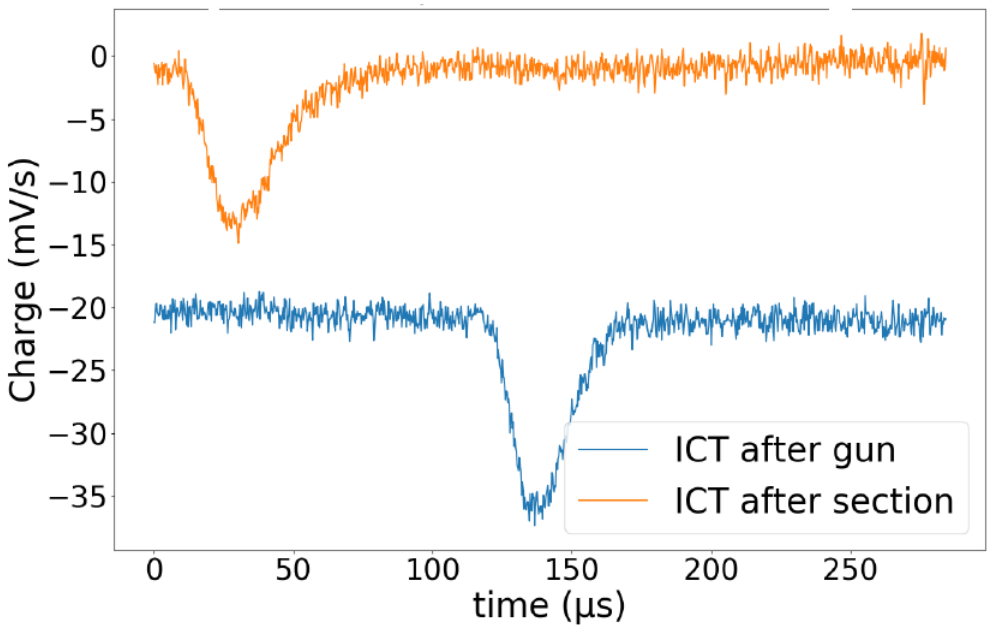

Figure 3.10: The typical signals produced by ICTs after the RF gun (blue) and after the LIL structure (orange).

3.2.1.2 Charge dependency on the RF phase

The charge measurement was carried out using the ICT(1) located downstream from the copper photocathode. The maximum accelerating gradient in the gun is about E_{max}=75 MV/m (1.25 dB on the attenuator). The photocathode was exposed to a Gaussian laser pulse of an energy E_{laser} = 50 µJ,

a pulse duration (FWHM) σ_t = 4 ps with transverse sizes (FWHM) of σ_x = 1.8 mm, σ_y = 1.1 mm and a wavelength λ_l = 257 nm. In this type of photocathode, the charge measurement as a function of the gun RF-phase, or the so-called "phase-scan", is usually performed to characterise the charge emission which changes according to the RF phase. Indeed, the electric field is changing on the cathode surface with the RF phase. So, the electron photo-emission is modified due to the lowering of the work function of the cathode material. The reduction in the work function (δW) of the cathode is known as the Schottky effect [50, 51] and it can be calculated using the formula [52]:

$$\delta W = \sqrt{\frac{e\, E_z(\varphi)}{4\pi\varepsilon_\circ}} \tag{3.4}$$

where E_z is the applied electric field which depends on the RF phase (φ), $\varepsilon_\circ$ is the dielectric permittivity of vacuum (8.85^{-12} F/m). In this type of electron guns, laser pulses are incident on a cathode and electrons are released after receiving a sufficiently amount of energy (hν) higher than the effective work function of the cathode material, see Fig 3.11.

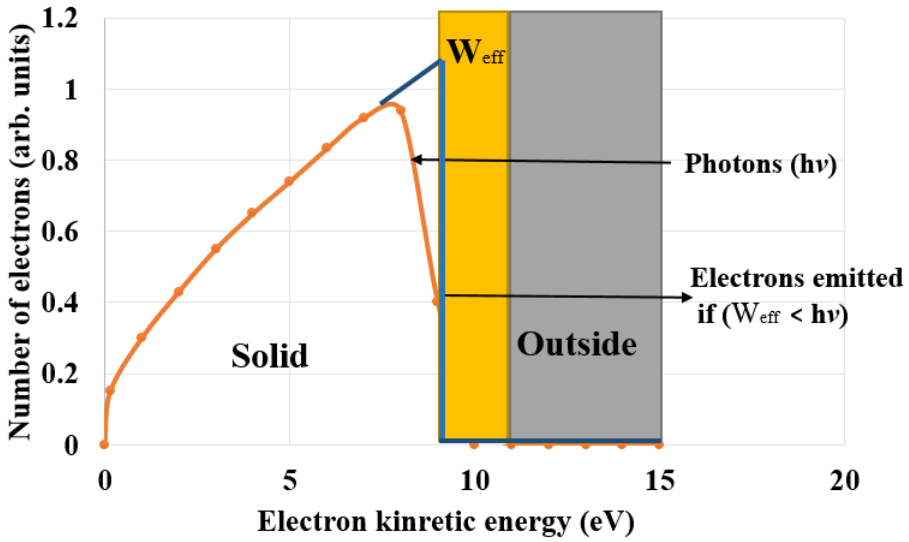

Figure 3.11: The basic physical principle of the photoelectric emission. W_{eff} is the work function of the material and hν is the photon energy, with ν the photon frequency and the Planck constant h = 6.626 $\times$ 10^{-34} J.s. Blue curve: 0 K; Orange curve: 2000 K [53].

In addition, the charge represented by the current density J_{FD} is directly linked to the work function

as:

$$J_{FD} = \sum_n J_n, \text{ with } J_n = Aa_n T^2 I(1-R)F\left(\frac{nh\nu - W_{eff}}{k_b T}\right)\left(\frac{e}{h\nu}\right) \tag{3.5}$$

where R is the reflectivity of the cathode material, I is the laser pulse power surface density, A is the Richardson constant, n is the order of multi-photon emission, a_n is a constant that depends on the cathode material, k_b is the Boltzmann constant ($1.38*10^{-23} m^2 kg s^{-2} K^{-1}$) and F is the Fowler function [54].

Generally, at the moment of emission, electron bunches have the same longitudinal and transverse profiles as incident laser pluses [55]. Once electrons are emitted, they are accelerated by a standing wave electric field. The profile of the electric field in an photoinjector is longitudinally oriented in the propagation direction (z), namely $TM_{010-\pi}$ and has an opposite sign in each adjacent cavity. The applied electric field, which depends on the RF phase of the gun, can be described as:

$$E_z = E_{max} \cos(kz) \sin(\omega t + \varphi_0) \tag{3.6}$$

where E_{max} is the maximum electric field (MV/m), z is the length of the photoinjector, k is a propagation constant equal to ω/c, ω is the angular frequency ($2\pi f$), f is the RF frequency, and φ_0 is the RF phase of the gun [54]. Fig 3.12 illustrates the profile of the electric field E_z along a photoinjector of length 0.125 m (2.5 cell cavity) at E_{max} of 80 MV/m for different RF phases. Since the emitted electrons are accelerated by a sinusoidal electric field, the first cavity of the photoinjector is designed to be shorter than the other cavities, so as to have no zero electric field on the cathode surface. As the electric field varies with time and space, the field changes its sign at each half period and due to the synchronism the electrons motion, the electrons can only see an accelerating field during their motion along the photoinjector. It can be also seen the direct influence of the RF phase on the electric field along the photoinjector. On the photocathode surface, where z=0, the electrons see an electric field of $E_{max} \sin(\omega t + \varphi_0)$, which is at maximum when $\varphi_0 = \pi/2$ (90°). However, the RF phase is usually adjusted to optimise other beam properties, which will be later explained in more detail.

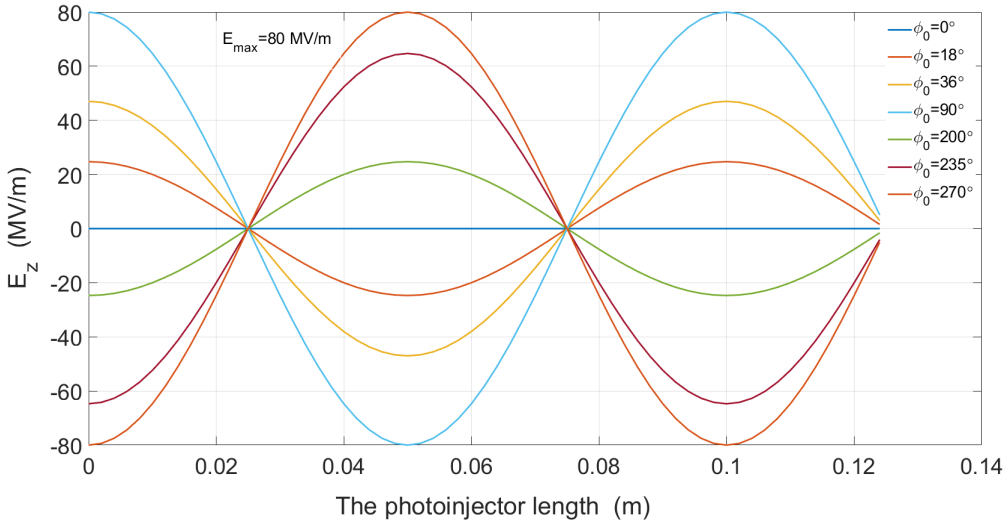

Figure 3.12: The electric field E_z along the photoinjector at different RF phases.

Fig 3.13 shows the "phase-scan" measured at the gun exit with the Diag1 ICT. At the RF phase $\varphi_0 \leq 0°$ and at the RF phase $\varphi_0 \geq 125°$, there are no electrons, because the RF field is reversed when the laser is incident on the photocathode [56] then, the electrons see a decelerating field which will bring them back the photocathode. At the RF phase $\varphi_0 > 0°$, the electron photo-emission becomes more significant due to the Schottky effect. The maximum extracted charge can be seen at 90° (Q is around 105 pC) because of the maximum applied electric field on the cathode $E_{z\ \mathrm{cathode}}$, which is around 75 MV/m, enhances the photo-emission process as described by Eq.3.5. On the right side of the maximum charge, the slope is very sharp in less than 15°, where the electron charge is significantly lowered by up to 80%, due to the defocusing of the beam. This high drop shows that the beam performances are very sensitive to the RF phase [57]. In the RF phase region of $105° \leq \varphi_0 \leq 125°$, there is an insignificant region of electron charges corresponding to electron secondary emission. Operating at the RF phases below than 105° therefore, not only increases the dependency of the charge-phase but also provides a direct measurement of the relative phase stability between the laser and the photoinjector [58].

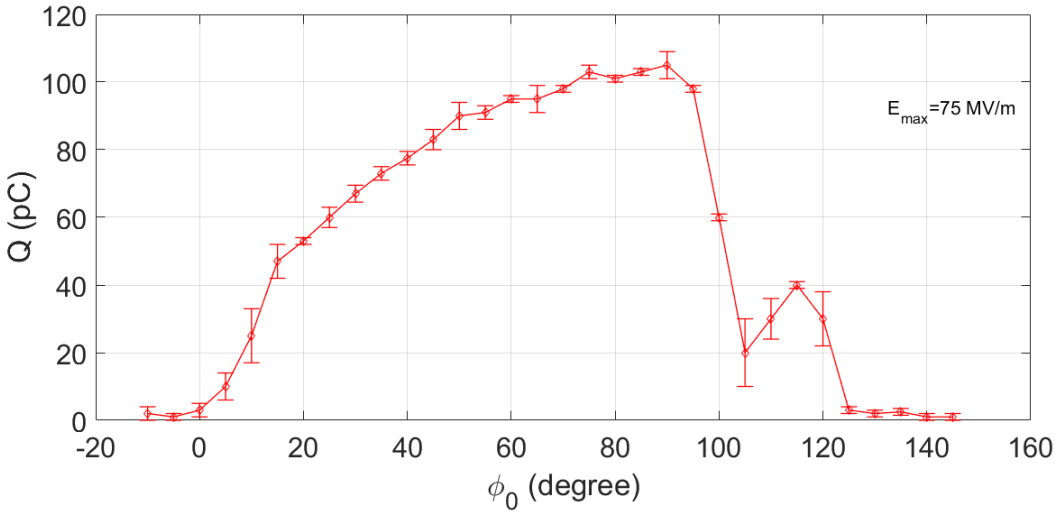

Figure 3.13: The measured electron charge Q as a function of the RF gun phase φ_0 at E_{max}=75 MV/m (1.25 dB) on 2 Dec 2021.

The corresponding electric field on the photocathode surface $E_{z\ cathode}$ is simulated using Eq.3.6 for the interesting range of the RF phase i.e. 10° to 95°. The measured charge Q and the lowering of the work function δW (Eq.3.4) are plotted as a function of the accelerating field, as shown in Fig 3.14. As the E-field increases, consequently the work function decreases, for example; when $E_{z\ cathode}$=14 MV/m, the energy function barrier of the copper photocathode $W_{eff\ Cu}$, which is equal to 4.6 eV, is lowered in 0.14 eV to become 4.46 eV. Also, when the maximum field on the photocathode $E_{z\ cathode}$=75 MV/m, the $W_{eff\ Cu}$ is reduced by around 0.33 eV to become 4.27 eV instead. Thus, lowering the work function barrier enables the extraction of more charges, as shown in Fig 3.14, where Q is equal to 30 pC at 14 MV/m and it goes up to 105 pC at 75 MV/m.

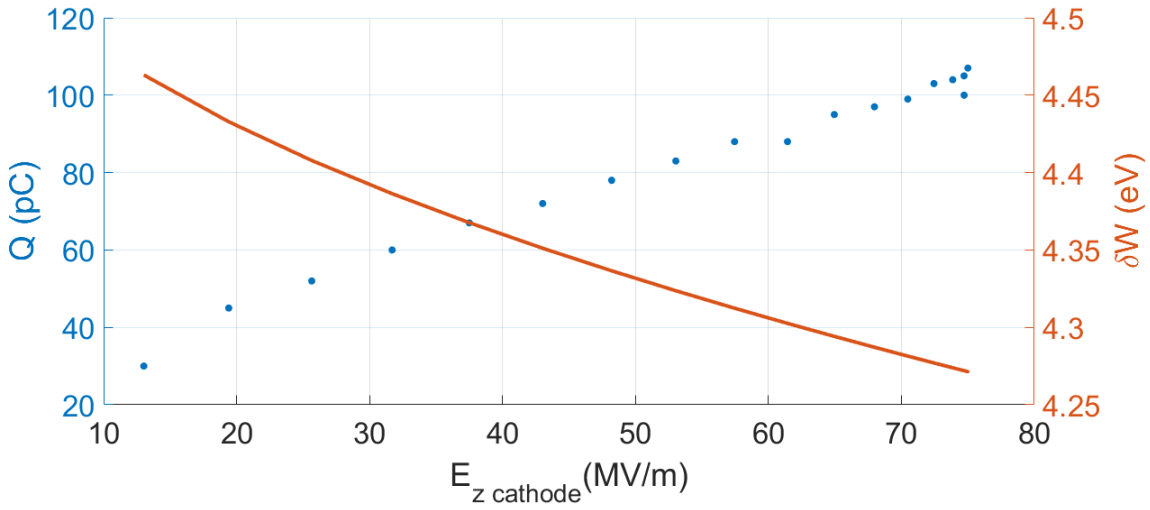

Figure 3.14: The measured charge Q (blue) and the lowering of the work function δW (orange) as a function of the accelerating field on the photocathode E_z.

3.2.2 Energy measurement in the photoinjector

In this subsection, I will present energy behavior in the RF gun according to measurements. I also compare measurement with an analytical approximation model. I used two energy measurement methods: the steerer magnets and the dipole spectrometer. I will first introduce the model to understand the energy behavior in an RF gun.

3.2.2.1 An analytical approximation model of the photoinjector

This model is part of the PhD thesis in [54].

The main challenge to derive an analytical model of beam dynamics in the photoinjector comes from the fact that the electrons velocities are not constant in the photoinjector because they start with an almost zero velocity at the photocathode and become relativistic (very close to c) at the photoinjector exit. It is then impossible to consider the electron velocities constant in the photoinjector. The assumption is based on the fact that the velocities can be divided into two zones, very close to the photocathode surface ($z \approx 0$) and few centimeters after, where the electrons become relativistic. In the first zone, electrons are not synchronous with the accelerating field due to the high velocity variation. This is known as phase slippage [59]. This slippage has to be taken into account in the model. This

variation was also established and extended further away from the photocathode via defining the effective accelerating phase φ_z as given:

$$\varphi_z = \varphi_0 + \frac{1}{2\alpha \sin(\varphi_0)} \left(\sqrt{(\gamma_0 + 2\alpha k \sin(\varphi_0) z)^2 - 1} - 2\alpha k \sin(\varphi_0) z - \gamma_0 + 1 \right) \tag{3.7}$$

where $\alpha = \frac{eE_{max}}{2m_e c^2 k}$ and it represents the strength of the accelerating field. It can be remarked that the acceleration phase φ_z varies much more slowly as z increases, as shown in Fig 3.15. This figure shows the variation of the accelerating phase φ_z along the photoinjector of length 0.125 m, for an RF phase φ_0=57° and for various maximum accelerating fields; E_{max} of 50 MV/m ($\alpha \approx 0.78$), 60 MV/m ($\alpha \approx 0.9$), 70 MV/m ($\alpha \approx 1$) and 80 MV/m ($\alpha \approx 1.25$). Close to the photocathode, at the moment of the electron emission, the accelerating phase φ_z varies rapidly for all the fields. φ_z becomes more stable once the electrons become relativistic and stable faster for higher fields as in the case of $\alpha \approx 1.25$. After a few centimeters from the cathode, the electrons are almost synchronised with the accelerating field which in turns means that the electron slippage on the RF field is only limited to the cathode region.

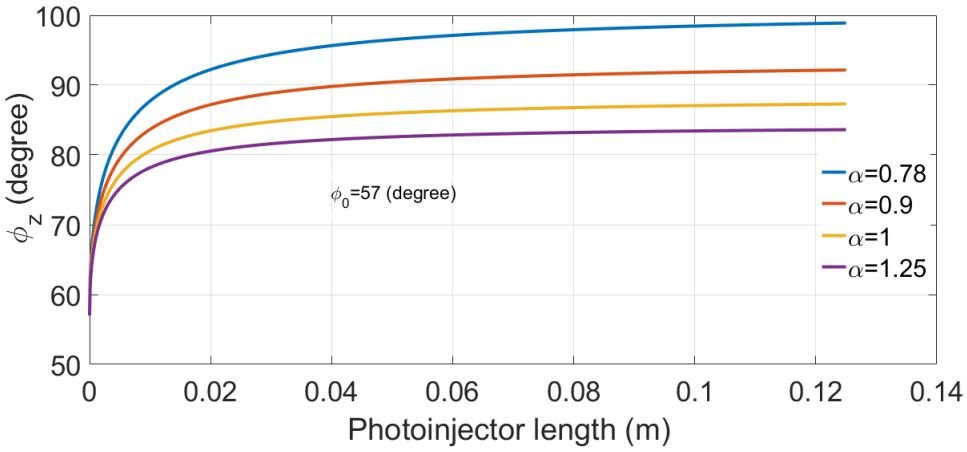

Figure 3.15: The accelerating phase φ_z of the electrons as a function of the photoinjector length at $\varphi_0 = 57°$ for different accelerating fields.

Additionally, an approximation of γ (where γ is the Lorentz relativistic factor of the electron) far from the photocathode (i.e. in the second zone) is obtained considering that φ_z is constant since its

variation is slow in this region. We therefore obtain:

$$\gamma_z = \gamma_0 + \alpha\left(k\sin(\varphi_z)z + \frac{1}{2}(\cos(\varphi_z) - \cos(\varphi_z + 2kz))\right) \tag{3.8}$$

Then, the kinetic energy of the electrons can be easily given by:

$$E_{kin} = (\gamma_0 - 1)m_e c^2 + \alpha m_e c^2\left(k\sin(\varphi_z)z + \frac{1}{2}(\cos\varphi_z - \cos(\varphi_z + 2kz)\right) \tag{3.9}$$

Using Eq.3.9, two gradient cases are represented in Fig 3.16. The maximum kinetic energy for E_{max}= 56 MV/m is around 3.6 MeV while for E_{max}= 80 MV/m, it is approximately 5 MeV. The electron energy starts dropping at the RF phases below 20° and above 80°, indicating that the electrons see less electric field. Moreover, at high RF phases (i.e. $\geq$130°), the reduction in the energy gain indicates that the electrons slip onto a decelerating phase and thus lose energy. Eventually, the electrons are stopped and are accelerated back toward the cathode [60]. Fig 3.16 illustrates the dependency of the electron kinetic energy E_{kin} on both the electric field and the RF phase φ_0. Fig 3.17 shows the ramping of the electron energy as a function of the photoinjector length at a fixed RF phase φ_0 of 57° and for E_{max} 56 MV/m. The electrons gain 3.6 MeV at the exit of the photoinjector.

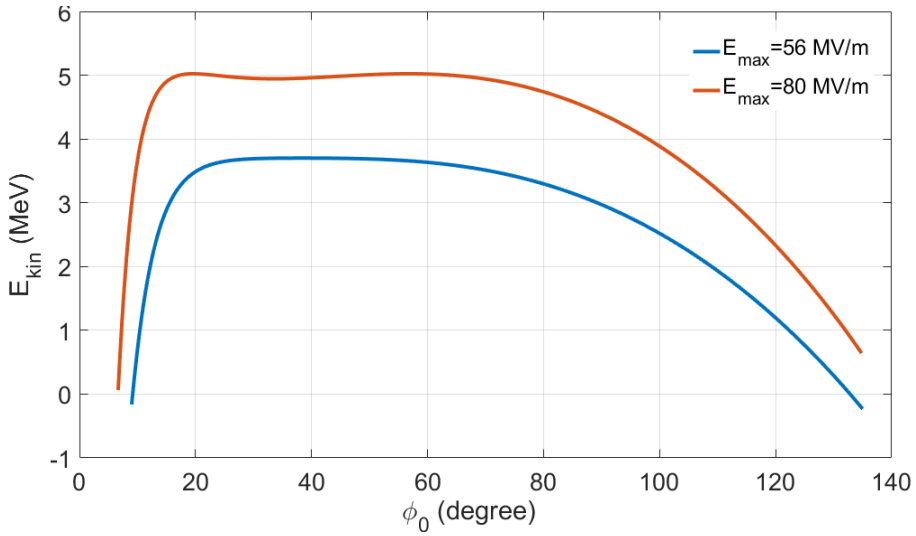

Figure 3.16: The electron kinetic energy E_{kin} as a function of the RF phase φ_0 for electric fields E_{max} of 56 MV/m and 80 MV/m at the photoinjector exit.

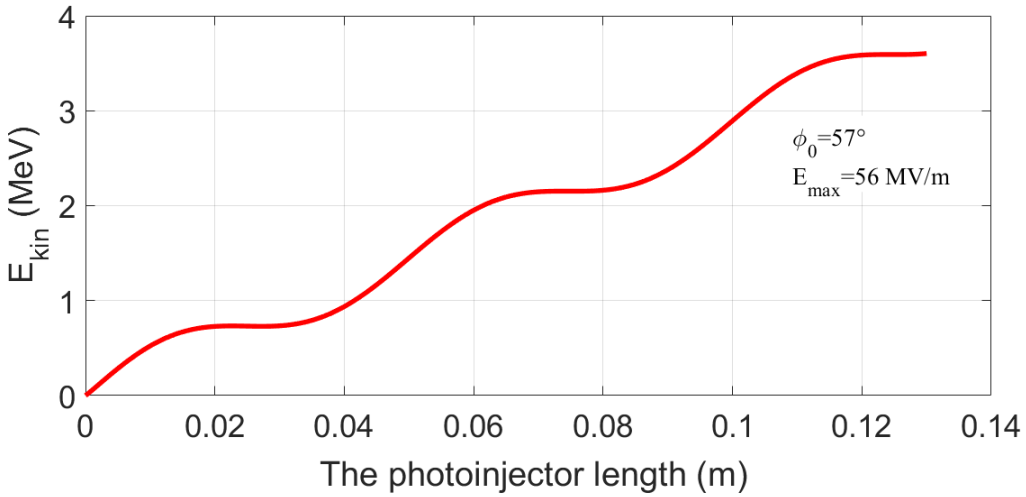

Figure 3.17: The ramping of the electron kinetic energy E_{kin} in the photoinjector at the RF phase φ_0 57° for an electric field E_{max} 56 MV/m.

3.2.2.2 Energy measurement of the ThomX gun using a steerer magnet

In this subsection, the beam kinetic energy measurement is carried out using a steering magnet located after the RF gun. In this method, the magnetic field of a steering magnet is varied to measure simultaneously the induced displacement of the beam transverse barycenter on a YAG screen which is located downstream this steerer, as shown in Fig 3.18. The working principle of the YAG screen is based on the interaction of beam with the YAG:Ce crystal. A part of the deposited electron energy causes an excitation of electronic states which de-excite by light emission [61]. The emitted light goes through an achromatic lenses doublet on a CCD pixel chip. In Fig 3.18, l is the magnetic length of the steerer, Θ is the deviation angle induced by the steerer on the beam, x is the bunch barycenter displacement on the YAG screen and L is the distance between the steerer entrance and the YAG screen. It is assumed that the steerer behaves as a thin lens (since it has a very small thickness) thus the traveled distance in the steerer ($\rho\Theta$) is equal to its magnetic length l, where ρ is the curvature radius of the beam path in the steerer. Thus, the beam trajectory crossing the YAG screen forms a right-angled triangle with the trajectory in case of turned-off steerer (see Fig 3.18). This assumption is only valid when the following simple inequality : L >> l is established. Another important assumption is to keep small the Θ angle. It is verified if L >> the YAG screen radius, which is around a few centimeters.

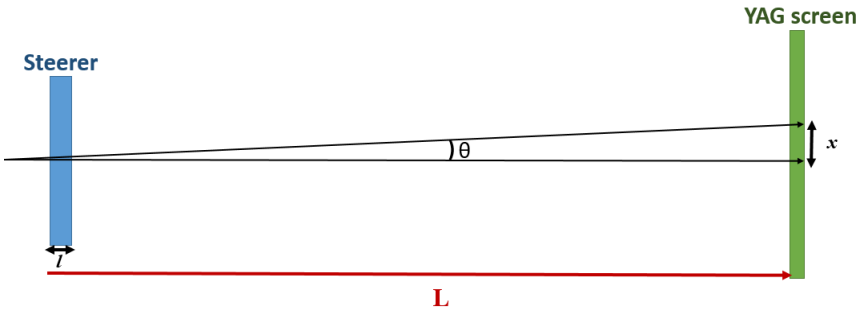

Figure 3.18: Scheme of the steerer configuration for the energy measurement.

Beginning from $l \approx \rho\Theta$, ρ has to be substituted, because it is unknown, through multiplying by the steerer magnetic field B to obtain the beam magnetic rigidity as given:

$$B\rho = \frac{p}{e} = \frac{\sqrt{E_{kin}^2 + 2E_{kin}m_e c^2}}{qc} \tag{3.10}$$

where B is the magnetic field of the magnet (Tesla), p is the electron momentum (GeV/c), e is the electron charge, E_{kin} is the mean electron kinetic energy (MeV) and c is the speed of light (3.10^8 m/s). Thus, $p \approx \frac{eBl}{\Theta}$. Moreover, Θ can be written as $\Theta \approx \arctan(\frac{x}{L}) \approx \frac{x}{L}$. Now, we can obtain the momentum of the beam by $p = \frac{eBlL}{x}$ then we can deduce E_{kin} from Eq.3.10. For a high precision of the measurement, it is recommended to measure several values of x by varying the steerer B field to plot a linear fit of the x(B) curve. The slope of this fit, $d = \frac{elL}{p}$, allows to extract the momentum p and E_{kin}. In the measurement at ThomX, the distance L_{gun} between the steerer and the YAG for the photoinjector is 0.7 m, the magnetic length of the steerer l is 0.07 m and the maximum electric field of the photoinjector is E_{max}=75 MV/m. Fig 3.19 shows a visualised displacement of the electron beam on the YAG1 screen after the photoinjector as a function of the steerer magnetic field B at the RF phase φ_0=95°.

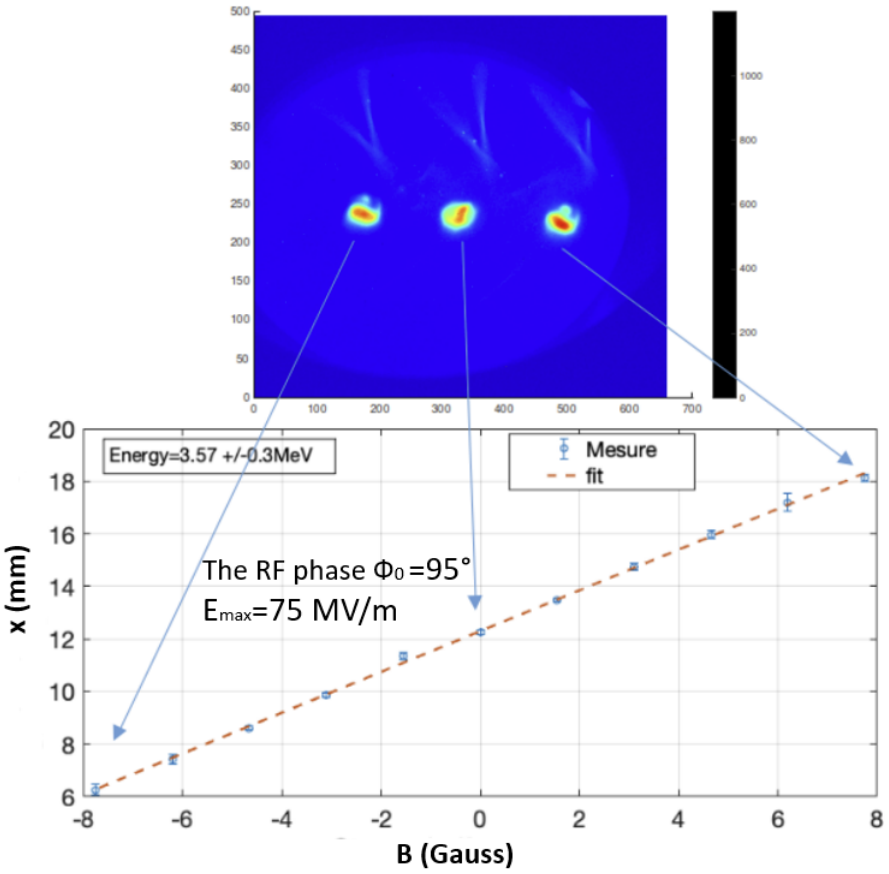

Figure 3.19: The visualisation of the beam displacement on YAG1 screen after the photoinjector as a function of the steerer magnetic field B (Gauss) [62].

Furthermore, Fig 3.20 shows the energy measurements fitted with the analytical model. The maximum energy E_{kin} in the photoinjector is about 4.6 MeV at E_{max}=75 MV/m and the RF phase of φ_0=57°, which is considered as a reference to match the experimental RF phase with the one of the analytical model. As the RF phase φ_0 increases above 80°, the electron starts loosing their energy indicating that they see less mean electric field up to RF phase of $\geq$140°, then, the electrons slip onto a reverse field "decelerating phase" and thus lose energy.

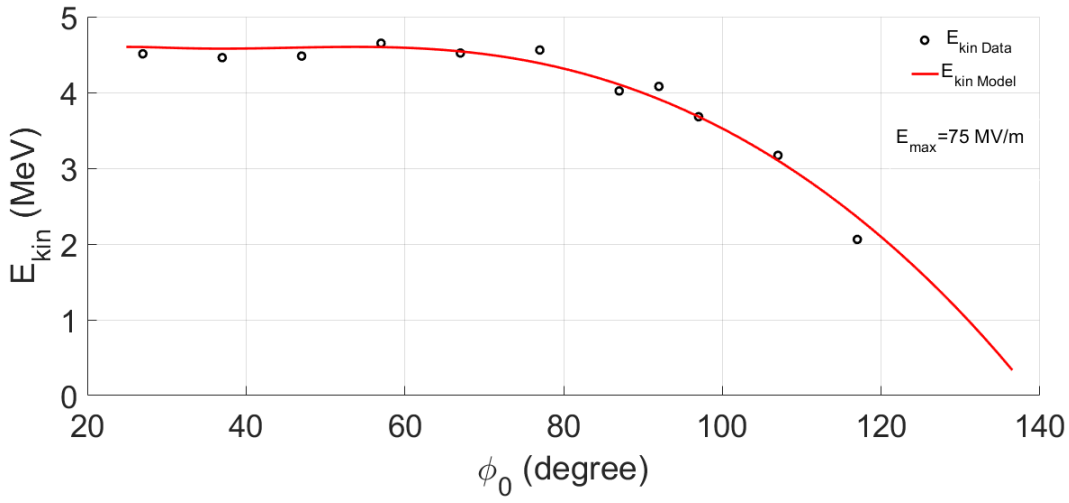

Figure 3.20: The experimental and analytical electron kinetic energy E_{kin} at the exit of the ThomX gun as a function of the RF phase of the photoinjector φ_0 at E_{max}=75 MV/m.

To conclude, the measurements of the electron kinetic energy via the steerer magnet match fairly well the model ensuring that the ThomX RF gun is capable for delivering a beam of energy 4.5 MeV.

3.2.2.3 Energy measurement of the PHIL photoinjector using a dipole magnet

Energy is usually measured with spectrometers. Unfortunately, spectrometers are not available at the gun exit for ThomX. Then, I used an other facility, "PHIL", to measure the energy at a gun exit thanks to a spectrometer.

The PHIL photoinjector

The PHIL photoinjector is a 3 GHz RF-gun test line consisting of 2.5 accelerating cavities (cells) of a total length of 0.125 m located at IJCLab- Orsay. For energy measurements, a dipole magnet is used. The transverse beam size is measured using a scintilltor YAG screen supported with a Charge-Coupled Device camera (CCD) [54]. The layout of the PHIL photoinjector is shown in Fig 3.21.

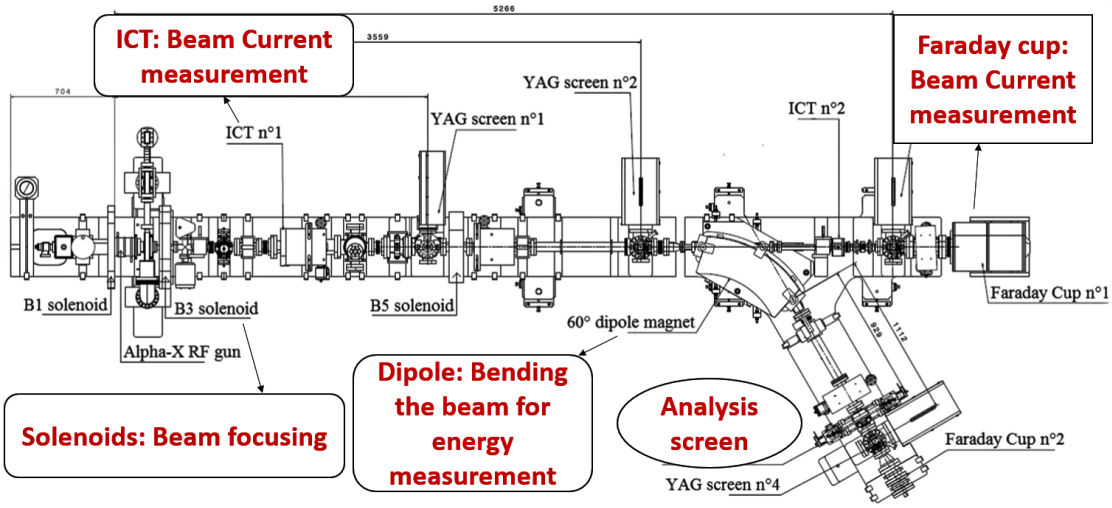

Figure 3.21: A layout of the PHIL photoinjector at IJCLab [63].

The principle of the kinetic energy measurement of electrons is illustrated in Fig 3.22. It obeys the law of the magnetic rigidity (Eq.3.10). The electrons of higher energy than the reference energy ($p>p_o$) travel longer paths (lesser bending angle) whereas the electrons of lower energy than the reference energy travel shorter paths (higher bending angle).

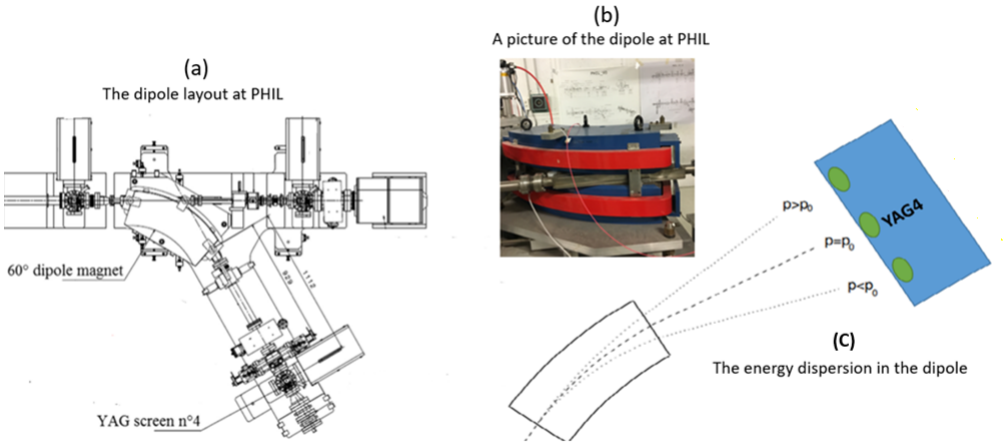

Figure 3.22: The layout of the dipole at PHIL (a), a picture of the dipole at PHIL site (b) and a sketch of the kinetic energy dispersion in the dipole (c).

At the PHIL accelerator, the diagnostic station (n°4) is located after the dipole and is used for the beam energy measurement. It is mainly composed of a screen holder with a YAG4:Ce screen inserted on 90° of the electron beam axis with the pneumatic actuator, a mirror placed at 45° for reflecting the beam profile to be analysed by a CCD camera at the end of the optical girder, and a

calibration grid for the pixel calibration [55], as shown in Fig 3.23.

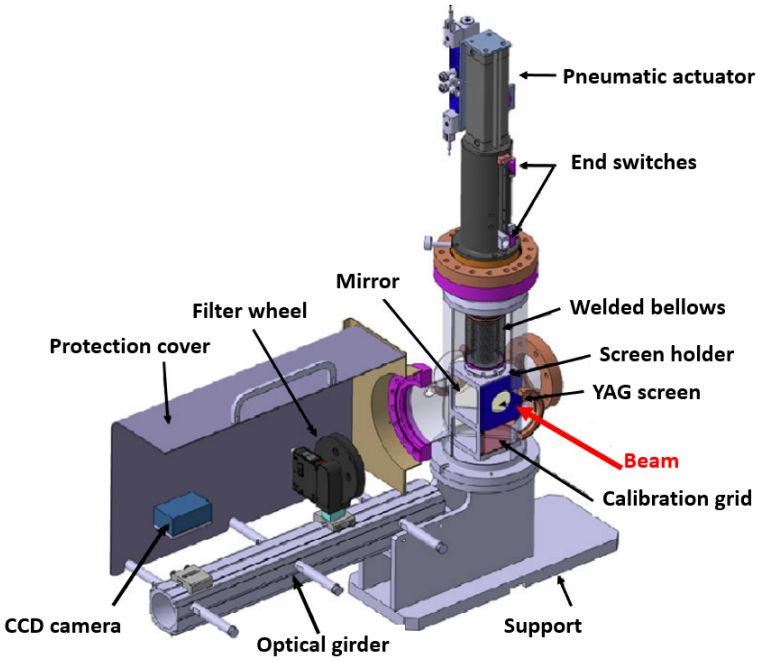

Figure 3.23: 3D view of the screen station [55].

From the control room (shown in Fig 3.24), few images of the beam spot (≈20 images as the one shown in Fig 3.25) at each RF phase φ_0 were collected using the CCD camera and saved in order to be analysed by a Matlab code developed at IJCLab for the purpose of beam profile analysis [55].

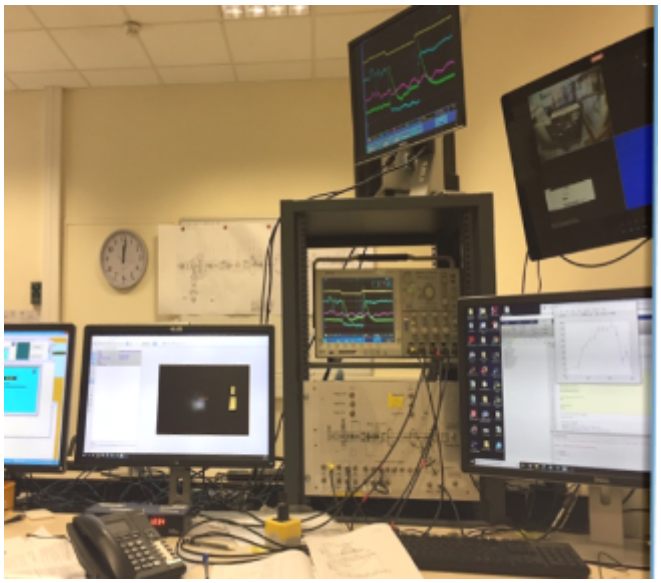

Figure 3.24: The control room at PHIL.

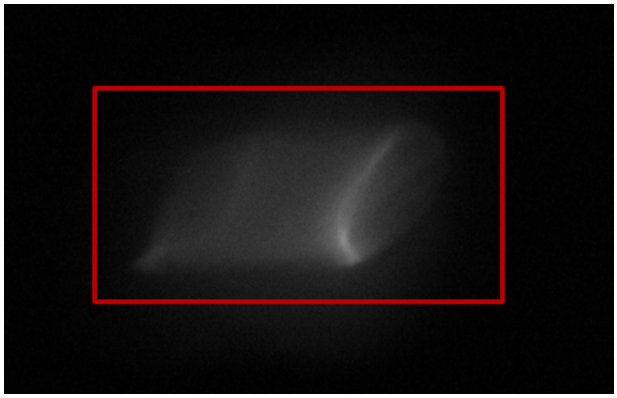

Figure 3.25: The beam spot at PHIL collected by a CCD camera.

One of the option of the analysis is a Gaussian fit on the horizontal and vertical distributions allowing to extract the electron energies [55]. The Matlab platform of a visualised example of the transverse projection of the electron beam (upper) and the projected vertical intensity distribution (lower) is shown in Fig 3.26.

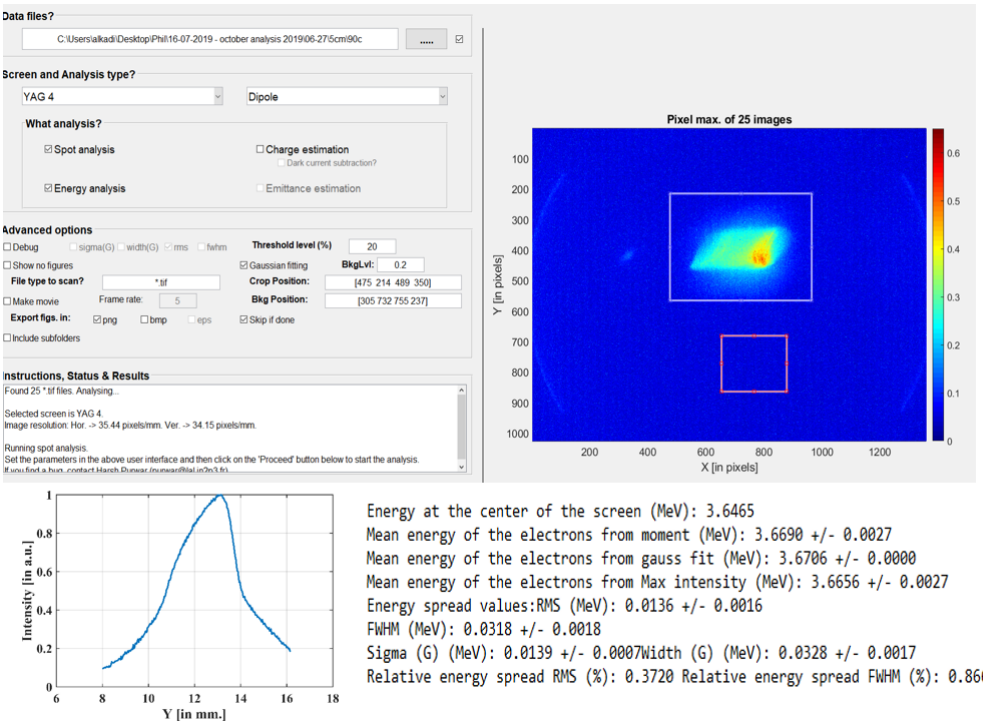

Figure 3.26: The Matlab platform of the visualised transverse projection of the electron beam (upper), and the projected vertical intensity distribution (lower).

Fig 3.27 shows the energies extracted from the YAG data for several RF phases φ_0 and the analytical model of the electron energy E_{kin} (indicated by the black line) previously deduced in subsection

3.2.2.1 for E_{max}=56 MV/m. The good agreement between the data and the model allows to have more confidence in the approximation model for the calculation of the electron kinetic energy in the photoinjector. The maximum energy is around 3.7 MeV observed at the RF phase φ_0 around 57° which is in fact considered as a reference to match the experimental RF phase with the one of the analytical model. Further away from this RF phase, the electrons see less and less electric fields until they disappear after 100°. Away from the RF phase ranging between 37°and 100°, it was impossible to collect enough charges as we started loosing the beam. This is well explained and plotted in Fig 3.13 showing the charge extraction dependency on the RF phase.

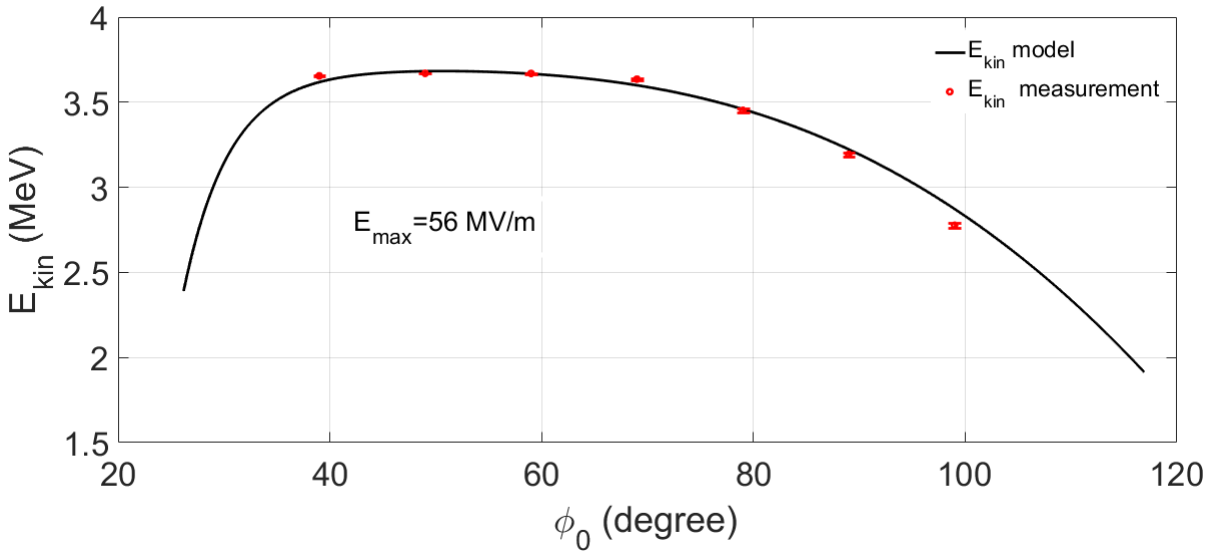

Figure 3.27: The experimental and analytical electron kinetic energy E_{kin} at the exit of the PHIL gun as a function of the RF phase φ_0 for E_{max}=56 MV/m.

3.2.3 Energy measurement in the LIL accelerating structure

This part briefly describes the analytical model of the energy in the travelling wave structures. It also presents the first energy measurement of the LIL structure during the commissioning phase of ThomX.

3.2.3.1 An analytical model of the travelling wave structure

In the case of a travelling wave structure, the relativistic electrons enter the travelling wave section and see an electric field in the form E_z=E_{max}cos(φ), where φ is the RF phase in the structure. The

maximum E_z is obtained at 180° which in turn provides a maximum kinetic energy to the electrons. Eq.3.11 highlights the acceleration in such structure:

$$E_{kin} = E_i - eE_{max}L\cos(\varphi) \tag{3.11}$$

where E_i is the initial kinetic energy coming, for example from the photoinjector, and L is the structure length.

3.2.3.2 Energy measurement using a steerer magnet

At ThomX, the distance L_{LIL} between the steerer and the YAG located after the LIL structure is 2.9 m and the maximum electric field is E_{max}=12.6 MV/m. Fig 3.28 shows the energy measurement fitted with the analytical model of the travelling wave structure. The maximum energy E_{kin} in the LIL structure is around 50 MeV at E_{max}=12.6 MV/m taking into account that $E_i \approx 4.6$ MeV coming from the RF gun. This maximum can be seen in the RF phase of $170° \leq \varphi \leq 190°$. The reference is chosen at 180° to match the experimental RF phase with the one of the analytical model. Out of this region, the electron starts loosing the energy until being also slip into reversed field.

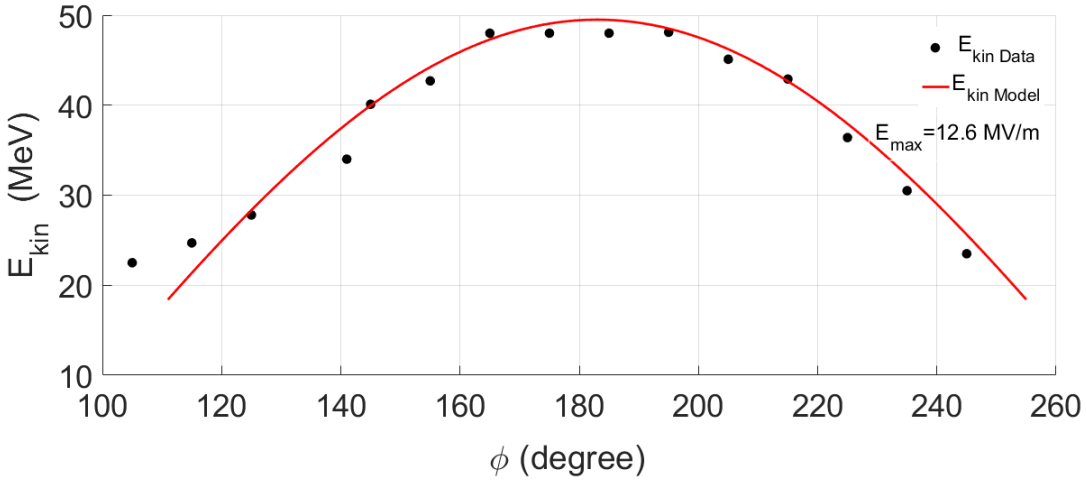

Figure 3.28: The experimental and analytical electron kinetic energy E_{kin} at the exit of the LIL structure as a function of the RF phase φ for E_{max}=12.6 MV/m.

To conclude, the measurements of the electron kinetic energies via steerers, after the standing wave photoinjector and the travelling wave LIL structure match fairly well the models.

3.2.4 Energy spread measurement

This part presents the analytical model considered for the modelisation of the energy spread of the electron beam in the photoinjector and the travelling wave structure. It also presents the energy spread measurement at PHIL. The model and measurements are then compared.

3.2.4.1 An analytical model of the photoinjector

As the non linearities of the external fields and the coupling between the longitudinal and transverse beam motion are supposed negligible, the linearity of the beam transportation can be described by the longitudinal transfer matrices as:

$$\begin{pmatrix} \Delta t_f \\ \Delta E_f \end{pmatrix} = \begin{pmatrix} R_{11} & R_{12} \\ R_{21} & R_{22} \end{pmatrix} \begin{pmatrix} \Delta t_i \\ \Delta E_i \end{pmatrix}$$

leading to:

$$\Delta t_f = R_{11}\Delta t_i + R_{12}\Delta E_i \tag{3.12}$$

$$\Delta E_f = R_{21}\Delta t_i + R_{22}\Delta E_i \tag{3.13}$$

where Δt and ΔE are the time and energy differences respectively between one electron and the reference electron with mean values through the photocathode (i subscript) to the exit of the photoinjector (f subscript).

To obtain ΔE_f, we have to determine R_{21} and R_{22} by differentiating Eq.3.8, with respect to γ_0 and φ_f where φ_f is defined in Eq.3.7. We easily obtain $\Delta\gamma_f = \frac{\partial\gamma_f}{\partial\gamma_0}\Delta\gamma_0 + \frac{\partial\gamma_f}{\partial\varphi_f}\Delta\varphi_f$, where $\Delta\varphi_f = 2\pi f\Delta t_f$ when the beam is at a fixed value of z (the exit). In Ref [54], Δt_f is also given as:

$$\Delta t_f = \left(1 - \frac{\cos(\varphi_0)}{2\alpha\sin^2(\varphi_0)}\right)\Delta t_0 \tag{3.14}$$

So, substituting Δt_f and $\Delta\gamma = \frac{\Delta E}{m_e c^2}$ allows to obtain:

$$\Delta E_f = \Delta E_i + 2\pi f m_e c^2\left(\alpha kz\cos(\varphi_f) - \frac{\alpha}{2}\sin(\varphi_f) + \frac{\alpha}{2}\sin(\varphi_f + 2kz)\right)\left(1 - \frac{\cos(\varphi_0)}{2\alpha\sin^2(\varphi_0)}\right)\Delta t_i \tag{3.15}$$

In comparison with Eq.3.13, we can deduce:
$R_{21} = 2\pi f m_e c^2 \left(\alpha kz\cos(\varphi_f) - \frac{\alpha}{2}\sin(\varphi_f) + \frac{\alpha}{2}\sin(\varphi_f + 2kz)\right)\left(1 - \frac{\cos(\varphi_0)}{2\alpha\sin^2(\varphi_0)}\right)$ and R_{22}=1 [54].
To extend the previous model to obtain the analytical model approximation of the energy spread, we have to consider the longitudinal beam matrix as follows:

$$\begin{pmatrix} \sigma_{tf}^2 & \sigma_{Etf} \\ \sigma_{Etf} & \sigma_{Ef}^2 \end{pmatrix} = \begin{pmatrix} R_{11} & R_{12} \\ R_{21} & R_{22} \end{pmatrix} \begin{pmatrix} \sigma_{ti}^2 & \sigma_{Eti} \\ \sigma_{Eti} & \sigma_{Ei}^2 \end{pmatrix} \begin{pmatrix} R_{11} & R_{21} \\ R_{12} & R_{22} \end{pmatrix}$$

where σ_{ti} and σ_{tf} are the rms initial and final bunch lengths respectively, σ_{Ei} and σ_{Ef} are the rms initial and final bunch energy spreads respectively, and σ_{Eti} and σ_{Etf} are the rms initial and final bunch energy/time correlations (chirp). The physical meaning of the energy/time correlation is to tell us what is the global relation (for the beam as a whole) between the energy and the longitudinal position (time). A zero correlation means that there is no such relation. Therefore, the energy is randomly distributed along the longitudinal position. A non zero correlation means that there is such a relation. Thus, the energy is not randomly distributed along the longitudinal position [54]. From the above matrix, the final energy spread at the exit of the photoinjector can be defined as:

$$\sigma_{Ef}^2 = (R_{21}\sigma_{ti})^2 + 2R_{21}\sigma_{Eti} + \sigma_{Ei}^2 \tag{3.16}$$

Fig 3.29 shows the energy and energy spreads calculated at the PHIL photoinjector exit (z=0.125 m) for E_{max}=56 MV/m and for two different bunch lengths as a function of the RF phase φ_0. The minimum of the energy spreads are at the RF phase φ_0 of around 50° since the matrix coefficient R_{21} becomes neglected at this phase.
For a bunch length of 1.2 ps (dashed line), called the longer bunch, the calculated energy spread varies dramatically when the RF phase φ_0 moves away from 50°, through coefficient R_{21}, up to its maximum of around 90 keV. However for the shorter bunch length of 0.3 ps (solid line), the energy spread is less sensitive to the RF phase φ_0, its maximum is 20 keV. This behaviour is well expected from the model in Eq.3.16 since the final energy spread proportionally depends on the initial bunch

length.

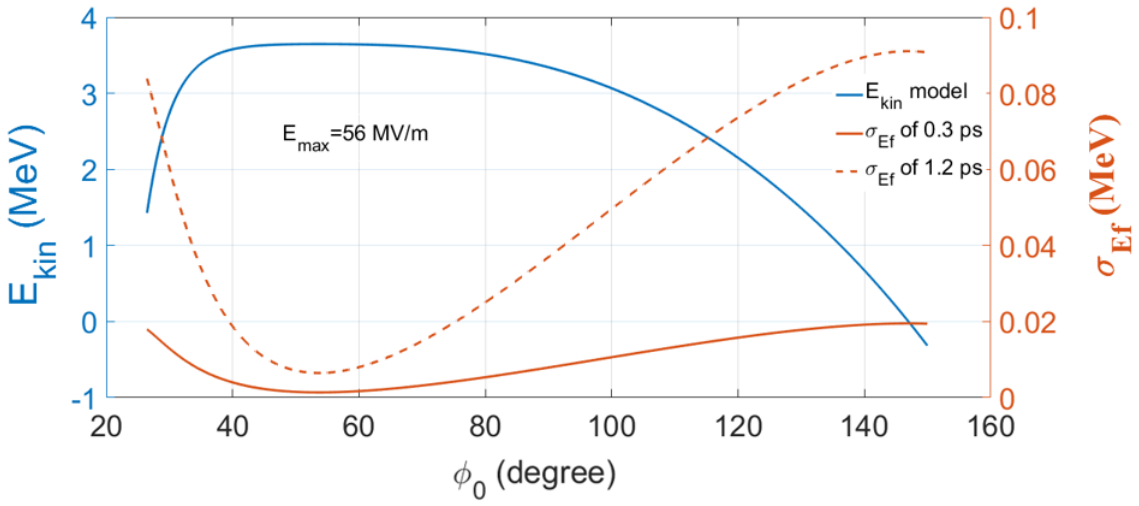

Figure 3.29: The kinetic electron energy E_{kin} simulated from Eq.3.9 and the energy spread σ_{Ef} simulated from Eq.3.16 for 2 bunches (0.3 ps and 1.2 ps) as a function of the RF phase φ_0 at the photoinjector exit (z=0.125 m) for E_{max}=56 MV/m (to simplify, σ_{Ei} and σ_{Eti} are assumed to be 0 keV and 0 MeV.ps respectively).

3.2.4.2 Energy spread measurement at the PHIL photoinjector

To obtain the energy spread at PHIL, we use the same images of the beam spot size in the dipole focal plane, presented previously in the energy measurement part 3.2.2.3, and these images have to be analysed using the following dispersion matrix formalism [64]:

$$\begin{pmatrix} x_s \\ x_s' \\ \frac{\Delta E}{E_s} \end{pmatrix} = M_{drift}.M_{dipole} \begin{pmatrix} x_0 \\ x_0' \\ \frac{\Delta E}{E_0} \end{pmatrix}$$

where

$$M_{drift} = \begin{pmatrix} 1 & L_D & 0 \\ 0 & 1 & 0 \\ 0 & 0 & 1 \end{pmatrix}$$

and

$$M_{dipole} = \begin{pmatrix} \cos(\frac{L}{\rho}) & \rho \sin(\frac{L}{\rho}) & \rho(1-\cos(\frac{L}{\rho})) \\ \frac{-1}{\rho}\sin(\frac{L}{\rho}) & \cos(\frac{L}{\rho}) & \sin(\frac{L}{\rho}) \\ 0 & 0 & 1 \end{pmatrix}$$

$$x_s \approx D(s)\frac{\Delta E}{E_\circ} \tag{3.17}$$

where x_0 and x_s are the beam position on the entrance plane before and after the dipole (m) respectively. $x_0^{'}$ and $x_s^{'}$ are the transverse angle on the entrance plane before and after the dipole respectively. $\frac{\Delta E}{E_0}$ and $\frac{\Delta E}{E_s}$ are the relative energy spread (%) on the entrance plane before and after the dipole respectively. L and L_D are the dipole and drift tube lengths (m) respectively. ρ is the curvature radius of the dipole (0.7 m) [64]. D(s) is the dispersion function (m), which represents the linear correlation between transverse position and momentum introduced by the dipole [65].

Fig 3.30 shows the kinetic energy E_{kin} and energy spread σ_{Ef} from the model and measurements, carried out at PHIL, of two beams of lengths 3 ps and 0.6 ps as a function of the RF phase φ_0 at E_{max}=56 MV/m. The initial longitudinal parameters used for the energy spread model of the 3 ps bunch are σ_{Ei}=19 keV and σ_{Eti}= 0.02 MeV.ps. And for the 0.6 ps bunch, these parameters are σ_{Ei}= 26 keV and σ_{Eti}=-0.015 MeV.ps. These parameters are deduced using the 3-phase method, which is described in detail in Ref [66]. The upper and lower plots represent the bunches of length 3 ps and 0.6 ps respectively. The measured energy spread curves show a really good agreement with the model with a very low discrepancy of around 3 keV. The measured energy spread σ_{Ef} of the bunch of 3 ps, the upper plot in Fig 3.30, is minimum $\approx$ 15 keV when the RF phase φ_0 is 45°, and it raises up to 65 keV when the RF phase φ_0 at 85°. Likewise, the measured energy spread σ_{Ef} of the bunch of 0.6 ps, the lower plot in Fig 3.30, is at minimum of $\approx$ 25 keV when the RF phase φ_0 is 38°, and it raises up to 46 keV when the RF phase φ_0 at 98°. The minimums σ_{Ef} of the bunch of 3 ps are lower than the minimums σ_{Ef} of the bunch 0.6 ps. The main reason is that a stronger effect of the space charge forces for the ultra-short electron bunches, which is clearly the case of the shorter bunch of 0.6 ps. At the RF phases higher than 65°, the proportional dependency becomes obvious as the final measured energy spread σ_{Ef} increases faster for the longer bunch (3 ps) than the shorter bunch (0.6

ps) as expected by $R_{21}\sigma_{ti}$ term.

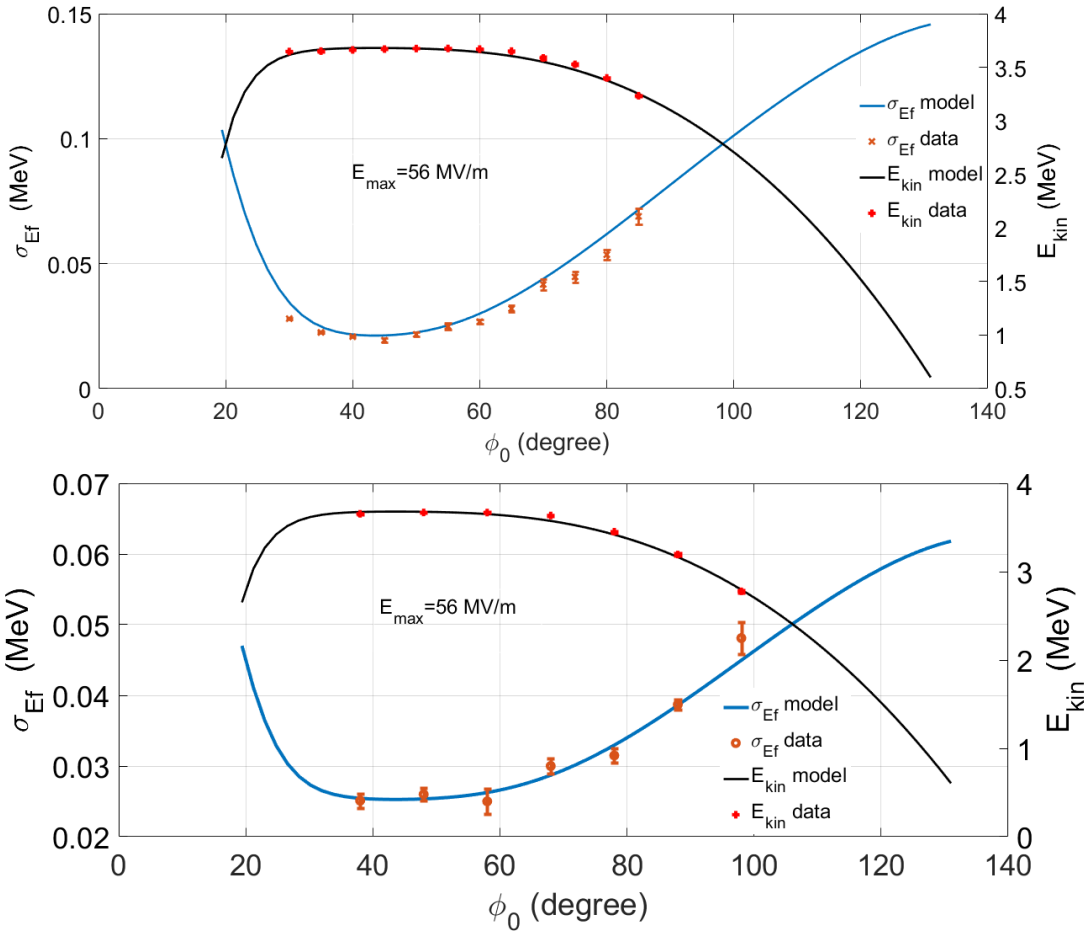

Figure 3.30: The kinetic energy E_{kin} and the energy spreads σ_{Ef} (model and measurement) for two electron bunches of length 3 ps (upper) and 0.6 ps (lower) as a function of RF phase φ_0 at E_{max}=56 MV/m.

3.2.4.3 An analytical model of the travelling wave structure

To calculate the energy spread according to Eq.3.16, one has to define the matrix coefficient R_{21} for the travelling wave structure via differentiating Eq.3.11 with respect to E_i and φ and considering that $\Delta\varphi = 2\pi f\Delta t_i$ [54] as:

$$\Delta E_{kin} = \Delta E_i - 2\pi f e E_{max} L \sin(\varphi)\Delta t_i \tag{3.18}$$

Then, the coefficient is R_{21}=$2\pi f e\, E_{max} L\, \sin(\varphi)$. Recalling Eq.3.11 to plot the kinetic energy E_{kin} and Eq.3.16 to plot the energy spread σ_{Ef} for two bunches of different lengths as a function of the RF phase φ taking the parameters of the LIL structure such as L=4.8 m and E_{max}=12.6 MV/m. The

maximum kinetic energy E_{kin} is 50 MeV with minimum energy spreads of the bunches at the RF phase φ of 180° because R_{21} is zero at this phase, thus the initial energy spreads at the structure entrance stay constant as predicted in Eq.3.16. Moreover, the energy spread of the bunch of 6 ps strongly increases far from this phase point up to 9 MeV at 270°. This is also higher than that of the maximum of shorter bunch. This is expected in the model in Eq.3.16 because of the proportional dependence of the final energy spread on the initial bunch length.

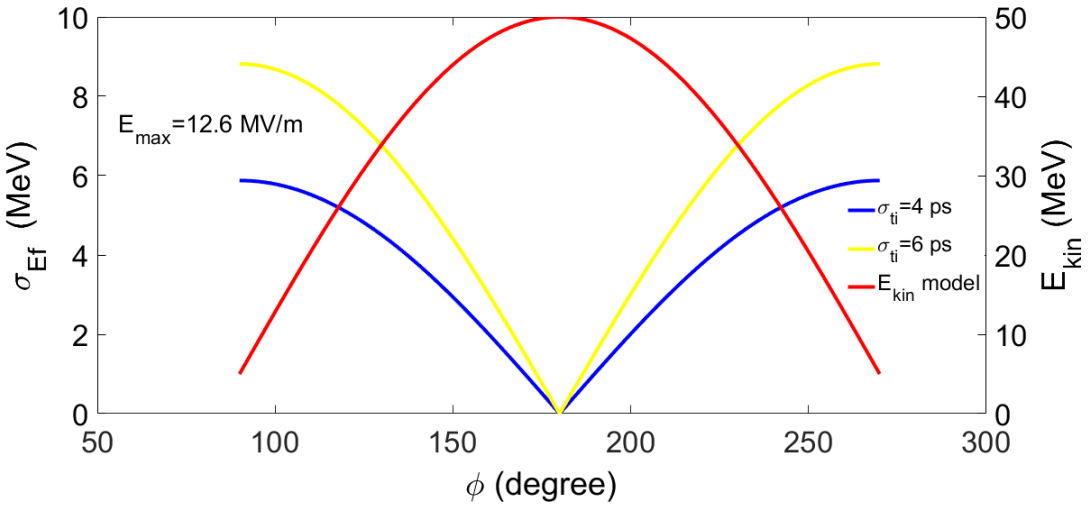

Figure 3.31: The kinetic energy E_{kin} and the energy spread σ_{Ef} for two bunches 4 ps and 6 ps as a function of the RF phase φ in the LIL TW section at E_{max} 12.6 MV/m.

Lastly, the first phase of the beam commissioning of the ThomX linac presents an excellent team work in achieving the goal of delivering a beam energy of 50 MeV at the linac exit with an electron charge of $\approx$ 100 pC at a repetition rate of 10 Hz. An another essential observation is that the modelling fits considered previously for the energy and energy spread calculations providing more confidence in using such models for longitudinal beam dynamics estimations. So far, the beam is ready to be sent to the transfer line and in the ring. The first X-ray beam is expected during 2023 depending on the national safety authorisation [62].

Chapter 4

Development of a dual feed travelling wave accelerating structure

4.1 Introduction

RI Research Instruments GmbH, a world leading company in the particle accelerator field, designs, manufactures and installs linear accelerators, accelerator modules, RF cavities, etc. RI masters key technologies related to machining (forming, milling and turning), joining (vacuum and induction brazing, electron beam welding and TIG welding) chemical surface preparation, coating, dimensional inspection, clean room assembly and system integration, for a wide range of materials including copper, niobium, aluminum, high grade stainless steel, zirconium, titanium and ceramics. Over the past decades, RI has developed and produced a variety of S-band structures and cavities for institutes all over the world. The S-band accelerating module developed by RI Research Instruments GmbH [67] consists of a painted steel girder with a painted steel strong back that is equipped with a 3.5 meter S-band accelerating structure. A waveguide power splitter sitting on the input coupler cell is part of the assembly. The module features elements to align and position the cavity and water manifolds as shown in Fig 4.1.

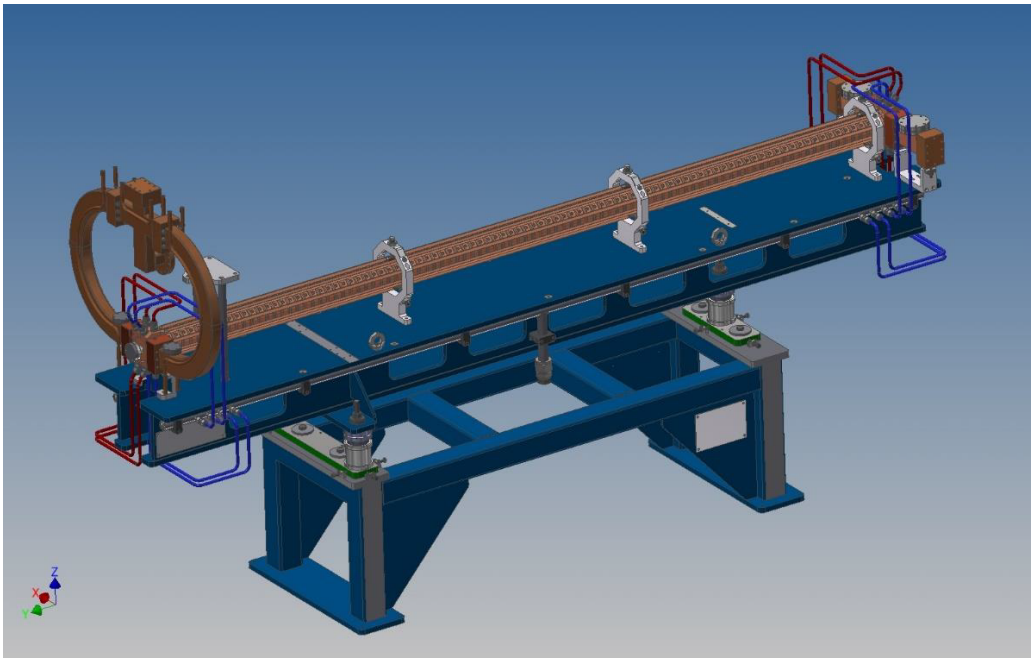

Figure 4.1: 3D CAD model of the S-band accelerating module.

The dual feed accelerating linac presented is of the constant gradient (CG) travelling wave (TW) type and operates with a $2\pi/3$ phase advance per cell. With a flange to flange of 3.5 m, it consists of 98 cells (96 regular cells and 2 coupling cells) and works at 2998.55 MHz (30°C in vacuum) (see Fig 4.2). This structure will be installed as a replacement for the LIL accelerating structure in ThomX to provide a final energy of more than 50 MeV.

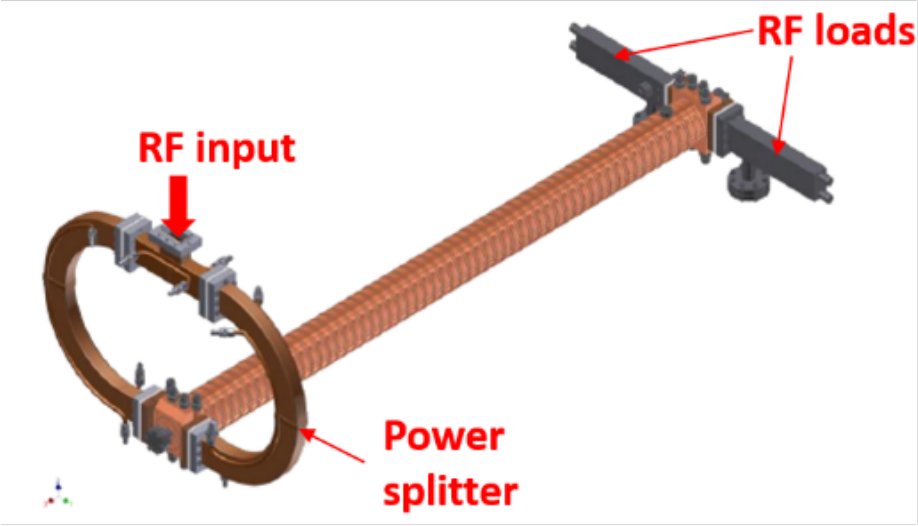

Figure 4.2: Mechanical design of the RI S-band structure.

The peculiarity of this S-band structure is that the cell-to-cell iris and cell radii are optimised to obtain a constant accelerating gradient along the structure. The cells consist of cups and the cell irises have an elliptical profile to minimise the peak surface electric field. The coupler cells are of the double-feed type with a racetrack cross-section to cancel the dipolar components of the fields and to minimise their quadrupolar components [68, 69]. The input coupler converts the RF waveguide mode into the accelerating mode TM_{01}-like thus, avoiding power reflections. The electromagnetic field propagates into the structure through the cells with a phase velocity equal to the beam velocity c, accelerating the beam itself. The output coupler converts the residual power not dissipated into the metallic wall of the structure or not absorbed by the beam, into the waveguide mode. This residual power is dissipated into RF loads connected at the out coupling ports in order to avoid reflections (Fig 4.2). All components are made from oxygen-free high conductivity (OFHC) copper according to CW009A (EN13604:2002). All RF surfaces are machined with diamond tooling, leading to minimised surface roughness, highest quality factor and low field emission. The cavity is joined by vacuum and induction brazing processes. In the following sections, the electromagnetic simulation results and the manufacturing process are presented and discussed. A detailed description of the low power RF measurement before and after tuning of the structure is also given.

4.2 Electromagnetic simulations and analysis

The RF properties for the complete S-band accelerating structure were simulated with the CST Microwave Studio [42] at IJCLab using an RI parameter design at the operating frequency (30°C in vacuum) in order to verify and validate the project requirements and specifications.

4.2.1 Matching of input and output couplers using reduced cavity symmetric models

The couplers are designed to ensure a symmetric feed with a power splitter assembly at the input coupler and two waveguide loads at the output coupler cell. The RF coupler is matched to the accelerating structure by adjusting both the slot aperture and the radius of the coupling cell

(respectively W and Rc in Fig 4.3). The coupling slot introduces a distortion in the field distribution, resulting in multi-pole field components, which affect the beam dynamics. Using symmetric feeding, which consists of two input waveguides on opposite sides of the coupling cell as indicated in Fig 4.3, the odd magnetic field components are suppressed, but there could still be even components such as quadrupoles, etc. [44]. A racetrack design of the coupling cells is introduced whose geometry, (optimising distance d between the two half-circles as shown in Fig 4.3), reduces the transverse gradients of the longitudinal electric field amplitude and phase which in turn degrades the beam emittance due to quadrupolar transverse momentum contributions. The shape of the coupling iris between the waveguide and the resonant cavity is optimised to lower the peak surface field strengths. All sharp edges are avoided to reduce pulsed thermal heating and consequent material fatigue. The goal values for symmetry are given in Table 4.1.

Table 4.1: Coupler symmetry requirements.

Parameter	Description	Limit
ΔE/E	dipole (residual)	0.1 %
Φ	dipole (residual)	0.1 degree
ΔE/E	quadrupole	0.2 %
Φ	quadrupole	0.1 degree

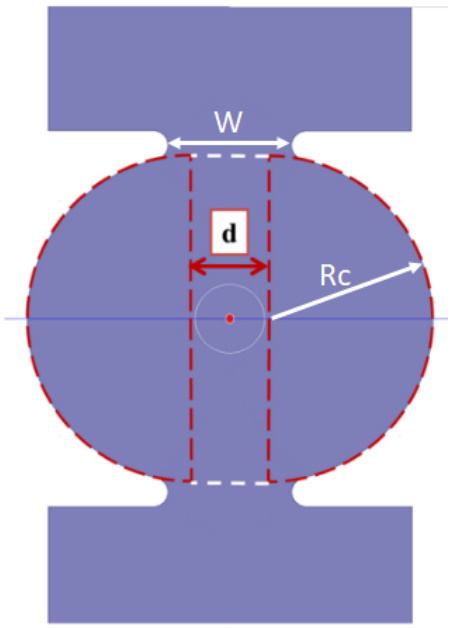

Figure 4.3: Dual-feed racetrack design of the RF coupler.

As a starting point for coupler design, optimisation by symmetric geometry is used. The racetrack parameters d, Rc and W are adjusted to obtain a reflection coefficient at the input of the coupler lower than -30 dB: the geometric parameters of couplers were tuned to match the travelling wave structure varying the number of regular cells in between the two couplers [70]. An example of the tuned reduced cavity model, consisting of two identical couplers and two identical periodic regular cells, is shown in Fig 4.4. The model dimensions for the simulations are scaled to operating temperature 30°C.

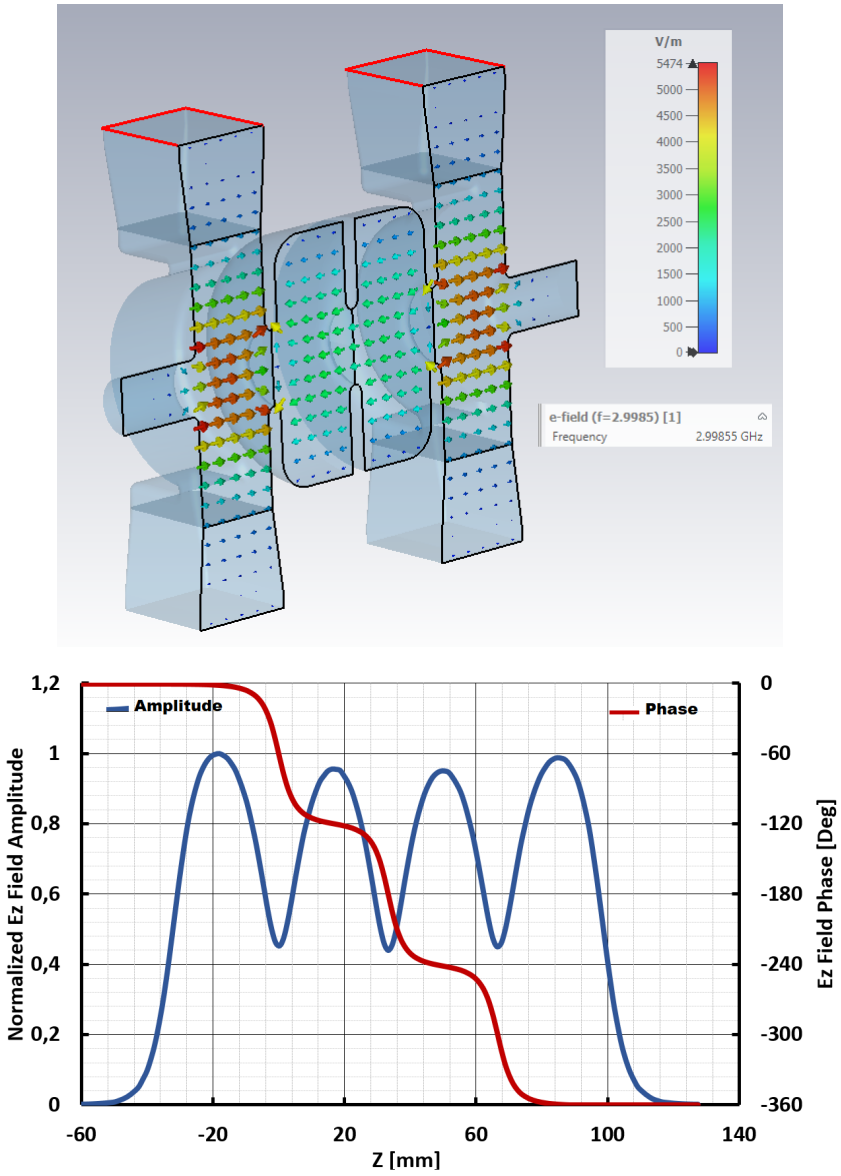

Figure 4.4: Reduced copper cavity model: Longitudinal electric field Ez ($TM_{010-2\pi/3}$) distribution (upper). Normalised Ez field amplitude and phase (Ez) on axis at working frequency 2998.55 MHz (30°C in vacuum) (lower).

The tuned couplers ensure a $2\pi/3$ phase advance per cell and good field flatness within the regular cells. The simulated S-parameters for the input and output couplers for the presented reduced cavity model (2 identical regular cells + 2 identical coupling cells) are shown in Fig 4.5. The results show good matching at the operating frequency for the accelerating mode $TM_{010–2\pi/3}$.

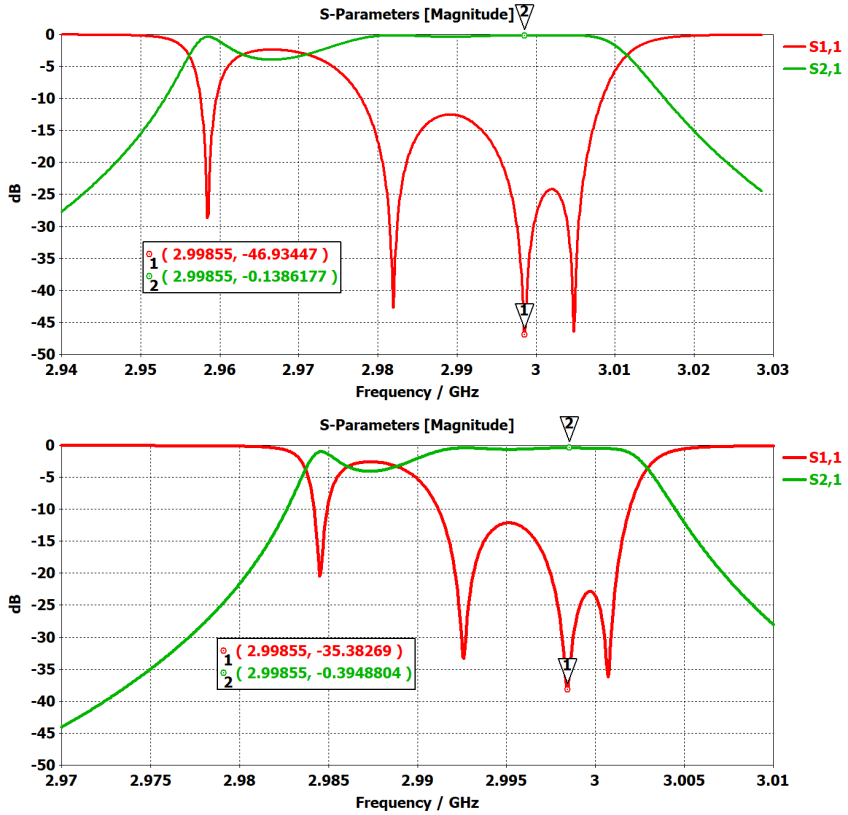

Figure 4.5: Reduced copper cavity model: S-parameters: input coupler (upper) and output coupler (lower).

4.2.2 Electromagnetic (EM) simulations of the complete accelerating structure

In order to validate the electromagnetic design of the complete accelerating structure along with the input and output couplers, end-to-end three dimensional EM simulations were performed using a frequency domain solver of computer code CST-MWS. The first part focuses on the discussion about the reflection and transmission properties of the linac structure, when the attenuation of the input RF power due to the finite resistivity of copper is taken into account, while the second part analyses RF performances and electromagnetic quantities such as surface electric field, magnetic field and

modified Poynting vector all of which determine the high-gradient performances of an RF accelerating structure. The presented accelerating structure is of the constant gradient (CG) travelling wave (TW) type and operates with a $2\pi/3$ phase advance per cell. With a flange to flange of 3.5 m, it consists of 98 cells (96 regular cells and 2 coupling cells), operates at 2998.55 MHz (30°C in vacuum) and is equipped with two dual feed racetrack couplers. The regular cells have a cup shape with curvature radius (on-side bending) at the operating temperature to reduce RF losses (see Fig 4.6). The irises all have the same elliptical cross-section with an aspect ratio of 1.5:1. A constant accelerating gradient along the structure is maintained by suitably shaping the iris aperture of each cell. The iris radius then decreases along the structure in order to obtain a flatness of the accelerating field amplitude through the whole section and to maintain a uniform cell-to-cell phase advance of 120 ° in the accelerating mode. Due to the difficulty of tuning and matching coupler cells with low group velocity, the radius of the last iris of the structure was chosen to be 9 mm. The length of each cell is 33.326 mm at 30°C. The simulations are performed using the CST Microwave Studio. To minimise CPU time and the memory use, appropriate boundary conditions, such as symmetry planes, were used (Fig 4.6).

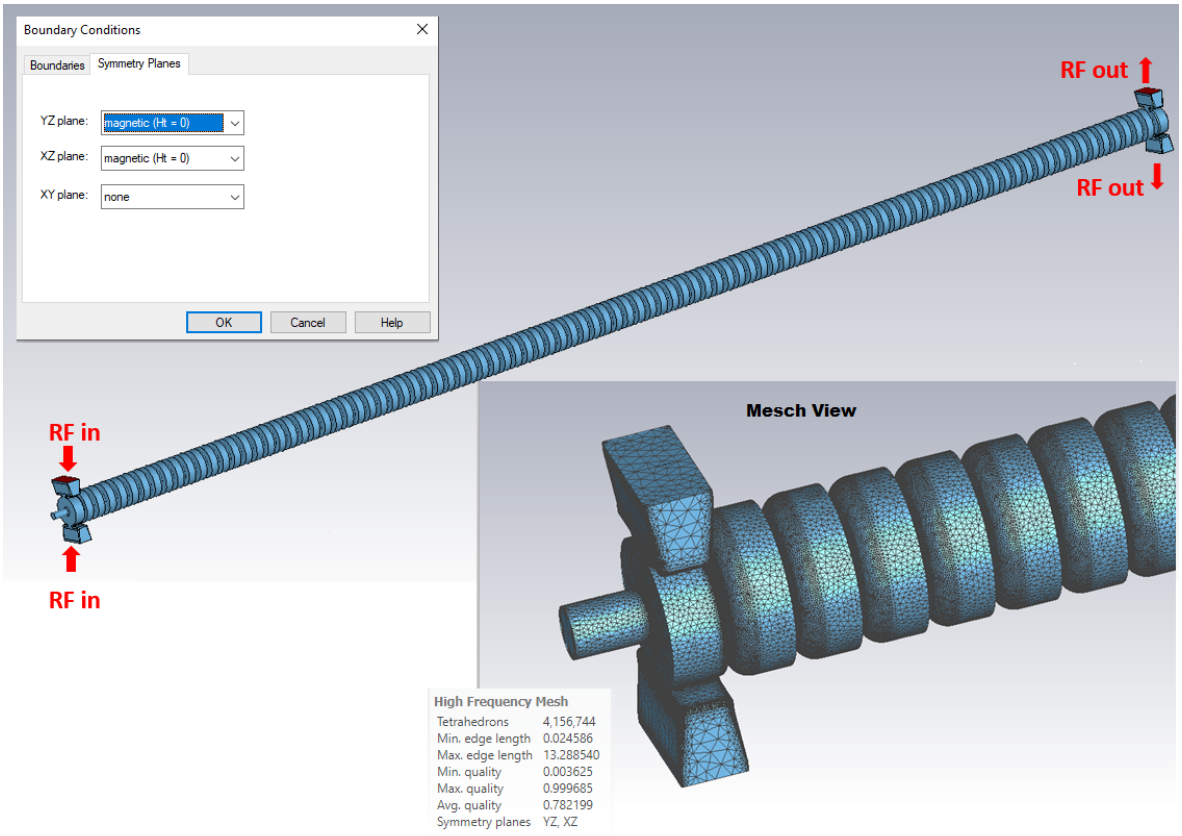

Figure 4.6: 3D CST model of the complete dual feed accelerating structure.

Fig 4.7 (upper plot) gives the plot of the input reflection coefficient versus frequency. At operating frequency of 2998.55 MHz (30 °C in vacuum) for the accelerating mode $TM_{010-2\pi/3}$, the input reflection coefficient is -40.8 dB, indicating that the power reflected is less than 0.01%. The structure is made of normal conducting OFHC copper and its resistivity ($1.7x10^{-8}\Omega.m$) was accounted for the simulations. Thus, a portion of the input RF gets attenuated while propagating through the structure. This is clear from Fig 4.7 (lower plot) which shows the plot of the transmission coefficient (insertion loss) from the input to the output of the structure versus frequency. At the working frequency, the insertion loss is -5.17 dB, indicating that $P_{RF\ out}$=0.3 $P_{RF\ in}$. This residual power $P_{RF\ out}$ is dissipated into RF loads connected at the out coupling ports.

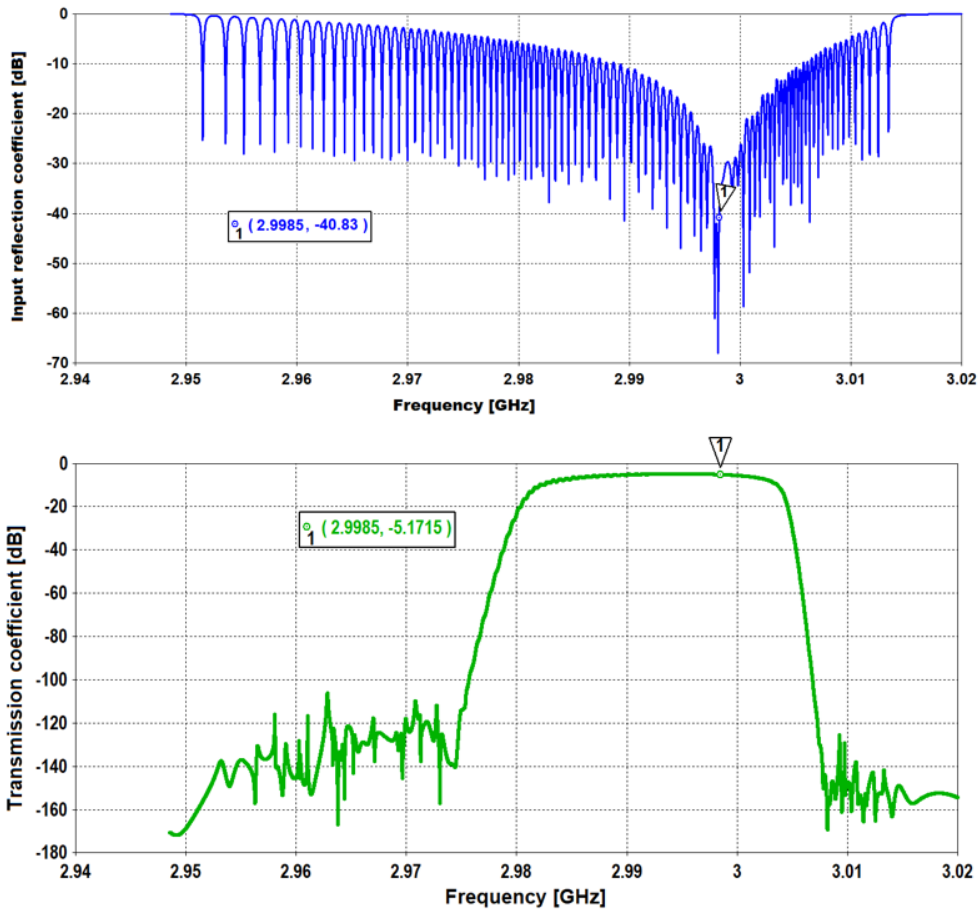

Figure 4.7: Input reflection coefficient (upper plot), transmission coefficient “insertion loss” (lower plot) versus frequency of the whole structure.

Fig 4.8 illustrates the axial electric field distribution for the accelerating mode $TM_{010\,-2\pi/3}$ at the resonant frequency of 2998.55 MHz in vacuum at 30°C for an input peak power of 40 MW.

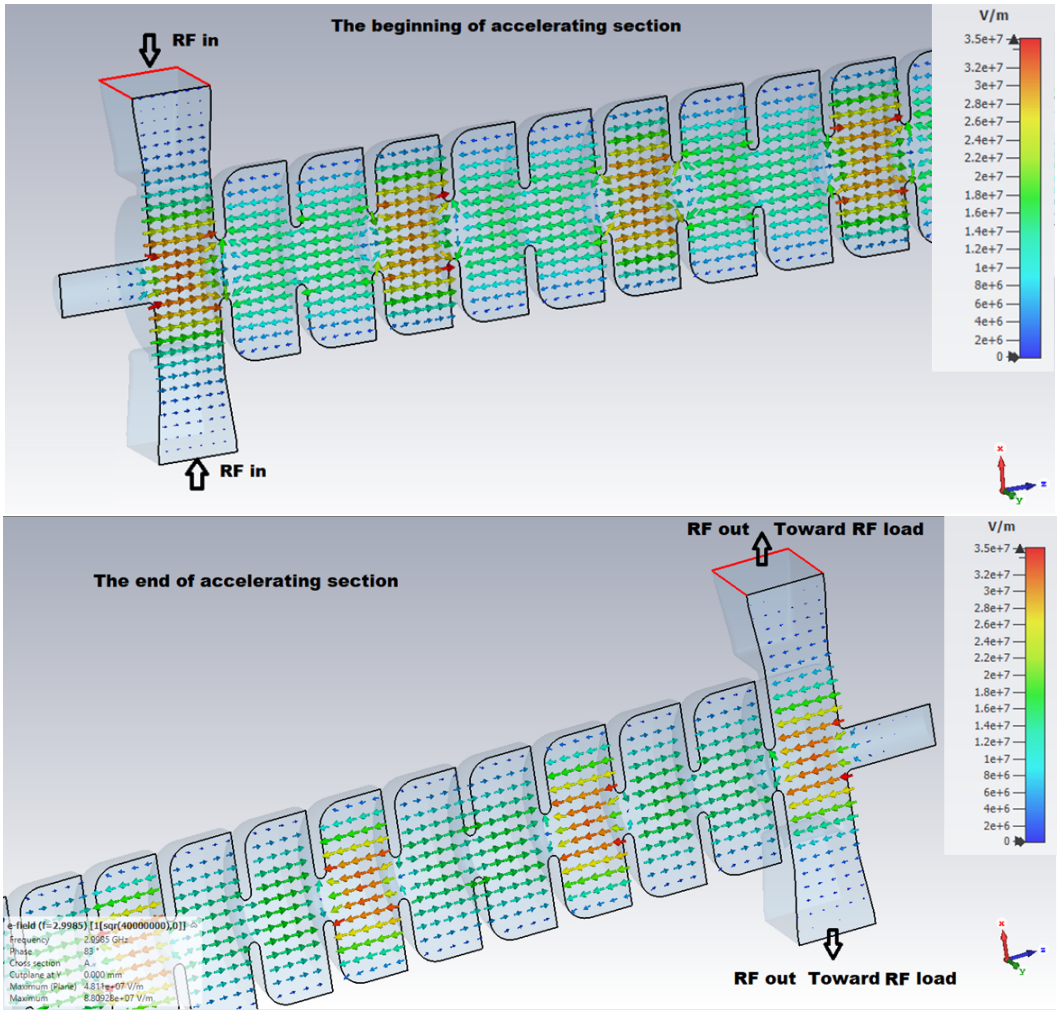

Figure 4.8: Longitudinal electric field distribution ($TM_{010\,-2\pi/3}$) of the whole structure for an input peak power of 40 MW (zoom at the beginning and at the end of the structure).

The resulting longitudinal electric field amplitude along the structure was determined as shown in Fig 4.9. It can be seen that the longitudinal electric field amplitude is almost constant along the total length of the structure. The maximum axial electric field at 40 MW is more than 30 MV/m using a frequency domain solver of computer code CST-MWS.

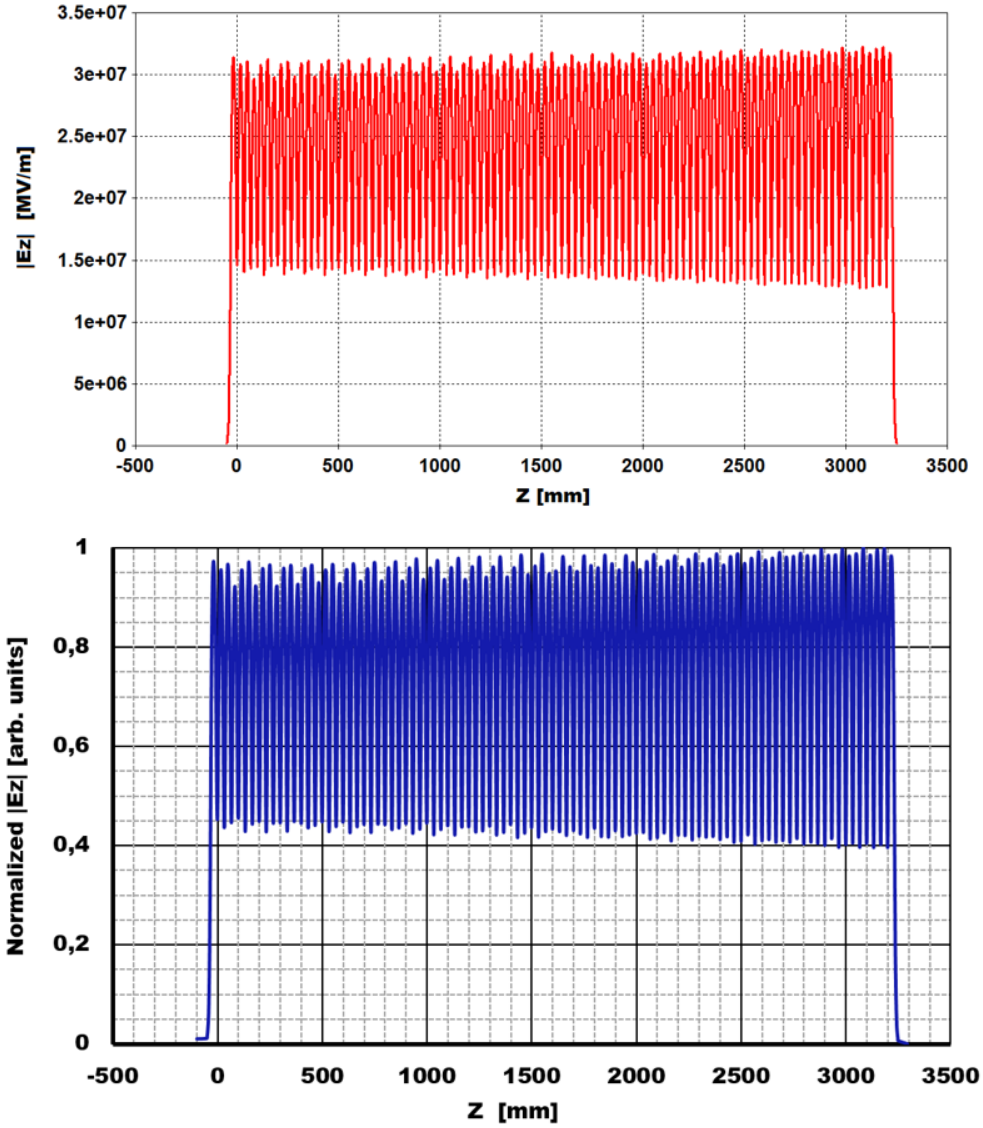

Figure 4.9: Ez field amplitude (upper) at 40 MW input peak power. Normalised Ez field amplitude (lower).

The cell-to-cell axial electric field amplitude variation versus cell number is calculated and the overall observation is 4%, which is under the specification limit of 10%, as shown in Fig 4.10.

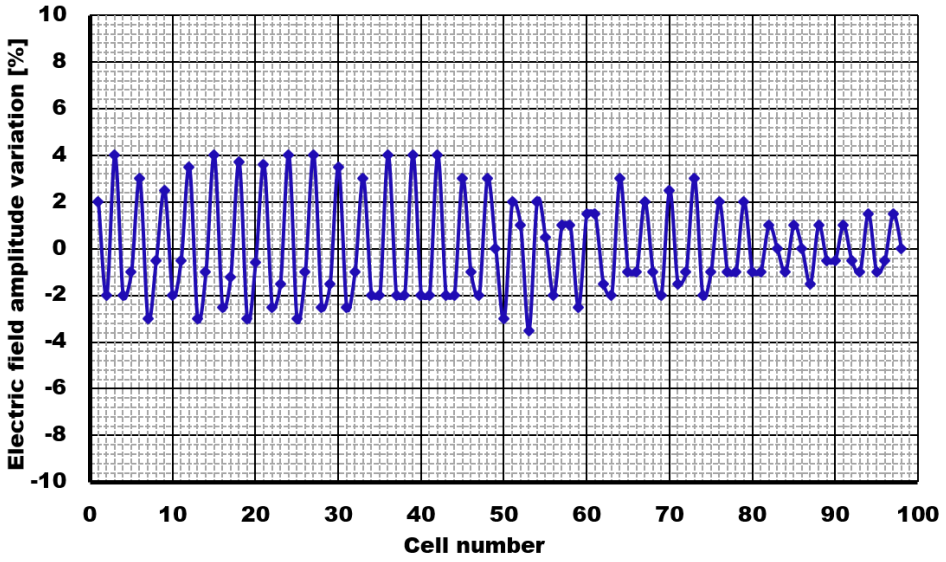

Figure 4.10: The simulated cell-to-cell axial electric field amplitude variation versus the cell number.

Fig 4.11 illustrates the simulation results for the energy gain and the longitudinal accelerating gradient E_{max} on axis (peak value) and the effective gradient E_{eff} on axis, seen by the electrons, as a function of the RF input power. For a 40 MW input power, an energy gain of about 76 MeV is obtained.

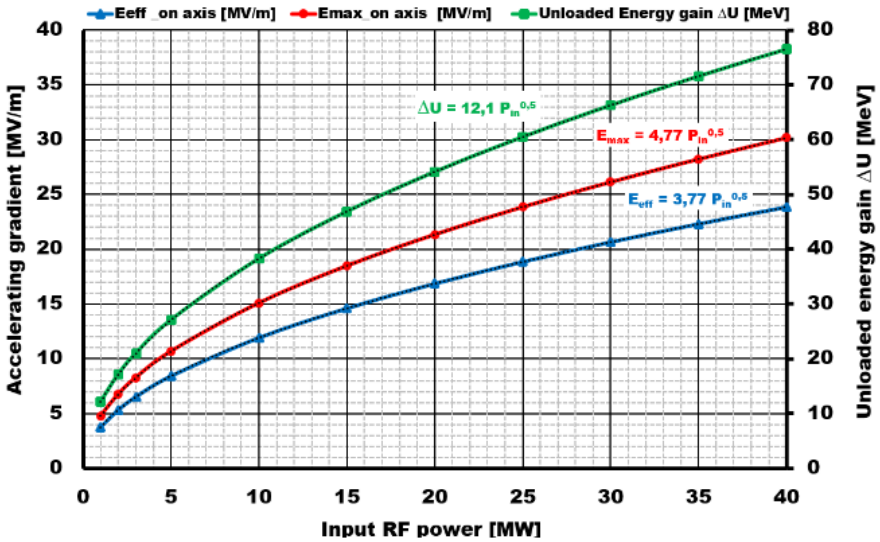

Figure 4.11: Electric gradient and energy gain versus input RF power.

Moreover, Fig 4.12 illustrates the plot of the Ez field phase ($TM_{010\,2\pi/3}$ mode) along the whole accelerating structure. This data was used to evaluate the phase advance per cell (Fig 4.13).

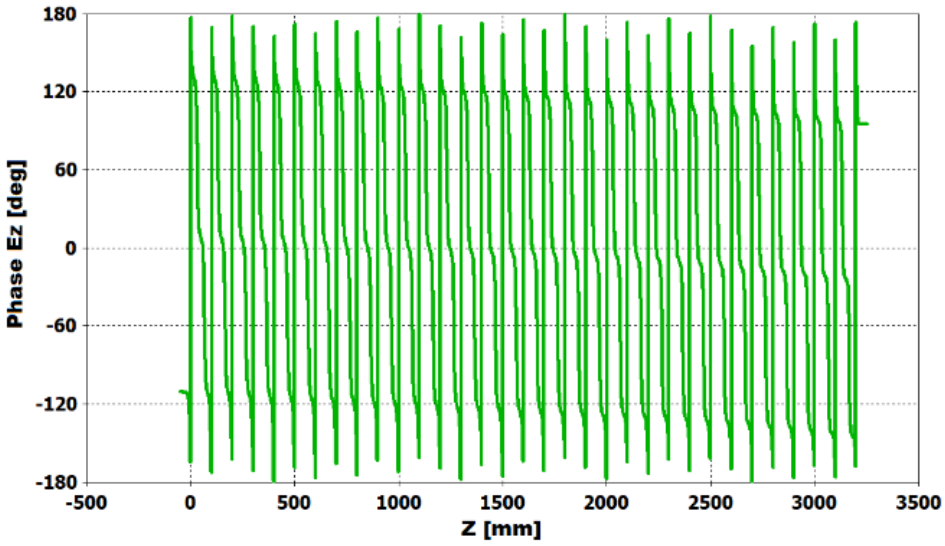

Figure 4.12: Ez field phase along the length of the structure.

The simulated average phase advance per cell obtained is 120°, which is the design phase required for acceleration of the electron beam, and the maximum cell-to-cell phase advance error is less than ± 2.5° (max error phase is fixed at ±2.5°, which is considered the limit for avoiding a significant reduction in the total accelerating gradient in the structure). This error is partly due to a numerical error in the simulations.

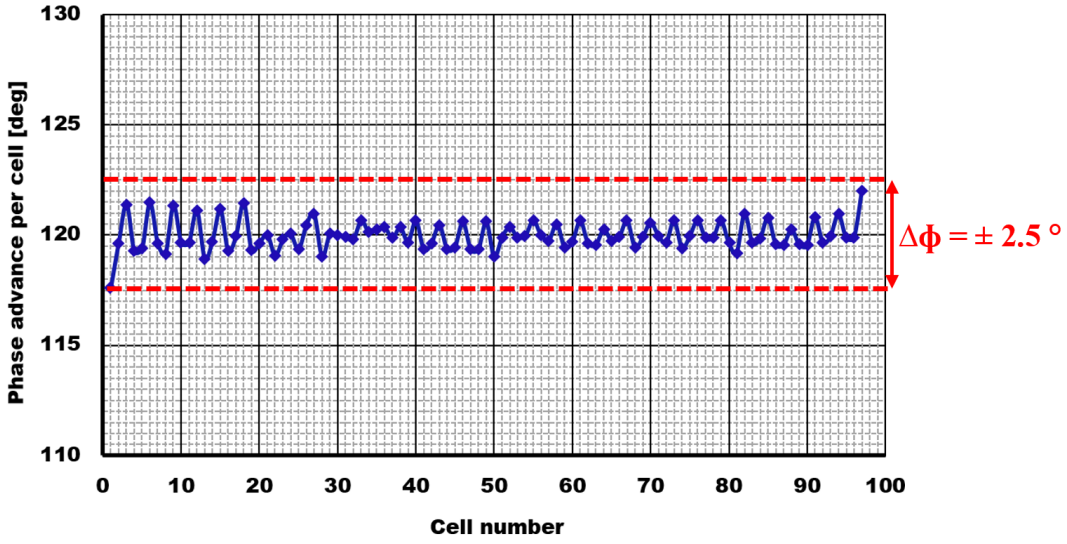

Figure 4.13: The simulated phase advance per cell versus cell number.

In normal conducting temperature accelerating structures, the achievable on-axis electric field is mostly limited by two main effects: RF breakdown and fatigue cracking due to the pulsed heating

[71]. Breakdowns lead to random beam kicks that can result in emittance growth or even loss of the beam if the kick is strong enough. Since the surface electric field is considered to be strongly connected to the field emission of electrons from the cavity surface, it was thought to be one of main quantities limiting the accelerating gradient. Historically, an empirical law determining a threshold between no-vacuum discharge and possible vacuum discharge regimes was established by Kilpatrick [72]. The Kilpatrick criterion was reformulated by Boyd [73] as follows:

$$f\,[\mathrm{MHz}] = 1.64\,(E_k[\mathrm{MV/m}])^2 e^{-\frac{8.5}{E_k[\mathrm{MV/m}]}} \tag{4.1}$$

where f is the RF frequency and E_K is the Kilpatrick limit for the surface electric field. The expression shows that higher fields can be reached with higher frequencies. At 3 GHz "S-band", the maximum surface electric field predicted by Kilpatrick's law is around 48 MV/m. At 5.7 GHz "C-band", it increases to 63 MV/m, while at 12 GHz "X-band" it reaches 90 MV/m. However, in recent years, new improvements in structure fabrication and cleaning techniques have demonstrated the reliable operation of cavities at surface electric field level double the Kilpatrick threshold [74]. For this reason, the maximum surface electric field could not be considered as the only constraint in the RF design because of the large variation it shows in the different structures. In the case of our structure, for an input power of 40 MW the simulated maximum surface electric field is 46 MV/m, just below the Kilpatrick limit. As shown in Fig 4.14, the maximum surface electric field is localised in the iris area.

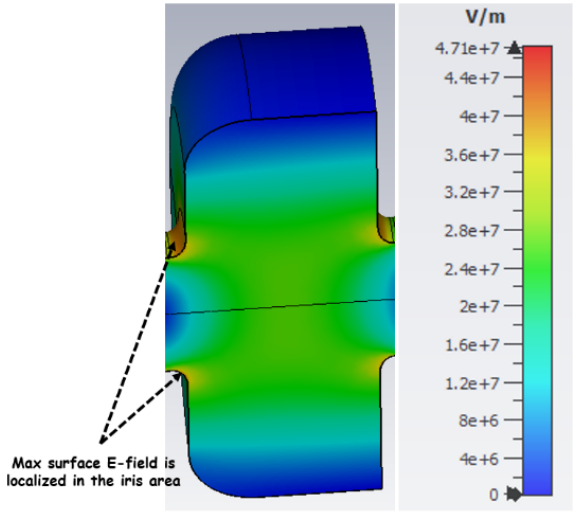

Figure 4.14: Maximum surface electric field localised in the iris area for an input power of 40 MW.

More recently other quantities have been considered to be responsible for high gradient limits. After analysis of the data from different experiments with varying RF parameters [75], a new criterion based on the power flow was proposed by Wuensch in 2006 [76]. This criterion is based on the observation that the structures with larger apertures and higher group velocities can tolerate higher power flows, but at the same time lower surface electric fields. This can be quantified as follows:

$$\frac{P_{in}.t_p^{\frac{1}{3}}}{C} < \text{const} \tag{4.2}$$

where P_{in} is the input power to the structure, C is the minimum circumference of the structure that is usually determined by the iris aperture, and t_p is the RF pulse length. The constant value of Eq.4.2 varies only in the range between 10 and 20 MW.ns$^{1/3}$.mm^{-1} for copper RF structures, even with changes of one order magnitude in group velocity and RF pulse length and changes of a factor 2-3 in frequency, iris diameter, input power and maximum surface field. In our case, for an input power of 40 MW, an RF pulse length of 3 μs and an iris diameter of 18 mm (last iris cell), the constant is evaluated at 10.2 MW.ns$^{1/3}$.mm^{-1}. This scaling law fits the data more closely than the peak surface electric field but still has limitations, one being that it does not account for standing wave structures which have no power flow through the beam aperture. Fig 4.15 depicts the simulated power flow field distribution along the whole structure at operating frequency f_{RF}=2998.55 MHz for an input

power of 40 MW as given:

$$\vec{S} = \vec{E} \times \vec{H} \tag{4.3}$$

The transmitted power decreases linearly along the structure. At the end of the structure, the remaining power of 12 MW is delivered to external RF loads.

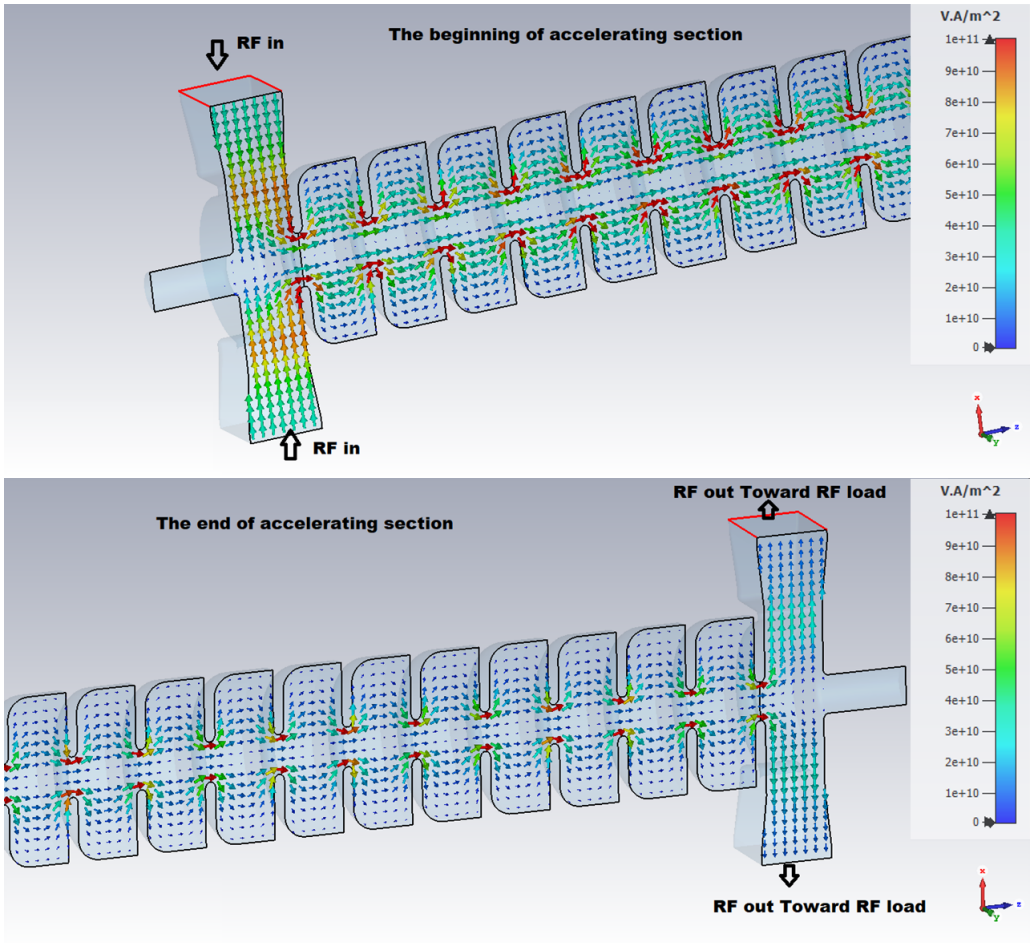

Figure 4.15: The power flow field distribution in the dual feed structure for an input power of 40 MW "zoom at the beginning (upper) and at the end (lower)".

A new model similar to the P_{in}/C criterion, but based on the idea that it is a combination of local fields which sets a limit to the achievable gradient rather than an integral parameter (which must then be scaled with frequency), was proposed by Grudiev in 2009 [77]. The model assumes that the field emission currents work at the expenses of the RF field and trigger RF breakdown. The current density will depend on the available power, the field enhancement factor and material of the emitter. The available power is given by the RF power passing through the emitter surface, described by the

Poynting vector. In the model, a local field quantity that takes into account active and reactive power flow in the structures, the modified Poynting vector, is proposed as a candidate to explain the limit to high gradient structure performances due to RF breakdown. Higher powers would increase the temperature of the emitter above the threshold beyond which the emitter could initiate the RF breakdown process. The inclusion of the reactive part of the Poynting vector makes it possible to extend the validity of the model to the standing-wave structures, which present no real power flow. The modified Poynting vector is defined as:

$$S_c = \Re(\vec{S}) + \frac{1}{6}\Im(\vec{S}) \tag{4.4}$$

where $\vec{S} = \vec{E} \times \vec{H}$ is the Poynting vector ($\vec{E}$ and $\vec{H}$ are the electric and magnetic field vectors respectively), $\Re(\vec{S})$ is the real part and $\Im(\vec{S})$ is the imaginary part. This local quantity S_c can be easily defined in electromagnetic simulation solver CST MWS as a geometry design parameter. The dependence of the modified Poynting vector on RF pulse length t_p at a fixed breakdown rate (BDR) [78] has a well established scaling law observed in many experiments as given:

$$\frac{S_c^{15} t_p^5}{BDR} = \text{const} \tag{4.5}$$

The breakdown rate is the magnitude that quantifies the number of breakdowns, N_{bd}, observed during the operation of an RF structure:

$$\text{BDR[bpp/m]} = \frac{N_{bd}\ \text{[breakdowns]}}{N_{pulses}\ \text{[pulses]}\ L\text{[m]}} \tag{4.6}$$

where N_{pulses} is the number of RF pulses sent to the structure during the measurement and L is the length of the structure. The breakdown rate is typically given in breakdowns per pulse per meter (bpp/m). As a design guideline for new RF structures, S_c should not exceed 4 MW/mm^2 if the structure is supposed to operate at a breakdown rate smaller than 10^{-6} bpp/m and a pulse length of 200 ns [77, 78]. By re-scaling these data to the pulse length of the ThomX linac, i.e. 3 μs, the maximum threshold in this case should not exceed $S_{c\,max}$=1.6 MW/mm^2, if the structure is supposed

to operate at a BDR smaller than 10^{-6} bpp/m, which corresponds to the acceptable breakdown rate for a medical accelerator. For an input RF power of 40 MW, the maximum modified Poynting vector from the simulation is $S_{c\ max}$=0.32 MW/mm^2 (Fig 4.16), which is far below the limit of 1.6 MW/mm^2. The expected BDR of 10^{-16} bpp/m is far bellow the BDR threshold of 10^{-6} bpp/m for medical accelerators at given $S_{c\ max}$=0.32 MW/mm^2, $E_{surf\ max}$=46 MV/m and for a RF pulse length of t_p=3μs. This limit is derived for structures which were constructed on the basis of the high gradient assembly procedure. This procedure includes keeping everything clean and having a high-temperature bonding or brazing cycle in hydrogen or in vacuum.

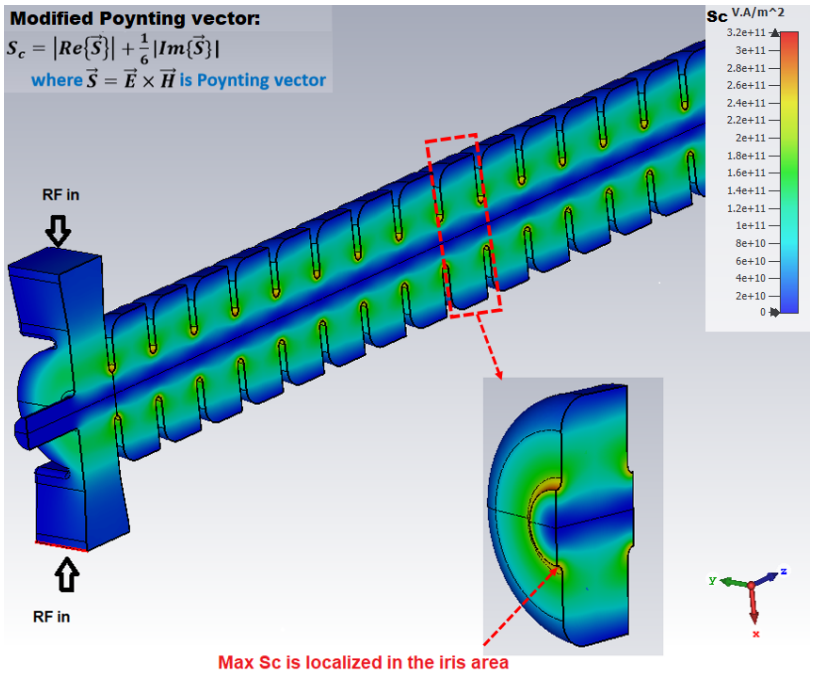

Figure 4.16: Modified Poynting vector field distribution in the dual feed structure for an input power of 40 MW.

Fig 4.17 shows maximum simulated surface electric fields and modified Poynting vectors versus input power in the range [1-40 MW].

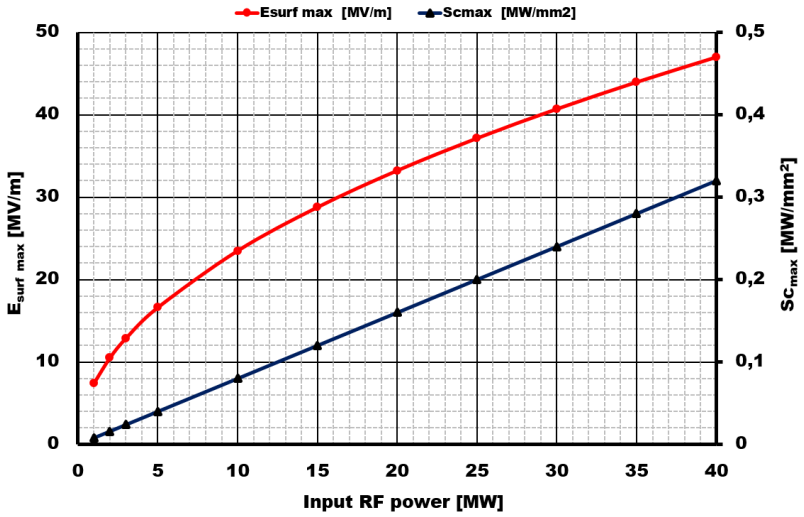

Figure 4.17: The maximum surface electric field and modified Poynting vector as a function of an input RF power.

Another important limiting quantity is RF pulsed heating [79] which is a process by which a metal is heated from RF magnetic fields on its surface. When the induced thermal stresses are larger than the elastic limit, micro-cracks and surface roughening can occur due to cyclic fatigue. Pulsed heating limits the maximum magnetic field on the surface and the maximum achievable accelerating gradient in a normal conducting accelerator structure. Many experiments demonstrated that the waveguide-to-coupler irises in couplers are prone to breakdowns for low group velocity TW and SW structures [80]. In fact, RF power enters the structure through the "coupling aperture" slots, the surface currents flow along the edges of the slots, and these edges are place of where local currents are significantly amplified. The high currents can give localised losses that can create hot spots and drive breakdown phenomena, damaging the coupler itself. RF pulsed heating causes a temperature rise ΔT on the metal at each RF pulse. For copper, it is possible to use the following simplified formula:

$$\Delta T[^{\circ}C] = 127|H_{||}[MA/m]^2|\sqrt{f_{RF}[GHz]\, t_p[\mu s]} \tag{4.7}$$

where $H_{||}$ is the tangential magnetic field, t_p is the RF pulse length and f_{RF} is the operating frequency. As a general experimental rule, if this temperature rise exceeds $\approx 100^{\circ}$C, there is a high probability of serious damage in the coupler region to occur. Below 50 $^{\circ}$C, damage to the couplers is practically avoided, while in the interval 50–100 $^{\circ}$C, there is some probability of coupler damage

[81]. One way of reducing the high magnetic field in the couplers is to increase the curvature radius of the coupling slots. In our structure, the coupling hole was rounded to reduce the pulsed heating. The surface magnetic field on the coupler was simulated using CST MWS, as reported in Fig 4.18. For an input power of P_{in}=40 MW and an RF pulse length of t_p =3 μs, a peak surface magnetic field $H_{||}$ equal to 1.45×10^5 A/m is obtained. The estimated temperature increase ΔT due to the pulsed heating on the input coupler is less than 10 °C, i.e. below the "safe limit".

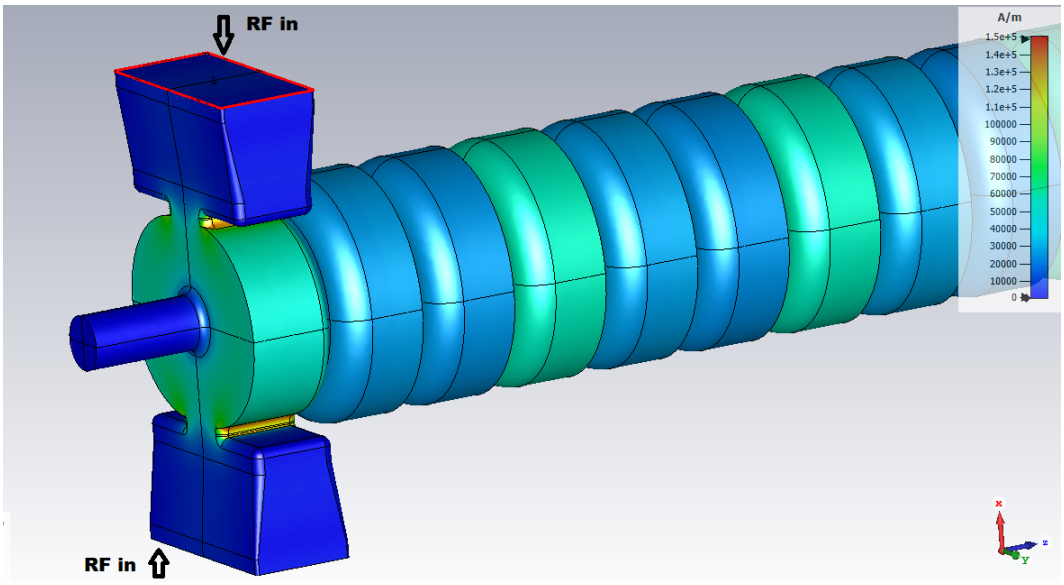

Figure 4.18: Distribution of the surface magnetic field in the input structure for an input peak power of 40 MW.

Table 4.2 summarises the CST simulation results of the RI dual feed accelerating structure.

Table 4.2: RF parameters of the RI dual feed structure (CST results).

Parameter	Value
Structure type	Constant gradient CG
Operation Frequency f_{oper}	2998.55 MHz @30 $^{\circ}$C under vacuum
Operation mode	$2\pi/3$
$\|S_{11}\|@f_{oper}$	-40 dB
$\|S_{21}\|@f_{oper}$	-5.2 dB
Number of cells	96 regular cells + 2 coupling cells
Couplers	Input/Output symmetric racetrack couplers
Structure length flange to flange	$\approx$ 3.5 m
Max. RF input power P_{in}	40 MW
Group velocity (v_g/c)	1.9 % $\rightarrow$ 0.7 %
Output power	0.3 P_{in}
Filling time	< 1 μs
Shunt impedance	60 $\rightarrow$ 76 [MΩ/m]
Flat top RF pulse length	3 μs
Repetition rate	50 Hz
Ave. unloaded quality factor Q	14200
Max. accelerating gradient	30 MV/m @ P_{in}=40 MW
Effective accelerating gradient	24 MV/m @ P_{in}=40 MW
Unloaded energy gain	76 MeV @ P_{in}=40 MW
Cell-to-cell axial E-field amplitude variation	$\leq$ 4 %
Phase advance per cell error	$\leq \pm$ 2.5°
$E_{surf\ max}$	46 MV/m $\leq$ Kilpatrick limit: 48 MV/m @ 3 GHz
Max modified Poynting vector $S_{c\ max}$	0.32 MW/mm^2 @ P_{in}=40 MW
$E_{surf\ max}/E_{eff}$	1.95 $\rightarrow$ 1.7
$S_{cmax}/E_{eff}{}^2$	5.6 $\times 10^{-4} \rightarrow 3 \times 10^{-4}$ A/V
$H_{surf\ max}$ (Input coupler)	145 kA/m@ P_{in}=40 MW
Max pulsed surface heating (input coupler)	< 10°C @ P_{in}=40 MW
Breakdown rate BDR	$\approx 10^{-16}$[bpp/m]@P_{in}=40 MW

4.3 Manufacturing process

Required manufacturing technologies such as precise machining, chemical cleaning, vacuum brazing of sub-assemblies and induction brazing of stacks, are well established technologies at RI Research Instruments GmbH. The regular cells are made of oxygen-free copper (electrical conductivity of 5.8 $\times 10^7$ S/m) of high purity and small grain size. This makes resistive RF power dissipation low, and most RF power can be preserved for beam acceleration. In particular, this material is good at vacuum leakage tightness, which is the required environment for beam acceleration. The body of couplers, except the stainless-steel beam pipe, the wave guide flange (LIL type), is also made of OFHC copper. To a large extent, machining and brazing techniques determine the performance of the accelerating structure, including frequency accuracy, quality factor and matching status; the procedure must therefore be strictly controlled. During the manufacturing process, the quality is assured by RF measurements as well as standard technologies such as dimension control and vacuum leak checking. Each individual cell is measured according to its RF properties prior to stack brazing.

4.3.1 Machining

The machining processes consists of mechanically cutting the material into a defined shape and size by a controlled material removal method requiring the best dimensional accuracy, surface finishes and tolerances which are normally achieved in several classical machining operations depending on the application. Table 4.3 illustrates the typical surface finish for classical machining operations [82, 83]. At RI Research Instrument GmbH, all RF surfaces were machined by means of the diamond turning technique using CNC machines which have the advantage of accurately cutting away thin layers of the surface with high quality surface finishes determined by the machine tool and the cutting process. However, some characteristics of the material can limit the surface finish such as grain and inclusion size, etc. Moreover, to achieve a perfect optical surface, the edge of the diamond tool should be free of defects and accurately moved with respect to the element used. RI regular cells were machined using precision CNC turning machines; the obtained surface roughness was less than 70 nm, and the precision on the internal dimensions lower than $\pm$ 10 μm.

Table 4.3: Typical surface finishes for classical machining operations.

Surface Finish	**N8**	**N7**	**N6**	**N5**	**N4**	**N3**	**N2**	**N1**
Ra (μm)	3.2	1.6	0.8	0.4	0.2	0.1	0.05	0.025
Planing	●	○	○					
Drilling	●	○						
Turning	●	●	● ○	○	○			
Diamond Turning					●	●	●	○
Milling	●	●	● ○	○	○			
Lapping					●	●	●○	○
Polishing				●	●	●	●	●

● Roughness obtained with usual workshop practice.
○ Roughness obtained with special care.

A picture of the regular cell is shown in Fig 4.19. Input and output couplers were machined using the milling technique. The obtained surface roughness was less than 100 nm.

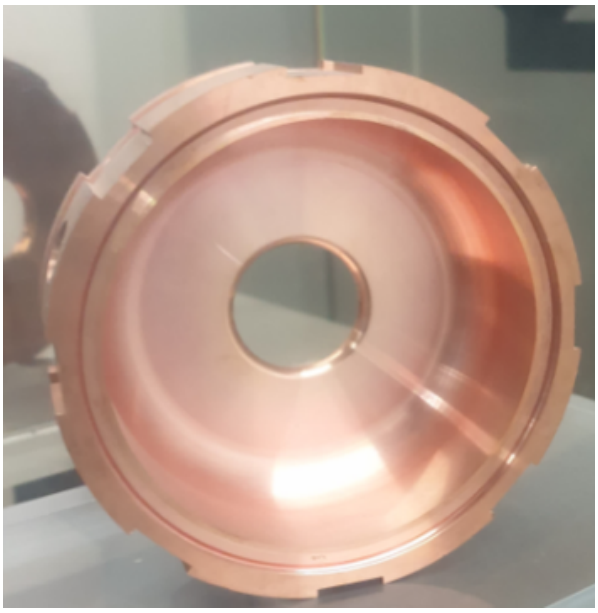

Figure 4.19: RI regular accelerating cell .

To achieve ultra-high vacuum (UHV) integrity, special care is taken in the cleanliness of the components. Before brazing, all components were cleaned and dried through a process which consists of ultrasonic degreasing, weak acid treatment and rinsing with ethanol.

4.3.2 Brazing

Brazing is a metal-joining process in which two or more materials are joined when a filler metal (with a melting point lower than those of the materials themselves) is drawn into the joint between them by capillary action. Vacuum brazing is carried out in the absence of air, using a specialised furnace, and delivers significant advantages: extremely clean, flux-free braze joints of high integrity and superior strength. RI Research Instrument GmbH operates two vacuum furnaces for brazing: a Degussa vacuum furnace (size: 1500 mm, Height 3000 mm; Max temperature: 1250°C; Pressure: 2×10^{-4} mbar) and an IPSEN vacuum furnace (size: width 600 mm, Length 1100 mm, Height 500 mm; Max temperature: 1250°C; Pressure: 8×10^{-5} mbar). RI also has equipment for performing induction brazing. The Degussa vacuum furnace allows for brazing structures of less than 3 m in length. For longer structures (up to 3.5 m, as in our case), the RI structure was brazed through various steps. First, two sub-assemblies consisting of several stacked regular cells and two others composed of input and output couplers joined with several regular cells; the stacks were brazed separately in a vacuum furnace. Second, a column composed of these four sub-assemblies was positioned vertically and brazed using the induction technique. The procedure was successful and vacuum tightness was obtained. To preserve the temperature of the accelerating structure at 30 ± 0.1°C at working frequency, a cooling channel distribution composed of eight channels was brazed to the cell surfaces. Each cooling channel has its own inlet and outlet connector (e.g. Swagelok). The flow rate for each channel was 7.5 l/min and the maximum pressure drop was 1 bar per channel. A pressure test of the complete cooling system, including manifolds of the structure was performed without any water leaks.

4.3.3 Alignment, bake out, He leak test and RGA analysis

After brazing, the dimensions and straightness of the structure were checked. The straightness of the structure was adjusted using a Leica Laser Tracker until the measured peak-to-peak straightness deviation was under 0.13 mm, i.e. lower than the specified value of 0.15 mm. Fig 4.20 shows the results of the dimensional inspection.

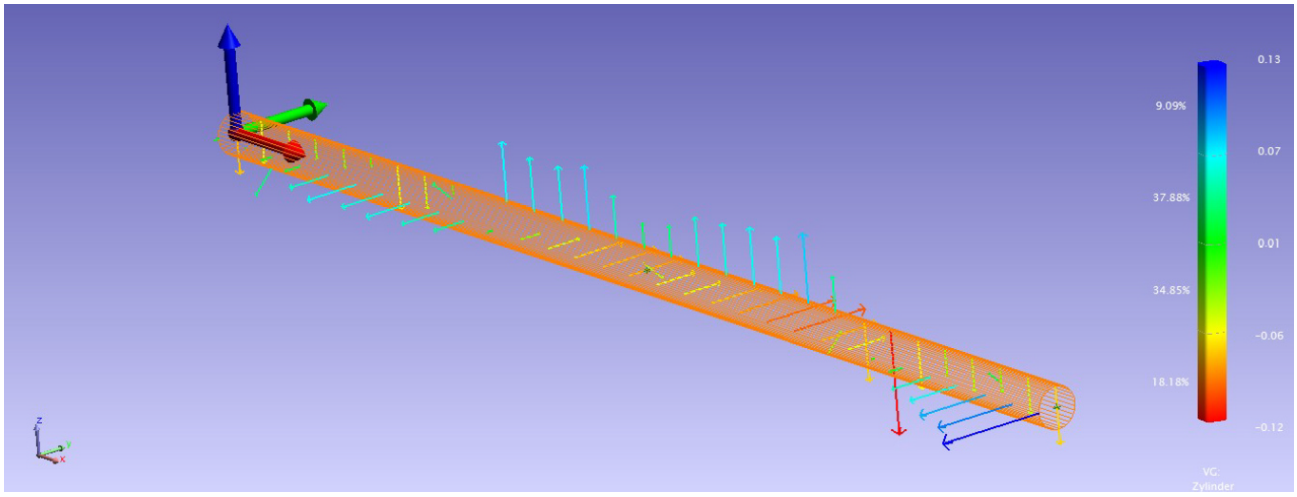

Figure 4.20: Spatial Analyzer 3D result view of the straightness.

Vacuum leaks inside the structure were checked using a helium leak detector (Fig 4.21). A leak test with a sensitivity lower than 10^{-10} mbar l/s was carried out after the final brazing and repeated after a bake-out at 150°C for 48 h.

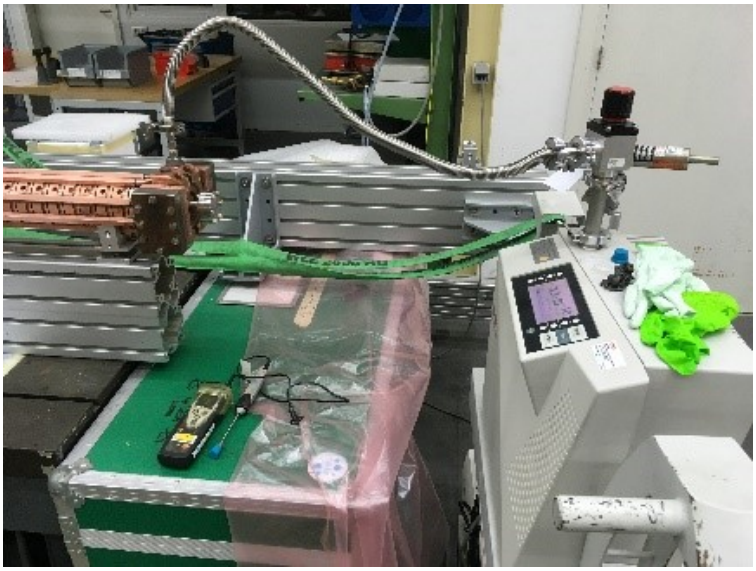

Figure 4.21: Leak test setup.

This bake-out was performed with a hot water baking unit (PT100 on copper) just to speed up the outgassing of the surfaces in order to reach the desired pressure more rapidly. A residual gas analysis (RGA) was also performed afterwards and the residual gas analyser scan results are given in Fig 4.22. From the plot, it is quite easy to note that there is a weak peak at the mass of water ($< 10^{-10}$ mbar). This was due to careful dry nitrogen venting and flushing during all phases of installation.

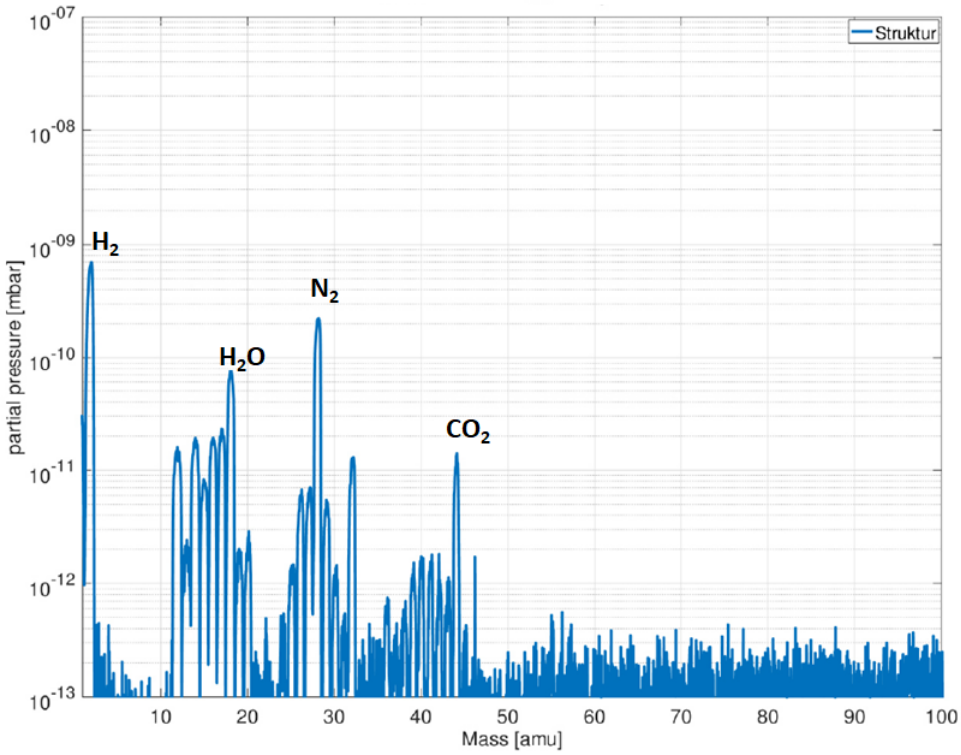

Figure 4.22: Residual gas analysis after bake-out up to mass 100 amu.

4.4 Low power RF tests and tuning

The structure is finely designed and realised. Nonetheless, the technology used to produce the pieces of a traveling wave structure provides limited precision in producing cells. Moreover, during the brazing process, the structure is subjected to high thermal stresses that can lead to further modifications in the inner dimensions of the cells which have to be compensated or corrected. Since the resonant frequencies of the cells depend on their geometrical parameters, errors in their dimensions introduce various effects that degrade the performance of the whole structure. Therefore, in general, a tuning procedure is necessary to ensure the right phase advance between adjacent cells, and to minimise reflection from the detuned cells. This makes it possible to avoid a standing wave in the structure, which give rise to local field and may limit the overall accelerating gradient. To ensure the correct phase and amplitude tuning of the final structure the frequency of each cell is measured before final brazing. A special test set-up was built up at RI GmbH for the measurement of the

0-mode and π-mode frequencies of each regular cell. This allows to calculate the 2π/3 mode frequency of the individual cells. Both the input and output RF couplers were machined to their simulated design topology and the matching was measured using the Kyhl method [84] before brazing of the whole structure. We measured the phases (angles) on the Smith Chart at the frequencies of the π/2 mode, the 2π/3 mode (operating mode) and the measurement frequency f_{mean} which is the arithmetic mean of $f_{\pi/2}$ and $f_{2\pi/3}$.The measured phase differences between the measurement frequency and the frequency of the π/2 mode and between the measurement frequency and the frequency of 2π/3 mode (operating mode) are reported in Table 4.4. Both phase differences are close to $\pm 60^{\circ}$ for input and output couplers, which means that the couplers are tuned and matched. Since the couplers are symmetric, a recombination of S-parameters is applied during the measurement.

Table 4.4: Measured phase differences from f_{mean} using the Kyhl technique.

Description	2π/3	π/2
Input coupler	-58.9°	60.4°
Output coupler	-61.1°	61.3°

To tune the whole TW structure after brazing, an automatic measurement system was developed by RI Research instrument GmbH. This system integrates the use of the" bead-pull" measurement, based on the non-resonant perturbation technique developed by Steele [85]. In this way, a complete tuning procedure was successfully applied to the S-band traveling wave structure. The experimental measurements and the achieved results are illustrated and discussed.

Tuning of the final brazed S-band TW structure

Bead pull measurement

The bead pull technique, based on the non-resonant perturbation theory was applied for measuring and tuning the field of the S-band accelerating structure, as shown in Fig 4.23. The method is capable of making non-contacting measurements of RF amplitude and phase, real time mismatch

feedback and RF tuning, so that this method can produce a better- performing linac accelerating structure than the conventional plunger-drift method.

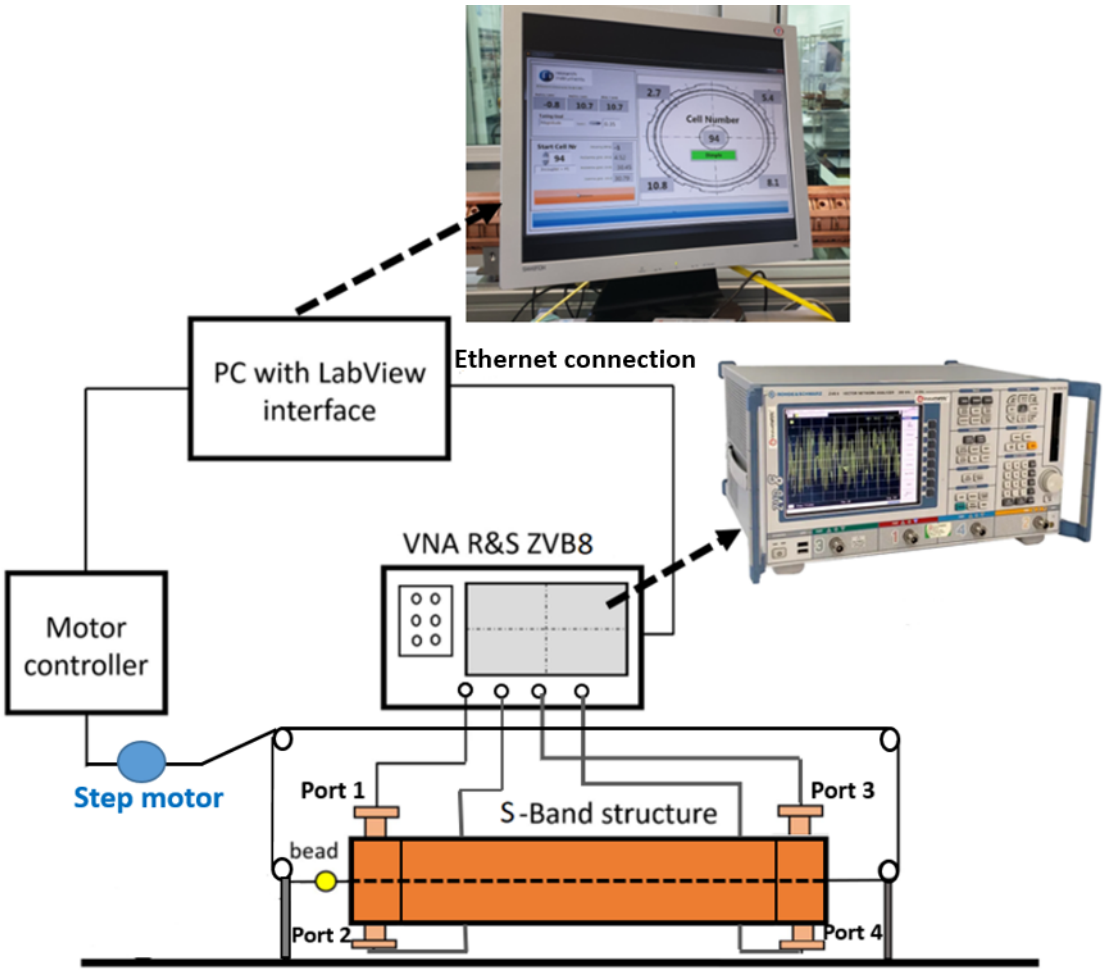

Figure 4.23: Schematic diagram of the RI bead-pull measurement set-up.

For an accelerating structure, the TM mode is used for beam acceleration and the crucial longitudinal electrical field E_z is the field component on axis (on the axis the magnetic field is zero). In the bead–pull technique, a small object is inserted on the beam axis of the travelling wave structure. It interacts with the stored electromagnetic field, which results in a modification of the reflection coefficient measured at the input of the structure. E_z field measurement can be deduced from Eq.4.8 using the reflection coefficient at the input structure measured by means of the vector network analyser (VNA).

$$2P_{in}(\Gamma_p - \Gamma_u) = -j\omega k_{steel} E_z^2 \tag{4.8}$$

where P_{in} is the input power entering the electromagnetic structure, Γ_p and Γ_u are the perturbed and

unperturbed reflection coefficients respectively, k_{steele} is a constant (which depends on the bead electric parameters and geometry), E_z is the electric field at the bead position and ω is the angular frequency. With this method it is possible to measure the electric field amplitude and phase at a given frequency in the perturbing bead position by measuring the complex variation of the reflection coefficient with and without the perturbing object. The perturbing object is a pierced cylindrical needle 0.8 mm in diameter and 4 mm in length, pasted on a nylon line 0.25 mm in diameter, oriented parallel to the axis of the structure. The bead can be moved along this axis using a step motor controlled by Labview. The set-up was tested at different bead velocities along the axis in order to avoid wobbling during the measurement and to check the accuracy of the system. Before starting the field measurement required to tune the structure, the measurement frequency $f_{RF\,meas}$ of the structure in the ambient conditions of temperature T_{amb} and pressure and humidity of the laboratory was calculated using the following formula [86]:

$$f_{meas} = \frac{f_{oper}}{(1 + 1.7 \times 10^{-5}(T_{amb} - T_{oper}))\sqrt{\varepsilon}} \tag{4.9}$$

where f_{oper}=2998.55 MHz is the operation frequency in vacuum of the structure at the operating temperature T_{oper}= 30°C, T_{amb} is the temperature of the structure during the measurement and ε is the relative dielectric constant. The tuning of the structure was performed at RI Research Instruments in Bergisch Gladbach (Fig 4.24). During the measurements, the structure was temperature stabilised by an external cooling unit of the "LAUDA T2200" type. The inside of the accelerating structure was flooded with dry nitrogen (N_2). The RF measurements were performed using a Rhode & Schwarz ZVB8 four port vector network analyser. Since the couplers are symmetric a recombination of S-parameters was applied during the measurement. During the tuning, the temperature of the structure was monitored and the operating frequency was converted to the given ambient conditions using the previous formula as illustrated in Table 4.5.

Table 4.5: Parameters of the ambient conditions during the tuning phase.

Operating temperature	30°C
Operating frequency (in vacuum)	2998.55 MHz
Ambient temperature	30°C
Structure temperature	30°C
Flow of N_2	5 l/min
Humidity	0%
Pressure	991.2 mbar
Relative dielectric constant of N_2	1.00056
Measurement frequency (in N_2)	2997.71 MHz

The tuning of a TW constant gradient accelerating structure consists in introducing a deformation on the cavity wall in order to correct the cell-to-cell phase advance, obtain a good E_z field amplitude flatness and minimise the input reflection coefficient. In the RI structure, this deformation is obtained by applying a force on the outer wall of a cell in order to decrease its internal volume. Each cell has four tuning holes arranged symmetrically around it, see Fig 4.24, with a diameter of 10 mm and a thickness from the internal walls of 1 mm allowing for an easy deformation-tuning using a special tool. This procedure is iterative, groups of several cells were tuned together for each iteration to verify the effects of the applied deformations. The procedure was started from the last cell near the output coupler and proceeded backwards up to the input coupler. We tuned the structure in order to obtain a phase advance per cell equal to 120±2.5°C, cell-to-cell E_z amplitude variation of less than 10% and an input reflection coefficient amplitude lower than -30 dB.

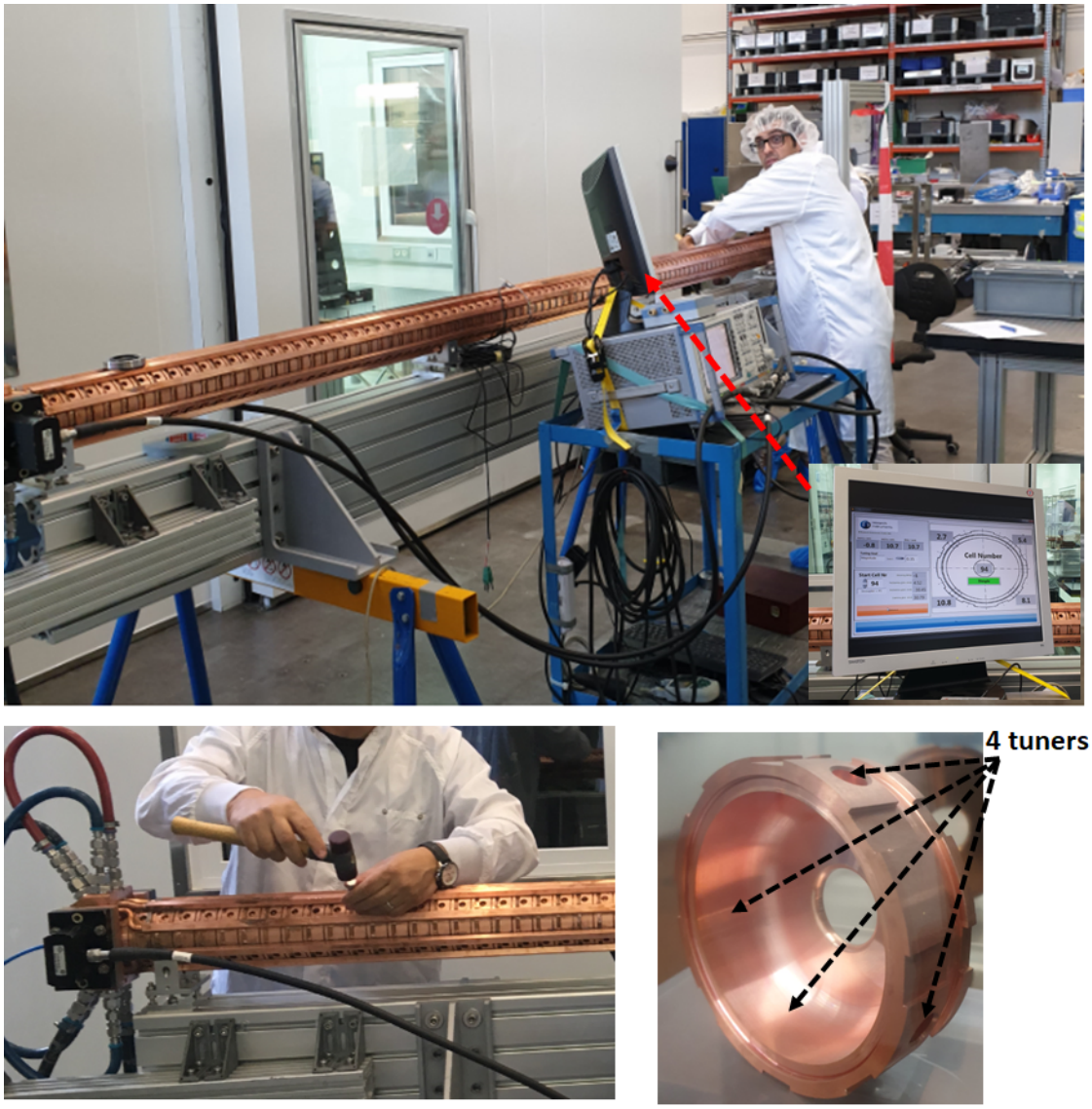

Figure 4.24: Pictures of the bead-pull measurement set-up used at RI.

Results and discussion

Before tuning, the S-band accelerating structure was significantly mismatched, as can be seen in the field measurement results in the figures below. After a long tuning process lasting one week (123 iterations), the structure was successfully tuned. The electric field profile inside the structure was reconstructed from the bead-pull measurement and it is shown in Fig 4.25 (upper plot) before and (lower plot) after tuning. Post processing results in Fig 4.25 (upper plot) show that several cells are strongly mismatched, which results in large reflections, giving a significant standing wave component to the field distribution “unflatness”. Comparing the upper and lower plots, one can see

the improvement in electric field magnitude with good flatness after tuning.

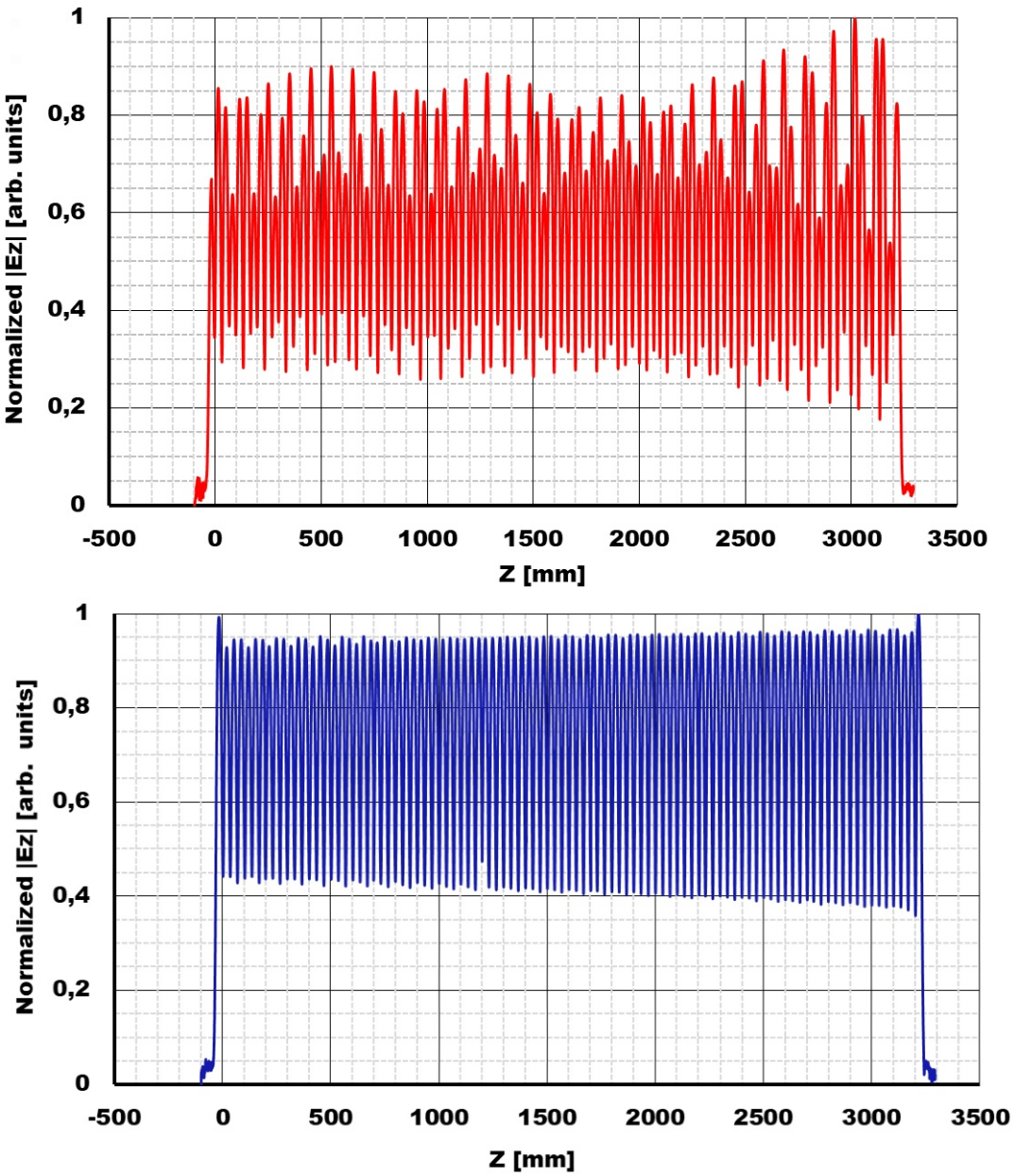

Figure 4.25: Normalised electric E_z field amplitude on the axis (upper plot) before and after (lower plot) tuning.

The cell-to-cell E_z amplitude variation goes from 60% to less than 4% for regular cells (< 6.5% including input and output couplers), which is under the specification limit of 10%, as shown in Fig 4.26.

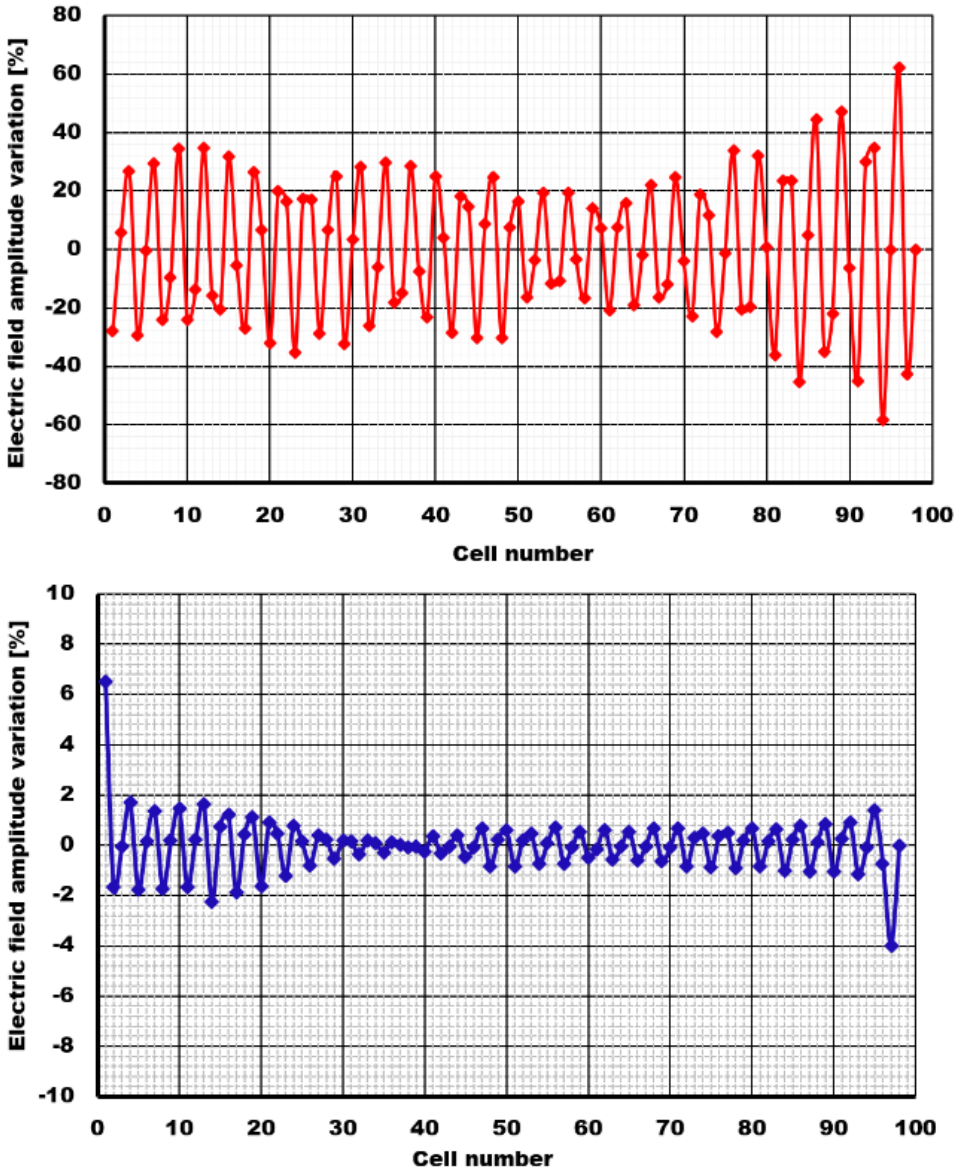

Figure 4.26: Cell-to-cell E_z field amplitude variation versus cell numbers (upper plot) before and (lower plot) after tuning.

In Fig 4.27, the phase advance per cell along the structure is represented. The phase advance per cell changed from more than $\pm$ 30° before tuning to less than $\pm$ 2.5° and 3.3° including output coupler to cell number 97 after tuning.

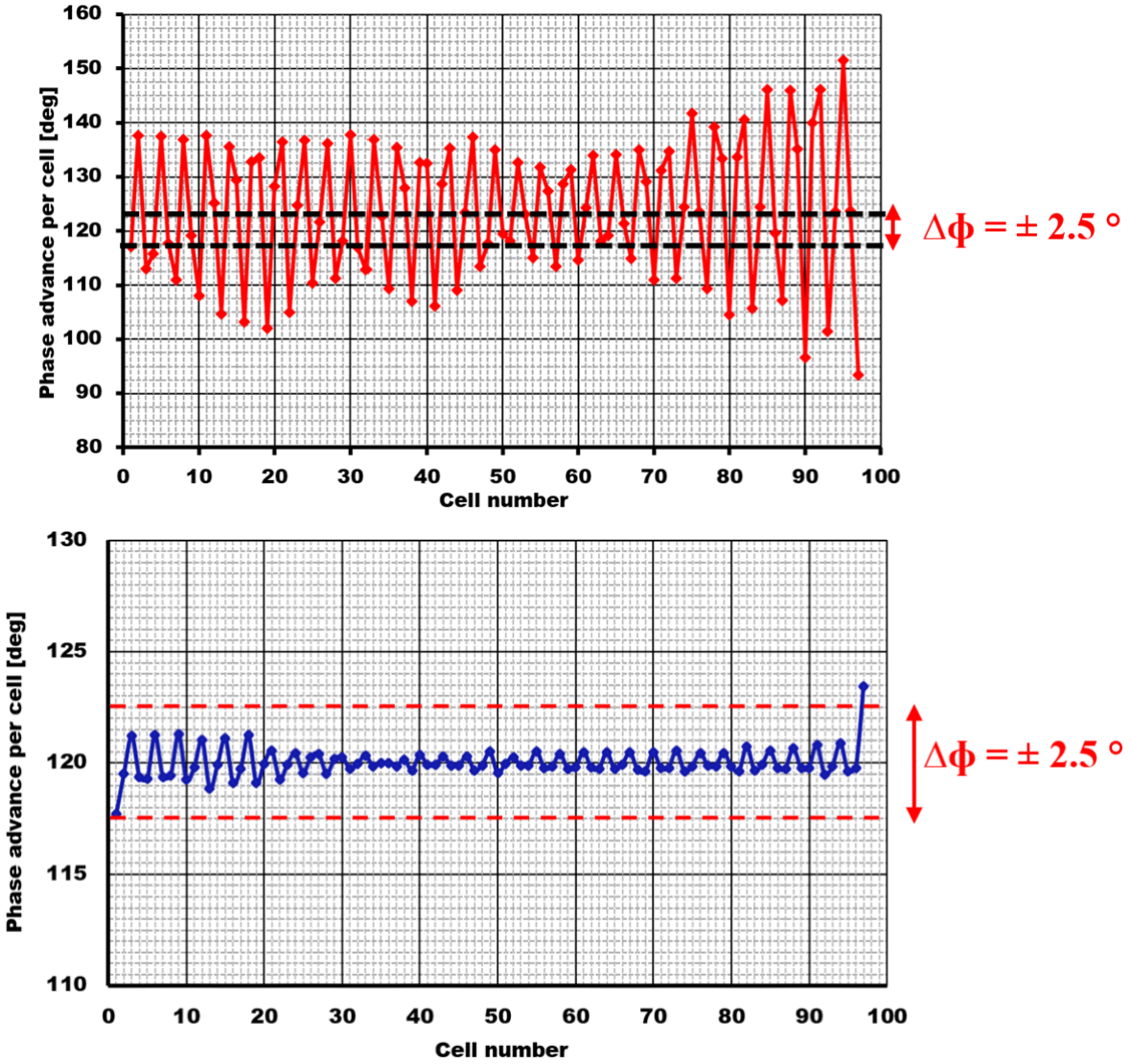

Figure 4.27: Measured phase advance per cell (upper plot) before and (lower plot) after tuning.

Fig 4.28 reports the plot of the real part of the input reflection coefficient Re (S_{11}) vs its imaginary part Im (S_{11}). The structure detuning is highlighted by the RF phase diagram in Fig 4.28 (upper plot) where the three "petals" are not superimposed (the Smith Chart plot corresponds to the measured quantity of Eq.4.8 proportional to E_z^2). It corresponds to a difference in the phase advance per cell (Fig 4.27 (upper plot) and to the E_z field unflatness Fig 4.25 (upper plot)). The superimposition of the three petals which present an angle of $2\pi/3$ between them is an indication of the structure tuning, as shown in Fig 4.28 (lower plot).

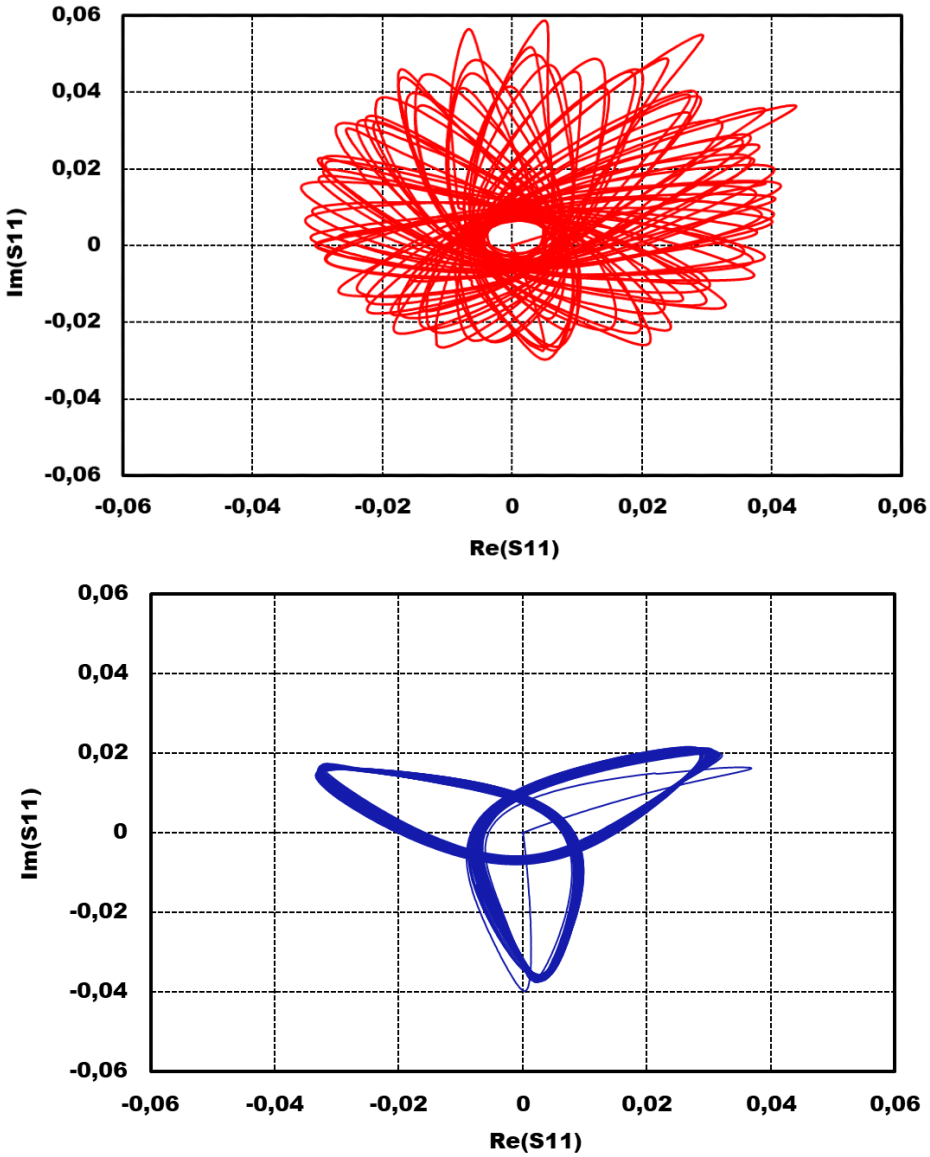

Figure 4.28: Plot of the Re(S_{11}) vs Im(S_{11}) of the structure (upper plot) before and (lower plot) after tuning.

At the end of the tuning procedure, the wire was removed and the scattering parameters of the structure were measured again. The input reflection coefficient is reported in Fig 4.29. At the working frequency, the measured input reflection coefficient moved from -15 dB (before tuning) to -40 dB (after tuning), which is lower than the specified value -30 dB.

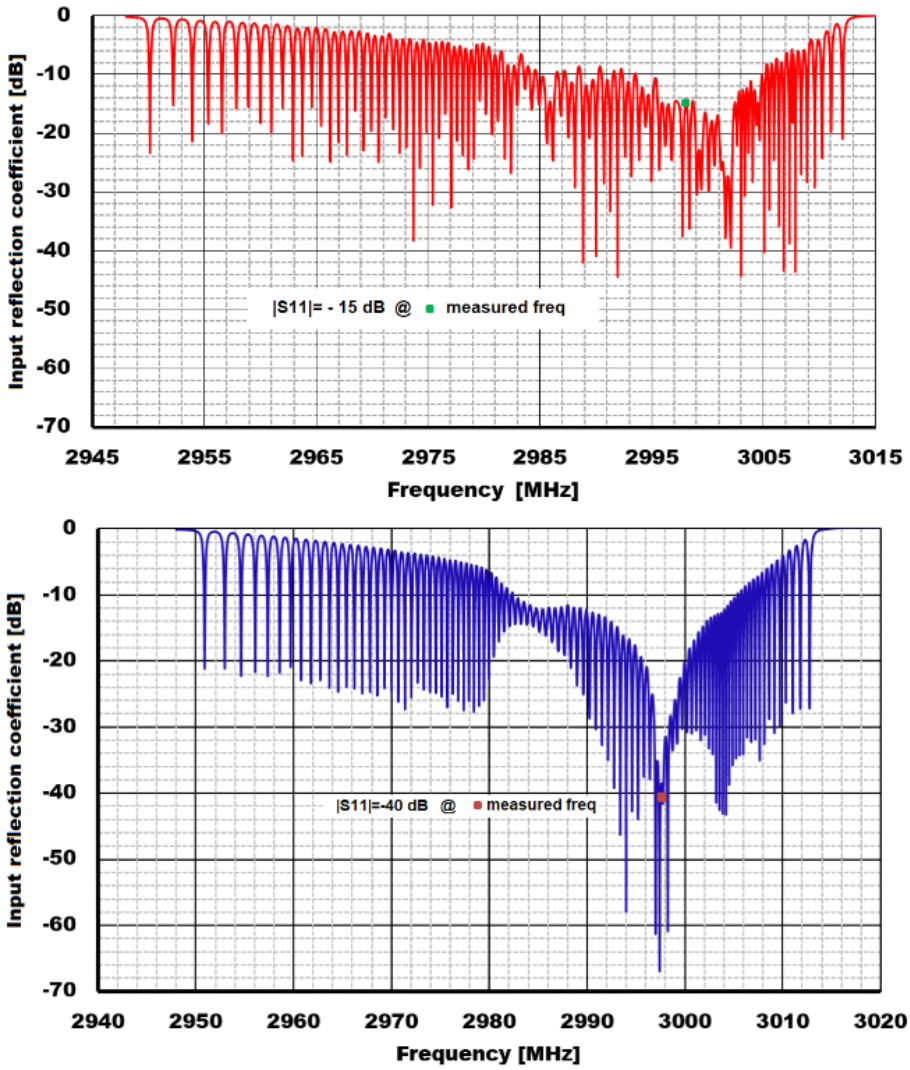

Figure 4.29: Measured input reflection coefficient (upper plot) before and (lower plot) after tuning.

The accelerating structure was finally assembled on its girder together with a cooling water manifold and the RF power splitter used to feed the two ports of the fully symmetric power input coupler. The RF characteristics of the power splitter developed by Spinner GmbH [87] are shown in Table 4.6. The final matching of the assembly of the cavity onto the girder together with the power splitter is given in Fig 4.30. The input reflection coefficient at the operating frequency is -39.8 dB, which means that the matching of the input coupler is very good.

Table 4.6: RF characteristics of the power splitter.

Frequency range	2998.5 ±10 MHz
Peak power capability	40 MW
VSWR max.	1.05
Average power (max)	9 kW
Collinear amplitude unbalance max.	0.07 dB
Collinear phase unbalance max.	1°
Isolation pumping ports min.	60 dB

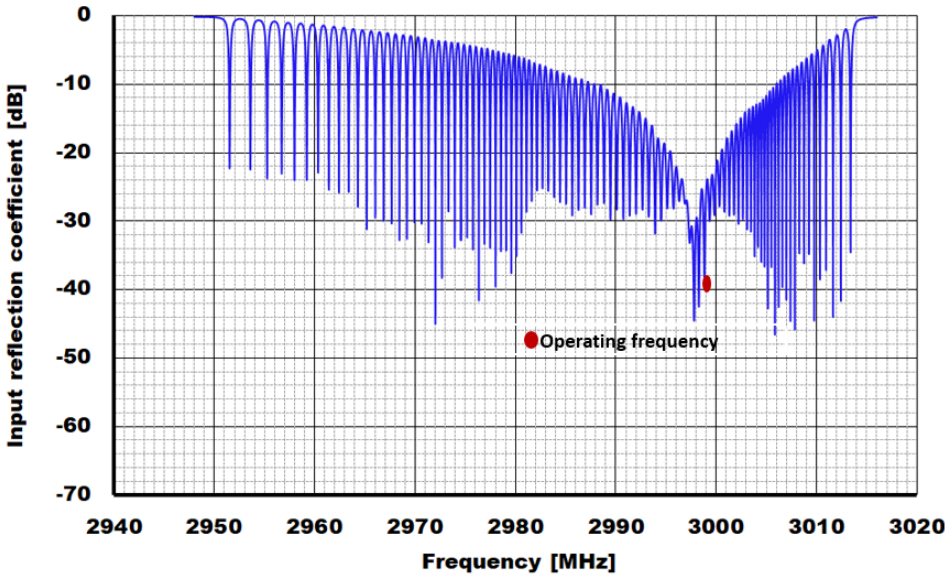

Figure 4.30: Measured input reflection coefficient with power splitter assembly.

The RF tests of the accelerating structure carried out at RI confirmed the validity of the technical specifications made by IJCLab. Table 4.7 summarises some crucial parameters which were simulated and measured, and then checked against the technical specifications.

Table 4.7: Specifications and results of RF testing and simulation for the whole accelerating structure.

Parameter	Specification	Simulation	Measurement
f_{oper} @ 30° C, vacuum	2998.55 MHz	2998.55 MHz	2998.55 MHz
$\lvert S_{11} \rvert$ @ f_{oper}	≤-30 dB	-40.8 dB	-39.8 dB
$\lvert S_{11} \rvert$ @ f_{oper}±1 MHz	≤ -20 dB	-28 dB	-25 dB
Phase advance per cell deviation	≤ 2.5°	≤ 1.5° (2.5° in/out coupler)	≤ 1.5° (2.5° in coupler, 3.3° out coupler to cell 97)
Cell-to-cell E_z ampl. variation	≤ 10 %	≤ 4%	≤ 2.5 % (6.5 % in/out coupler)

Table 4.7 clearly shows the excellent agreement between the measurements and the simulations of the TW accelerating structure and the technical specifications. The high power test of this structure

will be done once the LIL structure is returned to the French National Synchrotron Facility (SOLEIL).

Conclusion

This thesis is devoted to the study of the S-band linac for the ThomX machine in terms of RF characteristics and beam dynamics.

In Chapter 1, I briefly described the physics of Inverse Compton Scattering and the collision kinematics between photons and electrons. In addition, I provided an overview of both photon flux and brightness. The two main schemes of the Inverse Compton sources were briefly discussed, showing the advantages and disadvantages of each scheme. In this chapter, I also included a description of the ThomX machine, its layout, and possible applications.

Chapter 2 demonstrated in detail the power source, power network and the ThomX linac. The ThomX high power source (klystron and modulator) test was carried out in a factory and on the ThomX site in order to verify its reliability and its conformity with the ThomX requirements. These tests were successfully conducted in the ScandiNova factory in Uppsala, Sweden [30] and on the ThomX site after installation [31]. In terms of the power network, the power divider was tested to ensure the transmission of 33% (S_{31}=-4.79 dB) of the input power to the RF gun and 67 % (S_{21}=-1.79 dB) to the TW accelerating section. This power divider shows good performances and characteristics: high isolation and high directivity, low insertion loss and good matching. In addition, the ThomX attenuator has a very low insertion loss of less than 0.02 dB at the starting phase (zero position) and it has a very high range of attenuation of more than 30 dB at 2998.5 MHz. The maximum VSWR recorded was 1.05:1, perfectly within the specification limit of 1.10:1, and the best working area was in the step motor position range 0-1350. Moreover, the 4-port ferrite circulator showed good performances and characteristics: high isolation, low insertion loss, and good matching. Furthermore, the CST simulation of the electric field profile in the RF gun was studied.

The result showed that the excited electric field in the cavity has a phase advance per cell of exactly 180°(π) and a good field balance, “field flatness”, with a maximum value of 80 MV/m, unloaded energy of 5 MeV and a heating pulse ΔT_{max} of below 46 °C for an RF pulse of 3 μs at 6 MW input power. In addition, the simulation of main parameters for the LIL accelerating structure were performed : the average unloaded quality factor Q is 15080, an average shunt impedance of 70 MΩ/m, the group velocity v_g/c decreased from 0.023 to 0.005, the filling time was 1.35 μs, the average accelerating gradient $< E_{acc} >$ seen by electrons was 10.5 MV/m with an unloaded energy gain of 46 MeV at 9 MW and the dissipated power at the end load was only 20% of the input power. Considering an energy of around 5 MeV provided by the RF gun, the energy gain of the accelerating section is around 46 MeV, with an input power of 9 MW. This should be enough to accomplish the final goal of 50 MeV for the commissioning phase of the ThomX linac. Moreover, cooling system characteristics of the RF gun and the LIL accelerating section were simulated and performed using ANSYS. Furthermore, the high power RF conditioning of the ThomX linac (the RF gun and the LIL structure) were successfully carried out and performed.

Chapter 3 showed the commissioning of the ThomX linac in terms of the RF conditioning and the first beam commissioning. The conditioning of the LIL structure was successfully completed in two days, whereas the RF gun was about two weeks. Moreover, the measurement of electron charges as a function of the RF phase, the so-called "phase-scan", was presented to characterise the electric field interaction with the photocathode, thus enhancing the charge extraction phenomenon. The "relative phase between the laser and the gun" ranging between -15° to 145°, was scanned. The scan showed that the maximum electron charge, just above 100 pC, was measured at 90° due to the maximum applied electric field on the cathode, enhancing the photo-emission process. At around 105°, the charge slope was very abrupt where the electron charge was significantly lowered by up to 80%. This high drop showed that the beam performances are very sensitive to the RF phase. Another observation when the RF phase becomes closer to 100°, is that only half of the emitted electrons were accelerated (≈ 60 pC). Operating at the RF phase below 105° not only increased the dependency of the charge-phase, but also provided a direct measurement of the relative phase stability between the laser and the photoinjector. Furthermore, as the E-field increases, the work

function consequently decreases. For example; when E_z was maximum MV/m, the energy barrier of the copper photocathode was reduced by around 0.3 eV to become 4.27 eV allowing to collect up to 105 pC. This demonstrated the "good" performance of the copper photocathode for the phase (1) of ThomX commissioning. For the final phase of ThomX operation, it is proposed to use a magnesium photo-cathode which has a lower work function (3.6 eV) than copper in order to achieve an electron charge of 1 nC. Finally, I presented the measurements of the electron kinetic energy after the standing wave photoinjector and the travelling wave LIL structure, using the steerer-YAG method, as well as compared the results with the analytical models. The energies showed a good fitting with the models, ensuring that ThomX linac is able to deliver a beam of energy 50 MeV during the commissioning phase (1). The chapter also illustrated an experimental work carried out at the PHIL facility as a training stage before involving in the ThomX commissioning of linac. The PHIL energy measurements were performed using the dipole magnet which is similar to the case of the energy measurement of ThomX linac proposed for phase (2).

Chapter 4 focused on the electromagnetic simulations and analyses, manufacturing and low power tests of the dual feed TW linac components which will be installed for energy upgrade of more than (50 MeV). From the CST MWS, a good transmission of the RF power into the structure is indicated by the simulated results of reflection coefficient $|S_{11}|$, which is -40 dB with a transmission coefficient $|S_{21}|$ of around -5.2 dB for the accelerating mode $TM_{010-2\pi/3}$ at 2.9985 GHz in vacuum at 30 °C. Moreover, the simulated profile of the longitudinal electric field on axis along the structure for an input power of 40 MW presented a perfect constant flatness of the electric field on axis along the structure. In addition, the cell-to-cell axial electric field amplitude variation along the structure was calculated and the overall observation was $\leq 4\%$. The simulated average phase advance per cell of the axial electric field was 120°. In addition, for an input RF power of 40 MW, the simulated maximum surface electric field was around 46 MV/m, just below the Kilpatrick limit and the simulated maximum modified Poynting vector was S_{cmax}=0.32 MW/mm^2, far below the re-scaled threshold of 1.6 MW/mm^2. The maximum surface magnetic field $|H_s|$ obtained for an input power of 40 MW and an RF flat top pulse length of t_p=3 μs was 1.45 A/m with ΔT of less than 10 °C at P_{in}=40 MW, which is far below the safe limit. Furthermore, at an input power of 40 MW, the

unloaded energy gain was > 70 MeV for an effective accelerating gradient of 24 MV/m. Finally, this chapter performed the manufacturing and tuning of the structure, coupler and power splitter. The results were well within agreement with the technical specifications and the simulations.

Synthèse en français

De nos jours, il existe une forte demande de sources de rayons X lumineux, réglables et monochromatiques pour des applications en médecine, dans l'industrie, dans la science des matériaux et dans le patrimoine culturel. Les sources les plus performantes en termes de luminosité et de compatibilité sont les installations de rayonnement synchrotron, mais leur utilisation et leur diffusion à grande échelle sont soumises à de fortes contraintes en raison de leurs dimensions importantes, du coût de leur construction et de leur exploitation, ainsi qu'à la disponibilité et l'accès aux lignes de faisceaux. Néanmoins, les machines compactes de diffusion Compton sont capables de fournir un faisceau de rayons X quasi-monochromatique dans une salle expérimentale plus avantageuse en termes de taille et de coûts, inférieurs à ceux des synchrotrons. Dans ces machines, des paquets d'électrons interagissent avec des impulsions laser produisant un flux élevé de rayons X par diffusion Compton inverse (ICS), ce phénomène apparait lorsqu'une grande partie de l'énergie des électrons est transférée aux photons. Ces machines peuvent produire des rayons X avec une énergie électronique relativement faible par rapport aux machines synchrotron. Elles sont également compactes et peuvent être installées dans des environnements diverses tels que des hôpitaux, des laboratoires ou des musées. Grâce aux développements récents des systèmes laser et optiques, ces machines peuvent désormais fournir des flux de rayons X élevés et, par conséquent, des luminosités élevées. Actuellement, il existe différentes sources de rayons X par diffusion Compton , d'autres sont en cours de construction, nous avons cité quelques exemples, comme le Compact Light Source (CLS) de Munich, qui fournit quotidiennement aux utilisateurs des faisceaux de rayons X avec un flux de photons d'environ 10^{10}-10^{11} ph/s et une énergie de rayons X comprise entre 15 keV-35 keV. Il existe aussi la source de rayons X Tsinghua Thomson (TTX) produit des rayons X de 50 keV avec

un flux de 10^7 ph/s. Parmi les sources en cours de construction, nous citons le projet STAR (Southern European Thomson source for Applied Research) est en cours de construction pour produire un flux de rayons X d'environ 10^9 ph/s à des énergies de 20 à 140 keV. Alors que pour des énergies plus élevées,allant de 0,2 à 20 MeV, le projet Extreme-Light-Infrastructure Nuclear-Physics Gamma-Beam-Source produit des faisceaux de rayons X avec un flux de photons de 10^8 ph/s. Il existe également des machines qui fonctionnent dans des gammes d'énergie supérieurs, comme le projet SPARC en Italie (de 20 keV à 500 keV) avec un flux de rayons X de 10^{10} ph/s, NESTOR en Ukraine (de 10 keV à 900 keV) avec un flux de rayons X de 10^{13} ph/s. Toutes ces machines présentent des conceptions différentes avec un accélérateur linéaire (linac) ou un anneau de stockage pour le faisceau d'électrons, une cavité à tir unique, une cavité optique à passages multiples ou une cavité Fabry-Perot pour le faisceau laser. Il est difficile de citer toutes les sources basées sur la diffusion Compton, nous proposons donc au lecteur de consulter la liste non exhaustive des différentes machines Compton, de leurs conceptions et de leurs performances disponible dans les références suivantes. Le projet ThomX fait partie des sources à rayons X par diffusion Compton construitent récemment au Laboratoire Irène Joliot-Curie (IJCLab) sur le campus d'Orsay de l'Université Paris-Saclay. ThomX est conçu pour produire un flux total de rayons X de 10^13 ph/s et une luminosité de 10^{11} ph/s/mm^2/mrad^2.0,1% de bande passante avec une gamme d'énergie ajustable (45 keV à 90 keV). Pour atteindre ces performances, les paquets d'électrons et les impulsions laser sont empilés respectivement dans un anneau de stockage et dans une cavité Fabry-Pérot à haut gain. La mise en service du linac ThomX est en cours depuis juillet 2021. Cette thèse est consacrée à l'étude des caractéristiques RF et de la dynamique faisceau du linac en bande S de la machine ThomX. Dans le chapitre 1, j'ai brièvement décrit la physique de la diffusion Compton inverse et la cinématique des collisions entre photons et électrons. En outre, j'ai donné un aperçu du flux de photons et de la luminosité. Les deux principaux schémas des sources Compton inversées ont été brièvement discutés, en montrant les avantages et les inconvénients de chaque schéma. Dans ce chapitre, j'ai également inclus une description de la machine ThomX, de sa disposition et de ses applications possibles. Dans le chapitre 2, j'ai décrit en détail la source d'énergie, le réseau électrique et le linac ThomX. Le test de la source RF de haute puissance

(klystron et modulateur) a été effectué en usine et sur le site ThomX afin de vérifier sa fiabilité et sa conformité aux exigences ThomX. Ces tests ont été réalisés en deux temps, avec une première partie réalisée au sein de l'usine ScandiNova à Uppsala, en Suède et la seconde partie accomplie sur le site ThomX après installation de la machine. Le diviseur de puissance RF nécessaire à la répartition de la puissance entre la canon et la section accélératrice a été testé. 33% (S_{31}=-4,79 dB) de la puissance d'entrée est transmise au canon RF et 67 % (S_{21}=-1,79 dB) est transmise à la section d'accélération TW. Ce diviseur de puissance présente les performances et les caractéristiques suivantes : isolation élevée et directionnelle élevée, faible perte d'insertion et bonne adaptation. De plus, l'atténuateur ThomX a une très faible perte d'insertion de moins de 0,02 dB à la phase de départ (position zéro) et il a une très grande plage d'atténuation de plus de 30 dB à 2998,5 MHz. Le ROS maximal enregistré est de 1,05:1, parfaitement dans la limite de la spécification de 1,10:1, et la meilleure zone de travail se trouve dans la plage de position du moteur pas à pas 0-1350. De plus, le circulateur à 4 ports en ferrite a montré de bonnes performances : isolation élevée, faible perte d'insertion et bonne adaptation. En outre, la simulation CST du profil du champ électrique dans le canon RF a été étudiée. Les résultats ont montré que le champ électrique présent dans la cavité possède une avance de phase par cellule d'exactement 180°. Ce champ électrique possède également un bon équilibre "planéité du champ" et sa valeur maximale est de 80 MV/m, son énergie non chargée est de 5 MeV avec une impulsion de chauffage Δ Tmax inférieure à 46°C pour une impulsion RF égale à 3 μs lorsque la puissance d'entrée est égale à 6 MW. D'autre part, des simulations sur les principaux paramètres de la structure accélératrice LIL ont été réalisées. Cela nous a permis d'obtenir les résultats suivants : le facteur de qualité Q moyen à vide est de 15080, l'impédance de shunt moyenne est de 70 MΩ/m, la variation de vitesse de groupe vg/c est comprise entre 0,023 et 0. 005, le temps de remplissage est de 1,35 μs, le gradient d'accélération moyen Eacc vu par les électrons est de 10,5 MV/m avec un gain d'énergie à vide de 46 MeV à 9 MW et la puissance dissipée dans la charge finale est seulement de 20% de la puissance d'entrée. En considérant une énergie d'environ 5 MeV fournie par le canon RF, le gain d'énergie de la section d'accélération est d'environ 46 MeV, avec une puissance d'entrée de 9 MW. Cela devrait être suffisant pour atteindre l'objectif final de 50 MeV pour la phase de mise en service du linac de ThomX. En par ailleurs, les caractéristiques du système

de refroidissement du canon RF et de la section d'accélération du LIL ont été simulées et réalisées à l'aide d'ANSYS. En plus de cela, le conditionnement RF à haute puissance du linac ThomX (le canon RF et la structure LIL) a été réalisé avec succès. Lobjectif final est d'atteindre une énergie avoisinante les 50 MeV lors de la mise en service du Linac ThomX. Pour ce faire, l'énergie fournie pas le canon a été réglée à la valeur de 5MeV et une puissance d'entée égale à 9 MW. Le gain de la section d'accélération étant de d'environ 46 MeV, cela a été suffisant pour atteindre la valeur de l'énergie attendue proche des 50 MeV. Ces valeurs d'énergies très élevées nécessitent une machine équipée d'un système de refroidissement performant, nous avons donc réalisés des simulations sur les caractéristiques du système de refroidissement du canon RF et de la section d'accélération LIL à l'aide du logiciel ANSYS. Cette étude a donc contribué à la réussite du conditionnement de la partie haute puissance RF du Linac ThomX. Le chapitre 3 présente la mise en service du linac ThomX et particulièrement le conditionnement du champ RF et la génération du premier faisceau. Le conditionnement de la structure LIL a été réalisé avec succès en deux jours, alors que le canon RF a nécessité environ deux semaines. Par ailleurs, la mesure des charges des électrons en fonction de la phase RF, dite "phase-scan", a été étudiée pour caractériser l'interaction du champ électrique avec la photocathode, valorisant ainsi le phénomène d'extraction de charge. L'étude a été réalisée sur une plage de "phase relative entre le laser et le canon", comprise entre -15°et 145°. Le balayage de la phase relative a montré qu'il est possible d'atteindre la quantité de charge électronique maximale avoisinante les 100 pC, lorsque la phase relative est de l'ordre de 90°. En effet, le champ électrique maximal appliqué sur la cathode renforce le processus de photo-émission. Notre étude nous a permis également de mettre en évidence que la charge électronique est considérablement réduite (jusqu'à 80%) aux alentours de la phase relative égale à 105°. Cette forte chute montre que les performances du faisceau sont très sensibles à la phase RF.L'autre observation que nous avons effectuée dans le cadre de cette étude est que lorsque la phase RF se rapproche de 100°, seulement la moitié des électrons émis sont accélérés (a pprox 60 pC). Le fait de fonctionner à une phase RF inférieure à 105°a non seulement augmenté la dépendance de la phase de charge, mais a également fourni une mesure directe de la stabilité de phase relative entre le laser et le photoinjecteur. En effet, lorsque le champ Eaugmente, la fonction de travail diminue en conséquence. Par exemple, lorsque Ez (MV/m)

est au maximum, la barrière d'énergie de la photocathode en cuivre est réduite d'environ 0.3 eV pour atteindre 4.27 eV permettant de collecter jusqu'à 105 pC. Ce résultat a démontré la "bonne" performance de la photocathode en cuivre pour la première phase de la mise en service de l'accélérateur ThomX. Pour la phase finale du fonctionnement de ThomX, il est proposé d'utiliser une photocathode en magnésium qui a une fonction de travail (3,6 eV) plus faible que le cuivre permettant d'atteindre une charge électronique de 1 nC. Enfin, j'ai présenté les mesures de l'énergie cinétique des électrons à la sortie du photoinjecteur (ondes stationnaires) et également à la sortie de la structure LIL (ondes progressives), j'ai utilisé pour cela, la méthode steerer-YAG, et j'ai comparé les résultats avec les modèles analytiques existants. Les résultats obtenus ont montré une bonne adéquation des valeurs mesurées expérimentalement avec les modèles existants, assurant ainsi que le linac ThomX est capable de délivrer un faisceau d'énergie proche des 50 MeV pendant la première phase de mise en service. Le chapitre 3 présente également le travail expérimental effectué lors de l'installation de l'accélérateur PHIL comme une étape de préparation avant de procéder à la mise en service du linac ThomX. Les mesures d'énergie sur PHIL ont été effectuées à l'aide d'un aimant dipôle similaire à celui utilisé dans le cas des mesures d'énergie sur ThomX dans le cadre de la prochaine phase (2). Le chapitre 4 est consacré aux simulations et aux analyses électromagnétiques, à la fabrication et aux tests à faible puissance des composants du linac TW. Le linac a été considéré avec une double alimentation. pour augmenter l'énergie de manière à dépasser les 50 MeV lors de la prochaine phase. Les résultats de simulation sur les MWS CST ont permis de valider une bonne transmission de la puissance RF dans la structure avec un coefficient de réflexion S_{11} de -40 dB et un coefficient de transmission S_{21} d'environ -5,2 dB pour le mode d'accélération TM010-$2\pi/3$ à 2,9985 GHz dans le vide à 30°C. De plus, le profil du champ électrique longitudinal sur l'axe a été simulé le long de la structure en considérant une puissance d'entrée égale à 40 MW. Le champ électrique obtenu présente une parfaite planéité constante sur l'axe le long de la structure. En effet, la variation de l'amplitude du champ électrique axial d'une cellule à l'autre le long de la structure a été calculée et l'observation globale était de 4%. L'avance de phase moyenne simulée par cellule du champ électrique axial était de 120°. En conséquence, pour une puissance RF d'entrée de 40 MW, le champ électrique de surface maximal simulé est d'environ 46 MV/m, juste en dessous de la limite de

Kilpatrick. Le vecteur de Poynting modifié maximal Sc_max et de0,32 MW/mm^2, bien en dessous du seuil ré-échelonné de 1,6 MW/mm^2. Le champ magnétique de surface maximal Hs obtenu pour une longueur d'impulsion RF flat top de tp=3 μs était de 1,45 A/m avec un ΔT de moins de 10lorsque Pin=40 MW.Ces résultas démontrent bien que les conditions de fonctionnement sont inférieur au seuil de sécurité. Enfin, à une puissance d'entrée de 40 MW, le gain d'énergie à vide était de > 70 MeV pour un gradient d'accélération effectif de 24 MV/m. Enfin, le dernier chapitre est a été consacré à la réalisation, la fabrication et aux réglages de la structure, du coupleur et du diviseur de puissance. Les résultats présentés sont en accord avec les spécifications techniques et les simulations.

Appendix A

Appendix

Distribution of the elementary cells along the LIL structure

N° cell	Iris diameter 2a [mm]	N° cell	Iris diameter 2a [mm]	N° cell	Iris diameter 2a [mm]
1 → 13	25	48 → 58	22.375	93 → 103	19.750
14	24.825	59	22.200	104	19.575
15	24.650	60	22.025	105	19.400
16	24.475	61	21.850	106	19.225
17	24.300	63	21.675	107	19.050
18 → 28	24.125	63 → 73	21.500	108 → 118	18.875
29	23.950	74	21.325	119	18.700
30	23.775	75	21.150	120	18.525
31	23.600	76	20.975	121	18.350
32	23.425	77	20.800	122	18.175
33 → 43	23.250	78 → 88	20.625	123 → 135	18
44	23.075	89	20.450		
45	22.900	90	20.275		
46	22.725	91	20.100		
47	22.550	92	19.925		

Figure A.1: Distribution of the elementary cells along the LIL structure.

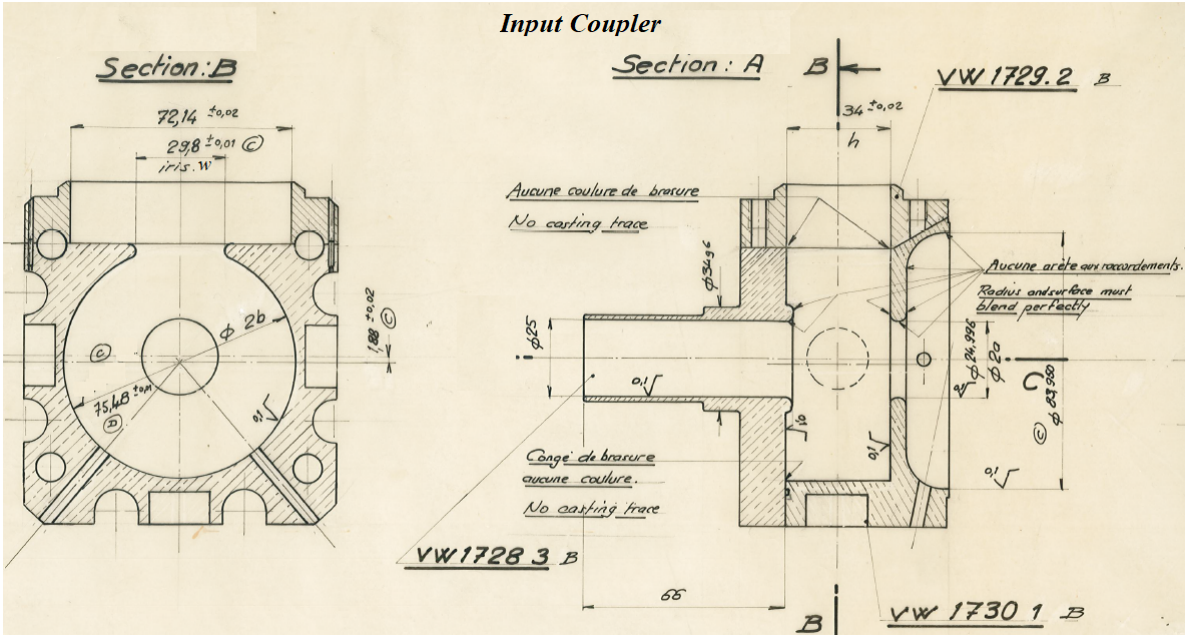

Figure A.2: Section drawings of the LIL input coupler.

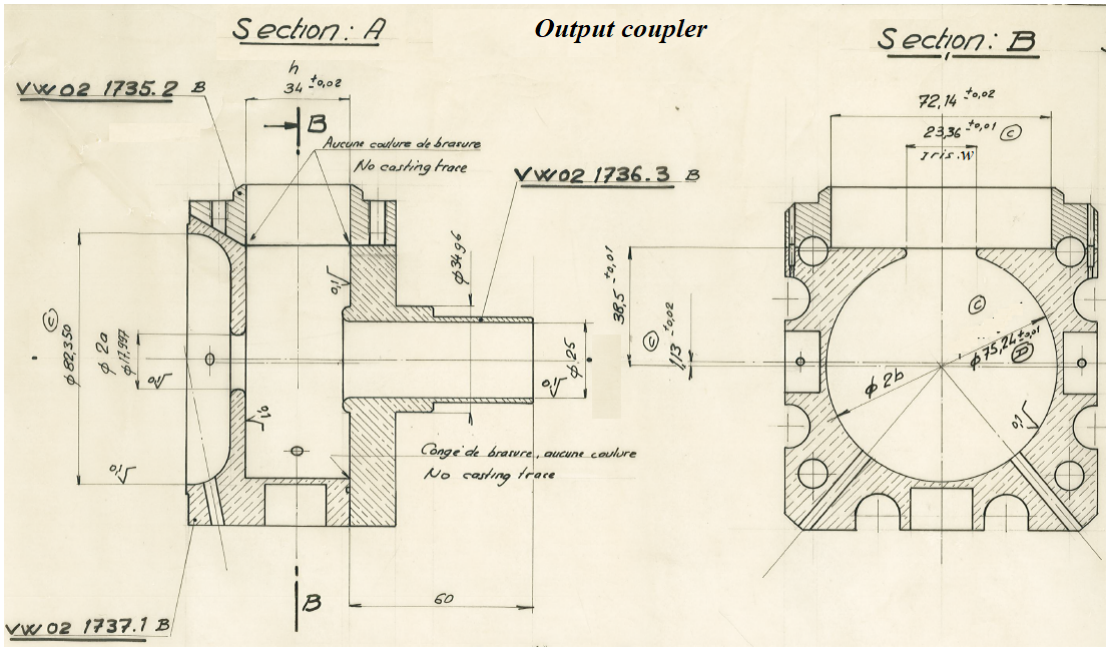

Figure A.3: Section drawings of the LIL output coupler.

Bibliography

[1] M. Jacquet. High intensity compact compton X-ray sources: Challenges and potential of applications. Nuclear Instruments and Methods in Physics Research Section B: Beam Interactions with Materials and Atoms, 331:1–5, 2014.

[2] E. Eggl et al. The munich compact light source: initial performance measures. Journal of synchrotron radiation, 23(5):1137–1142, 2016.

[3] B. Hornberger et al. A compact light source providing high-flux, quasi-monochromatic, tunable x-rays in the laboratory. In Advances in Laboratory-based X-Ray Sources, Optics, and Applications VII, volume 11110, page 1111003. International Society for Optics and Photonics, 2019.

[4] Chi. Zhijun et al. Recent progress of phase-contrast imaging at tsinghua thomson-scattering X-ray source. Nuclear Instruments and Methods in Physics Research Section B: Beam Interactions with Materials and Atoms, 402:364–369, 2017.

[5] F. Luigi el al. Status of compact inverse compton sources in italy: Brixs and star. In Advances in Laboratory-Based X-ray Sources, Optics, and Applications VII, volume 11110, pages 14–21. SPIE, 2019.

[6] O. Adriani et al. Technical design report eurogammas proposal for the eli-np gamma beam system. arXiv preprint arXiv:1407.3669, 2014.

[7] K. Dupraz et al. Design and optimization of a highly efficient optical multipass system for

γ-ray beam production from electron laser beam compton scattering. Physical Review Special Topics-Accelerators and Beams, 17(3):033501, 2014.

[8] K. Cassou et al. Laser beam circulator for the generation of a high brilliance gamma beam at eli-np. In High Intensity Lasers and High Field Phenomena, pages HW4A–7. Optical Society of America, 2018.

[9] V. Androsov et al. The first results of the nestor commissioning. In IPAC 2013: Proceedings of the 4th International Particle Accelerator Conference, pages 225–227, 2013.

[10] C. Vaccarezza et al. The SPARC_LAB Thomson source. Nuclear Instruments and Methods in Physics Research Section A: Accelerators, Spectrometers, Detectors and Associated Equipment, 829:237–242, 2016.

[11] K. Dupraz. Conception et optimisation d'un recirculateur optique pour la source haute brillance de rayons gamma d'ELI-NP. PhD thesis, Paris 11, 2015.

[12] Pierre Favier. Etude et conception d'une cavité Fabry-Perot de haute finesse pour la source compacte de rayons X ThomX. PhD thesis, Université Paris-Saclay (ComUE), 2017.

[13] K. Dupraz et al. The ThomX ICS source. Physics Open, 5:100051, 2020.

[14] L. Garolfi. High-gradient S-band electron linac for ThomX. PhD thesis, Université Paris Sud-Paris XI, 2018.

[15] V. Venugopal and PS. Bhagdikar. De Broglie wavelength and frequency of the scattered electrons in Compton effect. arXiv preprint arXiv:1202.4572, 2012.

[16] P. Eisenberger and PM. Platzman. Compton scattering of X-rays from bound electrons. Physical Review A, 2(2):415, 1970.

[17] J.D. Jackson. Classical electrodynamics, 1999.

[18] M. Jacquet. Potential of compact Compton sources in the medical field. Physica medica, 32(12):1790–1794, 2016.

[19] J. Bonis et al. Non-planar four-mirror optical cavity for high intensity gamma ray flux production by pulsed laser beam Compton scattering off Gev-electrons. Journal of instrumentation, 7(01):P01017, 2012.

[20] A. Variola. The ThomX project. In 2nd International Particle Accelerator Conference (IPAC'11), pages 1903–1905. Joint Accelerator Conferences Website, 2011.

[21] P. Walter et al. A new high quality X-ray source for cultural heritage. Comptes Rendus Physique, 10(7):676–690, 2009.

[22] AS. Gilmour. Klystrons, traveling wave tubes, magnetrons, crossed-field amplifiers, and gyrotrons. Artech House, 2011.

[23] W. Crewson et al. Power modulator. https://patents.google.com/patent/US5905646, May 18, 1999.

[24] RL. Cassel et al. A solid state induction modulator for SLAC NLC. In Proceedings of the 1999 Particle Accelerator Conference (Cat. No. 99CH36366), volume 3, pages 1494–1496. IEEE, 1999.

[25] C. Pappas et al. Power modulators for FERMI's linac klystrons. In 2007 IEEE Particle Accelerator Conference (PAC), pages=2448–2450 . IEEE, 2007.

[26] EG. Cook. Review of solid-state modulators. arXiv preprint physics/0008189, 2000.

[27] MPJ. Gaudreau et al. Solid state modulator applications in linear accelerators. In Proceedings of the 1999 Particle Accelerator Conference (Cat. No. 99CH36366), volume 3, pages 1491–1493. IEEE, 1999.

[28] S-band Klystron E37310 . https://www.toshiba.co.jp/worldwide/.

[29] Scandinova. Scandinova internal documents,(2019), the scandinova modulator, scandinova education v1, 4-5(85).

[30] L. Kanon et al. Klystron Modulator Factory Acceptance Test Report,Document N° 00947, 7/11/2016, ScandiNova, Uppsala, Sweden, 2016.

[31] R. Kalsoon et al. Klystron Modulator Site Acceptance Test Repor, Document N° 002148, 01/09/2017, ThomX site, Orsay, France, 2017.

[32] N. Janvier et al. IcePAP: an advanced motor controller for scientific applications in large user facilities. TUPPC081, ICALEPCS2013, San Francisco, 2016, 2013.

[33] C. Travier. Etude realisation et experimentation d'un canon hyperfrequence declenche par un laser subpicoseconde (candela) . PhD thesis, Université Paris Sud-Paris XI, 1995.

[34] MJ. De Loos et al. Construction of the ALPHA-X Photo-injector Cavity. In Tenth European Particle Accelerator Conference" EPAC'06", pages 1277–1279, 2006.

[35] J. Belloni et al. ELYSE—A picosecond electron accelerator for pulse radiolysis research. Nuclear Instruments and Methods in Physics Research Section A: Accelerators, Spectrometers, Detectors and Associated Equipment, 539(3):527–539, 2005.

[36] R. Bossart et al. A 3 GHz photoelectron gun for high beam intensity. Nuclear Instruments and Methods in Physics Research Section A: Accelerators, Spectrometers, Detectors and Associated Equipment, 375(1-3):ABS7–ABS8, 1996.

[37] R. Roux. CONCEPTION OF PHOTO-INJECTORS FOR THE CTF3. In The Physics and Applications of High Brightness Electron Beams: Proceedings of the 46th Workshop of the INFN ELOISATRON Project: Erice, Italy, 9-14 October 2005, volume 28, page 237. World Scientific, 2007.

[38] J. Brossard et al. Construction of the probe beam photo-injector of CTF3. In 10th European Particle Accelerator Conference" EPAC'06", pages 828–830, 2006.

[39] JE Clendenin. RF photoinjectors. Technical report, SLAC National Accelerator Lab., Menlo Park, CA (United States), 1996.

[40] M. El Khaldi et al. Electromagnetic, Thermal, and Structural Analysis of a ThomX RF Gun Using ANSYS. In Proceedings, 7th International Particle Accelerator Conference (IPAC 2016), THPOW002, 2016.

[41] Ansys. https://www.ansys.com/.

[42] Cst. https://www.3ds.com/products-services/simulia/products/cst-studio-suite/.

[43] M. Alkadi et al. Electromagnetic and beam dynamics studies of the thomx linac. In 12th International Particle Accelerator Conference, page WEPAB054, 2021.

[44] D. Alesini. Power coupling. arXiv preprint arXiv:1112.3201, 2011.

[45] B. Carlsten. New photoelectric injector design for the los alamos national laboratory xuv fel accelerator. Nuclear Instruments and Methods in Physics Research Section A: Accelerators, Spectrometers, Detectors and Associated Equipment, 285(1-2):313–319, 1989.

[46] F. Dupont et al. Status of the LEP e±Injector linacs. 1984.

[47] R. Belbeoch et al. Rapport d'études sur le projet des linacs injecteur de lep (lil). Technical report, Paris 11. Lab. Accél. Linéaire, 1982.

[48] D. Blechschmidt and DJ. Warner. Parameters of the LEP injector linacs. Technical report, 1988.

[49] Peter Forck. Beam Instrumentation and Diagnostics. arXiv preprint arXiv:2009.10411, 2020.

[50] H. Purwar et al. Experimental results for multiphoton nonlinear photo-emission processes on PHIL test line. In IPAC'17, Denmark, pages 1369–1371. JACOW, 2017.

[51] T. Vinatier et al. Performances of the Alpha-X RF gun on the PHIL accelerator at LAL. Nuclear Instruments and Methods in Physics Research Section A: Accelerators, Spectrometers, Detectors and Associated Equipment, 797:222–229, 2015.

[52] Robert Brogle. Studies of linear and nonlinear photo-emission processes in metals and semiconductors. PhD thesis, University of California, 1996.

[53] H. Monard. Les sources d'électrons. Master de Physique Spécialité Accélérateurs de Particules et Interaction avec la Matiére, Université Paris sud, 2012.

[54] T. Vinatier. Influence of laser parameters on the relativistic short electron bunches dynamics in linear accelerators based on RF-guns and development of associated diagnostics. PhD thesis, Université Paris Sud-Paris XI, 2015.

[55] M. Alves et al. PHIL photoinjector test line. Journal of Instrumentation, 8(01):T01001, 2013.

[56] I. Isaev. Stability and performance studies of the PITZ photoelectron gun. PhD thesis, University of Hamburg, 2017.

[57] C. Bruni et al. Experimental results on the PHIL photo-injector test stand at LAL. Proc. LINAC'12, pages 198–200, 2012.

[58] H. Schlarb et al. Beam based measurements of RF phase and amplitude stability at FLASH. In WEPC01, DIPAC,Venice, Italy, 2007.

[59] D. Alesini. Linear accelerators [introduction of accelerator physics], the CERN accelerator school, 2016 Budapest, Hungary.

[60] K. Floettmann. RF-induced beam dynamics in RF guns and accelerating cavities. Physical Review Special Topics-Accelerators and Beams, 18(6):064801, 2015.

[61] Center for the Advancement of Natural Discoveries using Light Emission. Electron beam parameter measurements. http://candle.am/german-armenian-school-2021/courses/relativistic-electron/, 2021.

[62] C. Bruni et al. First electron beam of the ThomX project. In IPAC'22, Thailand. JACOW, 2022.

[63] T. Vinatier et al. Measurement of low-charged electron beam with a scintillator screen. Proc. of IPAC, 14, 2014.

[64] C. Bruni et al. Travaux Pratique sur accélérateur de particules dynamique d'un faisceau d'électrons de quelques MeV et diagnostics associés, M2 - Grands Instruments, University of Paris sud, 2016-2017.

[65] A. Latina. Introduction to Transverse Beam Dynamics - JUAS, CERN, 2019.

[66] H. Purwar et al. Estimation of longitudinal dimensions of sub-picosecond electron bunches with the 3-phase method. In 8th Int. Particle Accelerator Conf.(IPAC'17), Copenhagen, Denmark, 14â 19 May, 2017, pages 139–141. JACOW, Geneva, Switzerland, 2017.

[67] RI Research Instruments. https://research-instruments.de/.

[68] H. Deruyter et al. Symmetrical double input coupler development. Technical report, Stanford Linear Accelerator Center, 1992.

[69] J. Haimson et al. A racetrack geometry to avoid undesirable azimuthal variations of the electric field gradient in high power coupling cavities for TW structures. In AIP Conference Proceedings, volume 398, pages 898–911. American Institute of Physics, 1997.

[70] N. Christopher et al. Low-field accelerator structure couplers and design techniques. Physical Review Special Topics-Accelerators and Beams , 7(7):072001, 2004.

[71] W. Wuensch. Progress in understanding the high-gradient limitations of accelerating structures. Technical report, 2007.

[72] WD. Kilpatrick. Criterion for vacuum sparking designed to include both RF and DC. Review of Scientific Instruments, 28(10):824–826, 1957.

[73] T.J. Boyd. Kilpatrick's criterion. Group AT-1 Technical Report: AT-1:82-28,. Technical report, Los Alamos, 1982.

[74] Jorge Giner Navarro. Breakdown studies for high-gradient RF warm technology in: CLIC and hadron therapy linacs. PhD thesis, Universitat de València, 2017.

[75] W. Wuensch. The scaling of the traveling-wave RF breakdown limit. Technical report, 2006.

[76] Walter Wuensch. Observations About RF Breakdown From the CLIC High-Gradient Testing Program. In AIP Conference Proceedings, volume 877, pages 15–21. American Institute of Physics, 2006.

[77] A. Grudiev et al. New local field quantity describing the high gradient limit of accelerating structures. Physical Review Special Topics-Accelerators and Beams, 12(10):102001, 2009.

[78] K. N. Sjobak et al. New criterion for shape optimization of normal-conducting accelerator cells for high-gradient applications. Technical report, 2014.

[79] David Peace Pritzkau. RF pulsed heating. PhD thesis, Stanford University, 2001.

[80] C. Adolphsen. Update on structure high gradient development,Tech. Rep. NLC News - Vol. 3, No. 7. Technical report, 2002.

[81] L. Laurent et al. Experimental study of rf pulsed heating. Physical review special topics-accelerators and beams, 14(4):041001, 2011.

[82] Ian H Wilson. Cavity construction techniques. 1992.

[83] R. Richard et al. Fabrication of optics by diamond turning. Handbook of optics, 1:41–41, 1995.

[84] E. Westbrook. Microwave impedance matching of feed waveguides to the disk-loaded accelerator structure operating in the $2\pi/3$ mode. SLAC, USA, Rep. SALCTN-63-103, 1963.

[85] Charles W Steele. A nonresonant perturbation theory. IEEE Transactions on Microwave theory and Techniques, 14(2):70–74, 1966.

[86] T. Khabiboulline et al. A new tuning method for traveling wave structures. In Proceedings Particle Accelerator Conference, volume 3, pages 1666–1668. IEEE, 1995.

[87] SPINNER GROUP. https://www.spinner-group.com.